Transport Properties of Intense Ion Beam Pulse Propagation for High Energy Density Physics and Inertial Confinement Fusion Applications

Mikhail A. Dorf

A DISSERTATION

PRESENTED TO THE FACULTY

OF PRINCETON UNIVERSITY

IN CANDIDACY FOR THE DEGREE

OF DOCTOR OF PHILOSOPHY

RECOMMENDED FOR ACCEPTANCE

BY THE DEPARTMENT OF

ASTROPHYSICAL SCIENCES

PROGRAM IN PLASMA PHYSICS

Adviser: Ronald C. Davidson

SEPTEMBER, 2010

Abstract

The design of ion drivers for warm dense matter and high energy density physics applications and heavy ion fusion involves the acceleration and compression of intense ion beams to a small spot size on the target. Typically, ion beam acceleration and transport in vacuum is provided by a periodic focusing accelerator. Then, a dense background plasma is used to neutralize the beam space-charge during the longitudinal compression process. Finally, additional transverse focusing can be provided by a strong (several Tesla) final focus solenoid. In this thesis, the transport properties of an intense ion beam pulse propagating in an ion driver are investigated by making use of advanced numerical particle-in-cell simulations and reduced analytical models.

In particular, in order to study the properties of an intense beam quasi-equilibrium matched to a periodic focusing lattice, a numerical scheme is developed that allows for the quiescent formation of a matched beam distribution. Also, the problem of controlling the transverse beam envelope by variations in the lattice amplitude is addressed, and a detailed quantitative analysis of the associated halo particle production is performed. Ion beam pulse transport though a dense background plasma is investigated with emphasis on the effects of a weak solenoidal magnetic field (~100 G), which can be present inside the long drift section due to the fringe fields of the strong final focus solenoid. In particular, whistler wave excitation and the effects of self-focusing on ion beam propagation through a background plasma along a solenoidal magnetic field are analyzed. Finally, the

feasibility of using a weak (~ 100 G) collective focusing lens for a tight final focus of the ion beam is investigated. The results of the thesis research are analyzed for the parameters characteristic of the Neutralizing Drift Compression Experiment (NDCX-I) and its planned upgrade (NDCX-II).

Dedicated to

my parents, Evgenia and Alexander Dorf,

my brother, Leonid Dorf,

and my grandmother, Haya Ratz,

for their endless love and support.

Acknowledgments

First and foremost, I would like to thank my thesis advisor, Ronald C. Davidson, whose deep physical insights and tremendous experience constantly guided me throughout this work. He provided me with a unique opportunity to work on a variety of incredibly interesting projects in the areas of beam and plasma physics, and taught me the invaluable skill of multitasking. I also deeply appreciate his dedicated and meticulous proofreading through which I learned a great deal about scientific writing. Ron's continuous encouragement and support made my graduate studies at Princeton an enjoyable experience, and his outstanding work ethic set an example for me to follow.

I am also greatly thankful to Igor Kaganovich and Edward Startsev for the pleasure of working with and learning from them. Their brilliant scientific intuition and profound expertise helped me find interesting problems and get motivated. In addition, I would like to thank Igor for devoting time to the reading of this thesis, and providing constructive suggestions.

I am much obliged to Genady Fraiman for encouraging me to apply to the Program in Plasma Physics at Princeton University, and to Nat Fisch and Barbara Sarfaty for welcoming me here. I would like to offer my sincere thanks and appreciation to Nat for his continuous interest in my academic and scientific achievements, as well as his

encouragement and strong support, and to Barbara for her tireless effort on behalf of any problem I was facing either as a foreign graduate student, or just on a personal level.

It was a pleasure to be a member of the Beam Physics and Nonneutral Plasma Division of PPPL. In addition to Ron, Igor, and Ed, I would like to acknowledge other past and present group members. It was an invaluable experience and great fun to assist Erik Gilson and Moses Chung by carrying out the numerical simulations of the Paul Trap Experiment. My sincere thanks are due to Hong Qin for the numerous fruitful discussions about beam physics, as well as for his careful reading of this thesis and suggested improvements. I am grateful to Adam Sefkow for introducing me to the LSP code, and helping with my initial simulations. Finally, I learned a lot from Phil Efthimion, Dick Majeski, Larry Grisham and Andy Carpe who provided their scientific expertise at group meetings. I also extend my heartfelt gratitude to Yevgeny Raitses, who frequently interacts with the members of the Nonneutral Plasma Division, and generously shared with me his deep knowledge in the areas of low temperature plasmas and experimental plasma physics.

It is hard to overestimate the contribution of the Institute of Applied Physics in Nizhny Novgorod, Russia to my education and perspective of physics research. My profound gratitude goes to Profs. V. E. Semenov, V G. Zorin, S. V. Golubev, and Dr. A.V. Savilov, whose ideas and insights always inspired me. The ECR Team has been a friendly and productive group of individuals, with whom I enjoyed interacting. Finally, my warmest and deepest thanks are due to Dr. Yurii V. Bykov for his endless support.

It was a pleasure to work together with my colleagues at Heavy Ion Fusion Virtual National Laboratory on the numerical modeling of the Neutralized Drift Compression Experiment. I would like to acknowledge John Barnard, Ron Cohen, Alex Friedman, Dave Grote, Irv Haber, Ed Lee, Steve Lidia, Grant Logan, Steve Lund, Peter Seidl, Bill Sharp, and Jean-Luc Vay for stimulating discussions and their warm-hearted hospitality during my visits to Berkeley. Special thanks are due to Dave Grote of Lawrence Berkeley National Laboratory and Dale Welch of Voss Scientific for their expert services in implementation of the WARP and LSP codes.

My years at Princeton were made much more pleasant by my fellow graduate students, Brendan, Lora, Adam, Jon-Kyu, Jeff and Jess, who were always there for a cheerful talk. Special thanks go to Brendan and Lora for introducing me to the many aspects of the U.S. culture. My Russian friends at Princeton were always there for me in the worst and best of times, and made my life full of exciting events, which will be deeply missed. I thank Artem and Dasha, Andrej and Lena, Ilya and Zhenya, Igor and Natasha, Mikhail and Tanya, Sasha and Sasha, Sasha and Nastya, Yrij and Olya, Zhenya and Anya, Andrey, Dima, Ira, Kolya, Kostya, Lena Z., Mitya, Sergej, Zaur, and many other really great people. It was a great joy to reunite in the U.S. with my good old friends Andrey “Sok” Sokolov, Alexander “Hammet” Zharov, Vitalij “Vitt” Potapov, and Sergej Antipov; and my trips to Russia have always been great fun due to the tireless and selfless effort of Andrey “Duv” Duvin.

Finally, this work would be absolutely impossible without the endless love and support of my family: my parents, Evgenia and Alexander, my brother Lenya, and my grandmother Haya, to all of whom I dedicate this thesis.

This research was supported by the U.S. Department of Energy.

Contents

List of Figures

List of Tables

Chapter 1

Introduction

The high efficiency of energy delivery and deposition makes intense ion beam pulses particularly attractive for high energy density physics applications and inertial confinement fusion [Davidson, 2002]. Recent advances in ion accelerators and focusing systems have made possible the production of high energy density condition and warm dense matter phenomena under controlled laboratory conditions. For instance, density-temperature regimes similar to the interiors of giant planets and low-mass stars can be accessible in compact beam-driven experiments [Logan *et al*., 2007]. In addition to fundamental physics applications, the use of intense heavy ion beams for compression and heating of a target fuel is a promising approach to inertial confinement fusion energy applications (so-called heavy ion fusion) [Arnold, 1978]. Ion-beam-driven high energy density physics and heavy ion fusion attract the interest of leading research institutions and laboratories around the world, including the United States [Logan *et al*., 2007; HIFS White Paper, 2008], Russia [Sharkov, 2007], Germany [Hoffmann *et al*., 2009], and Japan [Horioka *et al*., 2009].

An intense high energy ion beam is produced and delivered to the target by an *ion driver*. In this thesis work, transport properties of an intense ion beam pulse propagating in an ion driver are investigated.

1.1 Ion Drivers

A schematic of an ion driver for warm dense matter and high energy density physics applications, and heavy ion fusion is shown in Fig. 1.1. Leaving the ion source, an ion beam pulse is matched into the accelerator region, where the directed kinetic energy of the beam ions is significantly increased. The transverse confinement of the ion beam in the accelerator section against strong space-charge forces is typically provided by a periodic focusing lattice consisting of quadrupole or solenoidal focusing magnetic or electrostatic lenses. In order to increase the intensity of the long ion beam pulse, temporal and spatial compression occurs in the subsequent compression section. One of the modern approaches to the compression process is to use dense background plasma, which charge neutralizes the ion charge bunch, and hence facilitates compression of the charge bunch against strong space-charge forces. Finally, additional focusing is provided in the final focus section, and then the compressed ion bunch deposits its energy into the target.

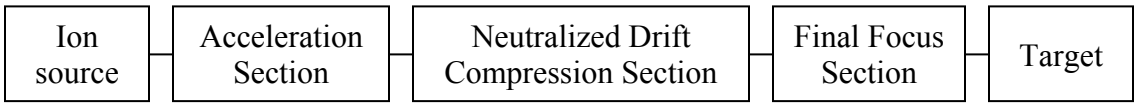

Fig. 1.1: Block diagram of an ion driver for ion-beam-driven warm dense matter and high energy density physics applications, and inertial confinement fusion.

Conceptual design of a heavy ion fusion driver:

A block diagram of a possible heavy ion fusion driver [Kwan, 2004] presenting the conceptual design parameters of an ion beam pulse as it propagates through the driver is shown in Fig. 1.2. The total beam current from the ion source is typically designed to be in the range 50-100 A. Therefore, to overcome the space-charge forces associated with high-current heavy ion beams, a heavy ion fusion driver is usually designed to contain an array of ~100 parallel ion beam channels at ~0.5 A each. The acceleration of the ion beam pulses starting from a 2-3 MeV injector to 100GeV can be provided by induction linear accelerators, which are also capable of compression of the beam pulses from ~10,000 ns at the source to ~100 ns at the end of the accelerator section [Kwan, 2004].

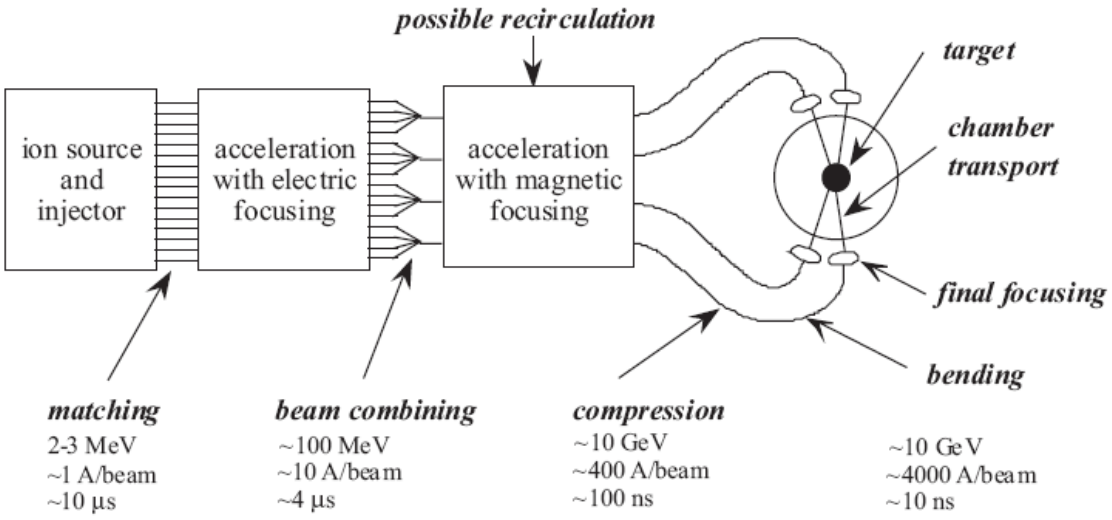

Fig. 1.2: Block diagram of a typical heavy ion beam driver for inertial fusion energy [Kwan, 2004].

Neutralized Drift Compression Experiment-I (NDCX-I):

Although a full-scale heavy ion fusion test facility with high-gain target physics is presently in a design stage, a compact heavy ion driver for warm dense matter experiments (NDCX-I) has been recently built at the Lawrence Berkeley National Laboratory [Seidl *et al*., 2009]. In this ion-beam-driven experiment the ion beam energy is deposited into a thin (a few microns) target aiming to reach warm dense matter conditions, regimes corresponding to solid-state densities and temperatures of order 1 eV. More specifically, a target temperature of 0.2 eV - 0.5 eV is expected to be achieved in experiments on the NDCX-I facility. It should be pointed out that a few micron target will hydro-expand in a few nanoseconds at 1 eV, and therefore the energy has to be deposited by short pulses of order 1 ns duration. The schematic of the Neutralized Drift Compression Experiment is shown in Fig. 1.3. A singly-ionized Potassium (K^+) ion beam pulse with duration of several microseconds and directed ion energy of ~300 keV is produced from an alumino silicate source powered by a Marx generator. The beam pulse carries a current I_b ~ 30 mA, and the characteristic beam radius is the order of 1 cm. Leaving the source, the beam is matched into a solenoidal transport lattice, which controls the beam envelope. In order to compensate for misalignments of the beamline components, which can lead to an offset of the beam centroid, three steering dipoles are placed inside the gaps between the solenoids. Passing through the final (4^{th}) transport solenoid, the ion beam acquires a radial convergence angle, typically of the order 10 mrad, and then a head-to-tail velocity tilt is imparted to the beam pulse inside the

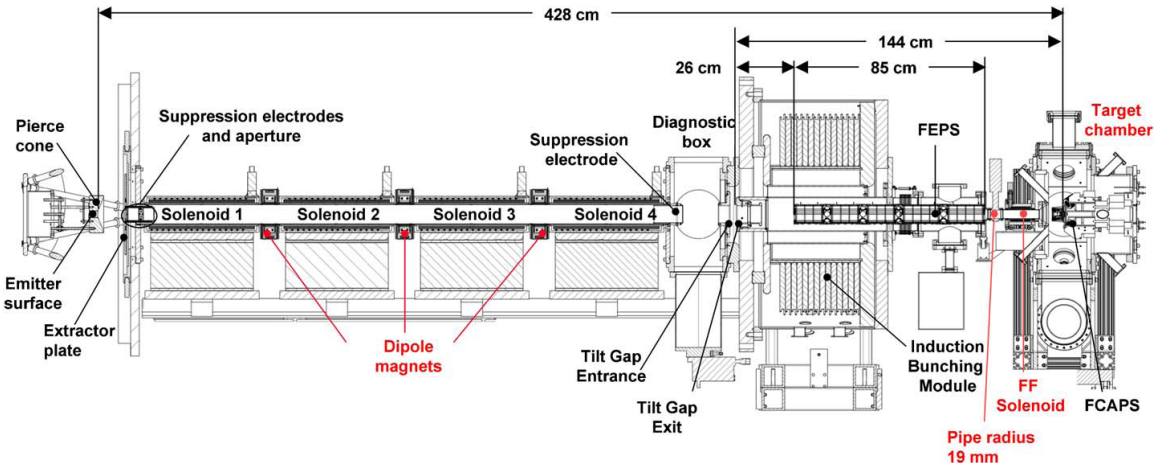

Fig. 1.3: Elevation view of the Neutralized Drift Compression Experiment - I (NDCX-I) [Seidl *et al*., 2009].

acceleration (tilt) gap of the induction bunching module. A schematic of the induction bunching module is shown in Fig. 1.4. A time-dependent current passes through high-voltage feedthroughs encircling the ferromagnetic core(s). As a result, the azimuthal magnetic flux through the ferromagnetic materials varies in time and induces a time-dependent longitudinal electric field in the accelerator gap as illustrated in Fig. 1.4. The charge bunch encounters the induced electric field only within the acceleration gap, and the pulse modulators and cores are external to the beam-plasma-chamber system. The time-dependent electric field produced inside the acceleration gap imparts a head-to-tail velocity tilt to the beam pulse by decelerating the head of the beam pulse, and accelerating the tail of the beam pulse. As a result, the ion bunch undergoes a longitudinal compression as it propagates through the long drift section (L_d=85 cm) filled with a dense neutralizing plasma. Provided the plasma is sufficiently dense it can effectively neutralize the charge and current of the ion beam pulse [Kaganovich *et al*.,

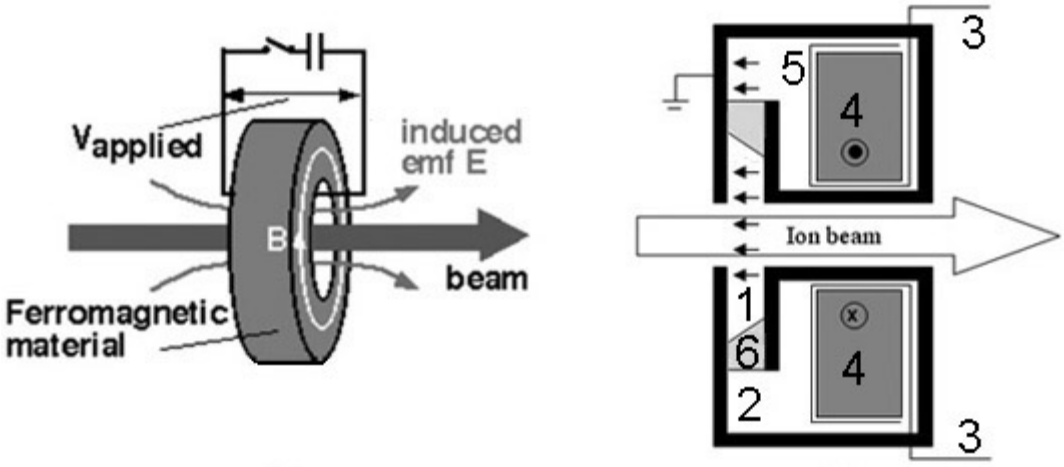

Fig. 1.4: The physics principles of the induction module (left). A cross-section (right, with φ symmetry) of the induction module: acceleration gap (load circuit region under vacuum) (1), transformer oil insulation for induction cavity (leakage circuit region) (2), insulated power feed (3), ferromagnetic core (4), exposed face of core (5), and vacuum insulator (6). The E_z field direction in the gap is indicated for the given B_φ field direction in the ferromagnetic core [Sefkow, 2007].

2010]. Therefore, nearly-ballistic (field-free) simultaneous longitudinal and transverse beam compression occurs inside the drift section. Finally, an additional transverse focusing of the ion beam pulse is provided by a short (l_s = 10 cm) high-field (B_s =8 T) final focus solenoid, which is placed downstream of the drift section. Note that in order to compensate for the strong space-charge forces of the compressed ion beam pulse, the final focus solenoid has to be filled with a neutralizing plasma as well.

In the present configuration of the Neutralized Drift Compression Experiment – I (NDCX-I), the large volume neutralizing background plasma inside the drift section is produced by a ferroelectric plasma source [Efthimion *et al.*, 2007]. This plasma source

utilizes the concept of large electric fields on a surface of a ferroelectric material (with a large dielectric constant), and allows for the generation of high-density surface plasma. In the present NDCX-I configuration, the walls of the drift section are made of a ferroelectric material, and a surface discharge is produced by applying a pulsed biased voltage between rear and front electrodes placed on both sides of the ferroelectric wall. A high-density surface plasma, initially created on the ferroelectric surfaces, then flows toward the axis and fills the entire drift section. It was demonstrated [Sefkow *et al*., 2008] that this source provides plasma density of $\sim 10^{10} cm^{-3}$ on the axis of the beamline, which can be enough to provide complete charge neutralization in the drift section for the ion beams explored in the NDCX-I.

The density of the plasma created by the ferroelectric plasma source decreases to zero outside the drift section over a short distance of several centimeters. Therefore, to provide a neutralizing background inside the final focus solenoid, four cathodic-arc plasma sources (CAPS) are used in the present configuration of the NDCX-I device. The sources are placed out of the line-of-sight of the beamline in order to avoid interaction with the ion beam, and angled toward the axis of the final focus solenoid (Fig. 1.3). It should be noted that filling the strong magnetic solenoid with a neutralizing plasma is itself a challenging problem [Roy *et al*., 2009], and providing improved neutralizing plasma background inside the final focus solenoid is still one of the critical problems in NDCX-I optimization.

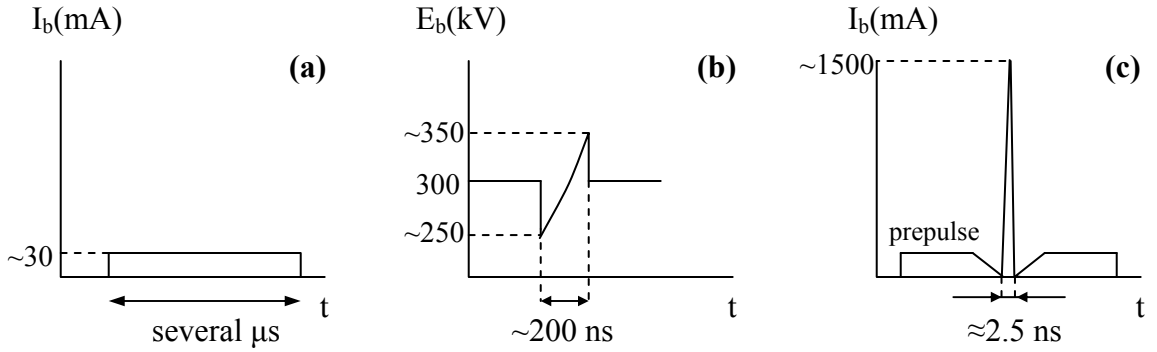

Fig. 1.5: Schematic of the longitudinal compression of ion beam pulses in the Neutralized Drift Compression Experiment – I (NDCX-I). The frames illustrate the time dependence of (a) the ion beam current at the ion source, (b) the directed beam energy at the exit of the tilt gap, and (c) the ion beam current at the longitudinal focal plane.

It is straightforward to show for the case of ballistic (field-free) beam compression that the beam tail will meet the beam head at the longitudinal focal plane, provided the voltage waveform, $\Delta V_{tilt}(t) = \int E_z(t) dz$, produced across the acceleration (tilt) gap of the induction bunching module is specified by [Welch *et al*., 2005; Sefkow, 2007]

$$\Delta V_{tilt}(t) = \frac{m_b c^2}{2e}\left[\beta_b^2 - \left(\frac{\beta_h}{1 - c\beta_h t / L_f}\right)^2\right].$$

Here, $\beta_b = v_b / c$ is the normalized directed beam velocity upstream of the tilt gap, $\beta_h = 0.0037$ is the normalized velocity of the beam head downstream of the tilt gap, and L_f corresponds to the drift length to the ideal longitudinal focal plane. The volt-second

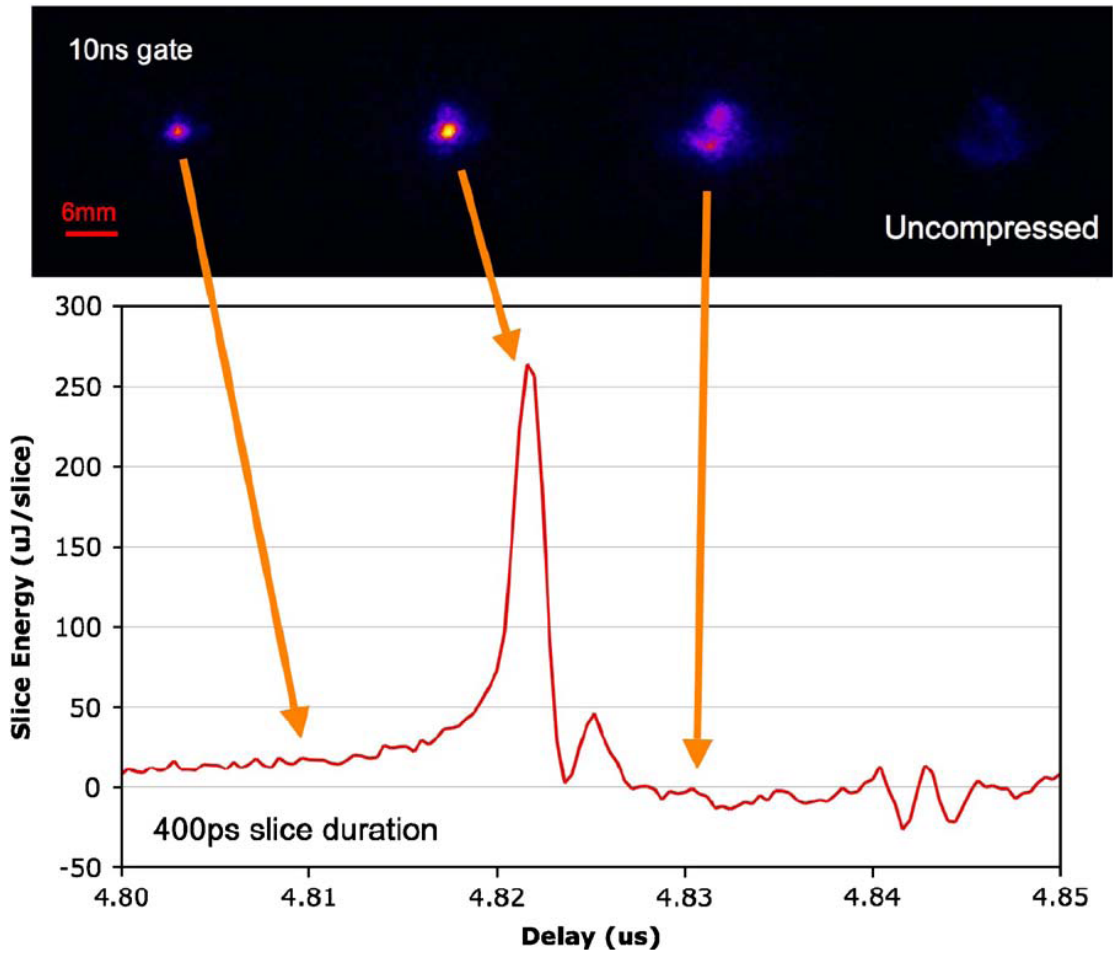

Fig. 1.6: (Color) Time-dependent transverse beam distributions demonstrating the simultaneous transverse focusing at the time of peak compression. The full width at half maximum (FWHM) of the peak is ≈2.5 ns [Seidl *et al*., 2009].

capability of the induction bunching module allows compression of only a ~200 ns portion of the entire (several microsecond) ion beam pulse, and the schematic of the longitudinal beam dynamics is shown in Fig. 1.5. Note that there is a long uncompressed part of the ion beam pulse (prepulse) that propagates ahead of the compressed portion of the ion beam.

The results of the experiments on the NDCX-I facility demonstrating the simultaneous longitudinal and transverse compression are shown in Fig. 1.6 [Seidl *et al*., 2009]. The longitudinal compression decreases the duration of the compressing (~200 ns) portion of the ion beam pulse to $\tau_c \approx 2.5$ ns, and the peak bunch current is increased to $I_p \approx 1.5$ A. Furthermore, at peak compression, 50% of the beam flux is located within a radius of 1.5mm due to the transverse compression.

Finally, it should be noted that the induction bunching module (IBM) has been recently upgraded, and the upgraded IBM has a nearly double volt-second capability. Design studies [Seidl *et al*., 2009] demonstrated that it is advantageous to use the increased capability for compression of a ~400ns portion of the beam pulse, with a shallower slope of the tilt and a correspondingly longer drift section. Accordingly, in the present configuration of the Neutralized Drift Compression Experiment – I (NDCX-I), the drift compression section has been increased by 1.44 m by extending the length of the ferroelectric plasma source. The experiments on ion beam compression including the upgraded IBM and longer drift section are currently being carried out on the NDCX-I facility.

Neutralized Drift Compression Experiment – II (NDCX-II):

While a target temperature of only 0.2 eV - 0.5 eV is expected to be achieved on the NDCX-I facility, its planned upgrade (NDCX-II) will operate at higher beam energies (few MeV), and will allow for target heating up to 1-2 eV [HIFS White Paper, 2008; Friedman *et al*., 2009]. Another important feature of the upgraded NDCX-II driver is that it will allow for highly uniform heating of a few microns target, using Li^+ ions which enter the target with kinetic energy of ~ 3 MeV, slightly above the Bragg peak for deposition (the peak in d*E*/d*x*), and exit with energies slightly below that peak. A schematic illustration of Lithium ion beam energy deposition in the aluminum foil is shown in Fig. 1.7, and the NDCX-II target concept and ion driver requirements for achieving a target temperature greater than 1 eV is shown in Fig. 1.8.

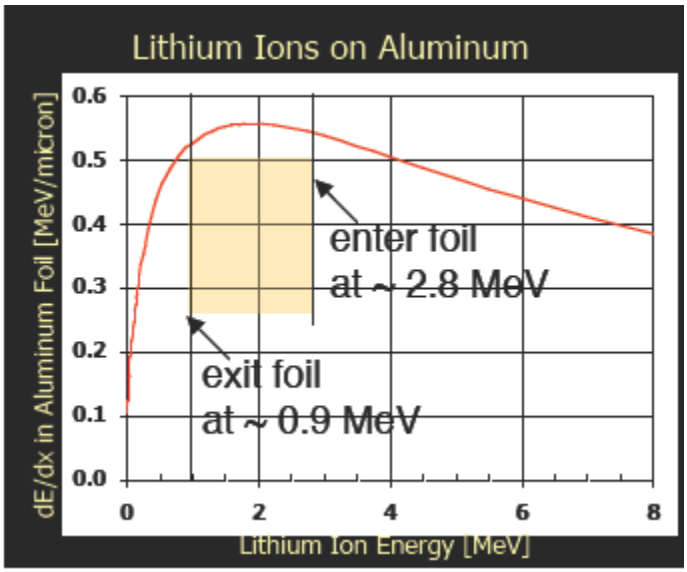

Fig. 1.7: (Color) Schematic of the energy deposition of lithium ions into an aluminum target, demonstrating the possibility of highly uniform heating of a few micron target by using ~3 MeV Li^+ ions beams in the NDCX-II facility [Friedman, 2007].

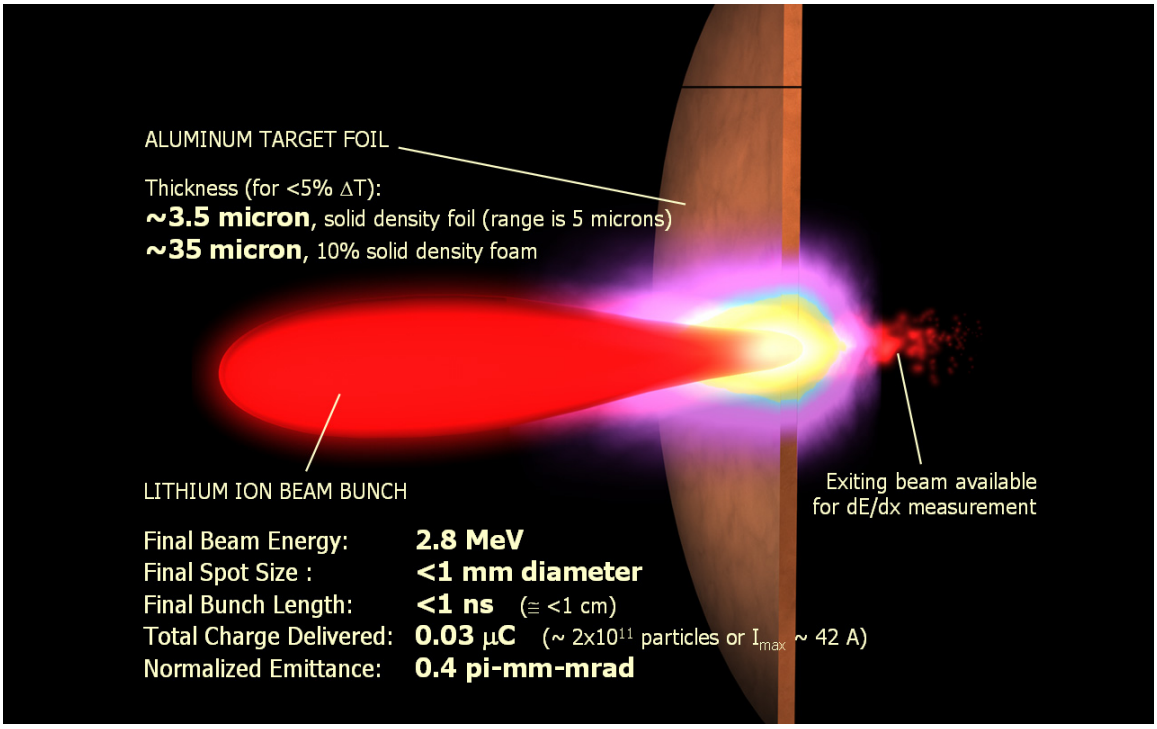

Fig. 1.8: (Color) Figure shows the NDCX-II target concept, and driver requirements to achieve target temperature higher then 1 eV [Friedman, 2007].

A schematic of the NDCX-II facility is shown in Fig. 1.9. Similar to the NDCX-I device, the NDCX-II ion driver utilizes the concept of simultaneous neutralized (near-ballistic) drift compression inside a few meters drift section, as well as final transverse focusing by a several-centimeter-long high-field (several Tesla) final-focus solenoid. However, the acceleration section of the NDCX-II facility is much more complex compared to the four-solenoid transport section of the NDCX-I device, where only the transverse beam envelope is controlled. The NDCX-II acceleration system accelerates the ion beam, provides longitudinal compression (thus increasing the beam current), and finally controls the transverse beam envelope. The acceleration and

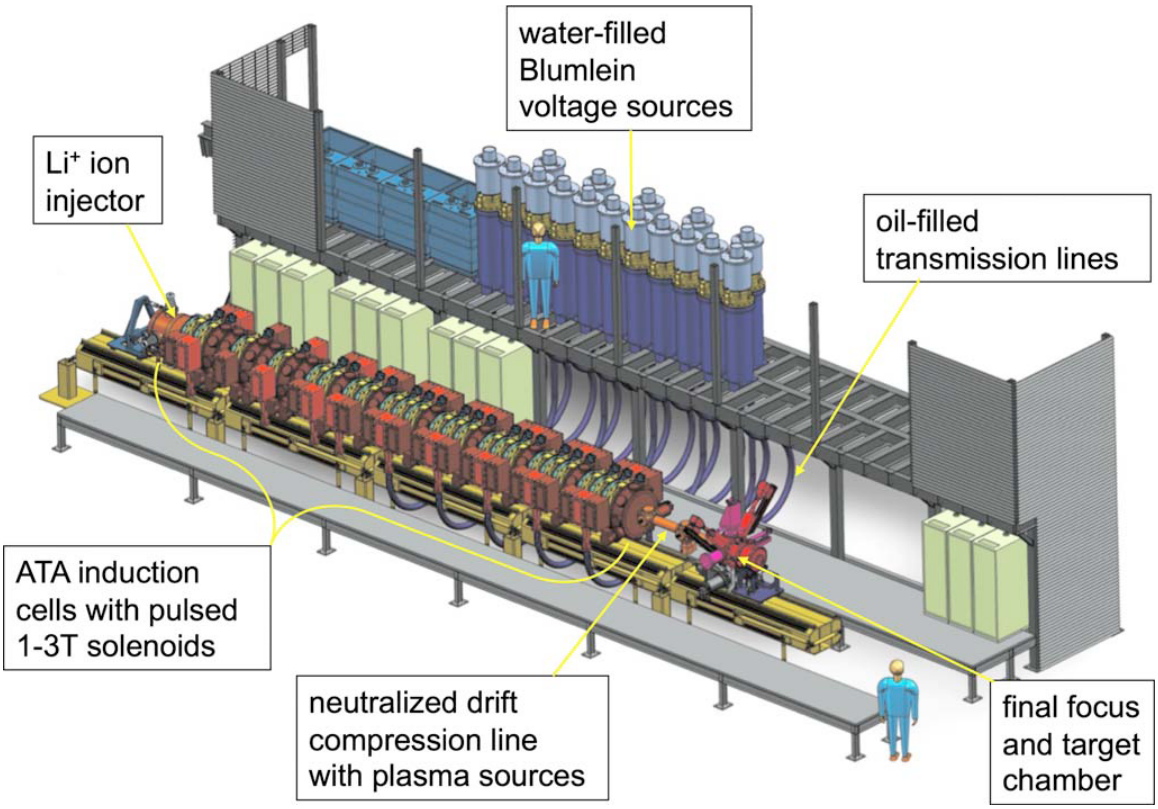

Fig. 1.9: (Color) NDCX-II layout for 23 induction cells [Friedman *et al*., 2010].

longitudinal compression of the ion beam pulse is provided by the induction cells from the decommissioned Advanced Test Accelerator (ATA) facility at Lawrence Livermore National Laboratory (hereafter, ATA cells). The operational principles of an ATA cell are the same as those of the NDCX-I induction bunching module. That is, depending on the voltage waveform applied in the acceleration gap of an ATA cell, each cell can accelerate the ion beam pulse and impart a head-to-tail velocity tilt. The control of the beam transverse envelope is provided by 2-3 T confining transport solenoids.

In recent design studies [Friedman *et al*., 2009; Friedman *et al*., 2010] it is assumed that the NDCX-II injector produces Lithium (Li^+) ion beam pulse with duration

of ~500 ns, directed beam energy of ~ 100 keV, and the current of ~70 mA. The ion beam pulse then propagates through the acceleration section, where it is accelerated to ~3.5 MeV, and its current increases to ~2 A due to the nonneutral longitudinal drift compression. Leaving the acceleration section, the radially convergent ion beam pulse with an imparted head-to-tail velocity tilt propagates through a few-meter-long neutralized drift section, then passes through a 10-15 Tesla final focus solenoid, and finally deposits its energy into the thin target. The results of the numerical design studies demonstrate that about 75% of the 30nC beam charge crosses the focal plane in a 1-ns window, with a minimal pre-pulse. The current of the compressed beam (averaged over that window) is 23 A, with a peak (averaged over a 0.1-ns window) of 32 A and a full-width at half maximum of 1 ns [Friedman *et al*., 2009].

Future facilities for ion-beam-driven high energy density physics and heavy ion fusion:
The future plans of the US heavy-ion-fusion program involve building of the Integrated Beam – High Energy Density Physics Experiment (IB-HEDPX) based on the knowledge base established by the NDCX-II device [HIFS White Paper, 2008]. The IB-HEDPX device will be a flexible user facility, with greater flexibility in choice of ion for Bragg-peak heating, higher kinetic energy (up to 25 MeV), advanced multiple-target handling capabilities, and a much richer set of diagnostics than NDCX-II. Beyond IB-HEDPX, and building on the anticipated achievement of ignition on the National Ignition Facility (NIF), high coupling efficiency will allow heavy ion beams to explore the implosion of

Table 1.1: Scientific objectives and key features of a sequence of heavy-ion-beam driven facilities for high energy density physics and fusion [HIFS White Paper, 2008].

HEDP/Inertial Fusion Energy Science Objective **(Facility)**	Ion	Linac voltage - MV	Ion energy - MeV	Beam energy - J	Target pulse - ns	Range -microns (in ..)	Energy density 10^{11}J/m^3
Beam compression physics, diagnostics. Sub-eV WDM. **(NDCX-I) (1 beam)**	K+	0.35	0.35	0.001-0.003	2-3	0.3/1.5 (in solid/ 20% Al)	0.04 to 0.06
Beam acceleration and target physics basis for IB-HEDPX. **(NDCX-II) (1 beam)**	Li^{+1}, or Na^{+3}	3.5 - 5	3.5 - 15	0.1 - 0.28	1-2 (or 5 w hydro)	7 - 4 (in solid Al)	0.25 to 1
User facility for heavy-ion driven HEDP. **(IB-HEDPX) (1 beam)**	Na^{+1} or K^{+3}	25	25 – 75	3 – 5.4	0.7 (or 3 w hydro)	11 – 8 (in solid Al)	2.2 To 5.8
Heavy-ion direct drive implosion physics. **(HIDDIX) (2 beams)**	Rb^{+9}	156	1000	2x7.5 (kJ)	2 - 4	1000 (in solid Z=1)	18
Heavy ion fusion test facility - -high gain target physics. **(HIFTF) (40-200 beams)**	Rb^{+9}	156	1000	300 to 1500 (kJ)	12 -24	1000 (in solid Z=1)	90

mm-scale cryo-targets at moderate energy and cost in the Heavy Ion Direct Drive Implosion Experiment (HIDDIX) facility. This would provide the capability to drive low-convergence-ratio (5-10) spherical implosions with ion beams for the first time, and to explore issues of hydrodynamic stability to Rayleigh-Taylor modes under the stabilizing influence of non-normal ion beam illumination. Encouraging results in those areas and others would motivate development of a Heavy Ion Fusion Test Facility (HIFTF) [HIFS White Paper, 2008].The Scientific objectives and key features of a sequence of heavy-ion-beam-driven facilities for high energy density physics and heavy ion fusion are summarized in Table 1.1.

1.2 Motivation

An noted earlier, an ion beam driver is a complex transport system involving ion beam pulse propagation through a vacuum acceleration system, propagation through a neutralizing background plasma, and strong magnetic final focusing. Therefore, in order to improve the performance of a heavy ion driver, it is of great importance to achieve a better physics understanding of the beam transport properties. In particular, it is important to realize nonlinear and collective effects that become increasingly important for high-intensity ion beams. In what follows we outline several critical problems in intense ion beam transport through the acceleration section, the neutralized drift compression section, and the final focus section of an ion driver.

Ion beam transport in the acceleration section:

Although, initial ion-beam-driven experiments (e.g. NDCX-I) can use several short solenoidal or quadrupole magnetic lens to control the beam envelope from the injector to the neutralized drift compression section, future ion-beam-driven facilities will operate at much higher beam energies, and will require a long acceleration section. Accordingly, a transport focusing system with a large number of focusing elements has to be employed to maintain transverse beam confinement against strong self-field forces during the acceleration. Typically, a periodic focusing lattice, which consists of ether solinodial or quadrupole focusing elements, is used for these purposes [Davidson and Qin, 2001a]. Quiescent propagation of an intense ion beam through a periodic focusing lattice with

minimal irreversible growth of the transverse beam phase-space area (emittance) is of particular importance for the subsequent neutralized drift compression phase. Therefore, analysis of intense beam quasi-equilibria (so-called *matched* distributions) in a periodic focusing lattice is critical for optimizing the ion driver design. However, imperfections in the focusing elements, as well as an initial mismatch between the injector and the transport lattice can result in collective *mismatch* oscillations of the transverse beam envelope. Also, the mismatch oscillations can be produced due to variations in the lattice amplitude designed to control the transverse beam envelope inside the accelerator. The relaxation of the beam mismatch can provide an increase in the statistical area of the transverse beam phase-space, and can also be responsible for the production of high-energy beam *halo* particles [Gluckstern, 1994]. The transverse excursion of these halo particles can be significantly outside the beam core, which degrades the beam quality and can lead to the activation of the chamber wall, or to an influx of particles released from the wall. The problem of halo particles becomes most pronounced for an intense charged particle beam with strong self-fields, and therefore it is of particular importance for an ion driver development to asses the influence of a mismatch on the beam transport properties.

Intense ion beam transport through a background neutralizing plasma:

Understanding the physical and technological limits of the neutralized drift compression of an intense ion beam pulse is of great practical importance both for present and future ion-beam-driven facilities. Even for the ideal case where a dense background plasma

provides ballistic (field-free) transport, simultaneous longitudinal and transverse compression can be limited by thermal effects of the ion beam, or due to the non-chromatic nature of the transverse aberrations acquired inside a finite-length tilt gap, where a head-to-tail velocity tilt is imparted to the beam pulse [Sefkow, 2007]. The ion beam compression can also be limited due to the development of various collective streaming instabilities, which can occur even for a perfectly neutralized initial state, i.e., complete initial neutralization of the beam charge and the beam current [Davidson *et al*., 2009; Startsev and Davidson, 2009]. Finally, it is of particular practical importance to estimate the degree of beam charge and current neutralization depending on the parameters of the background plasma, i.e., density, temperature, effects of ionization, etc. Although the critical problem of ion beam neutralization by a background plasma has been extensively studied in [Kaganovich *et al*., 2001, Kaganovich *et al*., 2010], a variety of new and unexplored physical properties appear in the presence of an external solenoidal magnetic field. A weak solenoidal magnetic field of order 100 G can be present inside the neutralizing drift section of a heavy ion driver over distances of a few meters from the strong final focus solenoid, which is located downstream of the beamline nearly after the drift section. Although, the V×B force produced by such a weak magnetic field typically do not have a pronounced influence on the ion beam dynamics, it can significantly modify the plasma electron response, and therefore alter the degree of ion beam charge and current neutralization [Kaganovich *et al*., 2008; Dorf *et al*., 2010]. It is therefore of particular importance for an ion driver development to asses the influence of a weak solenoidal magnetic field on the ion beam transport properties.

Final beam focusing:

Typically, in order to provide final transverse beam focusing, a strong (several Tesla) magnetic solenoid, placed downstream of the drift section, is involved in the design of an ion driver. Due to the strong space-charge self-fields of an intense ion beam pulse, a neutralizing plasma is also required inside the magnetic solenoid. Note that apart from the challenge of using a several Tesla magnetic solenoid, filling it with a background plasma provides additional technical challenges [Roy *et al*., 2009]. Furthermore, the fringe fields of the strong magnetic solenoid can penetrate deeply into the drift section at a magnitude of order 100 G, and can significantly influence the neutralized ion beam transport. In particular, strong nonlinear radial electric fields can be generated due to a local polarization of the magnetized plasma background by the moving ion beam [Dorf *et al*., 2009c]. These nonlinear fields can produce aberrations, thus limiting the transverse focus of the ion beam pulse. It is therefore of great practical interest to investigate alternative possibilities of the final beam transverse focusing.

1.3 Thesis Overview

In this thesis research, detailed numerical and analytical studies have been performed to improve theoretical understanding of the dynamics of intense beam propagation through an ion driver. An overview of this thesis is provided below.

Chapter 2 provides a brief overview of the general and reduced analytical models describing the nonlinear transverse dynamics of an intense charge particle beam

propagating through a periodic focusing lattice, and discusses critical problems in intense ion beam transport, including the production of halo particles and space-charge limits defining the stable regimes of beam propagation. It is shown that the oscillating nature of the focusing field, along with the nonlinear dynamics of the beam particles, provide a significant challenge for analytical studies of a matched quasi-equilibrium beam distribution. Therefore, to improve the theoretical understanding of beam quasi-equilibria distributions, a numerical scheme allowing for the quiescent formation of a matched beam distribution is developed. A quasi-equilibrium beam distribution matched to a periodic focusing lattice is achieved in numerical particle-in-cell simulations by means of the adiabatic turn-on of the oscillating focusing field. Quiescent beam propagation for over a hundred of lattice periods is demonstrated for a broad range of beam intensities, and the properties of the matched-beam distribution are investigated. In particular, self-similar evolution of the beam density profile is observed over a wide range of system parameters.

Chapter 3 addresses the problem of controlling the transverse beam envelope during its propagation through the acceleration section by variations in the strength of the periodic-focusing lattice. In particular, the transverse compression of an intense ion beam propagating though an alternating-gradient quadrupole lattice is investigated. It is evident that variations in a lattice amplitude can lead to a certain level of beam mismatch, which can result in emittance growth and production of halo particles. Hence, it is a matter of considerable practical interest to determine how smooth (adiabatic) the lattice transition should be to assure that matching is maintained during the compression. This problem is

investigated for a wide range of beam intensities, and it is concluded that ~10 lattice periods are typically required in order to maintain beam matching for ~2X compression. For the case of nonadiabatic compression, halo particle production by a beam mismatch acquired during the compression stage is studied. In particular, in order to perform a quantitative analysis of this effect, a novel spectral method for halo particle definition is developed. In addition, it is shown that the analysis, based upon the spectral method, can provide important insights into other critical problems in intense beam transport such as mismatch relaxation and the space-charge transport limits.

Chapter 4 discusses the propagation of an intense ion beam through a dense background neutralizing plasma along a weak (~ 100 G) solenoidal magnetic field. The electromagnetic field perturbations excited by the ion beam pulse are calculated analytically and verified by comparison with the numerical simulations. The degrees of beam charge neutralization and current neutralization are estimated, and the transverse component of the Lorentz force associated with the excited electromagnetic field is calculated. It is found that the application of a weak solenoidal magnetic field along the direction of ion beam propagation through a neutralizing background plasma can significantly enhance the beam self-focusing for the case where the beam radius is small compared to the collisionless electron skin depth. The enhanced focusing is provided by a strong radial self-electric field that is generated due to a local polarization of the magnetized plasma background by the moving ion beam. A positive charge of the ion beam pulse becomes overcompensated by the plasma electrons, which results in the radial focusing of the beam ions. The effect of the plasma-induced enhanced self-

focusing in the presence of weak fringe fields from a final focus solenoid is assessed for the parameters characteristic of the Neutralized Drift Compression Experiment-I (NDCX-I), and its planned upgrade NDCX-II. Finally, it is shown that the plasma response to the ion beam pulse is significantly different depending on whether the value of the solenoidal magnetic field is below or above the threshold value corresponding to the strong resonant excitation of large-amplitude whistler waves. The use of intense whistler wave excitations for diagnostic purposes is also discussed.

Chapter 5 investigates the feasibility of using a weak (~100 G) solenoidal magnetic field for tight collective final focusing of intense ion beams for the Neutralizing Drift Compression Experiment (NDCX-I). In the collective focusing scheme, a weak magnetic lens provides strong focusing of an intense ion beam carrying an equal amount of neutralizing electron background [Roberston, 1982]. For instance, a solenoidal magnetic field of several hundred gauss can focus an intense neutralized ion beam within a short distance of several centimeters. The enhanced focusing is provided by a strong self-electric field, which is produced by the collective electron dynamics. The numerical simulations are performed with the LSP particle-in-cell (PIC) code, and the results of the simulations are found to be in very good agreement with analytical predictions. Collective focusing limitations due to possible heating of the co-moving electrons during the transverse compression are also discussed. Finally, the original analysis of the collective lens operation, which assumes quasineutrality and small perturbations of the applied solenoidal magnetic field, is extended to the more general cases of nonneutral collective focusing and arbitrary perturbations of the applied solenoidal magnetic field

due to the presence of the beam. The influence of nonneutral collective focusing on the transverse dynamics of an ion beam pulse in the present configuration of NDCX-I, which involves a strong (8 Tesla) magnetic solenoid for the final beam focusing, is also discussed.

Finally, **Chapter 6** summarizes the conclusions drawn from the earlier chapters, and identifies possible areas of future research.

Chapter 2

Intense Charged Particle Beam Propagation through a Periodic Focusing Lattice

2.1 Introduction

Periodic focusing transport systems have a wide range of applications ranging from basic scientific research in high energy and nuclear physics to applications such as spallation neutron sources, nuclear waste treatment, ion-beam-driven high energy physics, and heavy ion fusion. Of particular importance at the beam intensities of practical interest are the effects of the intense self-fields produced by the beam space charge and current on determining the detailed equilibrium and nonlinear dynamics of the system. However, the nonlinear effects of the intense self-fields provide a significant challenge for detailed analytical studies. It is therefore increasingly important to develop reduced analytical models and advanced numerical techniques for an improved theoretical understanding of intense beam transport.

In Sec. 2.2 we present a brief overview of the general and reduced analytical models describing the nonlinear transverse dynamics of a charge particle beam propagating through a periodic focusing lattice, and discuss critical problems in intense ion beam transport, including the production of halo particles and space-charge limits defining the stable regimes of beam propagation. It is shown that the oscillating nature of the focusing field along with the nonlinear dynamics of the beam particles provide a significant challenge for analytical studies of a matched quasi-equilibrium beam distribution. Therefore, it is important to develop a numerical scheme allowing for the quiescent formation of a quasi-equilibrium beam distribution matched to a periodic focusing lattice. Section 2.3 presents a numerical method for the formation of a quasi-equilibrium beam distribution matched to a periodic focusing lattice by means of the adiabatic turn-on of the oscillating focusing field. Quiescent beam propagation for over a hundred of lattice periods is demonstrated for a broad range of beam intensities, and the properties of the matched-beam distribution are investigated.

2.2 Theoretical Models and Background

In this section, we summarize the general theoretical models used to describe the nonlinear transverse dynamics of a charged particle beam propagating through a periodic focusing lattice, and discuss critical problems in intense ion beam transport, including the production of halo particles and space-charge limits defining the stable regimes of beam propagation. The detailed self-consistent description of intense charged particle beam

transport based on the Vlasov-Maxwell equations is presented in Sec. 2.2.1. The simplified beam dynamics model, including the smooth-focusing approximation and the envelope equations are summarized in Sec. 2.2.2 and Sec. 2.2.3, respectively. In Sec. 2.2.4 the production of halo particles by a beam mismatch is described, and finally, Sec. 2.2.5 presents an overview of intense beam transport limits.

2.2.1 Vlasov-Maxwell Description

We consider an axially continuous intense charged particle beam propagating in the *z*-direction with average axial velocity V_b through a periodic focusing lattice with axial periodicity length *S*=const (Fig. 2.1). The beam is assumed to be *thin*, with characteristic transverse dimensions *a* and *b* in the *x* and *y* directions satisfying

$$a,b<<S. \tag{2.1}$$

Consistent with Eq. (2.1) we assume that the beam particle have large axial momentum $p_b = \gamma_b m_b \beta_b c$, and make use of the *paraxial approximation* [Davidson, 1990; Reiser, 1994]

$$p_x^2, p_y^2, (p_z - p_b)^2 << p_b^2 \tag{2.2}$$

$$K_b \equiv \frac{2N_b e_b^2}{\gamma_b^3 m_b \beta_b^2 c^2} << 1, \tag{2.3}$$

Here, p_x, p_y, and p_z are the components of a beam particle's momentum, K_b is the beam self-field perveance [Lawson, 1958], $N_b = \int dxdydx'dy' f_b(x, y, x', y', s)$ is the number of particles per unit axial length, $\gamma_b = (1-\beta_b^2)^{-1/2}$ is the relativistic mass factor, e_b and m_b are

the charge and rest mass of a beam particle, respectively, c is the speed of light *in vacuo*, and $\beta_b=V_b/c$. The beam dynamics in the transverse phase space (x, y, x', y') is described by the distribution function $f_b(x, y, x', y', s)$, where $s = s_0 + \beta_b ct$ is the effective axial coordinate, and $x' = dx/ds$ and $y' = dy/ds$ denote the dimensionless transverse velocities.

The thin-beam approximation permits a Taylor expansion of the applied focusing fields about the beam axis at $(x,y)=(0,0)$. The applied magnetic field of the focusing lattice can therefore be approximated as [Davidson, 1990]

$$\mathbf{B}_q = B_q'(z)\left(y\hat{\mathbf{e}}_x + x\hat{\mathbf{e}}_y\right), \tag{2.4}$$

for the case of an alternating-gradient *quadrupole lattice* [Fig. 2.1 (a)], and

$$\mathbf{B}_{sol} = B_z(z)e_z - \frac{1}{2}B_z'(z)\left(x\hat{\mathbf{e}}_x + y\hat{\mathbf{e}}_y\right), \tag{2.5}$$

for the case of a periodic-focusing *solenoidal lattice* [Fig. 2.1 (b)]. Here, $B_q'(z) = \left(\partial B_x^q/\partial y\right)_{(0,0)} = \left(\partial B_y^q/\partial x\right)_{(0,0)}$, and $B_z'(z) = \left(\partial B_z^{sol}/\partial z\right)_{(0,0)}$. It now follows that the applied focusing force is given by [Davidson, 1990; Davidson and Qin, 2001a]

$$\mathbf{F}_{foc} = -\gamma_b m_b \beta_b^2 c^2 \left[\kappa_x(s)x\hat{\mathbf{e}}_x + \kappa_y(s)y\hat{\mathbf{e}}_y\right], \tag{2.6}$$

where the corresponding lattice function $\kappa_x(s)$ and $\kappa_y(s)$ are specified by

$$\kappa_x(s) = -\kappa_y(s) \equiv \kappa_q(s) = \frac{e_b B_q'(s)}{\gamma_b m_b \beta_b c^2}, \tag{2.7}$$

for the case of a quadrupole lattice, and

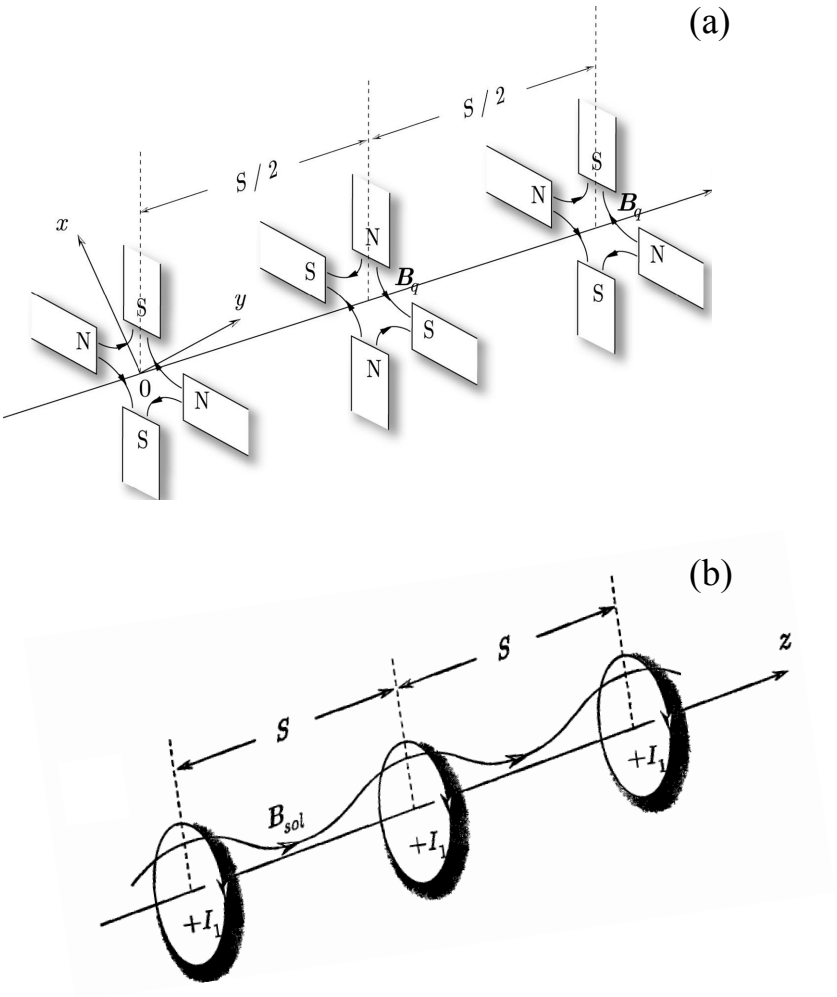

Fig. 2.1: Schematic of magnet sets producing (a) an alternating-gradient quadrupole field with axial periodicity *S*; and (b) a periodic focusing solenoidal field with axial periodicity *S*.

$$\kappa_x(s) = \kappa_y(s) \equiv \kappa_s(s) = \left(\frac{e_b B_z(s)}{2\gamma_b m_b \beta_b c^2} \right)^2 \tag{2.8}$$

for the case of a solenoidal lattice. The condition of lattice periodicity implies

$$\kappa_x(s) = \kappa_x(s+S)\,, \kappa_y(s) = \kappa_y(s+S)\,. \tag{2.9}$$

Finally, note that for the case of a quadrupole lattice $\langle \kappa_q(s) \rangle_s = 0$, and for the case of a solenoidal lattice $\langle \kappa_s(s) \rangle_s \equiv \bar{\kappa}_s > 0$, where $\langle ... \rangle_s = S^{-1} \int_{s_0}^{s_0+S} ds \cdots$ denotes the average of an *s*-dependent function over one lattice period *S*.

For an intense beam, the self-generated electric $\mathbf{E}^s(\mathbf{x},t)$ and magnetic $\mathbf{B}^s(\mathbf{x},t)$ fields have significant influence on the transverse dynamics of beam particles. In many regimes of practical interest the self-generated electric and magnetic fields can be approximated by [Davidson and Qin, 2001a]

$$\mathbf{E}^s = -\nabla \phi^s\,,$$

$$\mathbf{B}^s = \nabla \times A_z^s \hat{e}_z\,, \tag{2.10}$$

where the self-field potentials, $\phi^s(x,t)$ and $A_z^s(x,t)$, are determined self-consistently from

$$\nabla_\perp^2 \phi^s = -4\pi e_b \int dx'dy' f_b\,,$$

$$\nabla_\perp^2 A_z^s = -\frac{4\pi}{c} e_b V_b \int dx'dy' f_b\,. \tag{2.11}$$

Equations (2.11) yield $A_z^s = \beta_b \phi^s$, and it follows that the transverse component of the Lorentz force associated with the beam self-fields is given approximately by

$$\mathbf{F}_\perp^s = e_b\left(\mathbf{E}^s + \beta_b \hat{\mathbf{e}}_z \times \mathbf{B}^s\right) = -\frac{e_b}{\gamma_b^2}\nabla_\perp \phi \tag{2.12}$$

The reduction factor $1/\gamma_b^2 = 1-\beta_b^2$ in Eq. (2.12) is associated with focusing effect of the self-magnetic field created by the beam current. Therefore, the effects of the net beam self-field are weak for the case of a highly relativistic beam. However, self-field effects can become much more pronounced for weakly relativistic or nonrelativistic beams.

Introducing the normalized self-field potential $\psi(x,y,s) = \dfrac{e_b\phi(x,y,s)}{\gamma_b^3 m_b \beta_b^2 c^2}$, it is readily shown that the nonlinear Valsov-Maxwell equations describing the evolution of the beam distribution function, f_b, is given approximately by [Davidson, 1990; Davidson and Qin 2001a]

$$\frac{\partial f_b}{\partial s} + x'\frac{\partial f_b}{\partial x} + y'\frac{\partial f_b}{\partial y} - \left[\frac{\partial \psi}{\partial x} + \kappa_x(s)\right]\frac{\partial f_b}{\partial x'} - \left[\frac{\partial \psi}{\partial y} + \kappa_y(s)\right]\frac{\partial f_b}{\partial y'} = 0, \tag{2.13}$$

where the normalized self-field potential $\psi(x,y,z)$ is determined self-consistently from

$$\left(\frac{\partial^2}{\partial x^2} + \frac{\partial^2}{\partial y^2}\right)\psi = -\frac{2\pi K_b}{N_b}\int dx'dy' f_b \,. \tag{2.14}$$

Assuming that a perfectly conducting cylindrical wall is located at radius $r = \left(x^2+y^2\right)^{1/2} = r_w$, Eq. (2.14) is to be solved subject to the boundary condition

$$\left[\frac{1}{r}\frac{\partial}{\partial \theta}\psi(r,\theta)\right]_{r=r_w} = 0, \tag{2.15}$$

where (r,θ) corresponds to the cylindrical polar coordinates defined by $x = r\cos\theta$ and $y = r\sin\theta$.

2.2.2 Smooth-Focusing Approximation

Solutions to Eqs. (2.13)-(2.15) describe the self-consistent nonlinear evolution of an intense beam propagating through a periodic focusing lattice. Of particular practical importance are the "quasi-equilibrium" (matched) solutions in which the beam distribution function is periodic with axial periodicity length equal to the lattice period, i.e., $f_b(x,y,x',y',s+S) = f_b(x,y,x',y',s)$. However, the oscillating nature of the focusing field provides a significant challenge for a detailed determination of matched quasi-equilibrium solutions. The problem can be significantly simplified if the so-called smooth-focusing approximation [Channell, 1999; Davidson *et al*., 1999; Davidson and Qin, 2001b], which describes the *average* focusing effect of the oscillating confining field, is used for analysis of the average dynamics of the beam particles. Within this approximation, the average external focusing force has the form

$$\mathbf{F}_{foc}^{sf} = -\gamma_b m_b \beta_b^2 c^2 \kappa_{sf} \left(x\hat{\mathbf{e}}_x + y\hat{\mathbf{e}}_y \right), \tag{2.16}$$

where the constant κ_{sf} is defined by [Davidson and Qin, 2001b]

$$\kappa_{sf} = \left\langle \left(\int_{s_0}^{s} ds \kappa_q(s) - \left\langle \int_{s_0}^{s} ds \kappa_q(s) \right\rangle_s \right)^2 \right\rangle_s , \tag{2.17}$$

for a quadrupole lattice, and

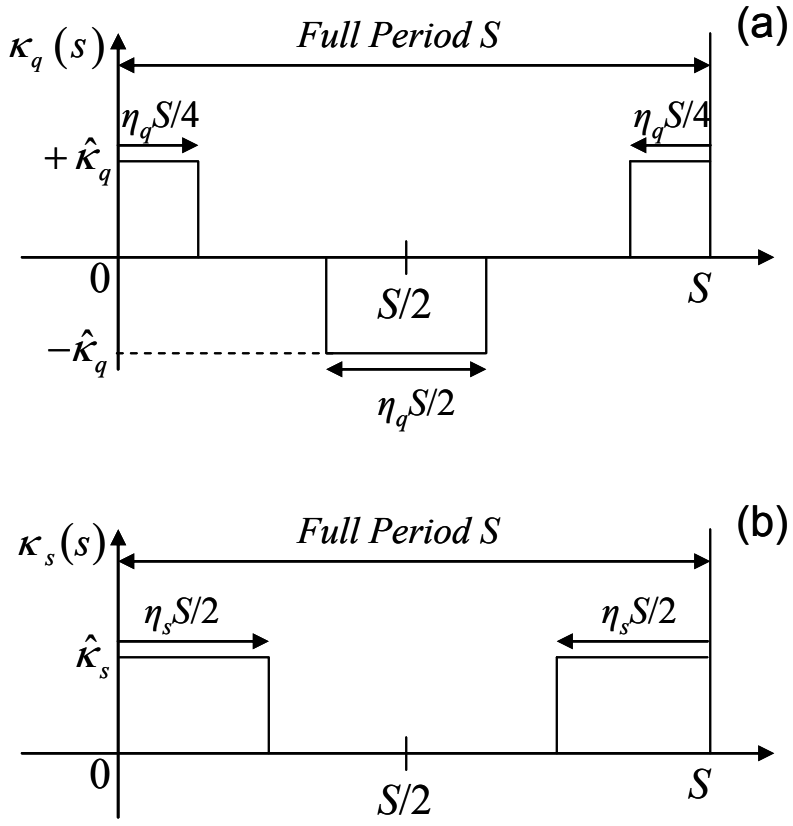

Fig. 2.2: Step-function model of a periodic lattice. The figure shows plots of periodic-focusing coupling coefficients corresponding to (a) a quadrupole lattice $\kappa_q(s)$, and (b) a solenoidal lattice, $\kappa_s(s)$. For the case of a quadrupole lattice, such a configuration is often called a FODO transport lattice (acronym for focusing-off-defocusing-off).

$$\kappa_{sf} = \overline{\kappa}_s + \left[\left\langle \left(\int_{s_0}^{s} ds \delta\kappa_s \right)^2 \right\rangle_s - \left\langle \int_{s_0}^{s} ds \delta\kappa_s \right\rangle_s^2 \right], \tag{2.18}$$

for a solenoidal lattice, where $\delta\kappa_s(s) \equiv \kappa_s(s) - \overline{\kappa}_s$.

If $\kappa_q(s)$ $[\kappa_s(s)]$ has the form of a step-function lattice with constant amplitude $\hat{\kappa}_q$ $(\hat{\kappa}_s)$ and constant filling factor η_q (η_s), as shown in Fig. 2.2, then it follows from Eqs. (2.17)-(2.18) that κ_{sf} is given to leading order by [Davidson and Qin, 2001a]

$$\kappa_{sf} = \frac{1}{16} \eta_q^2 \hat{\kappa}_q^2 S^2 \left(1 - \frac{2}{3} \eta \right), \tag{2.19}$$

for the case of a quadrupole lattice, and

$$\kappa_{sf} = \eta_s \hat{\kappa}_s + (1/12) \eta_s^2 \left(1 - \eta_s^2 \right) \hat{\kappa}_s^2 S^2, \tag{2.20}$$

for the case of a solenoidal lattice.

The smooth-focusing approximation significantly simplifies the analysis of the beam transverse dynamics. Indeed, the transverse smooth-focusing Hamiltonian defined by [Davidson and Qin, 2001a; Davidson and Qin, 2001b]

$$H_\perp^0 = \frac{1}{2} \left(x'^2 + y'^2 \right) + \frac{1}{2} \kappa_{sf} r^2 + \psi(r) \tag{2.21}$$

becomes an invariant of beam particles motion, and therefore the smooth-focusing approximation supports azimuthally symmetric equilibrium solutions for distribution functions of the form

$$f_b^0 = f_b^0 \left(H_\perp^0 \right) \tag{2.22}$$

For future references, here we present several examples of beam equlibria:

Thermal Equilibrium [Davidson, 1990; Brown and Reiser, 1995]:

$$f_b^0\left(H_\perp^0\right)=\hat{n}_b\left(\frac{\gamma_b m_b\beta_b^2c^2}{2\pi\hat{T}_{\perp b}}\right)\exp\left\{-\frac{\gamma_b m_b\beta_b^2c^2}{\hat{T}_{\perp b}}H_\perp^0\right\}, \tag{2.23}$$

Waterbag Equilibrium [Davidson and Chen, 1998; Davidson and Qin, 2001a]:

$$f_b^0\left(H_\perp^0\right)=\hat{n}_b\left(\frac{\gamma_b m_b\beta_b^2c^2}{2\pi\hat{T}_{\perp b}}\right)U\left(\frac{\gamma_b m_b\beta_b^2c^2}{\hat{T}_{\perp b}}H_\perp^0\right), \tag{2.24}$$

Kapchinskij-Vladimirskij (KV) Equilibrium [Kapchinskij and Vladimirskij, 1959; Davidson, 1990]

$$f_b^0\left(H_\perp^0\right)=\frac{\hat{n}_b}{2\pi}\delta\left(H_\perp^0-\frac{\hat{T}_{\perp b}}{\gamma_b m_b\beta_b^2c^2}\right). \tag{2.25}$$

Here, $\hat{T}_{\perp b}$ is a positive constant with units of energy, and U(x) is the Heaviside step function defined by U(x)=0 for x<0, and U(x)=1 for x≥0. Assuming, without loss of generality, $\psi\left(r=0\right)=0$, it readily follows from Eqs. (2.23)-(2.25) and (2.21) that $\hat{n}_b$ is the on-axis number density.

As evident from Eq. (2.16), within the smooth-focusing approximation, the beam particles exhibit oscillatory motion with axial periodicity length (smooth-focusing period) given by $2\pi\big/\sqrt{\kappa_{sf}}$ in the absence of the self-fields. Therefore, it is intuitively appealing to assume that the smooth-focusing approximation is valid if the lattice period is sufficiently small compared to the period of a smooth-focusing oscillation, i.e.,

$$\sqrt{\kappa_{sf}}S\big/2\pi<1. \tag{2.26}$$

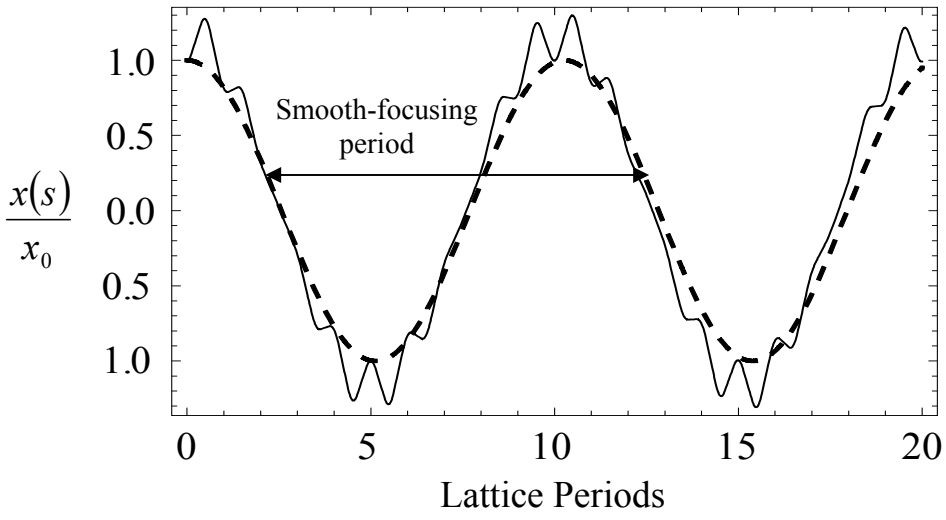

Figure 2.3: Illustrative example of the exact single-particle orbit $x(s)/x_0$ in a quadrupole FODO lattice (solid line) with filling factor $\eta_q = 0.5$ and $\sqrt{\kappa_{sf}}S = 0.61$. The dashed line corresponds to the smooth-focusing particle trajectory. The initial conditions are specified by $x(s=0) = x_0$ and $x'(s=0) = 0$.

Indeed, if the condition in Eq. (2.26) is satisfied, averaging over the rapid motion with length scale *S*, can provide an effective description of the average transverse dynamics of a beam particle. Detailed analysis of the validity limits of the smooth-focusing approximation is considered in References [Davidson *et al*., 1999; Dorf *et al*., 2009a; Startsev *et al*., 2009], and also later in this chapter. Here, as an illustrative example, we show the vacuum solution (obtained in the absence of self-fields) for the transverse motion of a single particle, making use of the smooth-focusing approximation, and taking into account the oscillating nature of the applied focusing force (Fig. 2.3).

The advance in phase of the slow transverse oscillation that the particle undergoes per oscillation period S (see Fig. 2.3) is called the *phase advance*. It is evident for the smooth-focusing particle trajectory that $\sigma_v^{sf} = \sqrt{\kappa_{sf}}S$, and for the illustrative parameters in Fig. 2.3 the smooth-focusing vacuum phase advance corresponds to $\sigma_v^{sf} = 35^0$. If the net defocusing effect of the self-field force is taken into account, the period of the particle motion increases, and the particle phase advance σ decreases compared to its vacuum value, σ_v. Therefore, the ratio σ/σ_v is often used as a normalized measure of the beam self-field strength. Another convenient parameter describing normalized beam intensity, which is often used in beam and nonneutral plasma physics is given by [Davidson and Qin, 2001a]

$$s_b = \frac{\hat{\omega}_{pb}^2}{2\gamma_b^2 \hat{\omega}_q^2}, \tag{2.27}$$

where $\hat{\omega}_{pb} \equiv \left(4\pi \hat{n}_b e_b^2 / \gamma_b m_b\right)^{1/2}$ is the relativistic plasma frequency, $\hat{n}_b$ is the on-axis plasma number density, and $\hat{\omega}_q \equiv \left(\kappa_{sf}\beta_b^2 c^2\right)^{1/2}$ is the average transverse focusing frequency associated with the (smooth-focusing) lattice coefficient κ_{sf}.

2.2.3 Envelope Equations for a Continuous Beam

Determining solutions to Eqs. (2.13)-(2.15), which describe the detailed self-consistent nonlinear evolution of an intense beam propagating through a periodic focusing field, can often require significant computational effort. However, for the case where the beam

distribution is close to a beam quasi-equilibrium, the evolution of the characteristic transverse beam dimensions $\bar{a}(s) = 2\langle x^2 \rangle^{1/2}$ and $\bar{b}(s) = 2\langle y^2 \rangle^{1/2}$ can be approximately described by the simplified *envelope equations* [Reiser, 1994; Davidson and Qin, 2001a]

$$\frac{d^2}{ds^2}\bar{a} + \left[\kappa_x(s) - \frac{2K_b}{\bar{a}(\bar{a}+\bar{b})}\right]\bar{a} = \frac{\varepsilon^2}{\bar{a}^3}, \tag{2.28}$$

$$\frac{d^2}{ds^2}\bar{b} + \left[\kappa_y(s) - \frac{2K_b}{\bar{b}(\bar{a}+\bar{b})}\right]\bar{b} = \frac{\varepsilon^2}{\bar{b}^3}, \tag{2.29}$$

where we have assumed $\varepsilon_x = \varepsilon_y \equiv \varepsilon$, and the transverse emittance, ε_x, is defined by

$$\varepsilon_x = 4\sqrt{\langle (x - \langle x \rangle^2) \rangle \langle (x' - \langle x' \rangle^2) \rangle - \langle (x - \langle x \rangle)(x' - \langle x' \rangle) \rangle^2}\,. \tag{2.30}$$

Here, $\langle \chi \rangle = N_b^{-1} \int dxdydx'dy' \chi f_b$ denotes the statistical average of a phase function χ over the beam distribution function, f_b. Note that the transverse beam emittance defined in Eq. (2.30) corresponds to an average statistical area of the transverse beam phase-space. For the special case of a Kapchinskij-Vladimirskij (KV) distribution [Eq.(2.25)], the beam density is uniformly distributed within the elliptical cross-section $0 \le \left[x^2/\bar{a}^2(s) + y^2/\bar{b}^2(s)\right] \le 1$, the transverse beam emittance is conserved, $\varepsilon(s) = const$, and Eqs. (2.28)-(2.29) describe the exact evolution of the outer edge $(\bar{a}, \bar{b})$ of the beam envelope [Davidson and Qin, 2001a].

The matched solutions to the envelope equations (2.28)-(2.29), satisfying $\bar{a}(s+S) = \bar{a}(s)$ and $\bar{b}(s+S) = \bar{b}(s)$, can be used for calculation of the phase advances

[Davidson and Qin, 2001a]. The vacuum phase advance, σ_v describing the normalized lattice strength can be expressed as

$$\sigma_v \equiv \lim_{K_b \to 0} \varepsilon \int_{s_0}^{s_0+S} \frac{ds}{\overline{a}^2(s)} = \lim_{K_b \to 0} \varepsilon \int_{s_0}^{s_0+S} \frac{ds}{\overline{b}^2(s)}, \tag{2.31}$$

and the depressed phase advance σ including self-field effects is given by

$$\sigma \equiv \varepsilon \int_{s_0}^{s_0+S} \frac{ds}{\overline{a}^2(s)} = \varepsilon \int_{s_0}^{s_0+S} \frac{ds}{\overline{b}^2(s)}, \tag{2.32}$$

Within the smooth-focusing approximation the envelope equations (2.28)-(2.29) have the following form

$$\frac{d^2}{ds^2}\overline{a} + \left[\kappa_{sf} - \frac{2K_b}{\overline{a}(\overline{a}+\overline{b})}\right]\overline{a} = \frac{\varepsilon^2}{\overline{a}^3}, \tag{2.33}$$

$$\frac{d^2}{ds^2}\overline{b} + \left[\kappa_{sf} - \frac{2K_b}{\overline{a}(\overline{a}+\overline{b})}\right]\overline{b} = \frac{\varepsilon^2}{\overline{b}^3}. \tag{2.34}$$

The matched smooth-focusing solutions are given by $\overline{a}(s) = \overline{b}(s) = \overline{r}_{b0}$, and it is straightforward to show that in the smooth-focusing approximation the phase advances are given by [Davidson and Qin, 2001a]

$$\sigma_v^{sf} = \sqrt{\kappa_{sf}}\, S, \tag{2.35}$$

and

$$\frac{\sigma^{sf}}{\sigma_v^{sf}} = \left[1 + \left(\frac{K_b}{2\varepsilon\sqrt{\kappa_{sf}}}\right)^2\right]^{1/2} - \left(\frac{K_b}{2\varepsilon\sqrt{\kappa_{sf}}}\right). \tag{2.36}$$

For the case of an azimuthally symmetric beam, the equilibrium beam radius $\bar{r}_{b0}$ determined from Eqs. (2.33) and (2.34) and $d\bar{a}/ds = 0 = d\bar{b}/ds$, and $\bar{a}(s) = \bar{b}(s) = \bar{r}_{b0}$, is given by the solution to the radial force balance equation

$$\left(\kappa_{sf} - \frac{K_b}{\bar{r}_{b0}^2}\right)\bar{r}_{b0} = \frac{\varepsilon^2}{\bar{r}_{b0}^3}. \tag{2.37}$$

Equation (2.37) represents the balance between the applied lattice focusing field, the beam self-fields, and the effective "thermal pressure" associated with the transverse velocity spread of the beam particles. It is readily seen from Eq. (2.37) that the dimensionless parameter $K_b\bar{r}_{b0}^2/\varepsilon^2$ can be used as a normalized measure of the self-field strength with $K_b\bar{r}_{b0}^2/\varepsilon^2 << 1$ corresponding to an emittance-dominated beam with negligible self-field force, and $K_b\bar{r}_{b0}^2/\varepsilon^2 >> 1$ corresponding to an intense, space-charge-dominated beam with very small transverse emittance.

2.2.4 Halo Particle Production by a Beam Mismatch

In order to maintain high beam quality and avoid activation of the chamber wall, it is important to minimize the transverse excursion and number of *halo particles* ejected from the beam core. Mechanisms that can cause the production of halo particles range from beam mismatch and envelope instabilities [Gluckstern, 1994; Gluckstern *et at*., 1998; Wangler *et al*., 1998; Allen *et al*., 2002], to collective excitations in the beam interior [Strasburg and Davidson 2000; Strasburg and Davidson 2001]. Here, we present brief overview of the beam mismatch mechanism developed by Gluckstern [Gluckstern, 1994],

in which halo particles gain their energies by means of parametric resonant interaction with the self-field perturbations produced by a beam mismatch.

For simplicity, we make use of the smooth-focusing approximation, and a more detailed analysis taking into account the effects of the oscillating focusing field is presented later in this chapter and also in Chapter 3. Assuming small-signal perturbations $\delta\bar{a},\delta\bar{b} << \bar{r}_{b0}$, we express $\bar{a} = \bar{r}_{b0} + \delta\bar{a}$ and $\bar{b} = \bar{r}_{b0} + \delta\bar{b}$. It is straightforward to show that the envelope equations (2.33)-(2.34) support mismatch oscillations around the equilibrium beam radius $\bar{r}_{b0}$ with normal mode oscillation periods determined by [Struckmeier and Reiser, 1984; Lund and Bukh, 2004]

$$L_s^{sf} = \frac{2\pi S}{\sqrt{2\left(\sigma_v^{sf}\right)^2 + 2\left(\sigma^{sf}\right)^2}} \tag{2.38}$$

$$L_q^{sf} = \frac{2\pi S}{\sqrt{\left(\sigma_v^{sf}\right)^2 + 3\left(\sigma^{sf}\right)^2}}. \tag{2.39}$$

Here, L_s^{sf} corresponds to the symmetric (even) mode with $\delta\bar{a} = \delta\bar{b}$, and L_q^{sf} corresponds to the quadrupole (odd) mode with $\delta\bar{a} = -\delta\bar{b}$. The quadrupole and symmetric modes represent collective transverse oscillations of the charged particle beam envelope. On the other hand, due to the nonlinear transverse dependence of the beam self-fields near and beyond the beam edge, individual beam particles can oscillate about and through the beam core with energy-dependent *betatron* frequency. Collective self-field perturbations produce modulation of the betatron frequency, and therefore parametric resonant

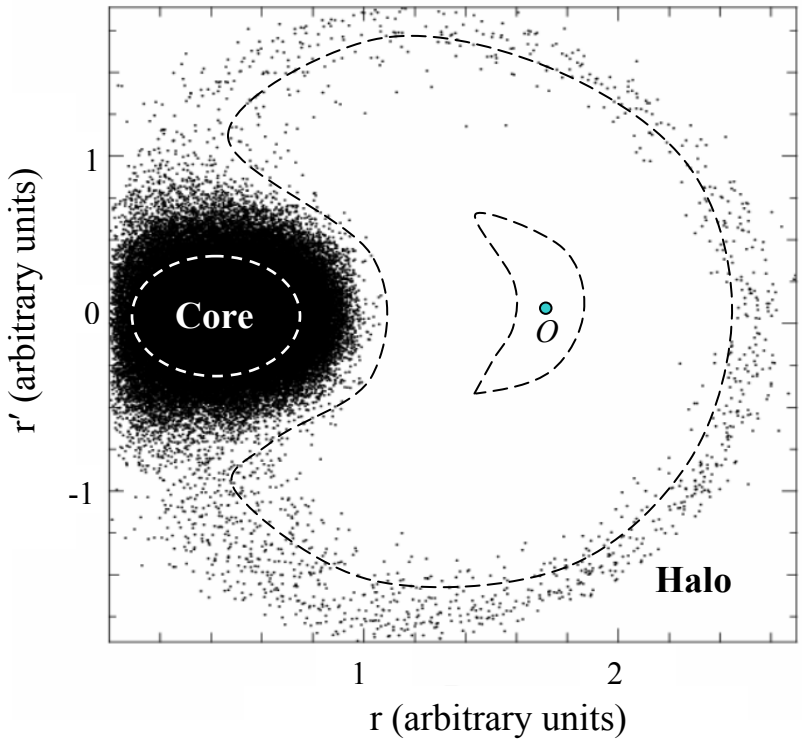

Figure 2.4: A snapshot of the radial beam (r,r') phase space for the case of a space-charge-dominated beam with $s_b = 0.9999$ $\left(\sigma^{sf}/\sigma_v^{sf} = 0.25\right)$. The halo is produced by a mismatch oscillations with amplitude $\delta\bar{r}_b \sim 0.3\bar{r}_{b0}$. The results are obtained with WARP simulations, using a smooth-focusing model. The dashed lines schematically illustrate different phase-space trajectories, corresponding to the Poincare sections with strobe time taken at the minimum of the beam radius. The "*O*-point" corresponds to a fixed stable point of 2:1 (fundamental) parametric resonance.

interaction between the edge beam particles and the collective modes may occur. In particular, beam particles, which are close to fundamental resonance with the collective mismatch oscillation, can gain transverse energy and populate the halo region [Gluckstern, 1994].

A snapshot of the radial beam (r,r') phase space shown in Fig. 2.4. illustrates the resonance halo structure, produced by an azimuthally symmetric mismatch oscillations with amplitude $\delta\bar{r}_b \sim 0.3\bar{r}_{b0}$. The beam intensity corresponds to a space-charge-dominated limit with $s_b = 0.9999$ $\left(\sigma^{sf}/\sigma_v^{sf} = 0.25\right)$; and the numerical results for this illustrative example are obtained using the WARP particle-in-cell (PIC) code [Friedman *et al.*, 1992; Grote *et al*., 1998]. The dashed lines schematically illustrate different phase-space trajectories, corresponding to the Poincare sections with the strobe time taken to coincide with the minimum of the beam radius. Note that most of the halo particles travel near the separatrix, which separates stable core trajectories from trajectories around the "*O*-point", corresponding to the stable fixed point of the parametric resonance.

2.2.5 Intense Beam Transport Stability Limits

Understanding stability properties of an intense charged particle beam propagating in a periodic focusing lattice is a critical problem in intense beam transport, especially in heavy ion fusion, which relies on high-brightness and high-current heavy ion beams to deliver high power to the target. An extensive scientific effort over the past several decades has revealed a wide range of collective unstable processes degrading beam

quality, ranging from higher-order kinetic instabilities internal to the beam to low-order beam envelope instabilities. A well-known example of a kinetically unstable distribution is the Kapchinskij-Vladimirskij (KV) distribution, where hypershell structure of the energy distribution provides the source of free energy to drive higher-order collective instabilities internal to the beam [Hofmann *et al*., 1983; Davidson and Qin, 2001a]. As a result, the KV distribution becomes unstable at sufficiently high beam intensities. On the other hand the low-order evolution of the beam edge envelope [Eqs (2.28)-(2.29)], can also become unstable in the region of high values of vacuum phase advances due to the parametric resonance coupling of mismatch oscillations to the periodic lattice structure (Fig. 2.5) [Struckmeier and Reiser, 1984; Lund and Bukh, 2004].

Over two decades ago, another class of unstable higher-order resonance processes attributed to beam space-charge effects was observed experimentally [Tiefenback *et al*., 1985; Tiefenback, 1986]. It was demonstrated that the quality of space-charge-dominated beam transport in alternating-gradient quadrupole focusing lattices is significantly degraded in the region where $\sigma_v^2 - \sigma^2 > (2\pi/3)^2/2$ (Fig. 2.5). Although, this criterion has been extensively used in the practical design of focusing systems, the origin of this limit had not been fully understood until recently, when a plausible theoretical model has been proposed [Lund and Chawla, 2006]. For future reference, we briefly summarize the properties of this space-charge transport limit.

Detailed numerical studies [Lund and Chawla, 2006] revealed the robustness of this transport limit, demonstrating that various choices of initial beam distribution are

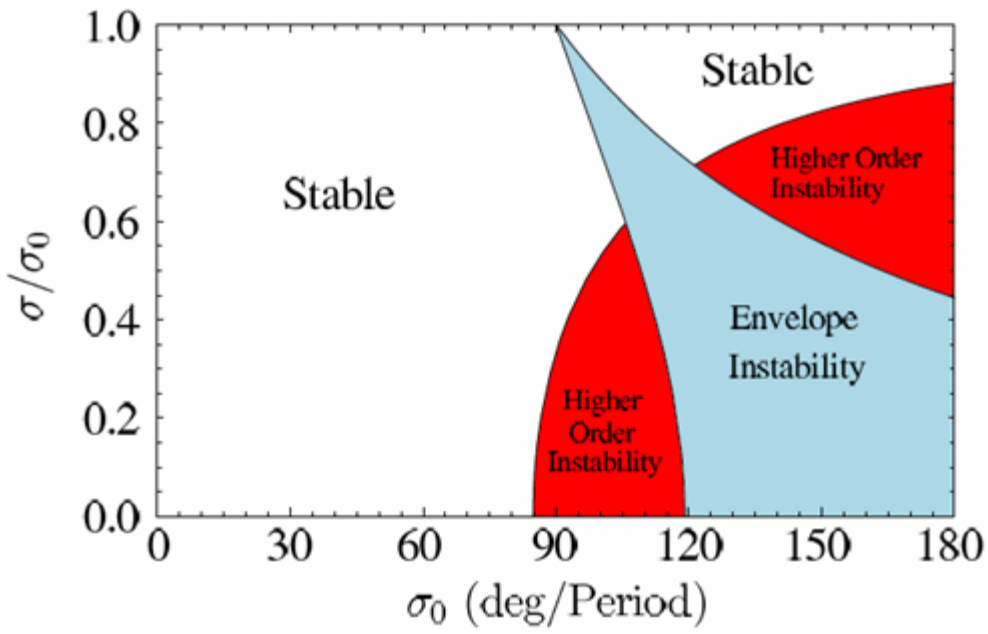

Figure 2.5: (Color) Beam stability regions in a FODO quadrupole lattice. The blue region illustrates band of strong parametric evelope instability. The red region corresponds to the higer-order resonance instability [Lund and Chawla, 2006].

subject to strong growth in statistical phase-space area (emittance growth), when $\sigma_{vac}^2 - \sigma^2 > (2\pi/3)^2/2$. Figure 2.6 shows a significant increase in the beam transverse emittance for the cases where the initial beam distribution is specified by the thermal equilibrium [Eq. (2.23)], waterbag [Eq. (2.24)], and semi-Gaussian (that is Gaussian in velocity and has a uniform distribution in position) distribution functions.

In order to probe the beam microstate, the *particle-core model* using a KV core was effectively utilized [Lund and Chawla, 2006]. The particle-core model is used to study a single particle dynamics governed by the applied lattice focusing fields and the self-fields produced by the oscillating beam core, whose evolution is described by the

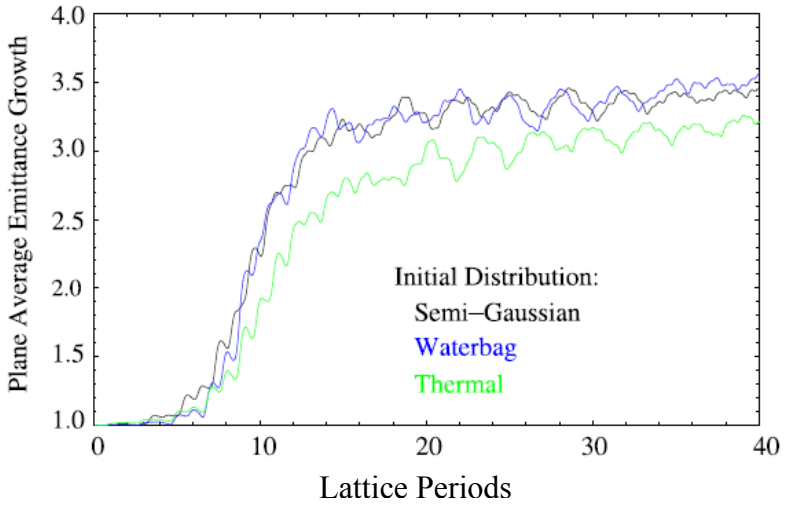

Figure 2.6: (Color) PIC simulations of the plane-averaged emittance growth for different initial distributions in a FODO quadrupole channel ($\sigma_v = 100^0$, $\sigma/\sigma_{vac} = 0.2$, $\eta_q = 0.5$). [Lund and Chawla, 2006].

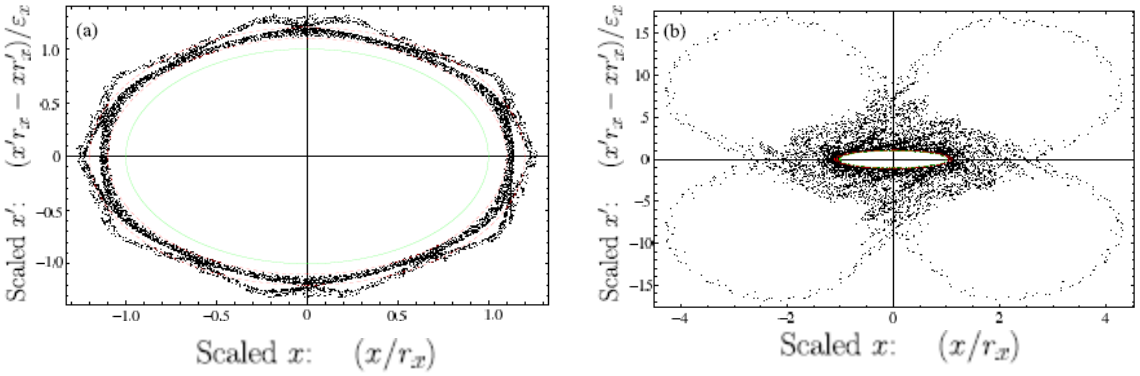

Figure 2.7: (Color) Core-particle Poincare phase-spaces for $\eta_q = 0.5$, $\sigma_v = 100^0$, (a) $\sigma/\sigma_{vac} = 0.67$, and (b) $\sigma/\sigma_{vac} = 0.2$. Results are obtained using the particle-core model with a KV core. The extent of the core is plotted in red, and r_x corresponds to the outer edge of the beam envelope. [Lund and Chawla, 2006].

envelope equations [Eqs. (2.28)-(2.29)]. Typically, the density distribution within the beam core is assumed to be uniform, which corresponds to a matched KV quasi-equilibrium. Figure 2.7 illustrates Poincare phase space plots obtained with the particle-core model for the cases of a moderate intensity beam with $\sigma/\sigma_v = 0.67$ and $\sigma_v = 100^0$ [Fig. 2.7(a)], and a space-charge-dominated beam with $\sigma/\sigma_v = 0.2$ and $\sigma_v = 100^0$ [Fig. 2.7(b)].

It is readily seen from Fig. 2.7 that for the unstable case [Fig. 2.7(b)], the core is surrounded by a chaotic sea region connected to a large 4:1 resonance structure that ultimately limits the particle oscillation amplitude. Therefore, near-edge particles can diffuse outside the beam core sufficiently to partake in the higher-order resonances, thus providing emittance growth. In contrast, for the case of a moderate intensity beam (stable case) [Fig. 2.7(a)] the particles remain close to the matched envelope. Note the large change in scale between the stable and unstable plots. Stability thresholds based on this resonance picture were found to be in approximate agreement with experiment and simulations [Lund and Chawla, 2006].

Finally, it should be noted that the effects of beam space-charge can also significantly modify the stability properties of beam transport at moderately weak beam intensities. In particular, it has recently been demonstrated that a similar 4:1 resonance structure appears, and associated higher-order effects can dominate over the envelope instability for the case of a lower intensity beam with $\sigma/\sigma_v \sim 0.8$ [Jeon *et al*., 2009; Groening *et al*., 2009].

2.3 Adiabatic Formation of a Matched-Beam Distribution for an Alternating-Gradient Quadrupole Lattice

This section develops a numerical method for the formation of a quasi-equilibrium beam distribution matched to an alternating-gradient quadrupole focusing lattice by means of the adiabatic turn-on of the oscillating focusing field. The motivation for this work and a summary of previous studies are described in Sec. 2.3.1. In Sec. 2.3.2 the method is investigated for a wide range of transport system parameters, making use of particle-in-cell simulations, and quiescent beam propagation for over a hundred of lattice periods is demonstrated. In Sec. 2.3.3, properties of the quasi-equilibrium matched-beam distribution are investigated, and compared with the predictions of the analytical theory developed by Davidson *et al*. [Davidson *et al*., 1999]. Finally, the analysis is extended to the case of a periodic-focusing solenoidal lattice, and various choices of the initial beam distribution in Sec. 2.3.4.

2.3.1 Motivation

As noted earlier, the equilibrium and stability properties of an intense charged particle beam propagating through an alternating-gradient quadrupole focusing lattice are of particular importance for a wide range of applications to high energy and nuclear physics,

ion-beam-driven high energy density physics and heavy ion fusion, and nuclear waste transmutation [Chao, 1993; Reiser, 1994; Davidson and Qin, 2001a]. It is therefore important to develop an improved theoretical understanding of intense beam transport. Although the nonlinear effects of the intense self-fields produced by the beam space-charge provide a significant challenge for analytical studies, various analytical models have been developed to describe an equilibrium beam distribution matched to an alternating-gradient quadrupole focusing lattice [Channell, 1999; Davidson *et al*, 1999; Davidson and Qin, 2001a]. To validate prospective models it is particularly important to develop numerical techniques allowing for the formation of a quasi-equilibrium beam distribution. Furthermore, numerical schemes describing the quiescent loading of a beam distribution into a transport lattice and minimizing the deleterious effects of beam mismatch are of particular importance for detailed numerical studies of various collective processes and instabilities. In this section, we present a numerical method for the formation of a quasi-equilibrium beam distribution matched to an alternating-gradient quadrupole focusing lattice by means of the adiabatic turn-on of the oscillating focusing field [Dorf *et al*., 2009a; Dorf *et al*., 2009b].

The approach of adiabatic turn-on of the oscillating focusing field has been previously investigated by means of nonlinear δF simulations by Stoltz *et al*. for the case of a periodic focusing solenoidal lattice [Stoltz *et al*., 1999]. In that work the total distribution function F_b of a beam propagating through a periodic focusing soleniodal field with coupling coefficient $\kappa_s(s+S)=\kappa_s(s)$ is divided into a zero-order part $\left(F_b^0\right)$

that propagates through the average focusing field $\overline{\kappa}_s = const$, plus a perturbation (δF_b), which evolves nonlinearly in the zero-order and perturbed field configurations. It was demonstrated that for the case where the oscillatory component of the coupling coefficient, $\delta\kappa_s(s) \equiv \kappa_s(s) - \overline{\kappa}_s$, turns on adiabatically over many periods of the focusing lattice, the amplitude of the mismatch oscillations reduces by more than an order-of-magnitude compared to the case where the field oscillation is turned on suddenly. The technique reported in [Stoltz *et al*., 1999], however, can not be applied to the case of an alternating-gradient quadrupole lattice, because the average component of the focusing field vanishes.

Here we generalize the method of adiabatic formation of a matched beam distribution to the case of an alternating-gradient quadripole lattice [Dorf *et al*., 2009a]. In this generalized approach, an equilibrium beam distribution is initially loaded into a uniform focusing channel with the focusing field given by the smooth-focusing approximation, which describes the average effects of the alternating-gradient lattice [Channell, 1999; Davidson *et al*., 2001b; Startsev *et al*., 2009]. The oscillating quadrupole focusing field is then adiabatically turned on as the amplitude of the uniform field component is adjusted to maintain the average (smooth-focusing) effects of the total focusing field fixed. It is demonstrated that the generalized method allows for quiescent formation of a quasi-equilibrium beam distribution matched to a quadrupole lattice for a broad range of beam intensities and vacuum phase advances describing the strength of the oscillating focusing field. For the case of sufficiently large values of the vacuum

phase advance, the deviations of the beam distribution function from the initial state can be significant. Therefore, in the present analysis we use the full particle-in-cell code WARP [Friedman *et al*., 1992; Grote *et al*., 1998] to perform the numerical simulations. However, we note that the formalism presented here will also provide a useful approach for initializing the choice of self-consistent quasi-equilibrium distributions f_0 in nonlinear δF simulations for intense beam propagation in periodic-focusing lattices [Qin *et al*., 2007; Startsev *et al*., 2007; Qin *et al*., 2008].

Properties of the quasi-equilibrium matched beam distribution are investigated in the present analysis. In particular, self-similar evolution of the transverse beam density profile is observed. Furthermore, the density profile of the beam distribution matched to the quadrupole lattice is found to be self-similar to the initial density profile corresponding to the smooth-focusing equilibrium distribution. These observations are consistent with predictions of the Hamiltonian averaging theory developed by Davidson *et al*. [Davidson *et al*., 1999]. The range of validity of the self-similarity feature is also investigated.

As noted earlier in this chapter, a mismatch between the beam and the transport lattice can produce halo particles, which may cause degradation of the beam quality and activation of the chamber wall [Gluckstern, 1994; Allen *et al*., 2002]. For intense beam accelerators and transport systems it is increasingly important to suppress beam halo production; therefore, quiescent beam matching from the source region into the transport lattice is of particular practical importance [Batygin, 1996; Prost *et al*., 2005; Chung *et al*,

2007]. Note that the method presented in this section for adiabatic formation of a matched beam distribution may possibly be utilized in the design of next-generation transport systems. Indeed, an intense beam produced by an emitting source typically has an azimuthally symmetric envelope with a negligible convergence (divergence) angle and can be easily matched to a uniform focusing channel. Then, a matching section where the oscillating quadrupole field is turned on adiabatically can be used to provide quiescent beam matching to the transport lattice. Conditions on the length of the adiabatic turn-on section required to assure that matching is maintained are discussed.

2.3.2 Quiescent Loading of a Matched-Beam Distribution for a Quadrupole Lattice

In this section we describe the numerical scheme that allows for the quiescent formation of a quasi-equilibrium beam distribution matched to an alternating-gradient quadrupole lattice [Dorf *et al*., 2009a]. The scheme is then examined for a range of values of beam intensity and lattice vacuum phase advance, making use of particle-in-cell numerical simulations performed with the 2D slice version of the WARP code. The scheme works as follows. First, the oscillating focusing field of the quadrupole lattice is replaced with the smooth-focusing force given by Eqs. (2.16) and (2.17), and the thermal equilibrium beam distribution [Eq. (2.23)]

$$f_b^0\left(H_\perp^0\right) = \hat{n}_b\left(\frac{\gamma_b m_b \beta_b^2 c^2}{2\pi \hat{T}_{\perp b}}\right)\exp\left\{-\frac{\gamma_b m_b \beta_b^2 c^2}{\hat{T}_{\perp b}} H_\perp^0\right\}, \tag{2.40}$$

is loaded into the uniform focusing channel. Then, the oscillating quadrupole focusing force in Eq. (2.6) is adiabatically turned on, and the uniform focusing component is correspondingly adjusted to maintain the smooth-focusing effect of the total focusing field fixed. That is, the *total* focusing force acting on the beam particles is specified by

$$F_{foc}^{q}(s) = \left[V^2(s) - 1\right]\kappa_{sf}\left(x\hat{\mathbf{e}}_x + y\hat{\mathbf{e}}_y\right) - V(s)\kappa_q(s)\left(x\hat{\mathbf{e}}_x - y\hat{\mathbf{e}}_y\right), \tag{2.41}$$

where $V(s)$ is a function describing the smooth transition of the focusing field in the matching section that satisfies $V(s=0)=0$ and $V(s=\infty)=1$. Here, we adopt a simple model in which $V(s)$ varies according to

$$V(s) = \left[1+\exp\left(\frac{L_{1/2}-s}{L_{tr}}\right)\right]^{-1} - \left[1+\exp\left(\frac{L_{1/2}}{L_{tr}}\right)\right]^{-1}, \tag{2.42}$$

where $2L_{1/2}$ is the length of the matching section, and L_{tr} is the characteristic length scale for variation of $V(s)$ from zero to unity, and $L_{1/2}>>L_{tr}>>S$ is assumed. We also assume a step-function (FODO) model of a quadrupole lattice, for which the corresponding smooth-focusing lattice coefficient, κ_{sf}, in Eq. (2.41) is given approximately by Eq. (2.19).

A plot of the transition function V(s) along with the corresponding evolution of the normalized rms envelope beam dimension $X_{rms} \equiv \left\langle x^2 \right\rangle^{1/2}$ is shown in Fig 2.8. For future reference, here we define $X_{\max}$ as the beam x-envelope local maximum value calculated at the end of each focusing cell. Detailed results of the numerical simulations

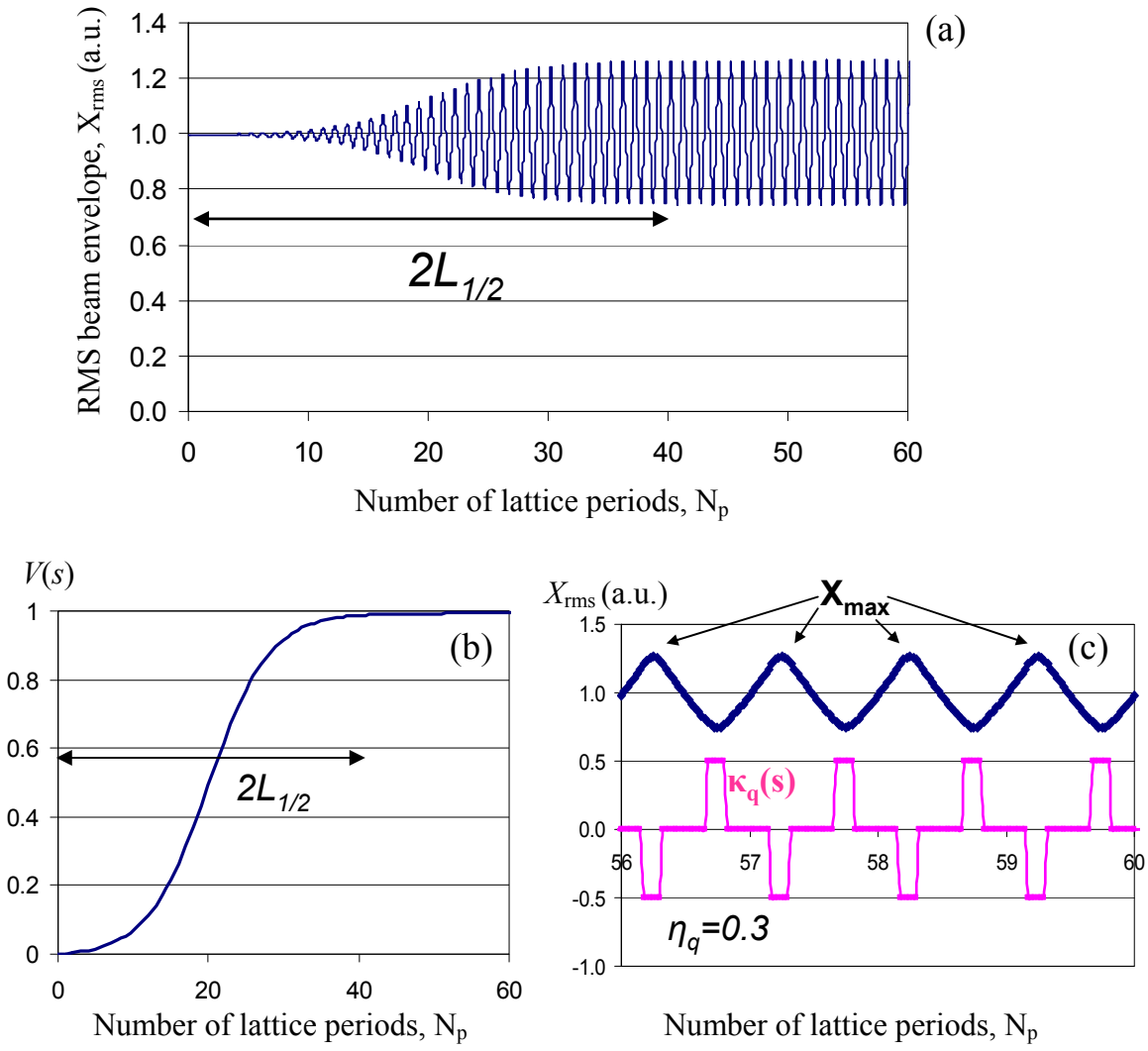

Figure 2.8: (Color) Evolution of a space-charge-dominated beam with $2K_b R_{b0}^2/\varepsilon^2 = 15.3$. Phase advances are given by $\sigma_v = 65.9^0$ and $\sigma/\sigma_v = 0.260$. The corresponding smooth-focusing parameters are $\sigma_v^{sf} = 61.8^0$, $\sigma^{sf}/\sigma_v^{sf} = 0.247$, $s_b = 0.9999$; and $2L_{1/2}/S = 40$. The figures show plots of (a) the evolution of the rms beam envelope, X_{rms}, versus number of lattice periods, N_p, (b) the lattice transition function $V(s)$, and (c) the evolution of the rms beam envelope in the final state (blue), and a schematic of the corresponding FODO lattice coefficient $\kappa_q(s)$ (pink).

for the illustrative parameters corresponding to the cases of a space-charge-dominated beam with $2K_bR_{b0}^2/\varepsilon^2 = 15.3$ ($\sigma/\sigma_v \approx 0.26$), and an emittance-dominated beam with $2K_bR_{b0}^2/\varepsilon^2 = 0.2$ ($\sigma/\sigma_v \approx 0.91$), are shown in Figs. 2.9-2.14 [Dorf *et al.*, 2009a]. Here, $R_{b0}^2 \equiv \left\langle \left(x^2 + y^2\right) \right\rangle_0$, is the mean-square beam radius, where $\langle \chi \rangle_0 = N_b^{-1} \int dxdydx'dy' \chi f_b^0$ denotes the statistical average of a phase function χ over the initial smooth-focusing beam distribution function f_b^0 in Eq. (2.40). Note that for the case of a KV distribution $R_{b0}^2 = \bar{r}_{b0}^2/2$, where $\bar{r}_{b0}$ is the outer edge of the beam equilibrium envelope [Eq. (2.37)]. For each value of the beam intensity, the following values of the lattice vacuum phase advance have been considered: $\sigma_v = 44.8^0$, $\sigma_v = 65.9^0$ and $\sigma_v = 87.5^0$. The corresponding values of the phase advances ($\sigma_v^{sf}, \sigma^{sf}$), and normalized beam intensity s_b, calculated for the initial beam equilibrium in the smooth-focusing channel are indicated in the captions to Figs. 2.9-2.14. Other important parameters of the numerical simulations correspond to filling factor $\eta_q = 0.3$ and wall radius r_w=4R_{b0}; the total number of macroparticles used in the simulation is $N_{pt} = 4 \times 10^6$, and the total number of grid cells in the x and y directions is $N_x = N_y = 128$. To assure that matching is approximately maintained in the matching section, we choose $L_{1/2}/L_{tr} = 5$ and take $L_{1/2} = 5L_s^{sf}$, where L_s^{sf} is the smooth-focusing period of the linear mismatched oscillations defined in Eq. (2.38). The ratio of the length of the matching section to the lattice period, $2L_{1/2}/S$, is indicated in the captions to Figs. 2.9-2.14. It value depends on the value of the phase

advances, and for the considered illustrative parameters it varies from $2L_{1/2}/S \approx 24$ for $\sigma_v = 87.5^0$ and $\sigma/\sigma_{vac} \approx 0.91$ to $2L_{1/2}/S \approx 51$ for $\sigma_v = 44.8^0$ and $\sigma/\sigma_v \approx 0.26$.

In each of Figs. 2.9-2.14, the frames in (a) illustrate the discrete evolution of the normalized rms envelope *x*-dimension, $X_{rms} \equiv \langle x^2 \rangle^{1/2}$, calculated at the end of each focusing cell where the beam *x*-envelope has a local maximum value. Such a graphical representation for a matched beam would be a horizontal straight line; therefore (a) provides a convenient representation of beam mismatch. The frames in (b) show fast-Fourier transform (FFT) plots of $X_{\rm rms}(s)$, where the continuous evolution of $X_{\rm rms}(s)$ is used for the FFT calculations. Finally, the frames in (c) show the evolution of the *x*-component of the normalized perturbations in transverse beam emittance, $\delta\varepsilon_x(s)/\varepsilon_0 \equiv [\varepsilon_x(s) - \varepsilon_x(s=0)]/\varepsilon_x(s=0)$. Along with the evolution of the beam parameters for the case of adiabatic turn-on of $V(s)$ shown by the solid curves, Figs. 2.9-2.14 also show the evolution of beam parameters (dashed curves) for the case where the initial distribution is loaded instantaneously into an alternating-gradient quadrupole lattice with $V(s) \equiv 1$ [Lund *et al*., 2009].

To load the particles for this case, first the matched solutions to the envelope equations (2.28)-(2.29) are found. Then, the smooth-focusing thermal equilibrium distribution that satisfies $2R_{b0}^2 = \overline{a}^2(s') = \overline{b}^2(s')$ is calculated. Here s' denotes the location inside the focusing cell where $\overline{a}(s') = \overline{b}(s')$. Finally, the positions and velocities

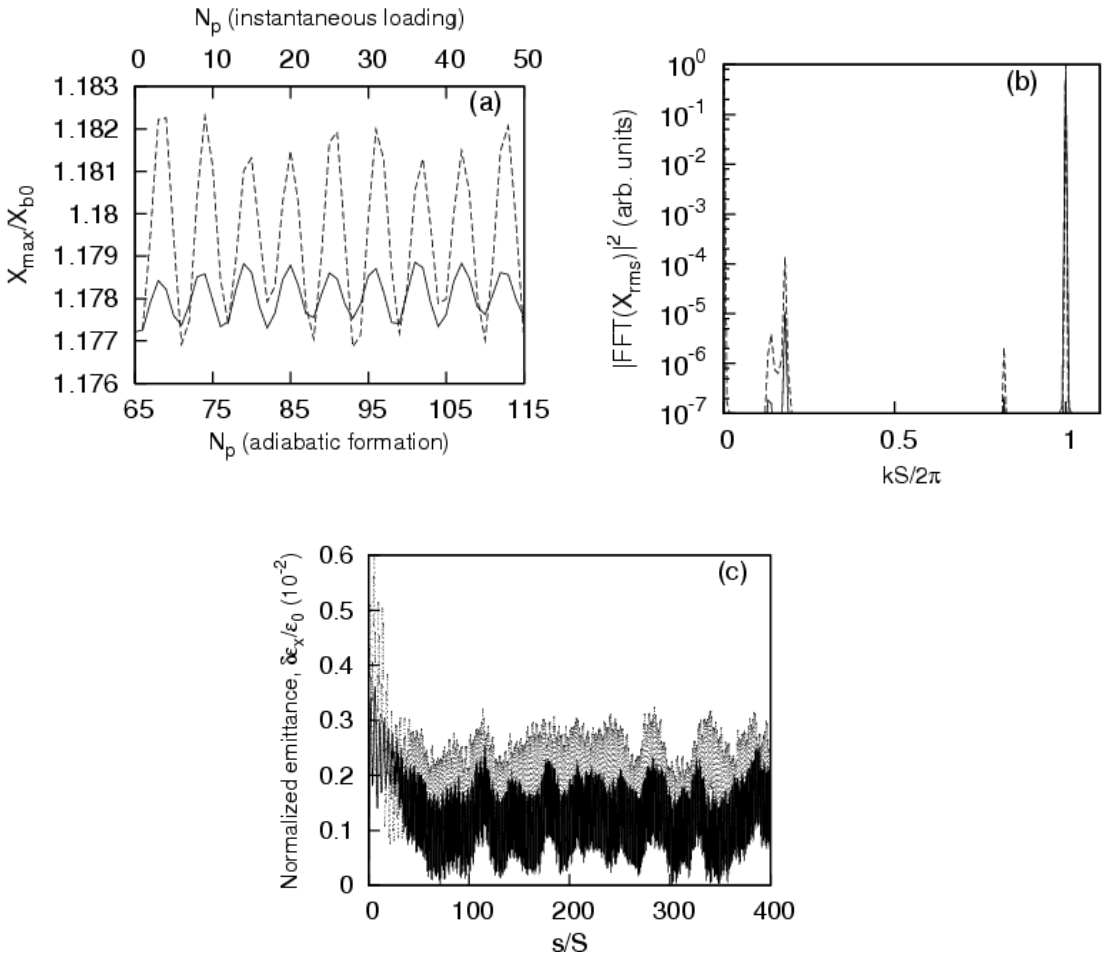

Figure 2.9: Evolution of a space-charge-dominated beam with $2K_b R_{b0}^2/\varepsilon^2 = 15.3$. Phase advances are given by $\sigma_v = 44.8^0$ and $\sigma/\sigma_v = 0.255$. The corresponding smooth-focusing parameters are $\sigma_v^{sf} = 43.3^0$, $\sigma^{sf}/\sigma_v^{sf} = 0.247$, $s_b = 0.9999$; and $2L_{1/2}/S = 57.1$. The figures show plots of: (a) $X_{\max}/X_{b0}$ versus number of lattice periods, N_p, where $X_{b0} = \langle x^2 \rangle_0^{1/2}$, and $X_{\max}$ corresponds to the value of X_{rms} calculated at the end of the focusing cell; (b) FFT of $X_{rms}(s)$ versus $kS/2\pi$; and (c) normalized perturbed emittance $\delta\varepsilon_x(s)/\varepsilon_0$ versus s/S. The solid curves correspond to an adiabatic turn-on of the lattice, and the dashed curves correspond to the case of an instantaneous beam loading.

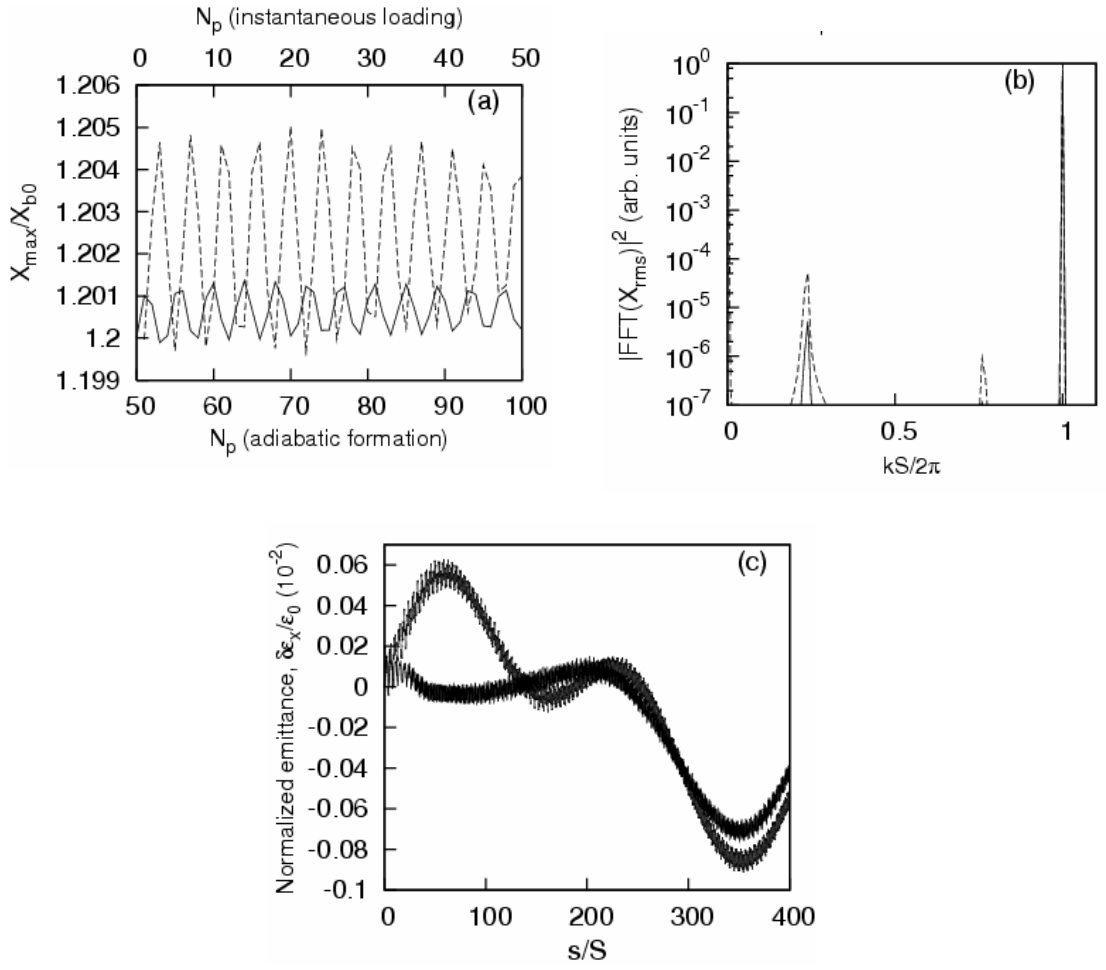

Figure 2.10: Evolution of an emittance-dominated beam with $2K_b R_{b0}^2/\varepsilon^2 = 0.2$. Phase advances are given by $\sigma_v = 44.8^0$ and $\sigma/\sigma_v = 0.913$. The corresponding smooth-focusing parameters are $\sigma_v^{sf} = 43.3^0$, $\sigma^{sf}/\sigma_v^{sf} = 0.91$, $s_b = 0.32$; and $2L_{1/2}/S = 43.5$. The figures show plots of: (a) $X_{\max}/X_{b0}$ versus number of lattice periods, N_p, where $X_{b0} = \langle x^2 \rangle_0^{1/2}$, and $X_{\max}$ corresponds to the value of X_{rms} calculated at the end of the focusing cell; (b) FFT of $X_{rms}(s)$ versus $kS/2\pi$; and (c) normalized perturbed emittance $\delta\varepsilon_x(s)/\varepsilon_0$ versus s/S. The solid curves correspond to an adiabatic turn-on of the lattice, and the dashed curves correspond to the case of an instantaneous beam loading.

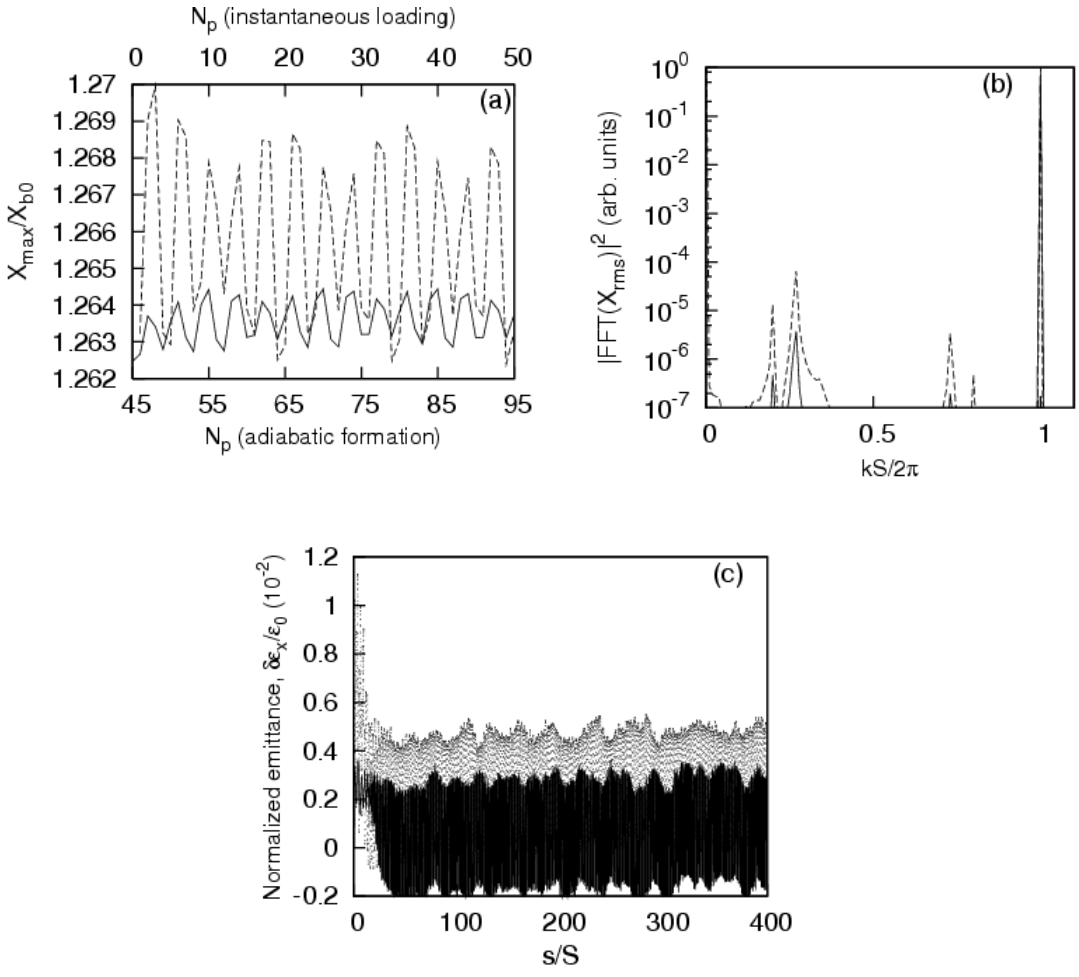

Figure 2.11: Evolution of a space-charge-dominated beam with $2K_b R_{b0}^2/\varepsilon^2 = 15.3$. Phase advances are given by $\sigma_v = 65.9^0$ and $\sigma/\sigma_v = 0.260$. The corresponding smooth-focusing parameters are $\sigma_v^{sf} = 61.8^0$, $\sigma^{sf}/\sigma_v^{sf} = 0.247$, $s_b = 0.9999$; and $2L_{1/2}/S = 40$. The figures show plots of: (a) $X_{\max}/X_{b0}$ versus number of lattice periods, N_p, where $X_{b0} = \langle x^2 \rangle_0^{1/2}$, and $X_{\max}$ corresponds to the value of X_{rms} calculated at the end of the focusing cell; (b) FFT of $X_{rms}(s)$ versus $kS/2\pi$; and (c) normalized perturbed emittance $\delta\varepsilon_x(s)/\varepsilon_0$ versus s/S. The solid curves correspond to an adiabatic turn-on of the lattice, and the dashed curves correspond to the case of an instantaneous beam loading.

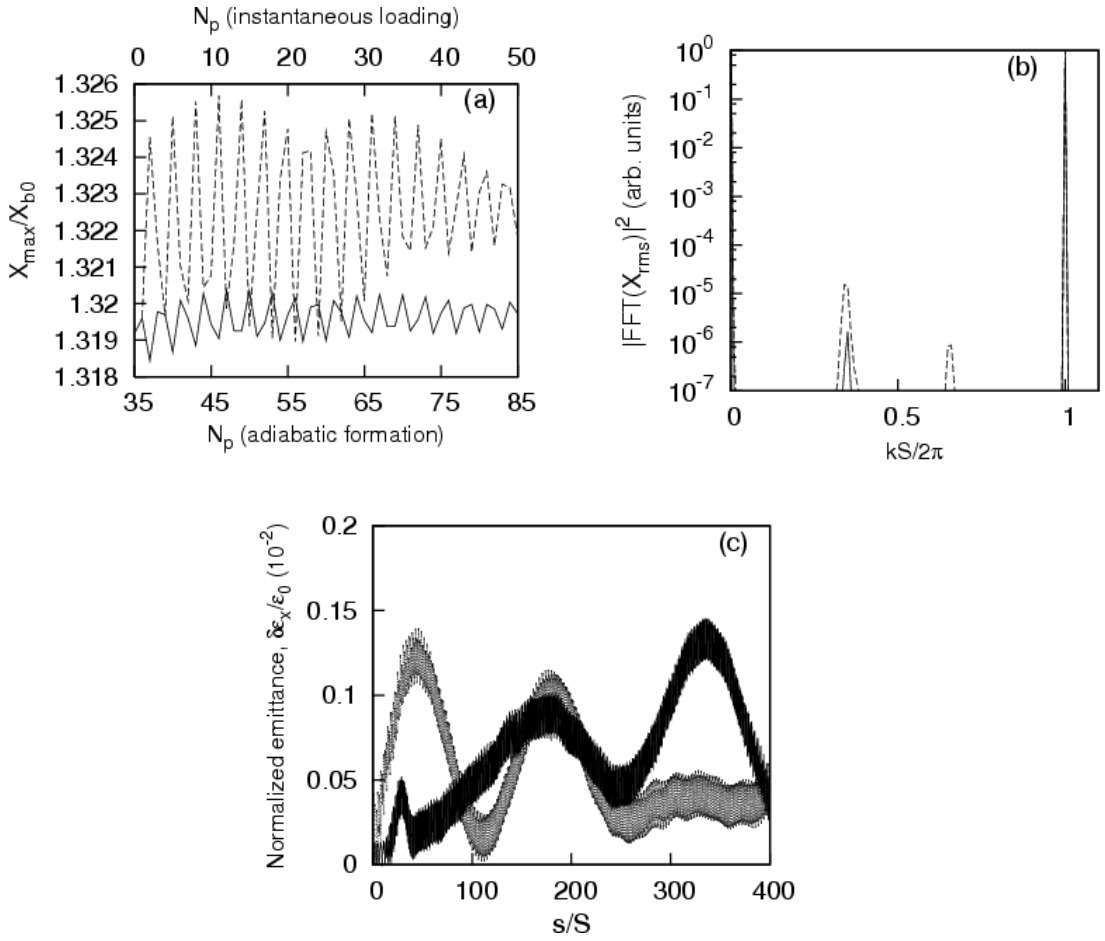

Figure 2.12: Evolution of an emittance-dominated beam with $2K_b R_{b0}^2/\varepsilon^2 = 0.2$. Phase advances are given by $\sigma_v = 65.9^0$ and $\sigma/\sigma_v = 0.915$. The corresponding smooth-focusing parameters are $\sigma_v^{sf} = 61.8^0$, $\sigma^{sf}/\sigma_v^{sf} = 0.91$, $s_b = 0.32$; and $2L_{1/2}/S = 30.5$. The figures show plots of: (a) $X_{\max}/X_{b0}$ versus number of lattice periods, N_p, where $X_{b0} = \langle x^2 \rangle_0^{1/2}$, and $X_{\max}$ corresponds to the value of X_{rms} calculated at the end of the focusing cell; (b) FFT of $X_{rms}(s)$ versus $kS/2\pi$; and (c) normalized perturbed emittance $\delta\varepsilon_x(s)/\varepsilon_0$ versus s/S. The solid curves correspond to an adiabatic turn-on of the lattice, and the dashed curves correspond to the case of an instantaneous beam loading.

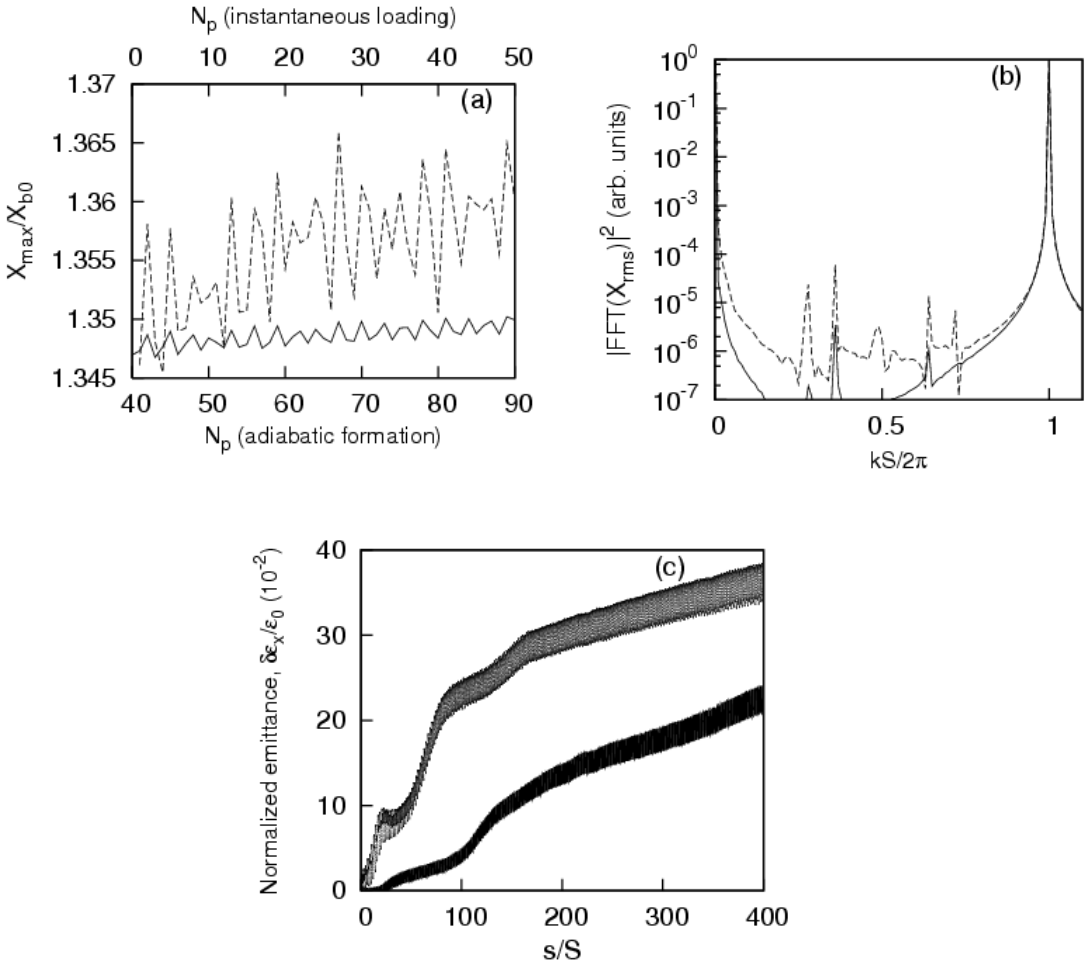

Fig. 2.13: Evolution of a space-charge-dominated beam with $2K_bR_{b0}^2/\varepsilon^2 = 15.3$. Phase advances are given by $\sigma_v = 87.5^0$ and $\sigma/\sigma_v = 0.265$. The corresponding smooth-focusing parameters are $\sigma_v^{sf} = 78.7^0$, $\sigma^{sf}/\sigma_v^{sf} = 0.247$, $s_b = 0.9999$; and $2L_{1/2}/S = 31.4$. The figures show plots of: (a) $X_{\max}/X_{b0}$ versus number of lattice periods, N_p, where $X_{b0} = \langle x^2 \rangle_0^{1/2}$, and $X_{\max}$ corresponds to the value of X_{rms} calculated at the end of the focusing cell; (b) FFT of $X_{rms}(s)$ versus $kS/2\pi$; and (c) normalized perturbed emittance $\delta\varepsilon_x(s)/\varepsilon_0$ versus s/S. The solid curves correspond to an adiabatic turn-on of the lattice, and the dashed curves correspond to the case of an instantaneous beam loading.

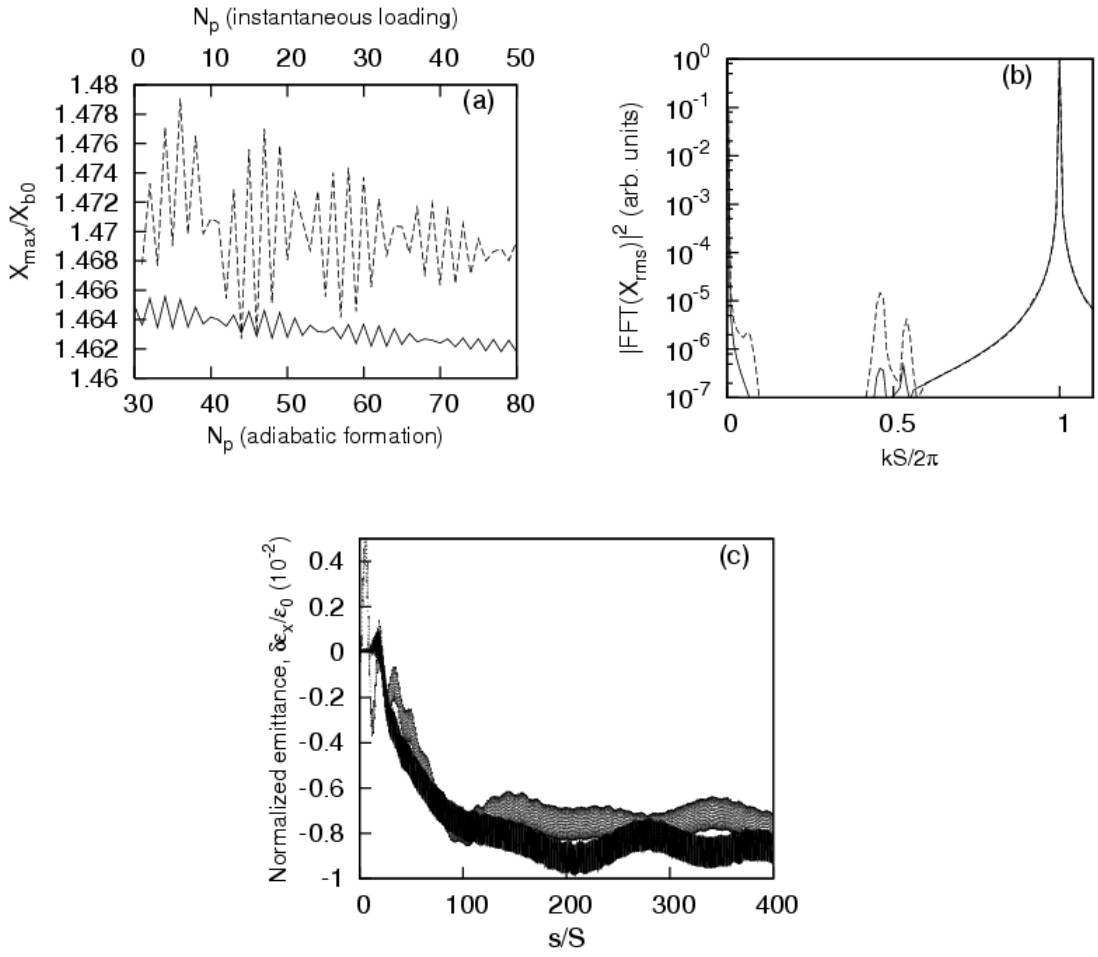

Figure 2.14: Evolution of an emittance-dominated beam with $2K_bR_{b0}^2/\varepsilon^2 = 0.2$. Phase advances are given by $\sigma_v = 87.5^0$ and $\sigma/\sigma_v = 0.918$. The corresponding smooth-focusing parameters are $\sigma_v^{sf} = 78.7^0$, $\sigma^{sf}/\sigma_v^{sf} = 0.91$, $s_b = 0.32$; and $2L_{1/2}/S = 23.9$. The figures show plots of: (a) $X_{\max}/X_{b0}$ versus number of lattice periods, N_p, where $X_{b0} = \langle x^2 \rangle_0^{1/2}$, and $X_{\max}$ corresponds to the value of X_{rms} calculated at the end of the focusing cell; (b) FFT of $X_{rms}(s)$ versus $kS/2\pi$; and (c) normalized perturbed emittance $\delta\varepsilon_x(s)/\varepsilon_0$ versus s/S. The solid curves correspond to an adiabatic turn-on of the lattice, and the dashed curves correspond to the case of an instantaneous beam loading.

of the beam particles are linearly scaled, providing the size and the slope of the beam envelope to be consistent with the matched solution to the envelope equations (2.28)-(2.29). Note that the frames in (a) in Figs. 2.9-2.14 illustrate the initial evolution of the beam mismatch for the case of instantaneous loading, and the evolution near the exit of the matching section, $s > 2L_{1/2}$, for the case of adiabatic formation of a beam quasi-equilibrium. Correspondingly, the averages for the FFT calculations are from $s = 0$ to $s = 100S$ for the case of instantaneous loading, and from $s = 2L_{1/2}$ to $s = 2L_{1/2} + 100S$ for the case of adiabatic turn-on of $V(s)$. Note that the 100-lattice-period window for the FFT averages is found to be sufficient for present purposes. It allows us to resolve the difference between the even (symmetric) and the odd (quadrupole) mismatch envelope mode frequencies as evident in Figs. 2.9, 2.11, and 2.13. Furthermore, for the case of an emittance-dominated beam the mismatch oscillations are significantly damped after ~100 lattice periods. Therefore an increase in the FFT-average window would result in noise integration.

It is evident from Figs. 2.9-2.14, for the case of adiabatic formation of the beam quasi-equilibrium, that the amplitude of the mismatch oscillations is reduced compared to the case of instantaneous loading of the beam distribution. Furthermore, for the case of adiabatic formation, note that the beam mismatch is attributed primarily to the numerical imprecision in loading the initial smooth-focusing equilibrium distribution, and therefore can be further suppressed if a finer grid structure, and larger number of macroparticles are used in the simulations. In contrast, the numerical scheme for instantaneous loading

cannot provide the detailed quasi-equilibrium intrinsically. Note that mismatch relaxation is more pronounced for the case of an emittance-dominated beam compared to the case of a space-charge-dominated beam, which is consistent with the studies in [Variale, 2001; Dorf *et al*., 2006; Dorf *et al*., 2007]. Of particular interest is the case of intense beam propagation with $2K_b R_{b0}^2/\varepsilon^2 = 15.3$ ($s_b = 0.9999$) through the quadrupole lattice with moderately high vacuum phase advance ($\sigma_v = 87.5^0$). In this case, appreciable emittance growth is evident even for adiabatic formation of the beam distribution [Fig. 2.13(c)]. The simulations demonstrate that the beam is well-matched to the lattice for over 450 lattice periods, and therefore the increase in the beam emittance cannot be attributed to mismatch relaxation. A plausible explanation of this phenomena can be attributed to "higher-order resonance" effects, which limit intense beam transport in the region where $\sigma_{vac}^2 - \sigma^2 > (2\pi/3)^2/2$ [Tiefenback *et al*., 1985; Tiefenback, 1986] as proposed in [Lund and Chawla, 2006]. As the system parameters approach this stability limit, higher-order resonances appear near the beam core in the transverse phase-space (Sec. 2.2.5); therefore, near-edge particles can diffuse outside the beam core sufficiently to participate in the resonances, thus providing emittance growth [Lund and Chawla, 2006].

As noted earlier, the matching section that provides adiabatic lattice transition from a uniform channel to an alternating-gradient quadrupole lattice could in principle be utilized to provide beam matching from the source into the quadrupole lattice for next-generation accelerators and transport systems. It is therefore of particular practical importance to estimate how smooth (adiabatic) the lattice transition should be to assure

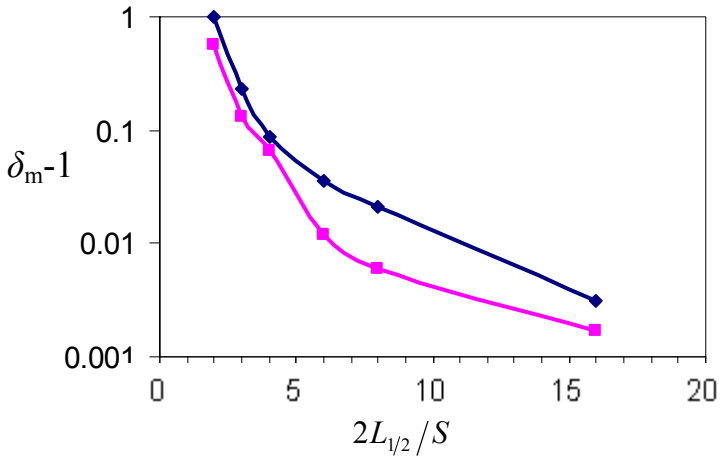

Figure 2.15: (Color) Degree of beam mismatch at the end of the matching section plotted versus the length of the matching section. Here, the vacuum phase advance is $\sigma_v = 65.9^0$, and the two cases correspond to normalized intensity $2K_b R_{b0}^2/\varepsilon^2 = 15.3$ and $s_b = 0.9999$ (blue curve), and $2K_b R_{b0}^2/\varepsilon^2 = 0.2$ and $s_b = 0.32$ (pink curve).

that matching is maintained during the transition [Dorf *et al.*, 2009a]. Figure 2.15 illustrates the degree of beam mismatch, δ_m, calculated at the end of the matching section ($s > 2L_{1/2}$) for different values of the matching section length, $2L_{1/2}$, for the case where the vacuum phase advance of the lattice σ_v is 65.9^0. Here, we measure the beam mismatch, δ_m, by the ratio of the maximum to minimum values of $X_{rms} \equiv \langle x^2 \rangle^{1/2}$ calculated at the end of each focusing cell within the first two periods of the smooth-focusing mismatch oscillationsafter the beam leaves the matching section, i.e., within the range $2L_{1/2} < s < 2L_{1/2} + 2\overline{L}_{sf}$. Recall that the beam rms envelope x-dimension, $X_{\rm rms}$, has a local maximum at the end of a focusing cell. It is readily seen from Fig. 2.15 that a

moderate length of the matching section, ~10 lattice periods, is sufficient to assure that the beam is well-matched to the lattice. Furthermore, a longer matching section is required for higher beam intensities. It should be noted that these observations are consistent with the results of detailed numerical and experimental studies in [Dorf *et al*., 2006; Gilson *et al*., 2007] of the beam response to the smooth variations of the lattice amplitude.

2.3.3 Self-Similar Evolution of the Beam Density Profile

In the previous section we demonstrated that the formation of a quasi-equilibrium beam distribution matched to an alternating-gradient quadrupole focusing lattice can be achieved in the numerical simulations by means of the adiabatic turn-on of the oscillating focusing field. In this section we investigate properties of the matched beam distribution in order to compare results of the numerical simulations with predictions of the analytical theory developed by Davidson *et al*. [Davidson *et al*., 1999]. Furthermore, we make use of the numerical simulations to investigate the validity limits of the theory. The analytical model developed in Refs. [Davidson *et al*., 1999; Startsev *et al*., 2009] applies Hamiltonian averaging techniques to the nonlinear Vlasov-Maxwell equations (2.13)-(2.14), assuming sufficiently small vacuum phase advance, σ_v. It has been demonstrated that the evolution of the beam density profile for the case of intense beam propagation through an alternating gradient-quadroupole lattice is given by [Davidson *et al*, 1999; Davidson and Qin, 2001a]

$$n_b(x,y,s) = \frac{R_{b0}^2}{a(s)b(s)} n_b^0\left[\frac{\widetilde{R}(x,y,s)}{R_{b0}}\right], \tag{2.43}$$

correct to order $\hat{\varepsilon}^3$, where $\hat{\varepsilon} \equiv \sigma_v/2\pi$ is the expansion parameter of the theory. Here, $n_b^0(r)$ is the beam density profile corresponding to an arbitrary smooth-focusing equilibrium, and $\widetilde{R}(x,y,s)/R_{b0}$ is defined by

$$\frac{\widetilde{R}(x,y,s)}{R_{b0}} = \left[\frac{x^2}{a^2(s)} + \frac{y^2}{b^2(s)}\right]^{1/2}, \tag{2.44}$$

where $a(s) = \sqrt{2}X_{rms}(s)$ and $b(s) = \sqrt{2}Y_{rms}(s)$. Note that the theory assumes that the conducting wall is sufficiently far removed from the beam $(r_w \to \infty)$.

We now investigate properties of the quasi-equilibrium beam density profiles obtained in the numerical simulations for the illustrative parameters considered in Sec. 2.3.2, and compare it with predictions of the analytical theory given by Eqs. (2.43) and (2.45) [Dorf *et al*., 2009a]. Recall, that for all of the simulations we take r_w=4R_{b0}, which corresponds to a sufficiently large radius of the conducting wall. Results of the numerical simulations are presented in Figs. 2.16-2.21, and the density profiles shown in the figures are calculated within the first lattice period after the beam leaves the matching section, i.e., $2L_{1/2} < s < 2L_{1/2} + S$. Figures 2.16 and 2.17 show contour plots of the beam density for the cases of a space-charge-dominated beam with $2K_bR_{b0}^2/\varepsilon^2 = 15.3$ [Fig. 2.16], and an emittance-dominated beam with $2K_bR_{b0}^2/\varepsilon^2 = 0.2$ [Fig. 2.17]. It is readily seen from the figures, plotted in the scaled coordinates $\{x/a(s), y/b(s)\}$, that the contours of

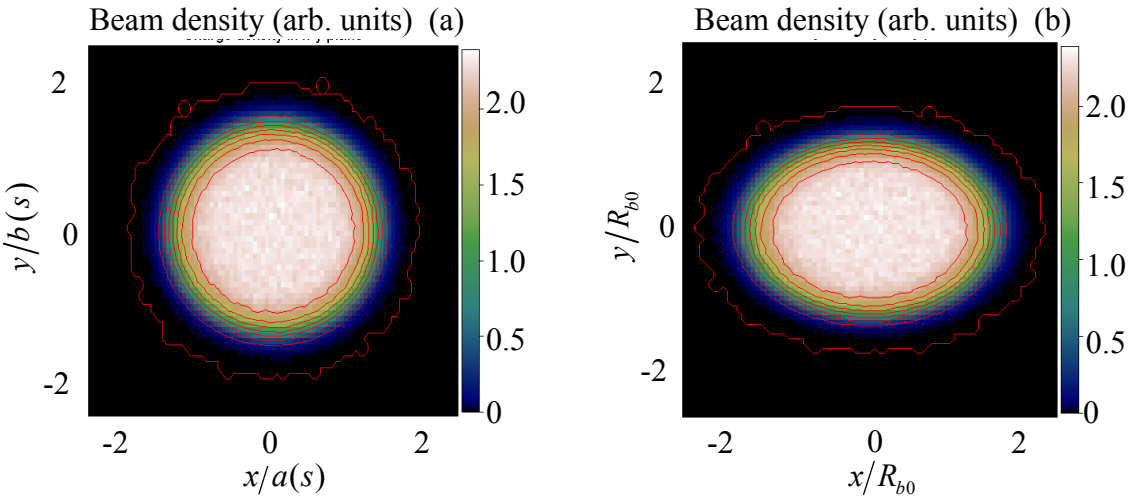

Figure 2.16: (Color) Contour plots of the beam density calculated at the end of the focusing cell and plotted in (a) scaled, and (b) regularly normalized coordinates. The vacuum phase advance is $\sigma_v = 44.8^0$, and the normalized beam intensity corresponds to $2K_b R_{b0}^2/\varepsilon^2 = 15.3$ ($s_b = 0.9999$).

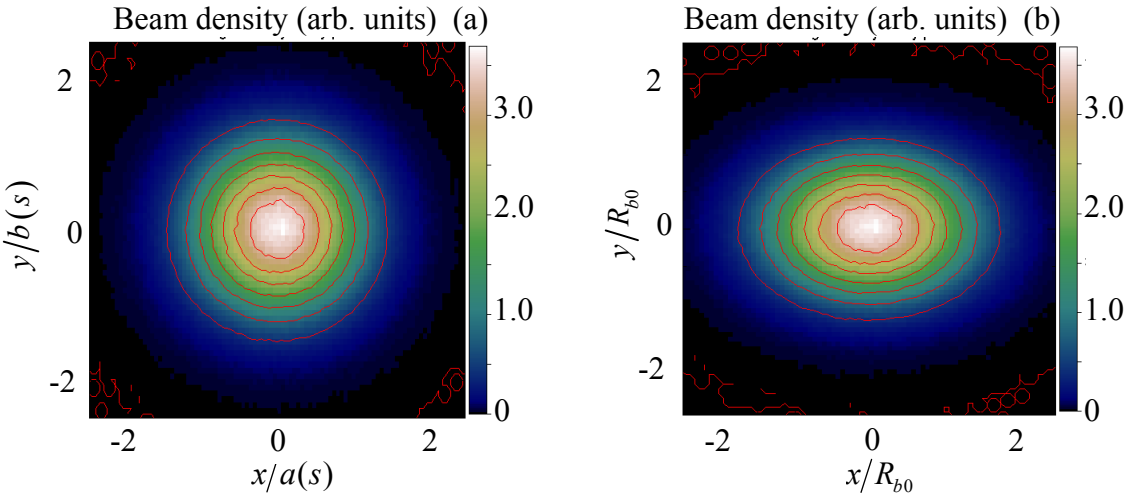

Figure 2.17: (Color) Contour plots of the beam density calculated at the end of the focusing cell and plotted in (a) scaled, and (b) regularly normalized coordinates. The vacuum phase advance is $\sigma_v = 44.8^0$, and the normalized beam intensity corresponds to $2K_b R_{b0}^2/\varepsilon^2 = 0.2$ ($s_b = 0.32$).

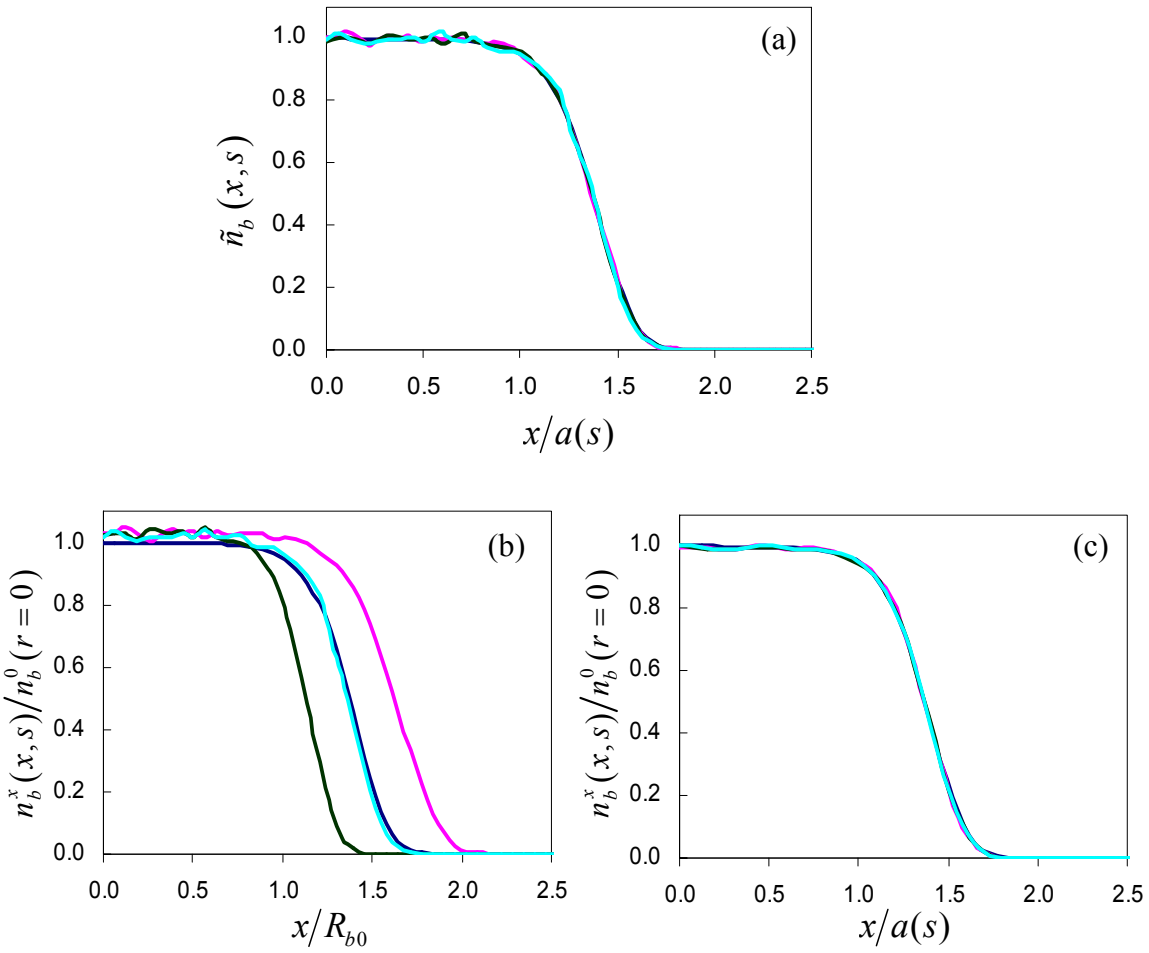

Figure 2.18: (Color) Plots of the beam density profile for a space-charge-dominated beam with $2K_bR_{b0}^2/\varepsilon^2 = 15.3$ ($s_b = 0.9999$). Phase advances are given by $\sigma_v = 44.8^0$ and $\sigma/\sigma_v = 0.255$. Shown are (a) the normalized density profile, $\tilde{n}_b(x,s) = \left[a(s)b(s)/R_{b0}^2\right]\left[n_b^x(x,s)/n_b^0(r=0)\right]$, plotted versus the scaled transverse coordinate *x/a(s)*; and (b) $n_b^x(x,s)/n_b^0(r=0)$ plotted versus x/R_{b0}. Density profiles correspond to: the initial smooth-focusing thermal equilibrium (blue curve); the maximum value of $X_{\rm rms}$ (pink curve); the minimum value of $X_{\rm rms}$ (green curve); and the location inside the focusing cell where X_{rms}=Y_{rms} (cyan curve). The flutter on top of the beam density profiles in Frame (a) is reduced in simulations with a larger number of macroparticles ($N_{pt} = 6\times10^6$) and coarser grid (N_x=N_y=64) as shown in Frame (c).

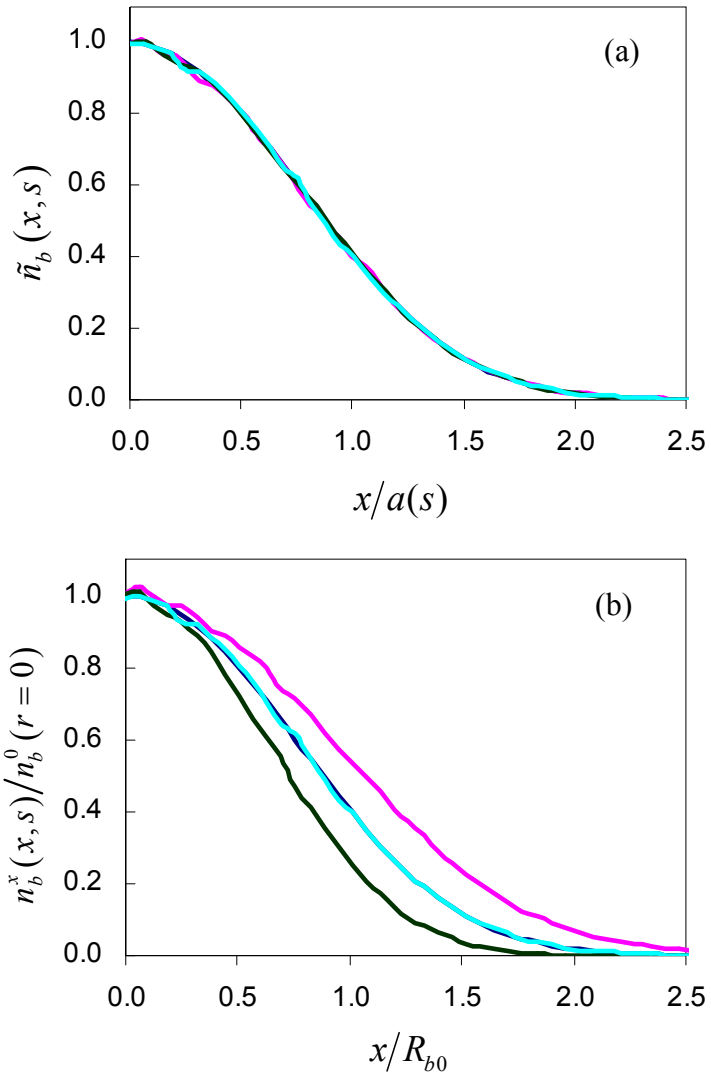

Figure 2.19: (Color) Plots of the beam density profile for an emittance-dominated beam with $2K_bR_{b0}^2/\varepsilon^2 = 0.2$ ($s_b = 0.32$). Phase advances are given by $\sigma_v = 44.8^0$ and $\sigma/\sigma_v = 0.913$. Shown are (a) the normalized density profile, $\tilde{n}_b(x,s) = \left[a(s)b(s)/R_{b0}^2\right]\left[n_b^x(x,s)/n_b^0(r=0)\right]$, plotted versus the scaled transverse coordinate *x/a(s)*; and (b) $n_b^x(x,s)/n_b^0(r=0)$ plotted versus x/R_{b0}. Density profiles correspond to: the initial smooth-focusing thermal equilibrium (blue curve); the maximum value of $X_{\rm rms}$ (pink curve); the minimum value of $X_{\rm rms}$ (green curve); and the location inside the focusing cell where X_{rms}=Y_{rms} (cyan curve).

constant beam density are approximately circular, which is consistent with Eqs. (2.43)-(2.44). Therefore, without loss of generality, in the following analysis we present results of the numerical simulations for the evolution of the beam density projected along the *x*-direction, $n_b^x(x,s) \equiv n_b(x, y=0, s)$. Figures 2.18 and 2.19 show the evolution of the beam density plotted in scaled coordinates [Fig. 2.18 (a) and Fig. 2.19 (a)], and regularly normalized coordinates [Fig. 2.18 (b) and Fig. 2.19 (b)] for the cases where $2K_b R_{b0}^2/\varepsilon^2 = 15.3$ and $2K_b R_{b0}^2/\varepsilon^2 = 0.2$, respectively. For these simulations, a relatively modest value of the vacuum phase advance of $\sigma_v = 44.8^0$ is considered. It is readily seen that the evolution of the quasi-equilibrium beam density is self-similar, i.e., $n_b(x, y=0, s) \equiv n_b^x(x,s) = n_b^x[x/a(s)]$ to very good approximation. Note that the flutter on top of the beam density profiles in Figs. 2.18(a) and 2.18 (b) is due to numerical noise, and a much lower noise level is observed in the numerical simulations with a larger number of macroparticles ($N_{pt} = 6\times10^6$) and coarser grid ($N_x = N_y = 64$) [compare Fig. 2.18(a) and Fig. 2.18(c)]. To good visual accuracy, it is evident that the beam density evolution in the quadrupole lattice is also self-similar to the initial beam density profile [plotted in Figs. 2.18-2.19 by the blue curves] corresponding to the initial smooth-focusing thermal equilibrium with the distribution function in Eq. (2.40). Note that the analytical theory [Davidson *et al*., 1999; Davidson and Qin, 2001a] predicts that the beam density profile is self-similar to the density profile determined from the choice of smooth-focusing equilibrium distribution function. Therefore, it is not expected *a priori* that the smooth-focusing equilibrium corresponding to the beam distribution matched to the

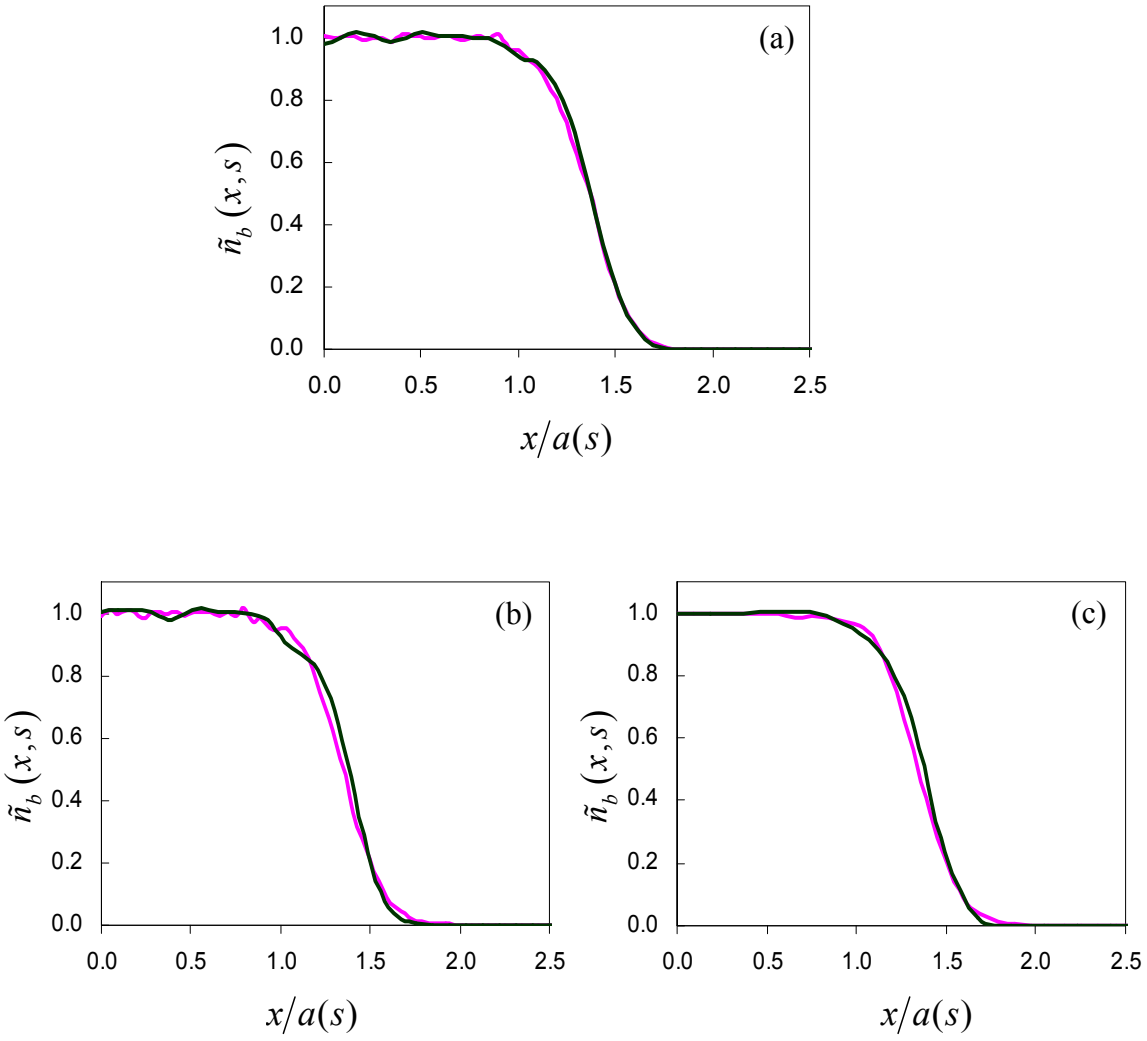

Figure 2.20: (Color). Plots of the normalized beam density profile, $\tilde{n}_b(x,s)=\left[a(s)b(s)/R_{b0}^2\right]\left[n_b^x(x,s)/n_b^0(r=0)\right]$, for a space-charge-dominated beam with $2K_bR_{b0}^2/\varepsilon^2=15.3$ ($s_b=0.9999$). Phase advances are given by (a) $\sigma_v=65.9^0$, $\sigma/\sigma_v=0.260$; and (b) $\sigma_v=87.5^0$, $\sigma/\sigma_v=0.265$. Density profiles correspond to: the maximum value of $X_{\rm rms}$ (pink curve), and the minimum value of $X_{\rm rms}$ (green curve). The flutter on top of the beam density profiles in Frame (b) is suppressed in simulations with a larger number of macroparticles ($N_{pt}=6\times10^6$) and coarser grid (N_x=N_y=64), as shown in Frame (c).

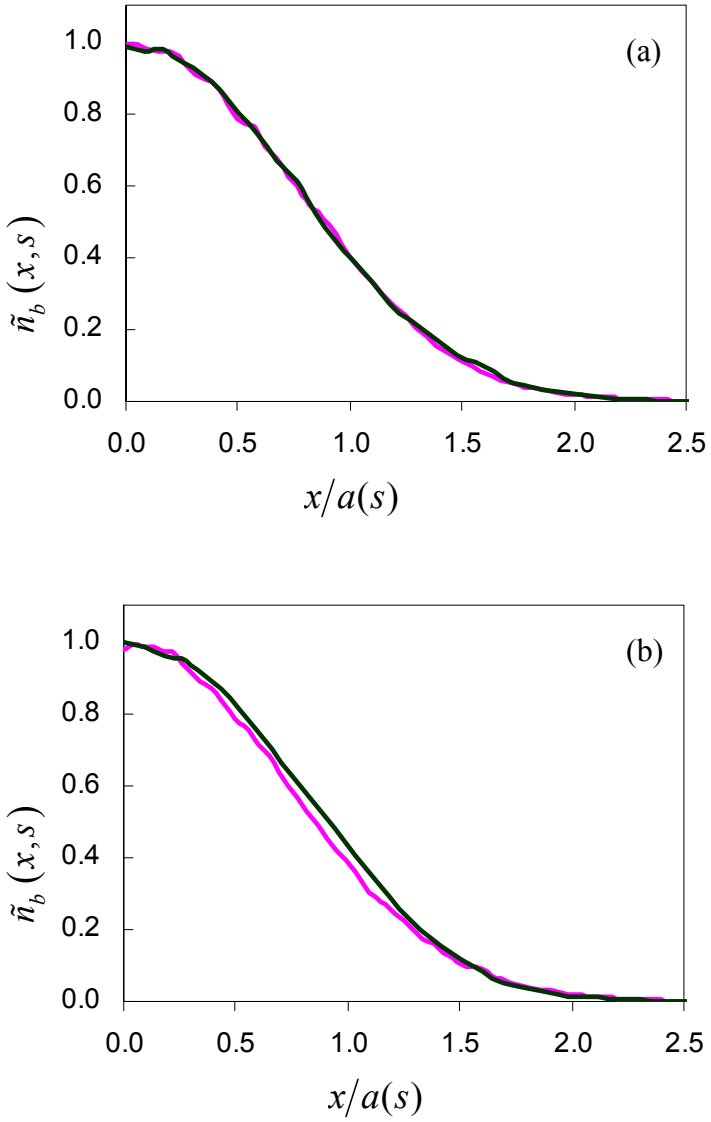

Figure 2.21: (Color) Plots of the normalized beam density profile, $\tilde{n}_b(x,s)=\left[a(s)b(s)/R_{b0}^2\right]\left[n_b^x(x,s)/n_b^0(r=0)\right]$, for an emittance-dominated beam with $2K_bR_{b0}^2/\varepsilon^2=0.2$ ($s_b=0.32$). Phase advances are given by (a) $\sigma_v=65.9^0$, $\sigma/\sigma_v=0.915$; and (b) $\sigma_v=87.5^0$, $\sigma/\sigma_v=0.918$. Density profiles correspond to: the maximum value of $X_{\rm rms}$ (pink curve), and the minimum value of $X_{\rm rms}$ (green curve).

quadrupole lattice should remain the same during the adiabatic transition phase in the matching section. Finally, Figs. 2.20 and 2.21 show the beam density evolution plotted in scaled coordinates for larger values of the vacuum phase-advance $\sigma_v = 65.9^0$ and $\sigma_v = 87.5^0$. It is readily seen that the beam density evolution is still self-similar to good visual accuracy for $\sigma_v = 65.9^0$. However, the self-similar feature becomes less accurate for $\sigma_v = 87.5^0$ for both space-charge-dominated and emittance-dominated beams. This illustrates the range of validity of the analytical predictions given by Eqs. (2.43)-(2.44). Again, we note that the flutter on top of the beam density profiles in Figs. 2.20(a) and 2.20(b) can be substantially suppressed if a larger number of macroparticles is used in the simulations. However, in the density-fall-off region, the difference in the beam density profiles remains very similar [compare Figs. 2.20(b) and 2.20(c)]. It is particularly interesting to note, for the case of an emittance-dominated beam with $\sigma/\sigma_v = 0.918$ and $\sigma_v = 87.5^0$, that the beam transport is stable, the effects of higher-order resonances are weak, however the analytical theory predictions is still of limited validity.

2.3.4 Extension of the Adiabatic Formation Scheme to the Case of a Periodic-Focusing Solenoidal Lattice and Various Choices of Initial Beam Distribution

The approach used in Sec. 2.3.2 for adiabatic formation of a beam quasi-equilibrium matched to a quadrupole lattice, can be generalized in a straightforward manner to the

case of a periodic solenodial lattice [Dorf *et al*., 2009b]. For the case of a solenoidal lattice, to maintain the average (smooth-focusing) effects of the average focusing field fixed, the transition of the applied lattice force is specified by

$$F_{foc}^{s} = -\{\kappa_{sf}\left[1-\left(1-\bar{\kappa}_{s}/\kappa_{sf}\right)V^{2}(s)\right]+V(s)\delta\kappa_{s}(s)\}(x\hat{\mathbf{e}}_{x}+y\hat{\mathbf{e}}_{y}), \tag{2.45}$$

where $V(s)$ is defined in Eq. (2.42). Here, we assume a step-function model of a periodic-focusing solenoidal lattice (Fig. 2.2), for which the corresponding smooth-focusing lattice coefficient, κ_{sf}, in Eq. (2.45) is specified by Eq. (2.20).

As noted earlier, a similar approach for formation of a quasi-equilibrium beam distribution matched to a periodic focusing solenoidal lattice by means of adiabatic turn-on of the oscillating focusing field has been previously reported by [Stoltz, *et al*., 1999]. However, the choice of the applied lattice force transition, $F_{foc}^{s}(s)$, considered in [Stoltz *et al*., 1999] did not provide a constant average (smooth-focusing) value of the focusing force. Furthermore, small oscillations of the beam envelope with variations in the rms beam radius of the order of 1% were considered, which allowed for the effective use of δF simulations, rather than full PIC simulations [Stoltz *et al*., 1999].

The results of the numerical simulations for illustrative parameters corresponding to a moderate intensity beam with $\sigma/\sigma_{v}=0.5$, propagating through quadrupole and solenoidal lattices, are presented in Figs. 2.22-2.24 [Dorf *et al*., 2009b]. For the case of beam propagation through a quadrupole lattice, note that thermal equilibrium [Eq. (2.23)] and waterbag equilibrium [Eq. (2.24)] distributions have been used for the initial beam

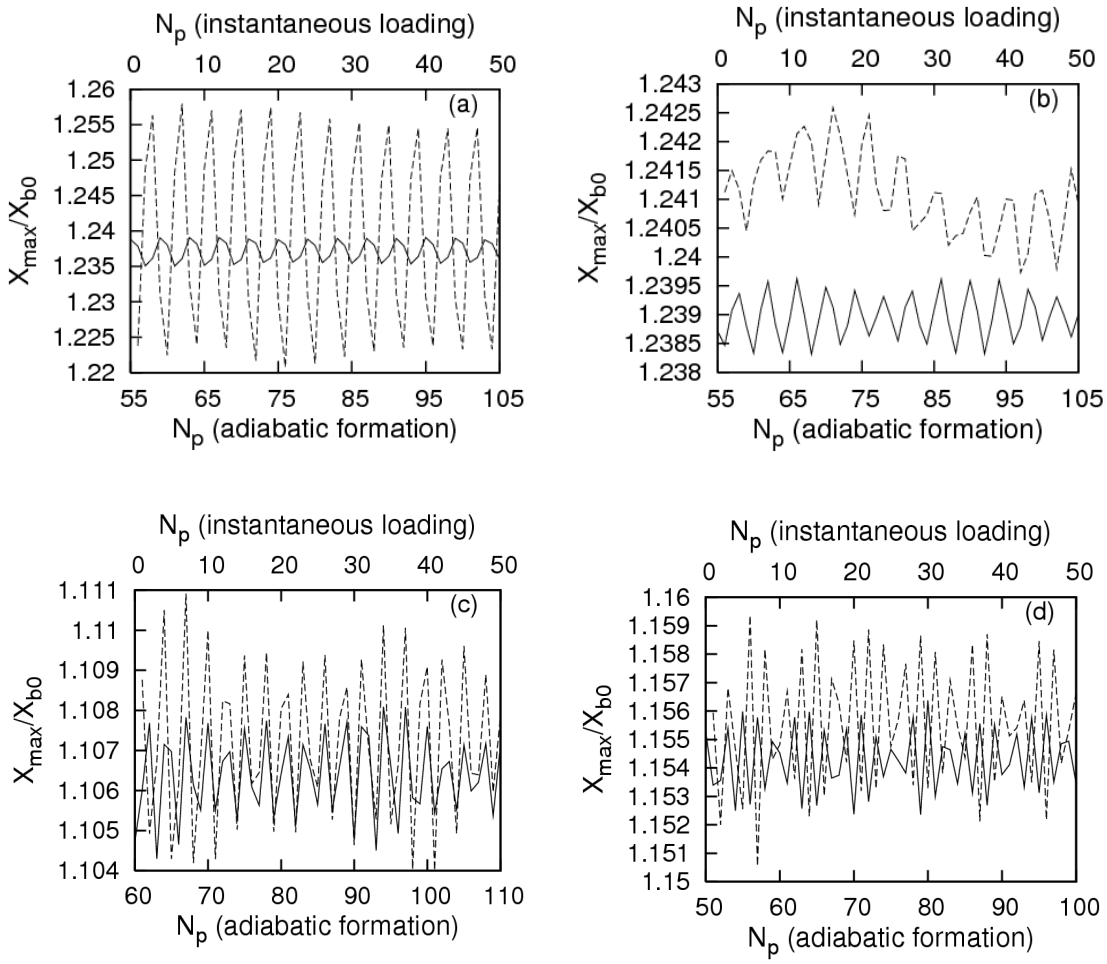

Figure 2.22: Plots of X_{max}/X_{b0} versus number of lattice periods, N_p, for the case of a moderate beam intensity with $\sigma/\sigma_v = 0.5$. Frames (a) and (b) correspond to a quadrupole lattice with $\eta_q = 0.3$, $\sigma_v = 57^0$ ($\sigma_v^{sf} = 54^0$), $2L_{1/2}/S = 42.4$, and the initial smooth-focusing beam equilibrium correspond to the thermal equilibrium and waterbag distributions, respectively. Frames (c) and (d) correspond to a solenoidal lattice with $\sigma_v = 84^0$ ($\sigma_v^{sf} = 83^0$), $2L_{1/2}/S = 55.5$, and $\sigma_v = 99^0$ ($\sigma_v^{sf} = 97^0$), $2L_{1/2}/S = 47.5$, respectively; here $\eta_s = 0.3$ and the initial smooth-focusing beam equilibrium corresponds to a thermal equilibrium distribution. The solid curves correspond to adiabatic turn-on of the lattice, and the dashed curves correspond to the case of instantaneous beam loading.

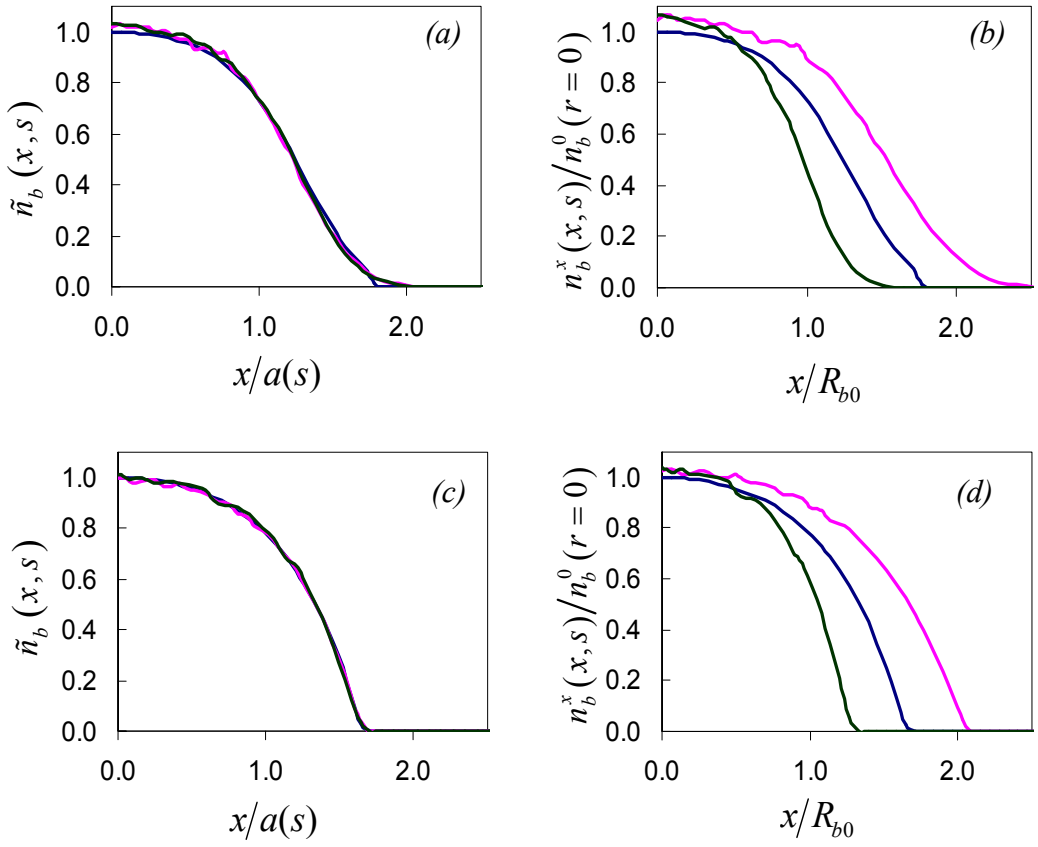

Figure 2.23: (Color) Plots of the beam density profile for the case of a quasi-equilibrium beam distribution matched to a quadrupole lattice with $\eta_q = 0.3$ and $\sigma_v = 57^0$. The normalized beam intensity corresponds to $\sigma/\sigma_v = 0.5$. Frames (a) and (b), and Frames (c) and (d) correspond to initial thermal equilibrium and waterbag distributions, respectively. The density profiles correspond to: the initial smooth-focusing thermal equilibrium (blue curve); the maximum value of $X_{\rm rms}$ (pink curve); and the minimum value of $X_{\rm rms}$ (green curve).

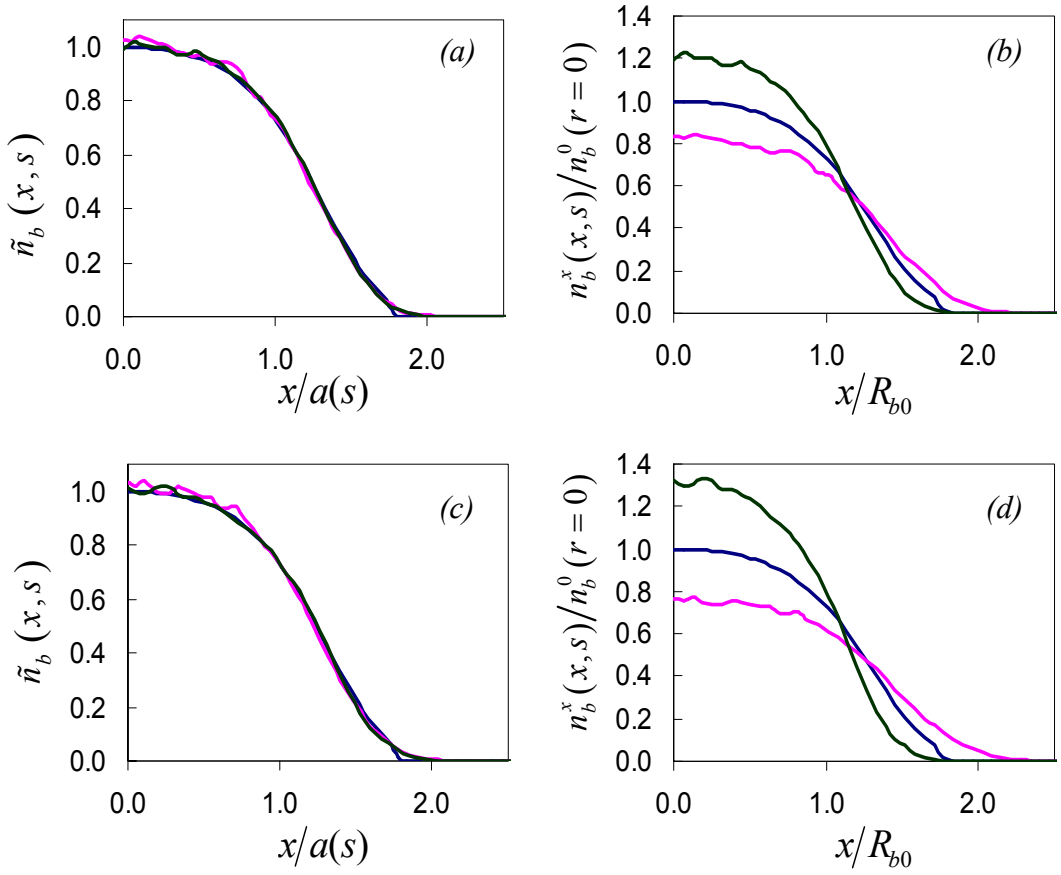

Figure 2.24: (Color) Plots of the beam density profile for the case of a quasi-equilibrium beam distribution matched to a solenoidal lattice with $\eta_s = 0.3$. The normalized beam intensity corresponds to $\sigma/\sigma_v = 0.5$. Frames (a) and (b), and Frames (c) and (d) correspond to $\sigma_v = 84^0$ and $\sigma_v = 99^0$, respectively. The initial smooth-focusing beam equilibrium corresponds to a thermal equilibrium distribution. The density profiles correspond to: the initial smooth-focusing thermal equilibrium (blue curve); the maximum value of $X_{\rm rms}$ (pink curve); and the minimum value of $X_{\rm rms}$ (green curve).

loading. To assure that matching is approximately maintained in the transition section, we choose $L_{1/2}/L_{tr}=5$ and take $L_{1/2}=5L_s^{sf}$ for the quadrupole lattice case, and $L_{1/2}=10L_s^{sf}$ for the solenoidal lattice case. The ratio of the length of the matching section to the lattice period, $2L_{1/2}/S$, is indicated in the captions to Fig. 2.22.

It is readily seen that the evolution of the beam density profile is self-similar for any choice of periodic lattice structure and initial beam distribution. In addition, it is interesting to note, for the case of a solenoidal lattice, that the self-similarity feature is preserved to good accuracy even for $\sigma_v=99^0$, whereas for the case of a quadrupole lattice the self-similarity feature becomes less accurate for smaller values of vacuum phase advance ($\sigma_v=87.5^0$) [Dorf *et al*., 2009b].

2.4 Summary and Discussions

It is increasingly important to develop an improved theoretical understanding of the equilibrium, stability, and transport properties of intense non-neutral beams propagating in periodic focusing accelerators and transport systems. A detailed self-consistent description of intense charged particle beam transport involves analysis of the Vlasov-Maxwell equations (Sec. 2.2.1), which offers a significant challenge for analytical studies due to the oscillatory nature of the applied focusing force, and the nonlinear effects of the intense self-fields produced by the beam space-charge. Therefore, various simplified beam dynamics models, including the smooth-focusing approximation (Sec. 2.2.2),

envelope equations (Sec. 2.2.3), Hamiltonian averaging techniques, etc., have been presented to provide insights on intense beam propagation. To validate prospective models it is particularly important to develop numerical techniques allowing for the formation of a quasi-equilibrium beam distribution. Furthermore, numerical schemes describing the quiescent loading of a beam distribution into a transport lattice, and minimizing the deleterious effects of beam mismatch (Sec. 2.2.4), are of particular importance for detailed numerical studies of various collective processes and instabilities (Sec. 2.2.5).

In this chapter we have described a numerical scheme allowing for the formation of a quasi-equilibrium beam distribution matched to an alternating-gradient quadrupole focusing lattice by means of adiabatic turn-on of the oscillating focusing field (Sec. 2.3.2). The scheme demonstrates the ability to load a matched-beam distribution into a quadrupole lattice for a broad range of beam intensity and vacuum phase advance $\sigma_v \le 66^0$. Furthermore, for higher values of vacuum phase advance (for instance, $\sigma_v = 87.5^0$), even in a regime where the parameters of the transport system approach the unstable transport criterion given by $\sigma_v^2 - \sigma^2 > (2\pi/3)^2/2$, and the transport of the intense beam is accompanied by beam emittance growth, it is found that the method of adiabatic formation described here still provides adequate beam matching. Therefore, the scheme described here can be effectively used for detailed studies of intense beam transport and stability properties, since it is able to suppress the effects of the initial beam mismatch. Finally, it is found that a relatively modest length of the

matching section (~10 lattice periods) is sufficient to assure that the beam is well-matched to the lattice, thus making the scheme attractive for practical applications.

Properties of the matched beam quasi-equlibrium obtained in numerical simulations have been investigated and compared with the predictions of the analytical theory developed by Davidson *et al*. in [Davidson *et al*., 1999] (Sec. 2.3.3). The theory shows that for sufficiently small values of $\hat{\varepsilon} \equiv \sigma_v / 2\pi$, the evolution of the beam density is self-similar correct to $\hat{\varepsilon}^3$. In accordance with the theory, the numerical simulations demonstrate self-similar evolution of the beam density profile for $\sigma_v \le 66^0$. However, for higher values of vacuum phase advance (for instance, $\sigma_v = 87.5^0$) the self-similarity feature becomes less accurate over a wide range of beam intensities, which demonstrates the validity limits of the theory.

The numerical scheme for describing formation of a quasi-equilibrium beam distribution matched to an alternating-gradient quadrupole focusing lattice, has been generalized to the case of a periodic-focusing solenoidal lattice (Sec. 2.3.4). Furthermore, various distributions have been considered for the initial beam equilibrium (Sec. 2.3.4). The self-similar evolution of the matched-beam density profile is observed for arbitrary choice of initial distribution function and lattice type.

It should be noted that the formalism developed here can provide a useful approach for initializing the choice of self-consistent quasi-equilibrium distributions f_0 in nonlinear δF simulations [Qin *et al*., 2007; Startsev *et al*., 2007; Qin *et al*., 2008] for intense beam propagation in periodic-focusing lattices.

Chapter 3

Transverse Compression of an Intense Ion Beam Propagating through a Quadrupole Lattice

3.1 Introduction

Alternating-gradient accelerators and transport systems have a wide range of applications ranging from basic scientific research to industrial applications [Davidson and Qin, 2001a; Reiser, 1994; Chao, 1993]. Of considerable practical importance for heavy ion beam applications to high energy density physics and fusion is the axial compression and transverse focusing of the (initially long) charge bunch to a small spot size at the target location. As noted earlier, one of the modern approaches to the compression process is to use dense background plasma which charge neutralizes the ion charge bunch, and hence facilitates compression of the bunch against strong space-charge forces [Henestroza *et al*., 2004; Roy *et al*., 2005; Davidson and Qin, 2005]. On the other hand, the transverse focusing can also be achieved by means of increasing the focusing strength of the alternating-gradient lattice along the beam propagation direction [Qin *et al*., 2004; Dorf *et*

al., 2006]. Although lattice compression significantly facilitates the technical realization of the process, uncompensated, high-intensity charge bunch propagation through the lattice transition region inevitably leads to a certain level of beam mismatch and emittance growth. Furthermore, a beam mismatch can produce halo particles [Gluckstern, 1994; Wangler *et al*., 1998; Allen *et al*., 2002; Qiang *et al*., 2002] that have much higher transverse energy than the core particles and may cause a degradation of beam quality (see Sec. 2.2.4).

It is evident that the beam mismatch will decrease as the length of the transition region is increased, assuming that the lattice amplitude is constant outside the transition region. Hence, it is a matter of considerable practical interest to determine how smooth (adiabatic) the lattice transition should be to assure that matching is maintained during the compression. In Sec. 3.2, a detailed investigation of this problem is performed for a long, coasting beam using the envelope equations and full particle-in-cell numerical simulations with the WARP code [Friedman *et al.*, 1992; Grote *et al*., 1998] in the smooth focusing approximation, which describe the average effects of a periodic lattice. In Sec. 3.3 the effects of the alternating-gradient quadrupole field are taken into account.

It is found that even a strong mismatch, produced during the compression process, can be consistent with moderate emittance growth. Nonetheless a certain fraction of the beam particles experience resonant interaction with the mismatch oscillations and populates the halo region. In Sec. 3.4, a qualitative analysis describing the details of halo formation during the compression process is performed. Finally, Sec. 3.5 develops a novel spectral technique for quantitative analysis of halo production by a beam mismatch

[Dorf *et al*., 2007]. The method is then applied to quantitative studies of the halo production during the transverse beam compression. In addition, it is shown that the analysis, based upon the spectral method, can provide important insights into other critical problems in intense beam transport such as mismatch relaxation and the space-charge transport limits (see Sec. 2.2.5).

The transverse compression of a long axially-stationary charge bunch has been extensively investigated in the Paul Trap Simulator Experiment (PTSX) [Chung *et al*., 2007; Gilson *et al*., 2007] that simulates the nonlinear transverse dynamics of intense beam propagation over large distances through an alternating-gradient transport lattice [Gilson *et al*., 2004; Gilson *et al*., 2006]. Therefore, the numerical studies presented here can provide important insights for interpretation of the experiments carried out on PTSX. Furthermore, since we study only transverse beam dynamics in the present chapter, it is convenient to perform the analysis in the axial rest frame of the charge bunch. In this frame axial ion velocity is equal to zero, $V_b = 0$, and the relativistic mass factor is equal to unity ($\gamma_b = 1$). Note that the axial rest frame of the charge bunch, described above, is the laboratory frame for the experiments carried out on PTSX.

3.2 Smooth-Focusing Analysis

In this section we make use of the smooth-focusing approximation (Sec. 2.2.2) to study the nonlinear response of long charge bunches to alternating-gradient waveforms with

time-varying amplitude [Dorf *et al*., 2006]. This model is used to describe the average effects of a quadrupole focusing field. Within this approximation, in the axial rest frame of the charge bunch the external focusing potential has the form

$$\varphi_{foc}(\vec{r},t)=\frac{1}{2}\frac{m_b}{e_b}\omega_q^2(t)r^2, \tag{3.1}$$

where $\omega_q(t)$ is the smooth focusing frequency, r is the radial distance from the beam axis, and e_b and m_b are the particle mass and charge, respectively. The normalized intensity parameter specified in the laboratory frame by Eq. (2.27), has the following form in the beam frame of references

$$s_b \equiv \omega_p^2 \big/ 2\omega_q^2, \tag{3.2}$$

where $\omega_p=\left(4\pi n_0 e_b^2/m_b\right)^{1/2}$ is the plasma frequency, and $n_0 \equiv n(r=0)$ is the on-axis number density.

The initial quasi-stationary distribution, which is used in the simulations later in this section, is assumed to correspond to a thermal equilibrium distribution [Eq. (2.23)], and the corresponding density profile $n(r)$ is given by [Davidson and Qin, 2001a]

$$n(r)=n_0\exp\left[-\frac{e_b\varphi_{foc}(r,0)+e_b\varphi^s(r)}{T}\right]. \tag{3.3}$$

Here, T=const is the transverse temperature, and the space-charge potential $\varphi^s(r)$ is determined self-consistently from Poisson's equation $\nabla^2\varphi^s(r)=-4\pi e_b n(r)$. Except for space-charge-dominated beams ($s_b \to 1$), numerical solutions of Poisson's equation

show that the radial density profile is bell-shaped, and is nearly Gaussian even for moderate values of s_b [compare Figs. 2.18(a) and 2.19(a)]. Regardless of the detailed shape of the density profile, the mean-square radius R_b^2 of the charge bunch is determined from the global radial force balance constraint [Davidson and Qin, 2001a]

$$m_b \omega_q^2 R_b^2 = 2T + N_b e_b^2 , \tag{3.4}$$

where $N_b = 2\pi \int_0^{r_w} dr r n(r)$ is the line density, and $R_b^2 = 2\pi N_b^{-1} \int_0^{r_w} dr r^3 n(r)$ is the mean-square beam radius.

This section is organized as follows. In Sec. 3.2.1 the transverse beam compression is investigated using the envelope equations; and the full self-consistent analysis is performed in Sec. 3.2.2, making use of particle-in-cell numerical simulations with the WARP code.

3.2.1 Rate Equation for the Beam Radius

From the fully nonlinear Vlasov-Maxwell equations describing a long charge bunch when the external focusing force has cylindrical symmetry [Eq. (3.1)], one can derive the following rate equation that describes the evolution of the rms radius of the charge bunch [Davidson *et al*., 1998; Davidson and Qin, 2001a]

$$\frac{d^2}{dt^2} R_b + \left(\omega_q^2(t) - \frac{K_b}{2R_b^2} \right) R_b = \frac{\varepsilon^2(t)}{4R_b^3} . \tag{3.5}$$

Here, $K_b = 2N_b e_b^2 / m_b$ is the effective self-field perveance, and $\varepsilon = \left(4R_b^2\left[\left\langle \dot{x}^2 + \dot{y}^2 \right\rangle - \dot{R}_b^2\right]\right)^{1/2}$ is the unnormalized transverse emittance defined in the beam frame. The super-dot $(\bullet)$ denotes time derivative and $\langle ... \rangle$ denotes the statistical average over the particle distribution function $f_b(x, y, \dot{x}, \dot{y}, t)$ in the transverse phase space $(x, y, \dot{x}, \dot{y})$. Although the emittance will vary due to nonuniformities in charge density, for present purposes we assume that $\varepsilon(t)$ is approximately constant if the focusing frequency $\omega_q(t)$ changes adiabatically. More detailed studies of the emittance behavior are presented in Sec. 3.2.2. Assuming that $\varepsilon(t) = const$, we can use Eq. (3.5) to analyze the evolution of the rms beam radius during the compression process. Following the analysis in [Gilson *et al*., 2005; Chung *et al*., 2007], we adopt a simple model in which $\omega_q(t)$ varies according to

$$\omega_q(t) = \omega_{qi} + \left(\omega_{qf} - \omega_{qi}\right)\left[\exp\left(\frac{\tau_{1/2} - t}{\tau_q}\right) + 1\right]^{-1}, \tag{3.6}$$

where $2\tau_{1/2}$ is the characteristic transition time, and τ_q is the characteristic time scale for variation of $\omega_q(t)$ from the constant value ω_{qi} to the constant value ω_{qf}.

Here, we consider long charge bunches, which are initially matched. This readily gives for the smooth-focusing model that $\left[\dot{R}_b\right]_{t=0} = 0$ and $\left[\ddot{R}_b\right]_{t=0} = 0$. Using the simplified Eq. (3.5), we now estimate the transition time $2\tau_{1/2}$ that is consistent with adiabatic compression. For a quantitative description of the adiabaticity of the

compression process we introduce the beam mismatch parameter $\eta = \Delta R / R_0$, where ΔR is the amplitude of the mismatch oscillations, and $R_0(t)$ is the quasi-equilibrium radius, which is determined from the instantaneous value of $\omega_q(t)$. Here, note that $\Delta R + R_0 = R_b$. Assuming that $\eta << 1$ during the adiabatic compression, we linearize Eq. (3.5) around the quasi-equilibrium radius $R_0(t)$, which gives

$$\Delta\ddot{R} + \overline{\omega}^2(t)\Delta R = -\ddot{R}_0, \tag{3.7}$$

where $\overline{\omega} = \left(K_b / R_0^2 + \varepsilon^2 / R_0^4\right)^{1/2}$ is the frequency of small-amplitude linear oscillations. It is evident from Eq. (3.7) that for adiabatic compression the inverse transition time $(2\tau_{1/2})^{-1}$ has to be much smaller than $\overline{\omega}$. Note, that the frequency $\overline{\omega}$ depends on R_0, and hence the inverse transition time needs to be much smaller than its minimum value, i.e., $(2\tau_{1/2})^{-1} << \overline{\omega}(R_{0i})$, where R_{0i} is the initial quasi-equilibrium beam radius.

For more detailed studies of the adiabaticity of the process we make use of the Van Der Pol method and introduce the following variables: $z = \Delta\dot{R} + i\overline{\omega}(t)\Delta R$ and $a = \frac{1}{\sqrt{\overline{\omega}}} z \exp\left(-i\int_0^t \overline{\omega} dt\right)$ [Fraiman, 2001]. Note that $|z|^2/2 = (\Delta\dot{R}^2 + \overline{\omega}^2\Delta R^2)/2 = E$ is the energy of the oscillator, and $|a|^2 = |z|^2/\overline{\omega}$ is a well-known adiabatic invariant for the pendulum equation (3.7). The physical interpretation of this adiabatic invariant corresponds to the area of the ellipse in the phase space (ΔR, $\Delta\dot{R}$). After some straightforward algebra, we obtain the following equation for the slow evolution of *a*,

$$\dot{a} = -\frac{\dot{\overline{\omega}}}{\overline{\omega}} a^* \exp(-2i\int_o^t \overline{\omega} dt) - \frac{\ddot{R}_0}{\sqrt{\overline{\omega}}} \exp(-i\int_0^t \overline{\omega} dt), \tag{3.8}$$

where star $(*)$ denotes complex conjugate. Recall that before compression the beam is matched, with $a(0) = 0$. Furthermore, the transition time should be large enough to assure $\eta << 1$. Hence we can neglect the first term on the right-hand side of Eq. (3.8). As a result, we obtain

$$a(t) \cong -\int_0^t \frac{\ddot{R}_0}{\sqrt{\overline{\omega}}} \exp(-i\int_0^{t'} \overline{\omega} dt') dt . \tag{3.9}$$

It is evident from Eq. (3.9) that the inverse transition time $2\tau_{1/2}$ must be much smaller than the frequency of linear oscillations $\overline{\omega}$ to assure that matching is maintained during compression. In this case $|a|^2 \propto \exp\left(-\langle\overline{\omega}\rangle\tau_q\right)$, where $\langle\overline{\omega}\rangle$ is a certain value of $\overline{\omega}$ between $\overline{\omega}(R_{0i})$ and $\overline{\omega}(R_{0f})$, and R_{0i}, R_{0f} are the initial and final quasi-equilibrium beam radii, respectively.

Illustrative numerical solutions to Eq. (3.5) are presented in Fig. 3.1 [Dorf *et al*., 2006]. To model a warm beam with moderate space-charge strength, and a space-charge-dominated beam, we consider the cases $s_b = 0.7$ and $s_b = 0.9999$, respectively. For the compression, we take $\tau_{1/2}/\tau_q = 5$ and $\omega_{qf}/\omega_{qi} = 2.3$ in Eq. (3.6). Figure 3.1 shows that a relatively fast compression, $\tau_q\overline{\omega}(R_{0i}) = 0.87$ for $s_b = 0.9999$, and $\tau_q\overline{\omega}(R_{0i}) = 0.64$ for $s_b = 0.7$, leads to a significant mismatch in the final state, whereas a more adiabatic

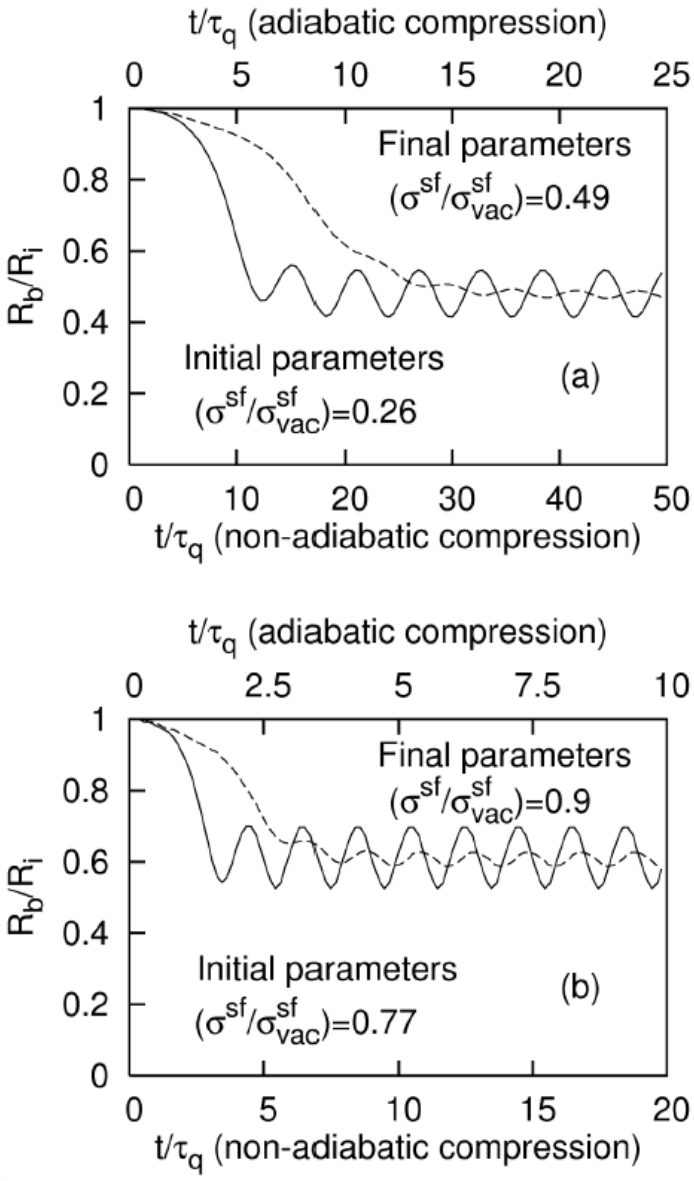

Figure 3.1: Numerical solutions to envelope equation (4) for ε=const. Plots of normalized rms beam radius R_b/R_i versus t/τ_q. The cases shown correspond to: (a) Space-charge dominated beam with $s_b = 0.9999$; Broken line: adiabatic compression with $\tau_q \overline{\omega}(R_{0i}) = 1.74$; Solid line: non-adiabatic compression with $\tau_q \overline{\omega}(R_{0i}) = 0.87$. (b) Moderate space-charge strength with $s_b = 0.7$; Broken line: adiabatic compression with $\tau_q \overline{\omega}(R_{0i}) = 1.28$; Solid line: non-adiabatic compression with $\tau_q \overline{\omega}(R_{0i}) = 0.64$.

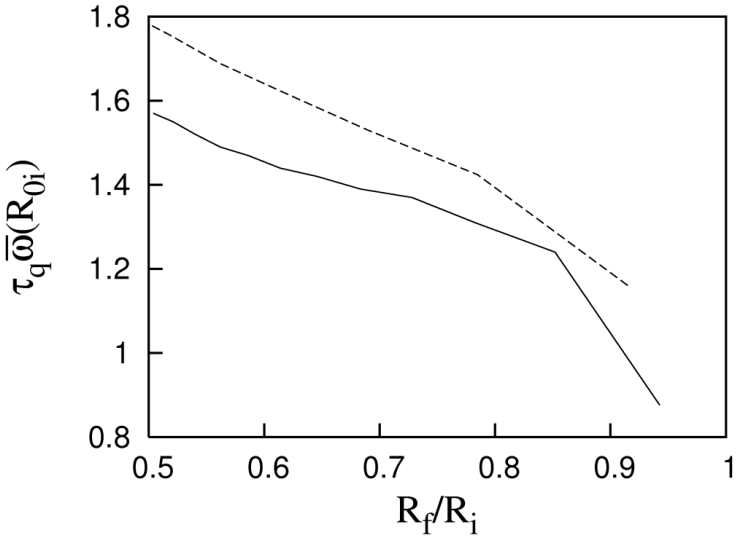

Figure 3.2: Plot of $\tau_q\overline{\omega}(R_{0i})$ versus R_f/R_i for adiabatic compression with η_f=2% . The two cases correspond to normalized intensity s_b=0.9999 (solid curve) and s_b=0.7 (broken curve).

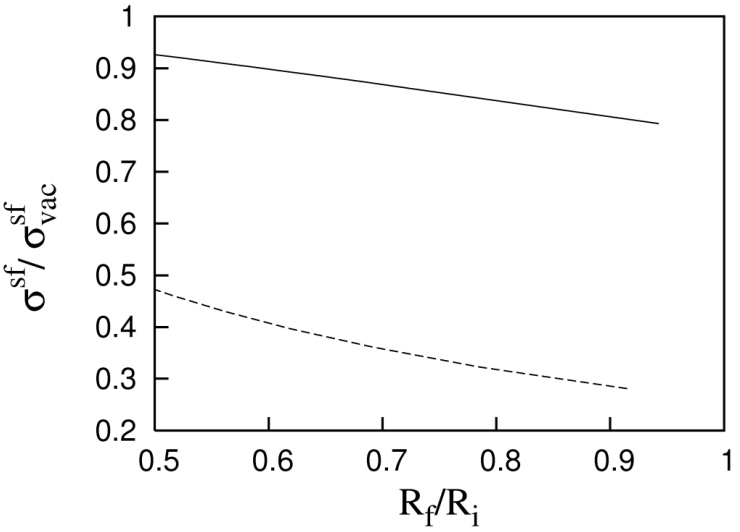

Figure 3.3: Plots of σ/σ_{vac} versus R_f/R_i for adiabatic compression with η_f=2%. The two cases correspond to normalized intensity s_b=0.9999 (broken curve) and s_b=0.7 (solid curve).

compression, $\tau_q\overline{\omega}(R_{0i})=1.74$ for $s_b=0.9999$, and $\tau_q\overline{\omega}(R_{0i})=1.28$ for $s_b=0.7$, provides a nearly matched beam envelope in the final stage. Figure 3.2 shows how the characteristic time scale for variation of $\omega_q(t)$ depends on the ratio of the final to initial beam radius, for adiabatic compression, and for several values of s_b [Dorf *et al*., 2006]. To estimate the transition time, we use the condition that the final mismatch parameter, $\eta_f=\Delta R/R_{0f}$, is equal to or less than 2%. To describe the change of the intensity parameter during the compression process, the ratio of the phase advances $\sigma^{sf}/\sigma_{vac}^{sf}=\left[1+\left(K_b/2\varepsilon\omega_q\right)^2\right]^{1/2}-\left(K_b/2\varepsilon\omega_q\right)$, calculated in the smooth focusing approximation [Eq. (2.36)] for different values of the final beam radius, is plotted in Fig. 3.3 [Dorf *et al*., 2006].

It should be noted from Fig. 3.3 that the relative space-charge strength as measured by $\sigma^{sf}/\sigma_{vac}^{sf}$ decreases during the adiabatic compression process. This result can be explained by recalling that $\varepsilon(t)\approx const$ has been assumed during the adiabatic compression process. Since $\left\langle \dot{X}^2+\dot{Y}^2\right\rangle >> \dot{R}_b^2$ for slow (adiabatic) compression, we obtain the following relation between the beam radius and effective transverse temperature, $R_bT^{1/2}\approx const$. Therefore, decreasing the beam radius results in an increase in the effective transverse beam temperature, and hence a decrease in the relative space-charge strength, which can also be measured in the beam frame by the dimensionless parameter $\delta=N_be_b^2/2T$ in Eq. (3.4) [Davidson and Qin, 1999; Davidson and Qin, 2001a].

3.2.2 Numerical Simulations of Beam Compression

The analysis of beam compression presented in Sec. 3.2.1 was made under the assumption that the transverse emittance remains approximately constant during the adiabatic compression process. To elucidate the details of the emittance behavior, the fully nonlinear Vlasov-Maxwell equations should be solved. In this section, we employ a two-dimensional transverse slice model using the WARP electrostatic particle-in-cell (PIC) code for this purpose [Dorf *et al*., 2006]. Results of the numerical simulations for the illustrative parameters used in Sec. 3.2.1 are shown in Fig. 3.4. Evidently, there is no significant emittance change during the adiabatic compression process. For a space-charge-dominated beam with $s_b = 0.9999$, the emittance decreases by 4% from its initial value, and for moderate space-charge strength with $s_b = 0.7$, the emittance variations are less than 1%. Such a small emittance change during the adiabatic compression process validates the assumptions made in Sec. 3.2.1. For the case of non-adiabatic compression, when the transition time is small compared to the inverse frequency of beam radius oscillations, $\overline{\omega}^{-1}$, the emittance variations are nearly 6% in both cases.

Despite such a moderate emittance change, an important qualitative difference is evident for the time evolution of the beam radius, when comparing results from the PIC code simulations and from the constant emittance model. To describe this phenomenon, it is convenient to introduce two stages of the compression process. *The transition stage* takes place during the transition phase of the smooth-focusing frequency, $\omega_q(t)$, i.e.,

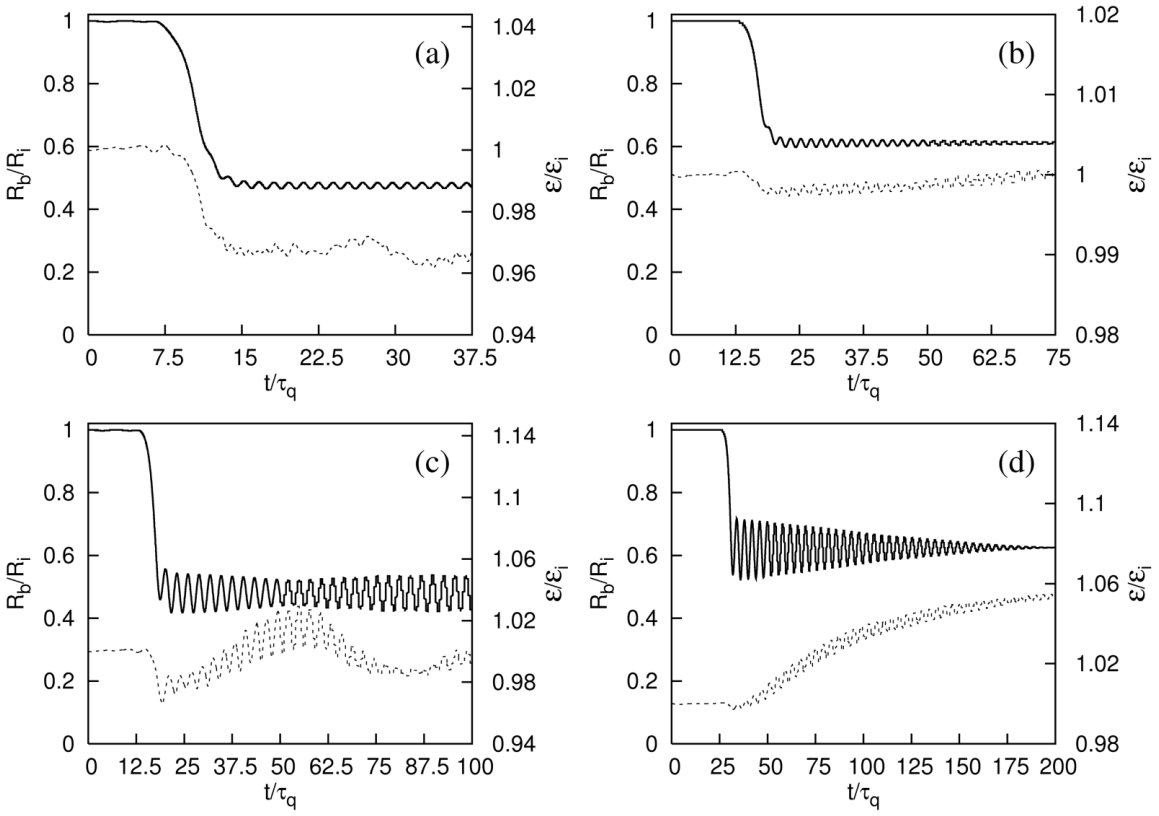

Figure 3.4: Evolution of the normalized beam radius R_b/R_i (solid line) and normalized transverse emittance $\varepsilon/\varepsilon_i$ (broken line) during the compression process. Figures (a) and (b) correspond to an adiabatic compression for $s_b = 0.9999$, $\tau_q \overline{\omega}(R_{0i}) = 1.74$, and for $s_b = 0.7$, $\tau_q \overline{\omega}(R_{0i}) = 1.28$, respectively. Figures (c) and (d) correspond to a non-adiabatic compression for $s_b = 0.9999$, $\tau_q \overline{\omega}(R_{0i}) = 0.87$, and for $s_b = 0.7$, $\tau_q \overline{\omega}(R_{0i}) = 0.64$, respectively . Results are obtained using the WARP code for a smooth-focusing field.

$0 < t < 2\tau_{1/2}$, and *the relaxation stage* for $t > 2\tau_{1/2}$ represents the mismatched beam behavior in the final focusing field with constant smooth-focusing frequency ω_{qf} . The largest difference in behavior is observed in the relaxation stage, during the non-adiabatic process when the beam is strongly mismatched after the transition. Figure 3.1 shows that the constant emittance model exhibits oscillations in beam radius with a constant amplitude, whereas the fully nonlinear Vlasov-Maxwell description gives a slight damping of the oscillations for a space-charge-dominated beam with $s_b = 0.9999$ [Fig. 3.4(c)], and an almost complete mixing of the oscillations for the moderate space-charge strength with $s_b = 0.7$ [Fig. 3.4(d)].

A plausible description of the damping mechanism of the mismatched oscillations is the following. Nonuniformities in the density profile produce nonlinear self fields. Therefore, particles move with energy-dependant betatron frequency and affect the oscillations of moments of the distribution function due to phase-mixing. References [Clauser *et al*., 1999; Variale, 2001] give a detailed explanation of these phenomena by means of Landau-like damping. In [Clauser *et al*., 1999] the particles are considered as an ensemble of betatron oscillators coupled to the collective mismatch oscillations (mismatch mode). The damping of the mismatch mode occurs due to the energy transfer from collective oscillations to the oscillators (beam particles) which are close to parametric 2:1 resonance with the mismatch mode. The relaxation time is determined by the phase-mixing of the trapped particles (resonant betatron oscillators). In the same work [Clauser *et al*., 1999] it is shown that for the case of a space-charge-dominated beam

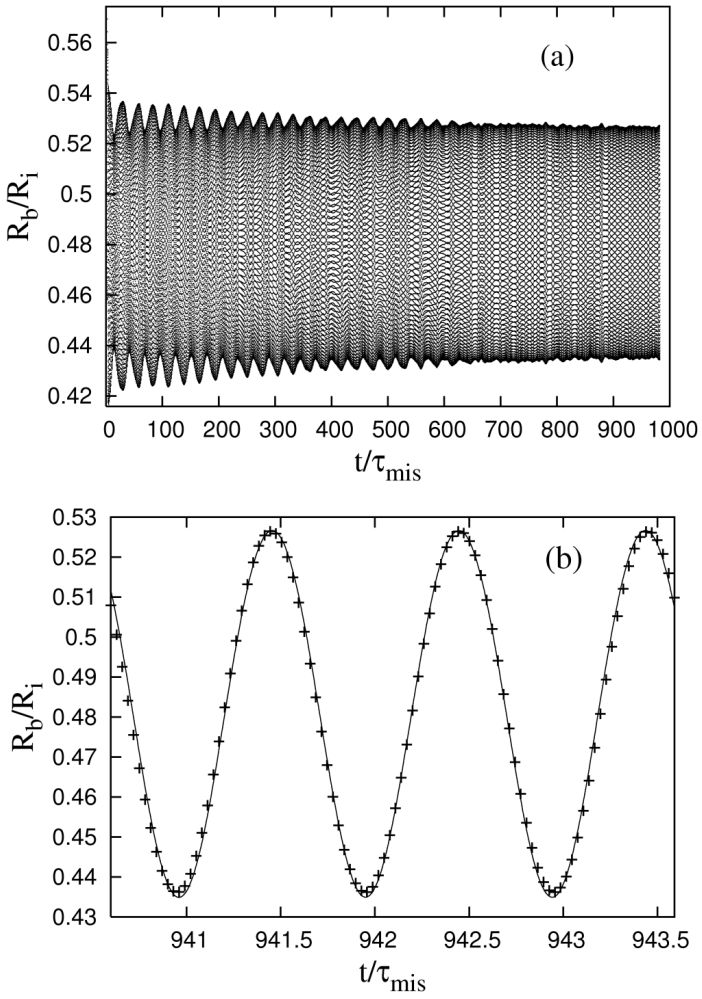

Figure 3.5: Relaxation of the large mismatch in a space-charge-dominated beam with s_b=0.9999 during the compression process using the smooth-focusing approximation. (a) Plot of R_b/R_i verses normalized time t/τ_{mis}, where τ_{mis} is the period of the mismatched oscillations in the final state. (b) Time dependence of R_b/R_i in the final state (solid line) can be fitted with a cosine function (broken line) with high accuracy. The ratio of the first and second harmonic amplitudes in the spectrum of the $R_b(t)$ dependence (obtained by applying FFT techniques) is equal to 2.5×10^4. Results are obtained using the WARP code [Dorf *et al*., 2006].

most of the betatron oscillators are far from resonance, providing a slight damping of the collective oscillations. As the beam space-charge intensity decreases, the mismatch frequency approaches the frequency distribution of the betatron oscillators, providing an increased mixing of the collective oscillations. This coincides well with the results presented here. We also emphasize that the present simulations show (Fig. 3.5) that a large mismatch for a space-charge-dominated beam tends to relax to a state with a non-uniform density profile, and to a distribution function which is periodic in time. This state corresponds qualitatively to the nonlinear saturation of Landau damping and has a significant number of trapped particles (see Sec. 3.3 for details). Future studies of this state may provide important insights for the construction of 'equilibrium' states for intense beam propagation in a periodic lattice.

The relaxation process described above transfers energy from the collective oscillations to the transverse motion of the resonant particles, thereby increasing the transverse phase space area (emittance growth). Figure 3.4(d) (for the beam radius) indicates that the phase-mixing time is about thirty times larger than the transition time. Hence, it is expected that there will be negligible emittance variations during the transition stage even during non-adiabatic compression. Indeed, Fig. 3.4(d) (for the emittance) shows that the emittance decrease during the initial transition of the smooth-focusing frequency is less than 0.5%, whereas the overall emittance growth is 6%. A theoretical model providing the estimate of the emittance growth due to the mismatch relaxation can be found in [Reiser, 1994]. The detailed behavior of the emittance validates the use of Eq. (3.5) with the $\varepsilon = const$ assumption to model the transition stage,

even for non-adiabatic compression. Comparing Figs. 3.1 and 3.4 indicates that the constant-emittance model and the PIC simulations give approximately the same initial amplitude of the mismatched oscillations.

Another interesting feature of the compression process is the emittance decrease during the initial transition stage. Examining Fig. 3.4 shows that the emittance decrease depends weakly on the transition time, and it is much larger for a space-charge-dominated beam than for a moderate intensity beam. To explain this phenomenon, we make use of the rate equation for the transverse emittance [Davidson *et al*., 1998; Davidson and Qin, 2001a],

$$\frac{1}{8}\frac{d}{dt}\varepsilon^2 = -R_b^2\frac{d}{dt}\left(E_F - E_{KV}\right). \tag{3.10}$$

Here, $E_F = (2K_b)^{-1}\int_0^{r_w} drr\left|\nabla_\perp\psi\right|^2$ is the normalized self-field energy, ψ solves $\nabla^2\psi = -\left(2\pi K_b/N_b\right)\iint d\dot{x}d\dot{y}f_b$, and $E_{KV} = (1/2)K_b\left(1/4 + \ln\left[r_w/(2^{1/2}R_b)\right]\right)$, where r_w is the radius of the conducting wall, is the self-field energy of the equivalent cold ($T = 0$) beam, having the same rms radius R_b and line density N_b. It can be shown that the self-field energy of the thermal equilibrium beam [Eq. (3.3)] with fixed rms radius and line density decreases with decreasing temperature and reaches its minimum value for a cold distribution ($T = 0$) with the flat-top density profile. During the transition stage, the effective beam temperature increases (see Sec. 3.2.2 for details), thereby increasing the difference between E_F and E_{KV} and leading to a decrease in the emittance.

3.3 Effects of Alternating-Gradient Quadrupole Field

In this section, we present numerical studies using the WARP code describing the beam response to an alternating-gradient quadrupole focusing field with time-varying amplitude [Dorf *et al*., 2006]. For present purposes, the instantaneous scheme (see Sec. 2.3.2) is used to load the initial distribution function. That is, first, for a specified intensity parameter s_b, effective temperature T, and on-axis number density n_0, we apply the smooth-focusing model to construct the initial equilibrium. Then, using the corresponding values for the emittance ε and perveance K_b, we determine the matched solutions of the envelope equations (2.28)-(2.29), which have the following form in the beam frame of reference

$$\begin{aligned} &\ddot{\overline{a}} + \kappa_q(t)\overline{a} - 2K_b/(\overline{a}+\overline{b}) = \varepsilon_x^2/\overline{a}^3, \\ &\ddot{\overline{b}} - \kappa_q(t)\overline{b} - 2K_b/(\overline{a}+\overline{b}) = \varepsilon_y^2/\overline{b}^3. \end{aligned} \tag{10}$$

Here $\overline{a}(t)$ and $\overline{b}(t)$ are the characteristic transverse beam dimensions in the x and y directions, respectively, $\varepsilon_x = \varepsilon_y = \varepsilon$ are the transverse emittances defined in the beam frame as $\varepsilon_x = 4\left(\langle x^2\rangle\langle \dot{x}^2\rangle - \langle x\dot{x}\rangle^2\right)^{1/2}$ and $\varepsilon_y = 4\left(\langle y^2\rangle\langle \dot{y}^2\rangle - \langle y\dot{y}\rangle^2\right)^{1/2}$, and $\kappa_q(t)$ is the alternating-gradient lattice function defined in the beam frame. To approximate the beam distribution coming out of the source (say, in PTSX), during the final stage of forming the initial quasi-equilibrium we load the particles with a semi-Gaussian distribution, which is Gaussian distribution in $\dot{x}$ and $\dot{y}$ and has a uniform (step-function) density profile, into the matched envelope. Similarly to the experiments on beam compression on

PTSX [Gilson *et al*., 2007; Chung *et al*., 2007], in the present simulations the beam is allowed to relax during 100 periods of the focusing lattice before compressing the lattice amplitude. The time dependence of the rms beam radius and the transverse emittance during the adiabatic and non-adiabatic processes including the first 100 lattice periods are shown in Fig. 3.6 [Dorf *et al*., 2006]. For a non-axysimmetric beam, which is studied in this section, we define the average beam radius as $R_b = \left(\tilde{a}^2 + \tilde{b}^2\right)^{1/2}$, where $\tilde{a} = \left\langle x^2 \right\rangle^{1/2}$ and $\tilde{b} = \left\langle y^2 \right\rangle^{1/2}$ are the rms envelope dimensions. The average transverse emittance ε is defined as $\varepsilon = (\varepsilon_x \varepsilon_y)^{1/2}$.

Consistent with the experiments carried out on PTSX [Gilson *et al.*, 2007], to model the lattice we take $\kappa_q(t) = 2^{3/2}\pi\omega_q\tau_L^{-1}\sin\left(2\pi t/\tau_L\right)$, where τ_L is the lattice period. All other parameters are the same as in Sec. 3.2. It should be noted that even for non-adiabatic compression the transition time is sufficiently large so that the smooth-focusing approximation is valid during the transition phase. Comparing Figs. 3.4 and 3.6, we note that the smooth-focusing approximation and the full alternating-gradient quadrupole field model give remarkably similar results. The differences are evident in the emittance behavior during the initial stage (before beam propagation through the lattice transition region) which is due to the initial beam mismatch in the quadrupole field model. Furthermore, the smooth-focusing model shows a complete mixing of the oscillations in beam radius for a beam with moderate space-charge strength, $s_b = 0.7$, during non-adiabatic compression, whereas in the quadrupole field model the amplitude of the

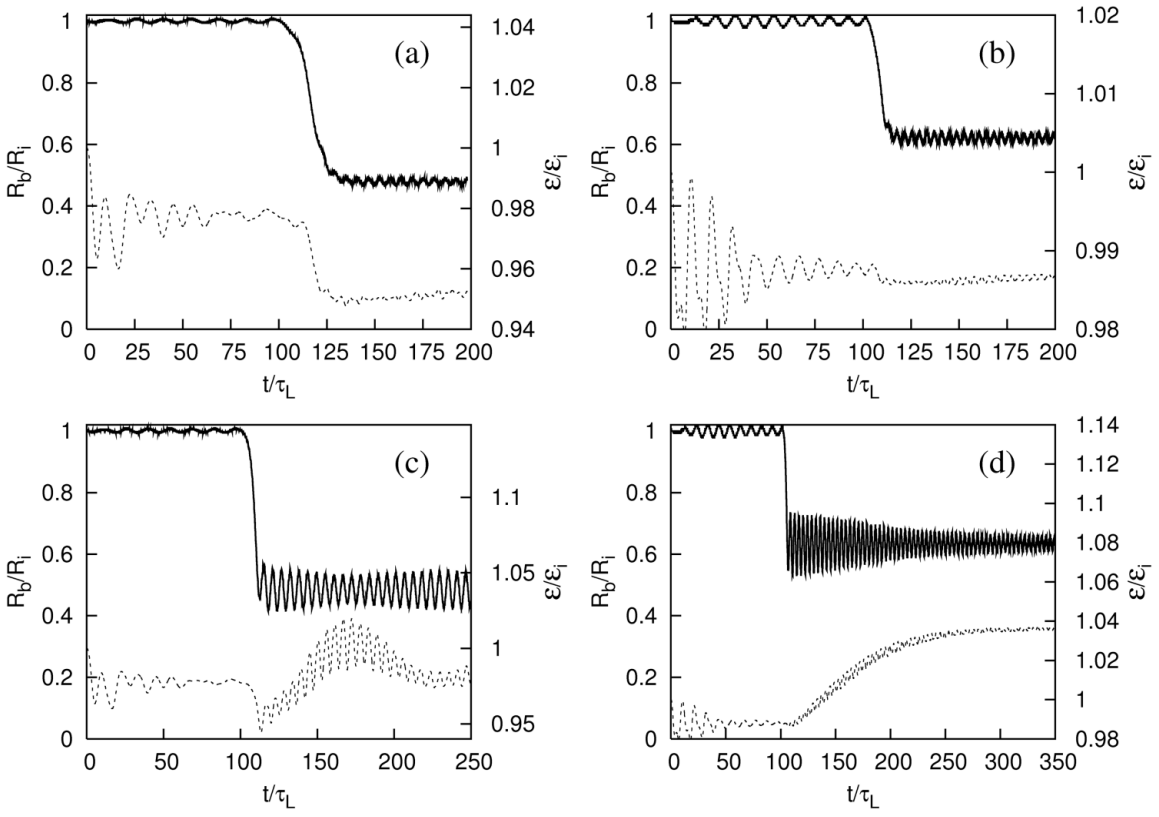

Figure 3.6: Evolution of the normalized beam radius R_b/R_i (solid line) and normalized transverse emittance $\varepsilon/\varepsilon_i$ (broken line) during the compression process. Figures (a) and (b) correspond to an adiabatic compression for $s_b = 0.9999$, $\tau_{1/2}/\tau_L = 20$ [corresponding to $\tau_q\overline{\omega}(R_{0i}) = 1.74$], and $s_b = 0.7$, $\tau_{1/2}/\tau_L = 10$ [corresponding to $\tau_q\overline{\omega}(R_{0i}) = 1.28$], respectively. Figures (c) and (d) correspond to a non-adiabatic compression for $s_b = 0.9999$, $\tau_{1/2}/\tau_L = 10$ [corresponding to $\tau_q\overline{\omega}(R_{0i}) = 0.87$], and $s_b = 0.7$, $\tau_{1/2}/\tau_L = 5$ [corresponding to $\tau_q\overline{\omega}(R_{0i}) = 0.64$], respectively . Results are obtained using the WARP code for an alternating-gradient quadrupole lattice.

oscillations only decreases to 30% of its initial value. However, contrary to the smooth-focusing approximation, the oscillations in average beam radius cannot be considered as a measure of the final-state mismatch. In fact, even for a perfectly matched beam (KV distribution), the sum of the rms envelope dimensions is nearly constant, $\widetilde{a}(t)+\widetilde{b}(t)\cong const$, but $R_b=[\widetilde{a}^2(t)+\widetilde{b}^2(t)]^{1/2}\neq const$. Therefore, to estimate the mismatch of the final state, it is important to analyze the behavior of the rms envelope dimensions $\widetilde{a}$ and $\widetilde{b}$, which are illustrated in Figs. 3.7 and 3.8 [Dorf *et al*., 2006]. It is evident from Fig. 3.7(b), which shows the time dependence of $\widetilde{a}$ and $\widetilde{b}$ for the non-adiabatic compression of a beam with $s_b=0.7$, that the beam is only slightly mismatched in the final state. The particle phase advances, defined as $\sigma=\varepsilon\int_t^{t+\tau_L} dt/\overline{a}^2(t)=\varepsilon\int_t^{t+\tau_L} dt/\overline{b}^2(t)$, and $\sigma_{vac}=\lim_{K_b\to 0}\varepsilon\int_t^{t+\tau_L} dt/\overline{a}^2(t)$ (see Sec. 2.2.3), are shown for the initial and final stages of compression process in Figs. 3.7 and 3.8.

As mentioned earlier, for the parameters used in the simulations, the smooth-focusing approximation is valid during the transition phase even for a non-adiabatic process. This means that the perturbations introduced to the beam in the transition region of the quadrupole lattice can be averaged and the averaged perturbation has azymuthal symmetry. Therefore, as shown in Figs. 3.7 and 3.8, only the symmetric mode (*x* and *y* envelope dimensions oscillate with zero relative phase shift) is excited during the compression process.

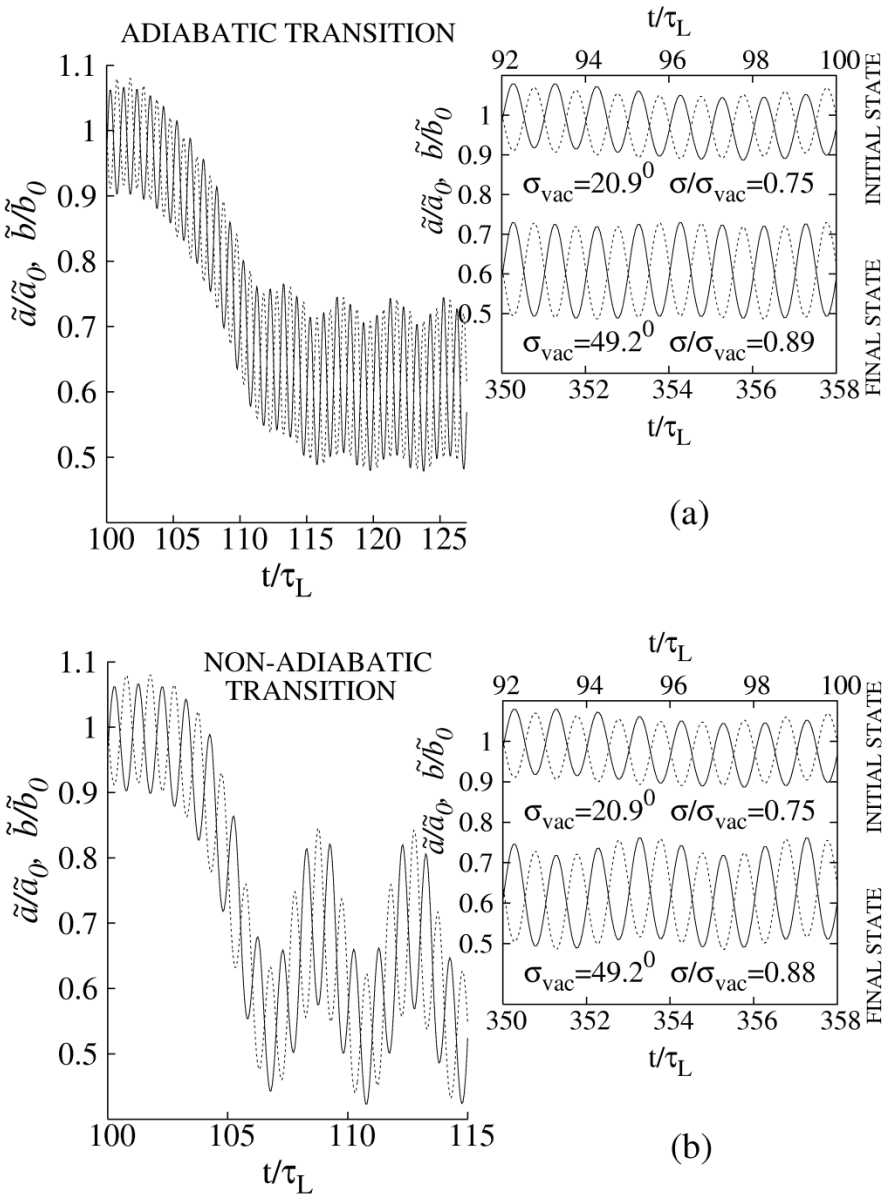

Figure 3.7: WARP simulations of the beam compression in an alternating-gradient quadrupole lattice. Evolution of the rms envelope dimensions $\widetilde{a}/\widetilde{a}_0$ (solid line) and $\widetilde{b}/\widetilde{b}_0$ (broken line) are plotted during (a) adiabatic compression with $\tau_{1/2}/\tau_L = 10$, and during (b) non-adiabatic compression with $\tau_{1/2}/\tau_L = 5$, for a beam with moderate space-charge intensity, $s_b = 0.7$.

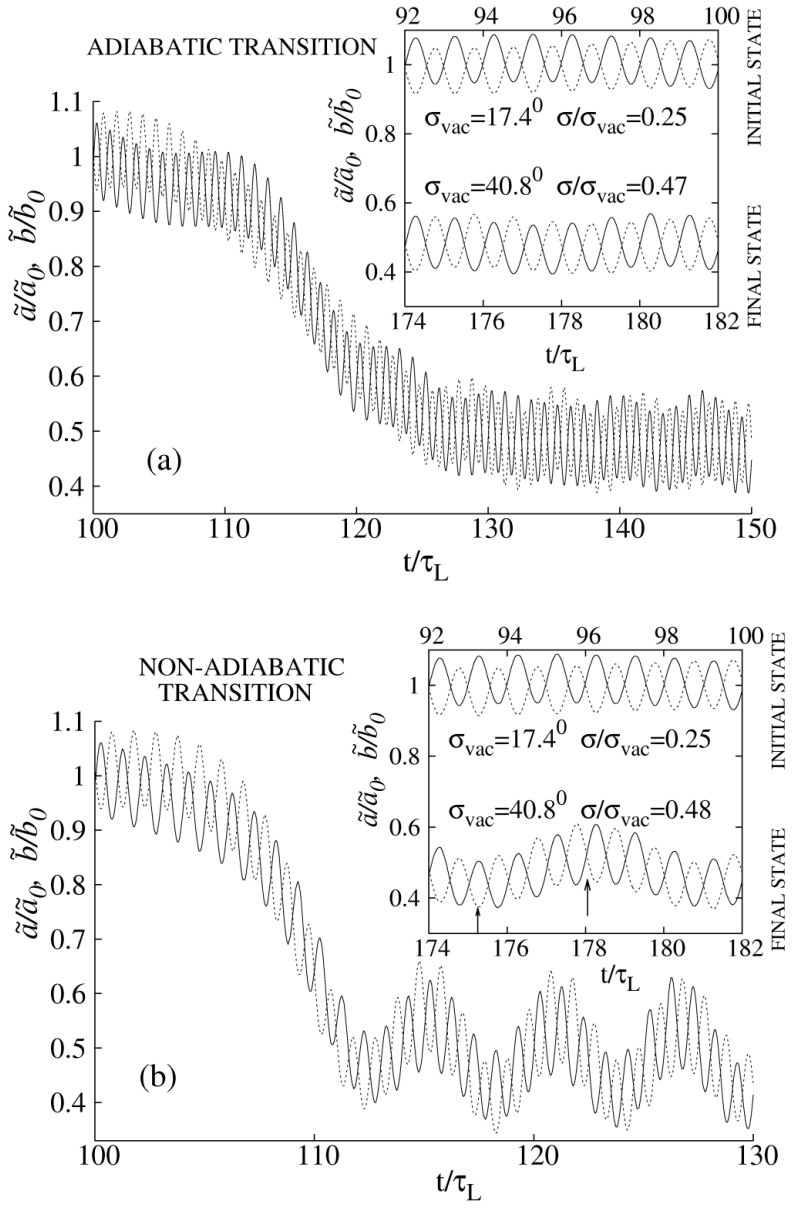

Figure 3.8: WARP simulations of the beam compression in an alternating-gradient quadrupole lattice. Evolution of the rms envelope dimensions $\widetilde{a}/\widetilde{a}_0$ (solid line) and $\widetilde{b}/\widetilde{b}_0$ (broken line) are plotted during (a) adiabatic compression with $\tau_{1/2}/\tau_L = 20$, and during (b) non-adiabatic compression with $\tau_{1/2}/\tau_L = 10$, for a space-charge-dominated beam with $s_b = 0.9999$.

3.4 Halo Formation During the Compression Process

In previous sections, the evolution of low-order moments of the distribution function (such as the rms envelope dimensions and transverse emittance) was studied. The results show that even non-adiabatic compression, which leads to significant beam mismatch by the end of the transition stage, does not result in large emittance growth ($\Delta\varepsilon < 6\%$). Nevertheless, it is well known that a beam mismatch produces halo particles that have much higher transverse energies than the core particles and may cause a deterioration in beam quality during the subsequent beam transport (Sec. 2.2.4). In this section, we present a detailed analysis of halo formation during the compression process using the WARP code for an alternating-gradient quadrupole lattice [Dorf *et al*., 2006].

Figures 3.9(a), 3.9(b) and Figs. 3.10(a), 3.10(b), respectively, illustrate the initial and final $(x,\dot{x})$ phase-spaces for both moderate and high values of the space-charge intensity parameter s. The scaled coordinates $X = x/(2\tilde{a})$ and $\dot{X} = 2\left(\dot{x}\tilde{a} - x\dot{\tilde{a}}\right)\Big/\varepsilon_x$ are plotted to remove the envelope oscillations [Lund and Chawla, 2006]. For a space-charge-dominated beam with the almost flat-top density profile shown in Fig. 3.11(a), the two-lobe shape of the final phase-space plot [Fig. 3.10(b)] clearly indicates 2:1 (fundamental) resonance interaction between the beam particles and the collective mismatch oscillations (Sec. 2.2.4). Note that the resonance structure of the $X-\dot{X}$ phase-space projection is filled with particles, as opposed to the $r-r'$ phase-space projection shown in Fig. 2.4, where the halo particles travel mostly near a separatrix. This difference

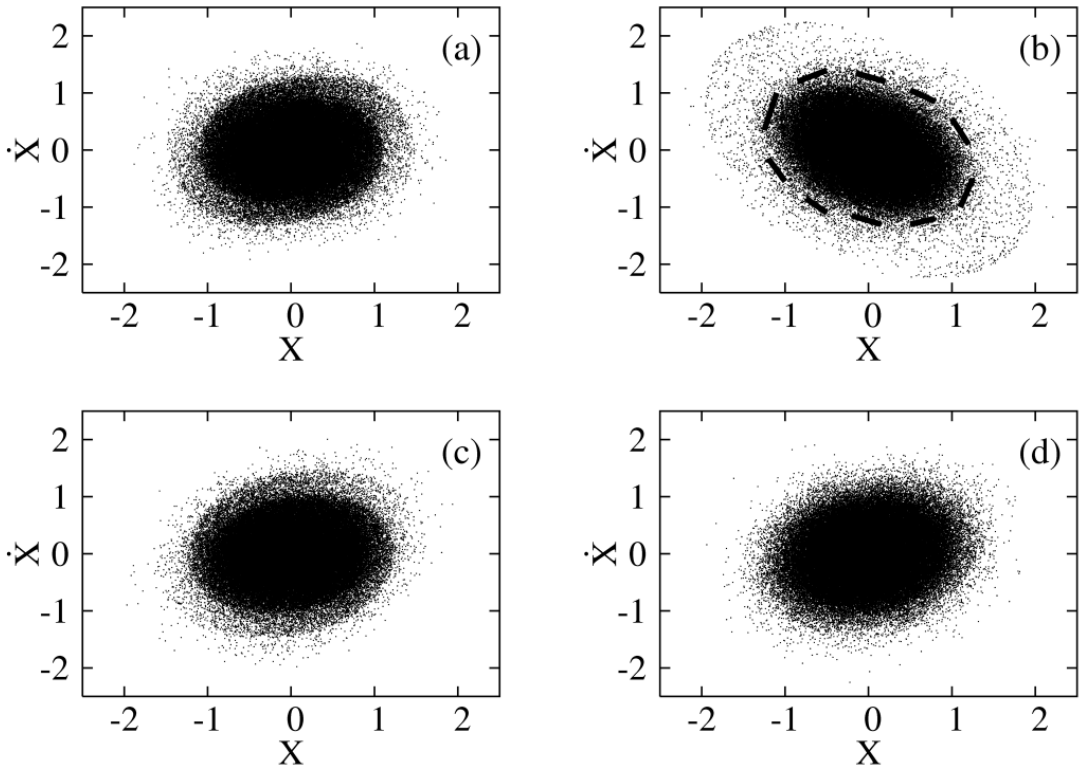

Figure 3.9: Plots of the instantaneous $(X,\dot{X})$ phase space for a beam with moderate space-charge intensity, $s_b = 0.7$: (a) Initial state at $t/\tau_L = 100$; (b) Final state at $t/\tau_L = 357.3$ for non-adiabatic compression with $\tau_{1/2}/\tau_L = 5$; (c) Final phase of the transition stage at $t/\tau_L = 110$ for non-adiabatic compression with $\tau_{1/2}/\tau_L = 5$; (d) Final state at $t/\tau_L = 309.95$ for adiabatic compression with $\tau_{1/2}/\tau_L = 10$ [Dorf *et al.*, 2006].

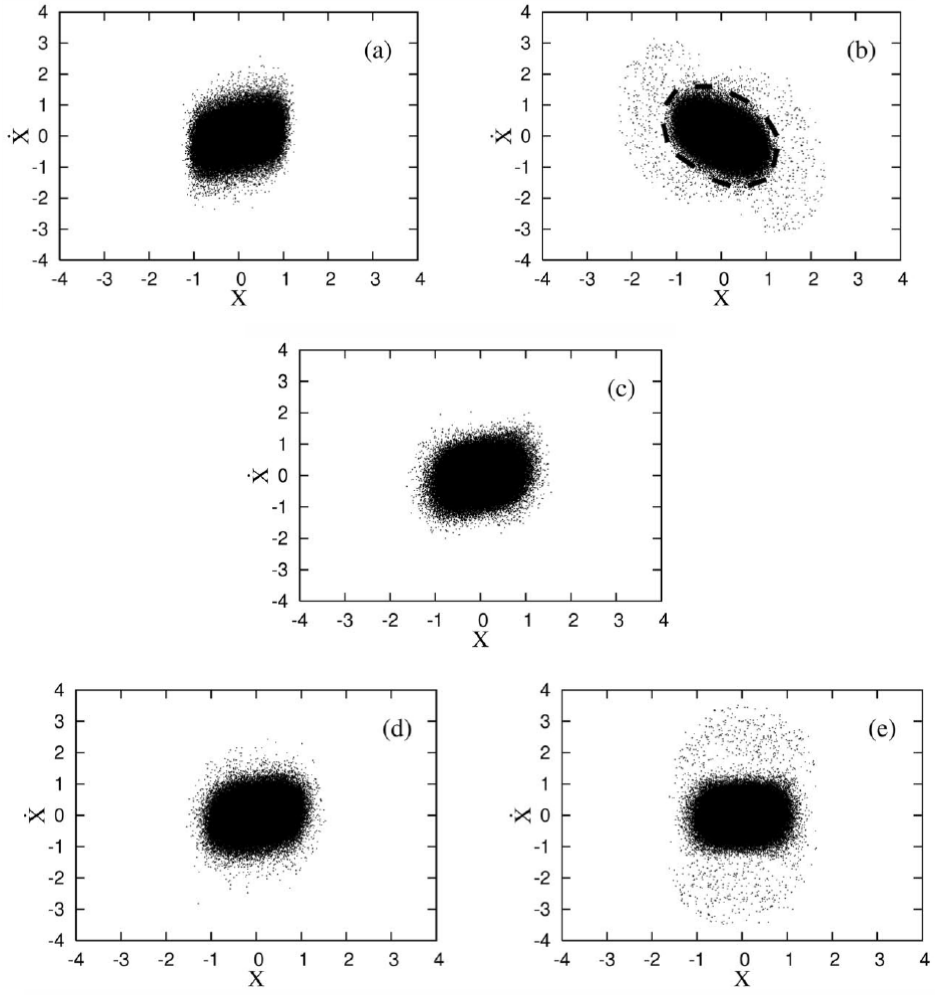

Figure 3.10: Plots of the instantaneous $(X, \dot{X})$ phase space for a space-charge-dominated beam, $s_b = 0.9999$: (a) Initial state at $t/\tau_L = 100$; (b) Final state at $t/\tau_L = 175.25$ (corresponds to the maximum beam radius) for non-adiabatic compression with $\tau_{1/2}/\tau_L = 10$; (c) Final phase of the transition stage at $t/\tau_L = 120$ for non-adiabatic compression with $\tau_{1/2}/\tau_L = 10$; (d) Final state at $t/\tau_L = 199$ for adiabatic compression with $\tau_{1/2}/\tau_L = 20$; (e) Final state at $t/\tau_L = 178.05$ (corresponds to the minimum beam radius) for non-adiabatic compression with $\tau_{1/2}/\tau_L = 10$ [Dorf *et al.*, 2006].

is due to the following factors. First, the azimuthal symmetry of an applied focusing force for the case shown in Fig. 2.4 provides conservation of a beam particle angular canonical momentum, in contrast to the case of the quadrupole lattice considered here. Second, is the proper choice of the projection plane, namely the $r-r'$ projection, since the equations governing the evolution of the r and θ particle coordinates are decoupled due to the conservation of a particle canonical momentum. Finally, note that the appearance of just one fixed point for the 2:1 parametric resonance structure in Fig. 2.4 (*O*-point in Fig. 2.4), in contrast to the two resonance points in Fig. 3.10(b), is simply due to the positive definition of the radial coordinate r [that is, for y=0, $r(-x)=r(x)$].

Of particular interest is the evolution of the beam halo. The halo evolution after one-half of the period of the mismatch oscillations period is illustrated in Fig. 3.10(e). The time instants for the phase-space plots are indicated by arrows in Fig. 3.8(b) for the rms envelope dimensions in the final state. Note that the 2:1 resonance points are located on the X axis when the core radius is a minimum, and on the $\dot{X}$ axis when the core radius is a maximum. This coincides well with the results obtained by Ikegami in [Ikegami, 1999], where the Poincare section for the particle-core model with the strobe time, taken at the minimum (maximum) of the beam size, gave the same location of the resonance islands. In the same work [Ikegami, 1999], the maximum halo extent (the width of the separatrix of the 2:1 resonance island) was found to be about twice as large as the maximal core radius, when the halo was driven by the symmetric mode. Fig. 3.10(d) illustrates approximately the same halo width.

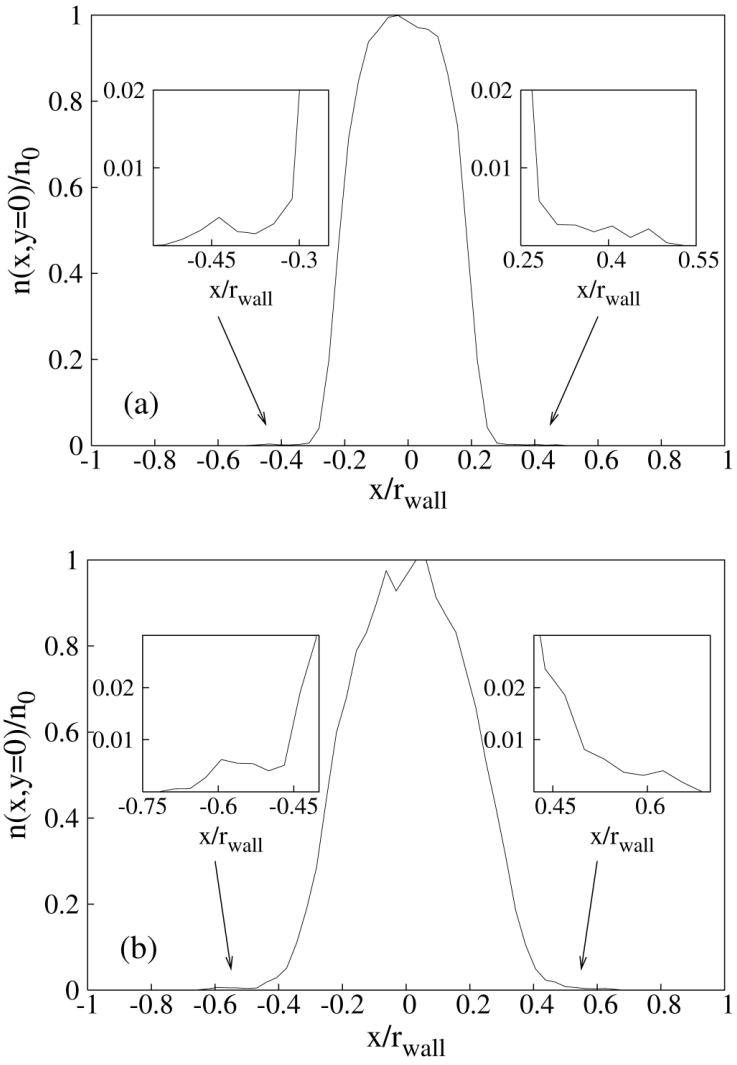

Figure 3.11: WARP simulation for an alternating-gradient quadrupole lattice. Normalized beam density profile $n(x,y=0)/n_0$ in the final state for non-adiabatic compression. The two cases correspond to (a) $s_b = 0.9999$, $\tau/\tau_L = 175.25$, and (b) $s_b = 0.7$, $\tau/\tau_L = 375.3$. The small graphical inserts correspond to the density profile at the core edge [Dorf *et al.*, 2006].

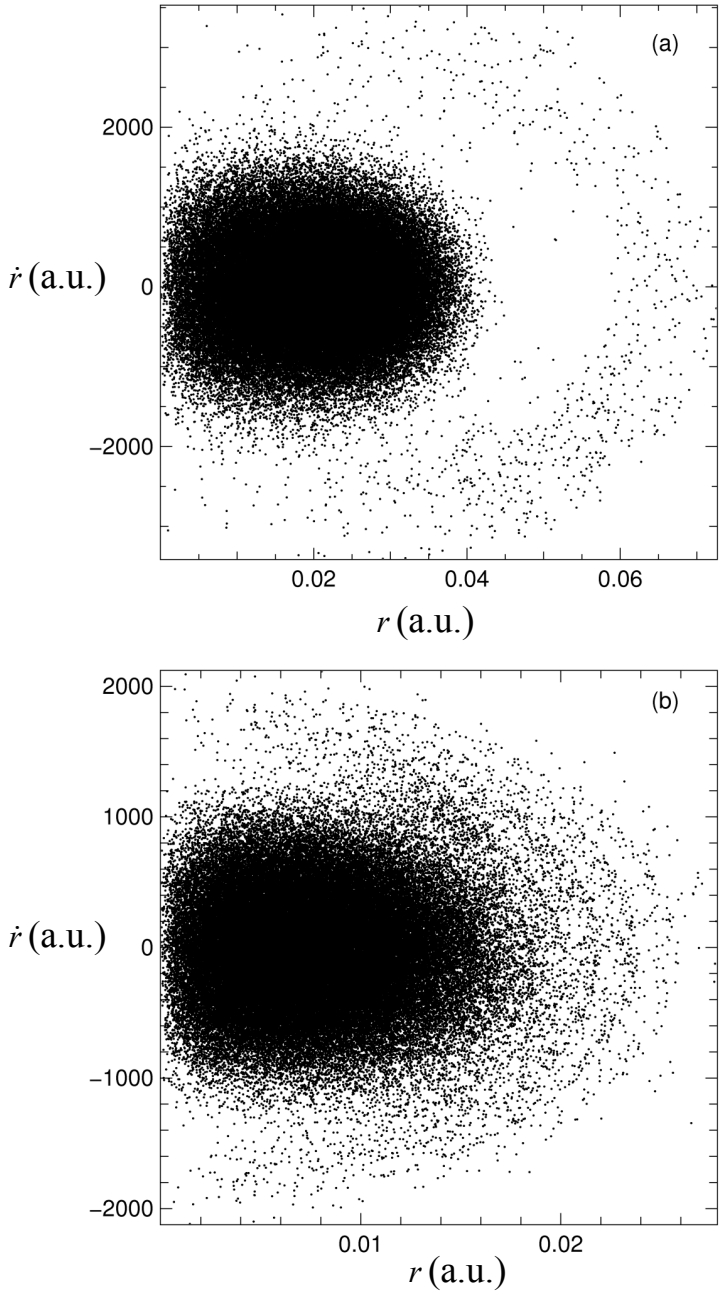

Figure 3.12: WARP simulation results using a smooth-focusing model. Plots of the radial $(r,\dot{r})$ phase space at the final state of the non-adiabatic compression process for (a) $s_b = 0.9999$, $t/\tau_L = 437.5$, and (b) $s_b = 0.7$, $t/\tau_L = 725.5$ [Dorf *et al.*, 2006].

The analogous studies were also performed for a beam with moderate space-charge strength, $s_b = 0.7$, and the results are illustrated in Fig. 3.9. The strong nonuniformities in the density profile [compare Figs. 3.11(a) and 3.11(b)] lead to a complete mixing of the mismatch oscillations, and therefore particles do not experience resonance interaction in the final state [Fig. 3.9(b)].

To assure that the simulation parameters do demonstrate halo formation, and that the above analysis is not a collateral effect due to the core tails, we use a smooth-focusing model with the same parameters and plot the radial $r - \dot{r}$ phase-space, (see Fig. 3.12). Note that in the smooth-focusing approximation there is no core flutter and we don't use the scaled coordinates. Figure 3.12(a) for a space-charge dominated beam with $s_b = 0.9999$ clearly illustrates the resonance structure, and the resonance structure is not observed in Fig. 3.12(b) for moderate space-charge intensity with $s_b = 0.7$. In Sec. 3.2.2 it was indicated that the relaxation of a large mismatch for a space-charge-dominated beam corresponds qualitatively to the nonlinear stage of Landau-like damping. Indeed, the halo particles illustrated in Fig. 3.12(a) are the trapped particles in the nonlinear interaction between the collective mismatch oscillations and the single particle motion.

We emphasize here some interesting features of the halo formation. The simulations show that during the transition stage only a small number of particles leave the core [compare Figs. 3.9 (a) and (c) and Figs. 3.10 (a) and (c)], whereas most particles populate the halo region during the relaxation stage [compare Figs. 3.9 (a) and (b) and Figs. 3.10 (a) and (b)]. Furthermore, it is found that the halo formation process saturates

along with the Landau-like damping of the mismatch mode. These details are evidence that the main mechanism for halo formation is indeed an energy transfer from the collective modes to the resonant particles (halo particles). When the transition stage is much shorter than the characteristic damping time, there is negligible collective energy transfer to the particles, and the particles stay trapped inside the beam core.

Of considerable practical interest are the halo particle contributions to the low-order moments of the beam distribution function. To investigate these phenomena qualitatively, we have also arbitrarily removed the halo particles from the simulation. No rigorous mathematical criteria were applied for the removal procedure. We simply removed particles from the $X-\dot{X}$ and $Y-\dot{Y}$ projections of the 4D phase-space using "visual criteria" to obtain approximate quantitative information about interesting phenomena. The contours which were used to divide the $X-\dot{X}$ phase space into the core and halo regions are illustrated in Figs. 3.9(b) and 3.10(b), and analogous contours were applied to the $Y-\dot{Y}$ phase space projection. The ratios of the values of rms envelope dimensions calculated with and without halo particles are $\tilde{a}^{with\ \ halo}\big/\tilde{a}^{without\ \ halo}=0.95$ for $s_b=0.9999$, and $\tilde{a}^{with\ \ halo}\big/\tilde{a}^{without\ \ halo}=0.91$ for $s_b=0.7$. For the transverse emittance we obtained $\varepsilon_x^{\ with\ \ halo}\big/\varepsilon_x^{\ without\ \ halo}=0.9$ for $s_b=0.9999$, and $\varepsilon_x^{\ with\ \ halo}\big/\varepsilon_x^{\ without\ \ halo}=0.85$ for $s_b=0.7$. It should be emphasized here that, after halo removal, the emittance drops somewhat below its initial value. Consequently, for the parameters used here, the core size variations in phase space during the relaxation stage

are smaller than the increase in the beam phase space area and related emittance growth attributed to the halo formation. The halo fraction of all simulation particles is about 2% for a space-charge-dominated beam with $s_b = 0.9999$, and about 4% for a moderate intensity beam with $s_b = 0.7$. This difference can be explained by recalling (Sec. 3.2.2) that more energy transfers from the collective oscillations to the transverse particle motion for $s_b = 0.7$ than for $s_b = 0.9999$. Another interesting feature is that a negligible number of new halo particles (less than 0.05% of all simulation particles) are observed for both values of s_b if we continue the simulations after the halo particle removal procedure (in these simulations, to conserve the line-charge, we placed the removed halo particles on the beam axis). This indicates that, despite charge density non-uniformities at the beam edge and mismatch oscillations, the phase space of the beam core is surrounded by a KAM surface, providing the core particles stay inside the core region and do not penetrate the halo region.

The results for adiabatic compression for different values of the space-charge intensity parameter are illustrated in Figs. 3.7(a) and 3.8(a) (rms envelope dimensions behavior) and Figs. 3.9(d) and 3.10(d) ($X - \dot{X}$ phase space). These figures show that a certain level of the final beam mismatch still persists. However, it should be noted that the final population of halo particles is similar to the initial one, which is produced by initial beam mismatch. Hence, a further increase in the transition time does not lead to an improved quality of the final beam state.

3.5 Spectral Method for Quantitative Analysis of Halo Production by a Beam Mismatch

In the previous section an extensive qualitative description of halo production by a beam mismatch has been presented. In this section, more emphasis is placed on providing quantitative treatment of the halo formation phenomena. Although, the presence of a beam halo is typically evident by visual inspection of a beam distribution [Sec. 3.4], it is of particular interest to obtain a more quantitative measure of this phenomena [Wangler and Crandall, 2000; Allen and Wangler, 2002; Dorf *et al*., 2007]. In [Wangler and Crandall, 2000], the *beam profile parameter* constructed from the second and forth spatial moments of the beam distribution,

$$h = \frac{\langle x^4 \rangle}{\langle x^2 \rangle^2} - 2 ,$$

has been proposed as a characterization of the halo in a 1D spatial projection. This formalism for calculating dimensionless halo parameters, based upon moments of the beam distribution function, has been then extended to quantify halo formation in 2D phase-space [Allen and Wangler, 2002]. The phase-space *halo parameter* [Allen and Wangler, 2002],

$$H = \frac{\sqrt{3\langle x^4 \rangle \langle x'^4 \rangle + 9\langle x^2 x'^2 \rangle^2 - 12\langle xx'^3 \rangle \langle x'x^3 \rangle}}{2\langle x^2 \rangle \langle x'^2 \rangle - 2\langle xx' \rangle^2} - 2 ,$$

generalized the spatial-profile parameter, h, using kinematic invariants of the particle distribution in phase space. These halo parameters can be efficiently used for comparing the 'halo intensity' for different beam distributions. For instance, it follows that $h=H=0$ for the Kapchinskij-Vladimirskij distribution, and $h=H=1$ for a Gaussian distribution.

Although the evolution of the halo parameters (h, H) can provide insights into the halo production process, no guidelines have been provided on how to quantitatively distinguish halo particles from core particles. Therefore, the actual 'halo fraction' of all beam particles for a given distribution cannot be estimated. Attempts to distinguish halo particles from the beam core particles were made in [Okamoto and Ikegami, 1997; Dorf *et al*., 2006]. However, those studies were based on a "visual analysis" (see Sec. 3.4) of the transverse phase-spaces, and no rigorous mathematical criteria were applied.

A simple quantitative definition a halo particle based on an analysis of the beam betatron frequency distribution has been proposed in [Dorf *et al*., 2007]. It has been demonstrated that the betatron frequency distribution function of a mismatched space-charge-dominated beam has a bump-on-tail structure attributed to the beam halo particles. In Sec. 3.5.1 we present the detailed analysis of the halo definition for a broad range of beam intensity, making use of the smooth-focusing approximation, and also taking into account the effects of an alternating-gradient quadrupole field. This formalism is then applied to quantitative studies of the halo production during the transverse beam compression in Sec. 3.5.2. Finally, in Sec. 3.5.3 it is shown that the spectral analysis can also provide important insights into other critical problems in intense beam transport, e.g., the mismatch relaxation process, and space-charge transport limits (see Sec. 2.2.5).

3.5.1 Spectral Method for Halo Particle Definition

This section develops a framework for the quantitative analysis of halo production by a beam mismatch. In Sec. 2.2.4, in order to describe the production of halo particles by a beam mismatch it was convenient to consider a beam propagating through a periodic focusing lattice as an ensemble of betatron oscillators coupled to the collective mismatch oscillations. This approach has also been used in [Clauser *et al*., 1999; Variale, 2001] for the analysis of beam mismatch relaxation. It has been noted that for the case of a space-charge dominated beam most of the betatron oscillators in the initial beam equilibrium distribution are far from the parametric (2:1) resonance with the collective mismatch mode (Fig. 3.13). Therefore, only a slight damping of the collective oscillations occurs. However, as the beam space-charge intensity decreases, the mismatch frequency approaches the frequency distribution of the betatron oscillators, providing an increased mixing of the collective oscillations (Fig. 3.13). It is also instructive to note that as the beam intensity increases the beam frequency spectrum shifts toward lower frequency values relative to the smooth-frequency, ω_q. This is consistent with the fact that the beam self-fields depress the total-focusing force acting on a beam particle, and therefore increase the period of particle transverse oscillations. Also, note that the frequency spectrum width is attributed to the nonlinear effects of the beam self-fields. Therefore, for the case of the smooth-focusing thermal equilibrium distributions shown in Fig. 3.13, the spectrum width has a maximum for a moderate beam intensity. Indeed, as the beam intensity increases the beam density profile approaches a flat-top distribution, and hence

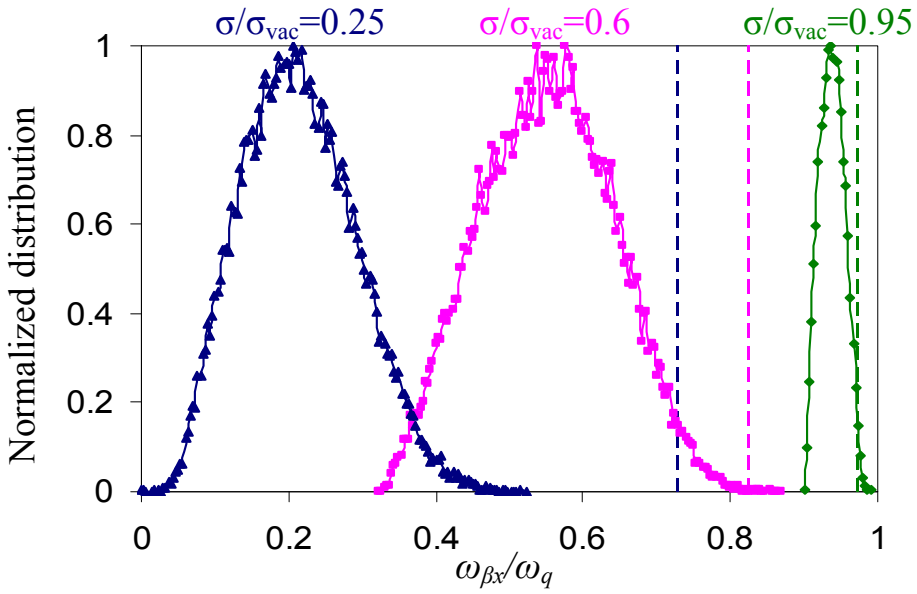

Figure 3.13: (Color) Plots of the normalized beam betatron frequency distribution for the smooth-focusing thermal equilibrium distribution obtained for different values of the beam intensity corresponding to $\sigma/\sigma_{vac} = 0.25$, $s_b = 0.9999$ (blue), $\sigma/\sigma_{vac} = 0.6$, $s_b = 0.9$ (pink), $\sigma/\sigma_{vac} = 0.95$, $s_b = 0.2$ (green). Each frequency distribution is normalized to its maximum value. The vertical dashed lines show the corresponding half-values of the mismatch oscillations frequency obtained within the smooth-focusing approximation, $\omega_s^{sf}/2$. Results are obtained using the WARP code for a smooth-focusing field.

the self-electric fields become nearly linear. On the other hand, as the beam density decreases the effects of the beam self-fields become less pronounced. Without loss of generality, here and throughout the remainder of Sec. 3.5, for illustrative purposes we show the betatron frequency distributions corresponding to the particle oscillatory motion in the *x*-direction (Fig. 3.13). Also, each plotted betatron frequency distribution is normalized to its maximum value.

In previous studies [Clauser *et al*., 1999; Variale, 2001] the spectral analysis was applied to the initial beam quasi-equilibrium. In this section, we extend the betatron spectral analysis to the case of a mismatched beam distribution [Dorf *et al*., 2007]. This allows us to develop a convenient framework for the quantitative analysis of halo production by a beam mismatch. Note that the energy-dependent betatron frequency increases with an increase in a particle energy. Therefore, the high-energy tail of an initial beam equilibrium distribution corresponds to the high-frequency tail in the betatron frequency distribution (Fig. 3.13). Inspecting the betatron frequency distribution of the initial beam thermal equilibrium distribution for the case of a space-charge-dominated beam, it is evident that only an exponentially small fraction of the beam particles has the energy corresponding to the parametrically resonant frequency, $\omega_s^{sf}/2$. However, during the relaxation of a large beam mismatch there is an energy transfer from the collective mismatch modes to the resonant particles, which gain energy and populate the halo region (Sec. 2.2.4 and Sec. 3.4). It is therefore intuitively appealing to expect that a "bump-on-tail" structure attributed to the high-energy halo particle will appear near the half-value of the mismatch oscillations frequency in the betatron frequency distribution of a *mismatched* space-charge-dominated beam.

For simplicity, we start the analysis by making use of the smooth-focusing approximation (Sec. 2.2.2), in which the oscillating focusing force is replaced with a uniform focusing force. Figure 3.14(a) shows the beam betatron frequency distribution

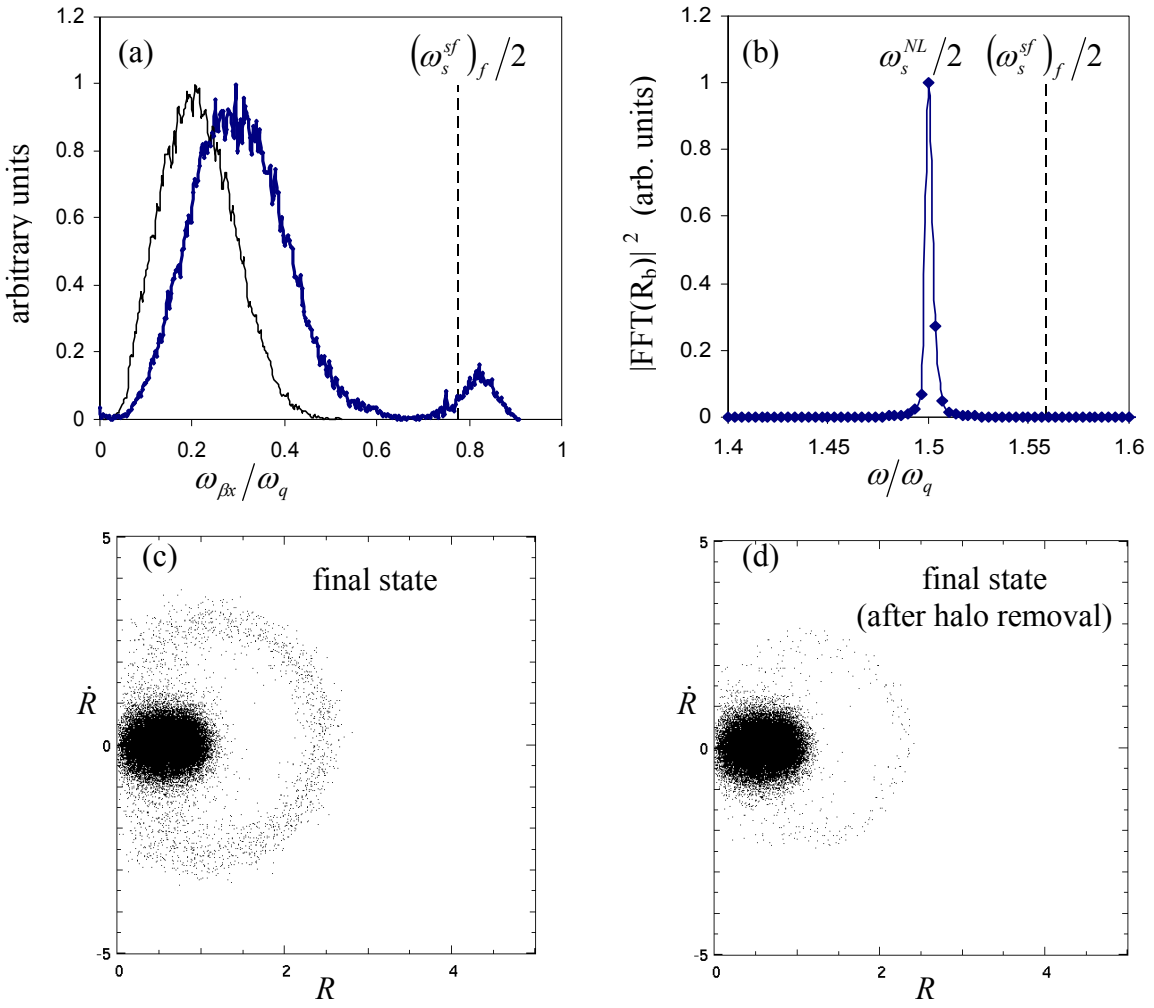

Figure 3.14: (Color) Relaxation of a beam mismatch for the case of a space-charge-dominated beam with $\sigma/\sigma_{vac}=0.25$, $s_b=0.9999$. Shown are plots of (a) beam betatron frequency distribution for the final 'quasi-relaxed' state (blue), and for the initial state corresponding to the smooth-focusing thermal equilibrium distribution (black), (b) FFT of $R_b(t)$, (c) and (d) the instantaneous $(\dot{R},R)$ phase space corresponding to the final beam state, and the same state after halo removal, respectively. The amplitude of the mismatch oscillations in the final state is $\delta R_b/R_b \cong 0.12$. Results are obtained using the WARP code for a smooth-focusing field.

for the case of a mismatched space-charge-dominated beam. For this illustrative example, a thermal equilibrium beam distribution with $\sigma/\sigma_{vac}=0.25$ ($s_b=0.9999$) was subjected to an instantaneous increase in the applied smooth-focusing force , $\omega_q^{inc}/\omega_q=1.3$. Then, after a time period, $\tau_{step}=\pi/2\left(\omega_s^{sf}\right)_i$, corresponding to one-quarter of the linear mismatch oscillation period calculated for the initial beam equilibrium, the applied force is returned back to its initial value. Here, $\left(\omega_s^{sf}\right)_i=\left(K_b/R_i^2+\varepsilon_i^2/R_i^4\right)^{1/2}$, and the subscript "*i*" denotes the initial beam state. Note that we assume an azimuthally symmetric initial beam distribution, and therefore only the symmetric (even) mode of mismatch oscillations is excited. After introducing the beam mismatch as described above, the beam is allowed to relax until the mismatch amplitude remains nearly constant. In the final ('quasi-relaxed') beam state, the *x* and *y* coordinates of each beam particle are tracked, and the FFT averages of the particle oscillograms are calculated [Fig. 3.15(c)]. It should be noted that the single-particle motion for the case of a mismatched intense beam is, in general, non-integrable, and the corresponding frequency spectra may have a complex structure [Fig. 3.15(c)]. Indeed, in addition to the fundamental (2:1) "halo" resonance, nonuniformities in the beam density profile along with the mismatch oscillations produce a higher-order resonance structure inside the beam core, and therefore even the core particle motion can become chaotic (Figs. 3.15). For the construction of the beam betatron frequency distribution [Fig. 3.14(a)], the particle's "betatron" frequency is assigned to the frequency corresponding to the maximum value in the Fourier power spectrum of the particle oscillogram. Shown in Fig. 3.15 the power frequency spectra and particle oscillograms

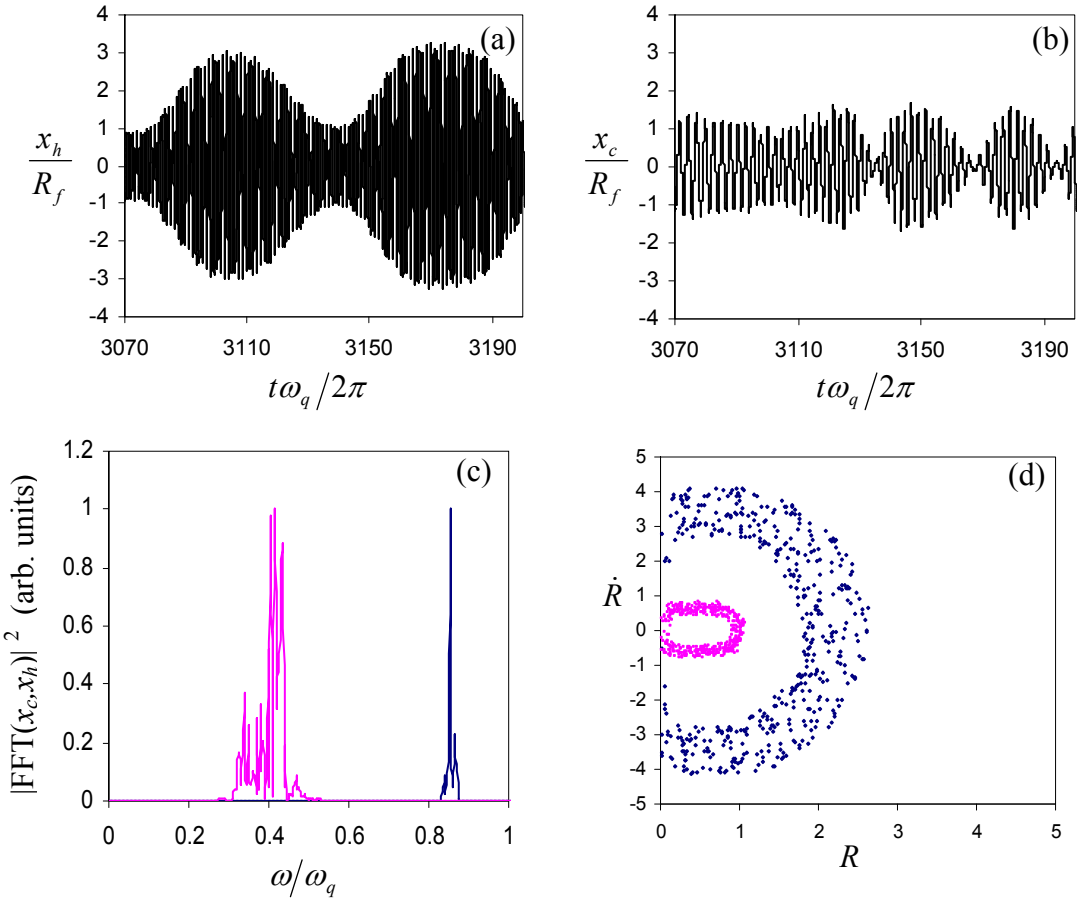

Figure 3.15: (Color) Dynamics of core and halo particles in the final state of a mismatched space-charge-dominated beam with $\sigma/\sigma_{vac}=0.25$ ($s_b=0.9999$): (a) and (b) Normalized x/R_f-oscillogram of the halo and core particles motion, respectively. Here, R_f corresponds to the RMS equilibrium radius calculated for the final beam state; (c) FFT of the core particle (pink) and the halo particle (blue) x-oscillograms; (d) Poincare section for the core (pink) and halo (blue) particles with the strobe time, taken at the minimum of the beam radius. Results are obtained using the WARP code for a smooth-focusing force. The parameters of the simulation are the same as in Fig. 3.14.

for typical core and halo particles elucidate the relevance of this approach for the purpose of distinguishing a halo particle from a core particle. The corresponding Poincare radial phase-space plots $\left(\dot{R}, R\right)$ for these halo and core particles are shown in Fig. 3.15(d). Here, $R \equiv \sqrt{X^2 + Y^2}$, $\dot{R} \equiv \left(\dot{X}X + \dot{Y}Y\right)/R$, X and $\dot{X}$ are the scaled coordinates defined in Sec. 3.4, and Y and $\dot{Y}$ are their analogs in the *y*-direction. Note that the "betatron" frequency values for the core and halo beam particles lie inside the "core" and "bump-on-tail" frequency ranges of the beam betatron frequency distribution, respectively [Fig. 3.14(a)].

Figure 3.14(a) shows that the betatron frequency distribution function of a mismatched space-charge-dominated beam has a clear bump-on-tail structure attributed to beam halo particles. Note that most of the bump is located to the right of the half-value of the mismatch oscillation frequency calculated for the final beam distribution, $\left(\omega_s^{sf}\right)_f = \left(K_b / R_f^2 + \varepsilon_f^2 / R_f^4\right)^{1/2}$. Here, ε_f corresponds to the average value of the transverse beam emittance in the final state, and R_f is the corresponding value of the equilibrium beam radius determined from Eq. (3.5) where $\varepsilon = \varepsilon_f$. This allows us to formulate the following simple quantitative definition of a halo particle. *If the particle betatron frequency is greater than one-half of the mismatch oscillation frequency then it designated as a halo particle*. Figures 3.14(c) shows the beam radial phase space at the final state, and Fig. 3.14(d) shows the same phase space after removing particles with betatron frequency in the *x* or *y* direction higher than $\left(\omega_s^{sf}\right)_f / 2$. The remaining small fraction of halo particles corresponds to the fraction of the bump-on-tail structure located

to the left of $\left(\omega_s^{sf}\right)_f/2$. In addition, a few more halo particles appear during the FFT averaging calculations, because the energy transfer process is not yet fully completed. Note that the actual frequency spectrum of an envelope rms dimension [Fig. 3.15(b)] has a finite band width with the central frequency ω_s^{NL}, which is slightly smaller than its linear approximation, $\left(\omega_s^{sf}\right)_f$ due to nonlinear effects, and also due to the coupling to the dynamics of the higher–order moments, e.g., beam emittance. Therefore, more halo particles can be selected by the proposed criteria if an improved model for describing the mismatch oscillations frequency spectrum is employed to determine the "cut-off" frequency.

It should be noted that according to the proposed halo definition, even a matched beam with a thermal equilibrium distribution function has a certain fraction of halo particles. This fraction is exponentially small for a space-charge-dominated beam, but it increases with decreasing beam intensity since the mismatch frequency approaches the frequency distribution of the betatron oscillators. Nevertheless, the spectral framework for a quantitative analysis of halo production developed above for a space-charge-dominated beam can also be efficiently utilized for the case of a low-intensity beam. The evolution of the beam betatron frequency distribution function due to beam mismatch relaxation for the case of a low-intensity beam with $\sigma/\sigma_{vac}=0.95$ ($s_b=0.2$) is shown in Fig. 3.16. For this illustrative example, the beam mismatch is introduced in the same way as described above for the case of a space-charge dominated beam, i.e., by increasing the

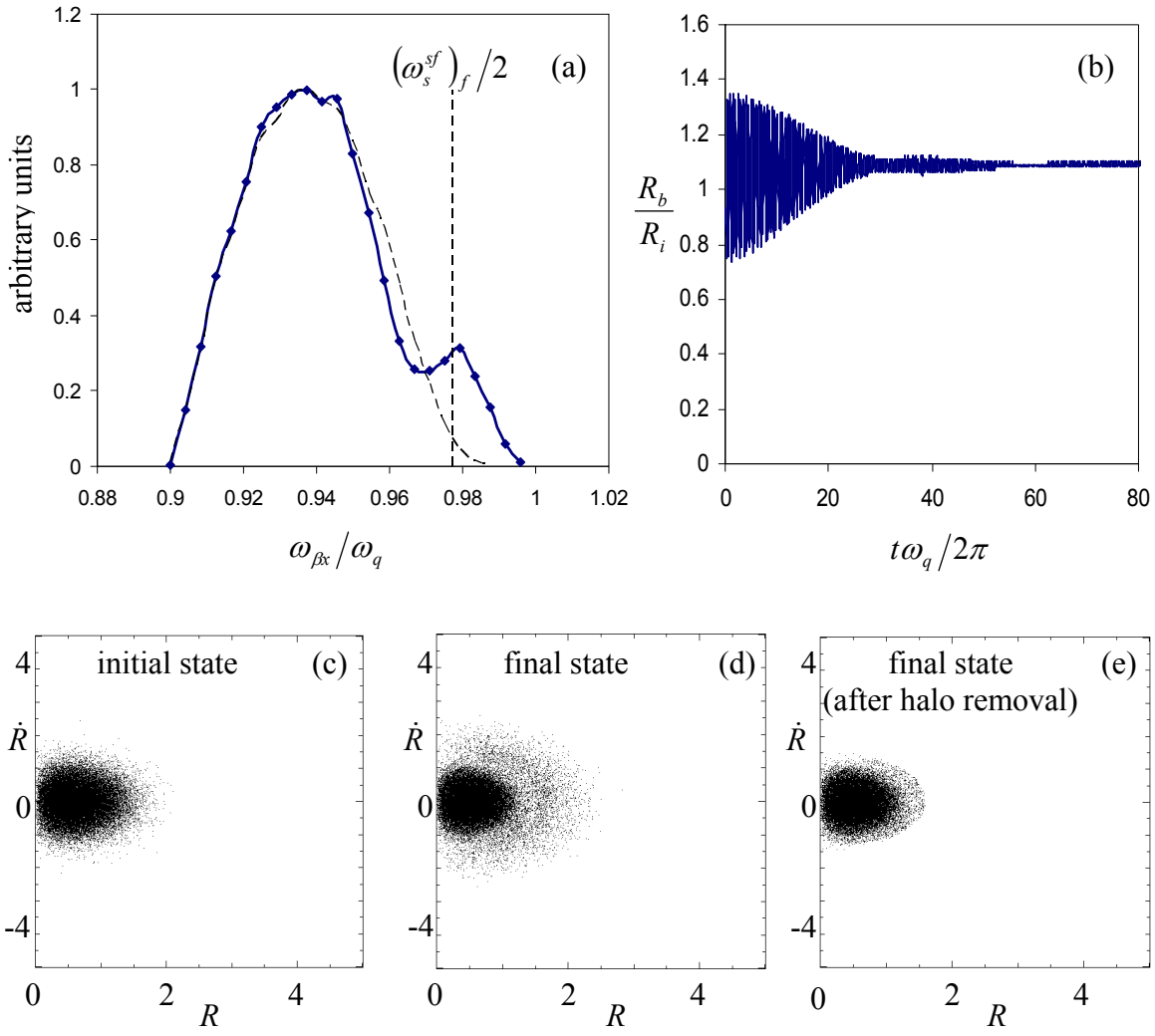

Figure 3.16: (Color) Relaxation of a beam mismatch for the case of an emittance-dominated beam with $\sigma/\sigma_{vac}=0.95$ ($s_b=0.2$). Shown are plots of (a) beam betatron frequency distribution for the final 'quasi-relaxed' state (blue), and for the initial state corresponding to the smooth-focusing thermal equilibrium distribution (black), and (b) the evolution of the normalized RMS beam radius R_b/R_i. Frames (c), (d), and (e) show the normalized $(\dot{R},R)$ phase-space corresponding to the initial state, final state, and final state after halo removal, respectively. Results are obtained using the WARP code for a smooth-focusing field.

focusing strength of the lattice to $\omega_q^{inc}/\omega_q = 1.3$ for a time period of $\tau_{step} = \pi/2\left(\omega_s^{sf}\right)_i$. Comparing the betatron frequency distributions for the initial and final states [Fig. 3.16(a)], it is natural to assign a pronounced difference in the tail region where $\omega_{\beta x} > \left(\omega_s^{sf}\right)_f/2$ to the generated beam halo. Note that for the case of an emittance-dominated beam the mismatch oscillations are completely relaxed [Fig. 3.16(b)], and therefore particles do not experience a resonance interaction in the final state [compare Fig. 3.16(d) and Fig. 3.14(c)].

The quantitative analysis of halo production by a beam mismatch developed above for a constant focusing field (smooth-focusing approximation) can be generalized in a straightforward manner to the case of an oscillating quadrupole focusing field. Figure 3.17(a) shows the evolution of the beam betratron frequency distribution function due to beam mismatch relaxation for the case of a space-charge-dominated beam with $\sigma/\sigma_{vac} = 0.25$ and $\sigma_{vac} = 55^0$. To save computational time, the initial beam distribution was loaded into a quadrupole lattice making use of the "instantaneous loading" scheme (Sec. 2.3.2), which provides an initial beam matching sufficient for present purposes. For this simulation a sinusoidal lattice wave form is assumed, $\kappa_q(t) = 2^{3/2}\pi\omega_q\tau_L^{-1}\sin\left(2\pi t/\tau_L\right)$, and a beam mismatch is introduced by an instantaneous increase in the lattice amplitude to $\omega_q^{inc}/\omega_q = 1.15$ at the zero phase of the sine function. The lattice amplitude is maintained fixed at ω_q^{inc} for one-half of the lattice period, and then instantaneously decreased to its initial value, ω_q.

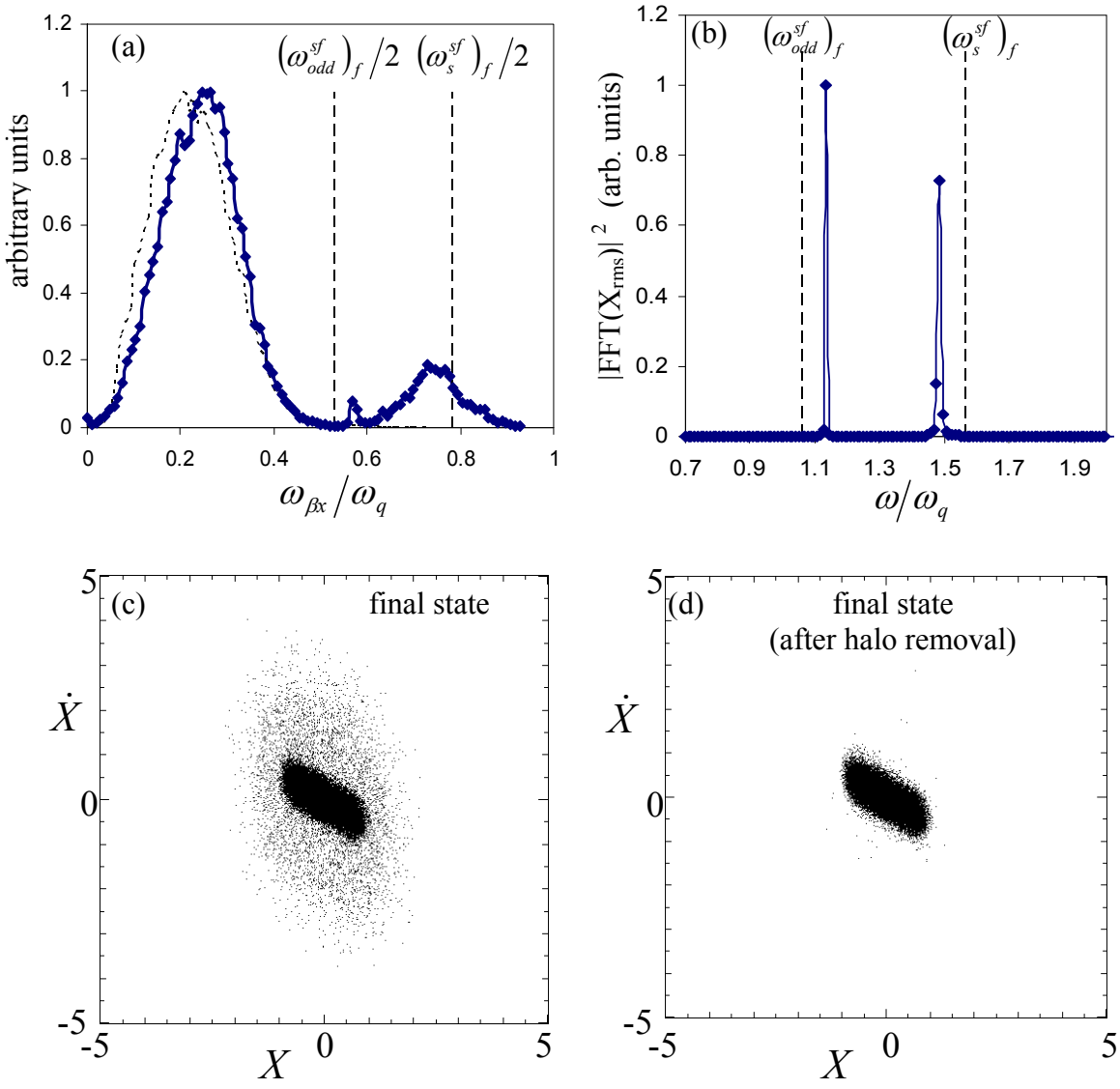

Figure 3.17: (Color) Relaxation of a beam mismatch for the case of a space-charge-dominated beam with $\sigma/\sigma_{vac}=0.25$ ($s_b=0.9999$), $\sigma_v=55^0$. Shown are plots of (a) beam betatron frequency distribution at the final 'quasi-relaxed' state (blue), and the initial state (black); (b) FFT of $X_{\mathrm{rms}}(t)$; and (c) and (d) the instantaneous $(\dot{X},X)$ phase space corresponding to the final state, and the final state after halo removal, respectively. Results are obtained using the WARP code for an alternating-gradient quadrupole field.

Note that the non-monotonic tail structure in Fig. 3.17(a) is now represented by the two bumps corresponding to half-values of the symmetric (even), ω_s, and the quadrupole (odd), ω_{odd}, mismatched envelope mode frequencies (Sec. 2.2.4). This is due to the fact that both modes are exited by the abrupt mismatch, and they both produce high-energy resonant halo particles. The quantitative criteria for a beam halo particle should therefore be generalized for the case of a quadrupole oscillating lattice in the following way: *if the particle betatron frequency is greater than the quadrupole (odd) envelope frequency half-value then it is a halo particle*. To further investigate this criteria we compare the normalized $(X, \dot{X})$ beam phase space shown in Fig. 3.17(c) with the same phase-space after removing particles with betatron frequency satisfying $\omega_\beta > \left(\omega_{odd}^{sf}\right)_f / 2$ [Fig. 3.17(d)], where $\left(\omega_{odd}^{sf}\right)_f = \left(\omega_q^2 + 3\varepsilon_f^2 / 4R_f^4\right)^{1/2}$ is the corresponding smooth-focusing value of the quadrupole (odd) mismatched envelope mode frequency in the final beam state. The actual spectrum of the beam rms envelope x-dimension obtained in the PIC simulations, taking into account the oscillating nature of the applied lattice and nonlinear effects, is shown in Fig. 3.17(b). Again, as noted earlier for the case of a constant focusing force (smooth-focusing approximation), a few more halo particles can be selected if an improved model accounting for the width and shape of the mismatch oscillations frequency spectrum is employed for determination of the "cut-off" frequency.

Finally, we present the evolution of the beam betatron frequency distribution due to mismatch relaxation for the case of a low-intensity beam, taking into account the effects of the oscillating applied lattice force (Fig. 3.18). For this illustrative example we

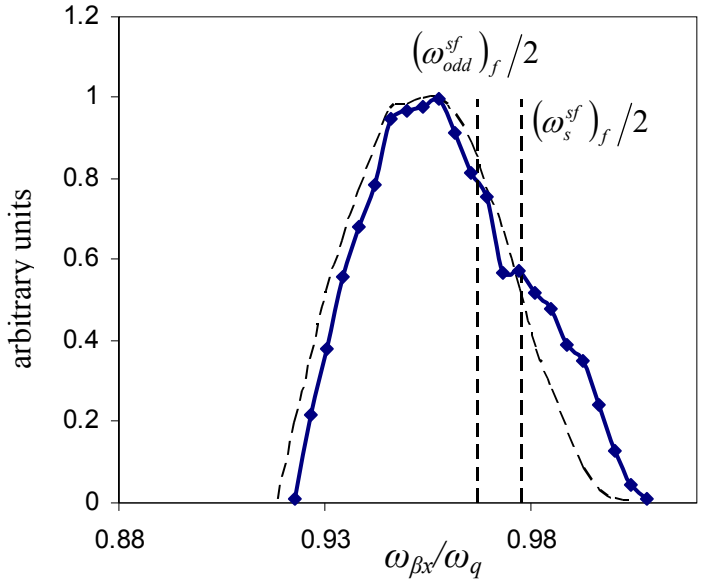

Figure 3.18: (Color) Evolution of the beam betatron frequency due to mismatch realxation for the case of an emittance-dominated beam with $\sigma/\sigma_{vac}=0.95$ ($s_b=0.2$), $\sigma_{vac}=40^0$. Shown are plots of the betatron frequency distribution at the final 'quasi-relaxed' state (blue), and at the initial state (black). Results are obtained using the WARP code for an alternating-gradient quadrupole field.

take $\sigma/\sigma_{vac}=0.95$, $\sigma_{vac}=40^0$, and the beam mismatch is introduced by an instantaneous increase in the lattice amplitude to $\omega_q^{inc}/\omega_q=1.2$ at the zero phase of the sine function. The lattice amplitude is maintained fixed at ω_q^{inc} for one lattice period, and then instantaneously decrease to its initial value ω_q. Inspecting the beam frequency distributions at the initial and final beam states, it again appears natural to assign a pronounced difference in the tail region for $\omega_{\beta x}>(\omega_{odd}^{sf})_f/2$ to the generated beam halo.

3.5.2 Quantitative studies of beam halo production during the compression process

In this section we apply the formalism for a quantitative definition of a beam halo particle (Sec. 3.5.1) to quantitative studies of halo production during the transverse compression of a charged particle beam propagating through an alternating-gradient quadrupole focusing lattice [Dorf *et al*., 2007]. As in previous sections of this chapter, here the lattice function is specified by $\kappa_q(t) = 2^{3/2}\pi\omega_q(t)\tau_L^{-1}\sin(2\pi t/\tau_L)$. The transition of the lattice strength, $\omega_q(t)$, is given by Eq. (3.6), and for the illustrative examples presented in this section we take $\tau_{1/2}/\tau_q = 4$ and $\omega_{qf}/\omega_{qi} = 2$. The initial beam distribution is loaded into a quadrupole lattice in the same way as described in Sec. 3.3, and the beam is allowed to relax during 50 periods of the focusing lattice before compressing the lattice amplitude. In this section we consider cases of a space-charge-dominated beam with $(\sigma/\sigma_{vac})_i = 0.25$, and a moderate intensity beam with $(\sigma/\sigma_{vac})_i = 0.43$. During the transition, the lattice strength measured by the vacuum phase advance is changing from $(\sigma_{vac})_i = 17.4^0$ to $(\sigma_{vac})_i = 35.3^0$. Here, the subscripts "*i*" and "*f*" correspond to the initial and final beam state, respectively.

The discrete evolution of the normalized rms envelope *x*-dimension calculated at each focusing period at the zero phase of the lattice sine function, X_0, are shown in Fig. 3.19 for the illustrative cases of adiabatic and non-adiabatic transitions [Dorf *et al*., 2007]. Note that such a graphical representation for a matched beam would be a

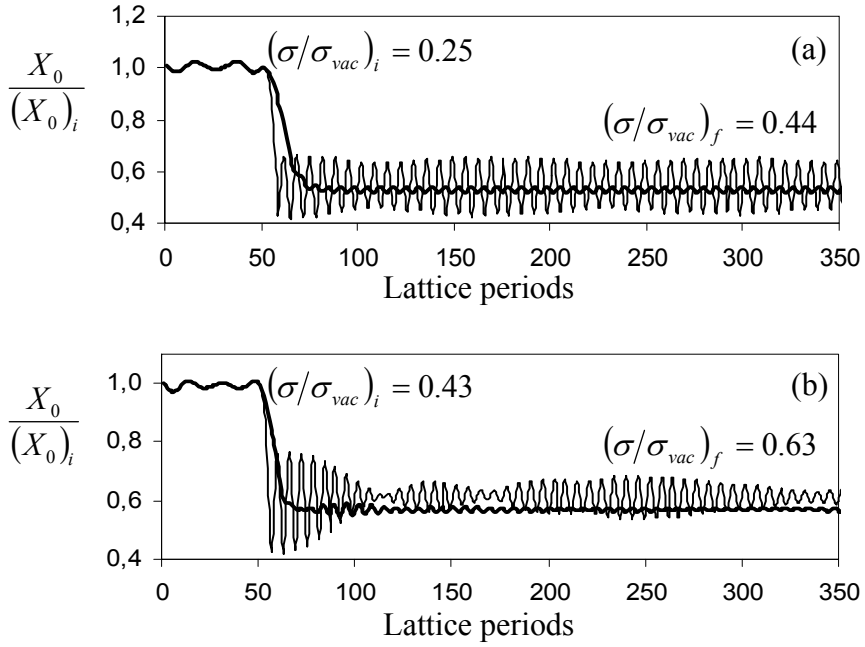

Figure 3.19: Rms envelope x-dimension plotted versus number of lattice periods. (a) Adiabatic compression with $\tau_{1/2}/\tau_L = 15$ (bold line) and nonadiabatic compression with $\tau_{1/2}/\tau_L = 6$ (fine line) for a space-charge-dominated beam. (b) Adiabatic compression with $\tau_{1/2}/\tau_L = 10$ (bold line) and nonadiabatic compression with $\tau_{1/2}/\tau_L = 4$ (fine line) for a beam with moderate intensity.

horizontal straight line; therefore Fig. 3.19 provides a convenient representation of beam mismatch (see Sec. 2.3.2). The detailed dependence of the beam emittance increase on the transition time, $2\tau_{1/2}$, is illustrated in Fig. 3.20 for different values of the beam intensity. Finally, we use the quantitative definition of a beam halo particle (Sec. 3.5.1), and calculate the corresponding number of halo particles produced by the beam mismatch, which is acquired during the compression process. Figure 3.21 shows the halo fraction of all the simulation particles at the final beam state as a function of the transition

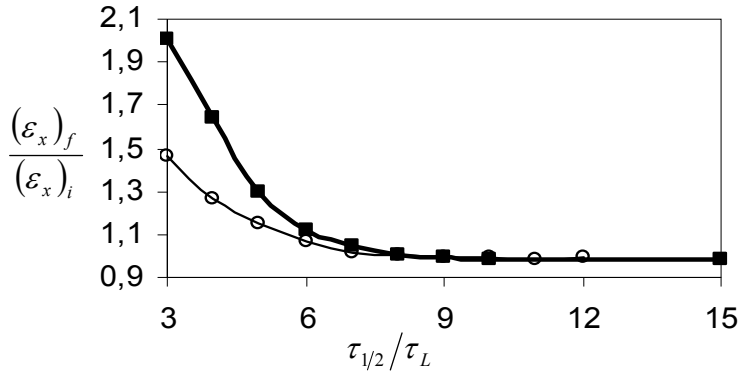

Figure 3.20: Ratio of the final to initial beam emittance *versus* characteristic transition time, $\tau_{1/2}$. Circles correspond to $(\sigma/\sigma_{vac})_i = 0.43$, and squares to $(\sigma/\sigma_{vac})_i = 0.25$ [Dorf *et al*., 2007].

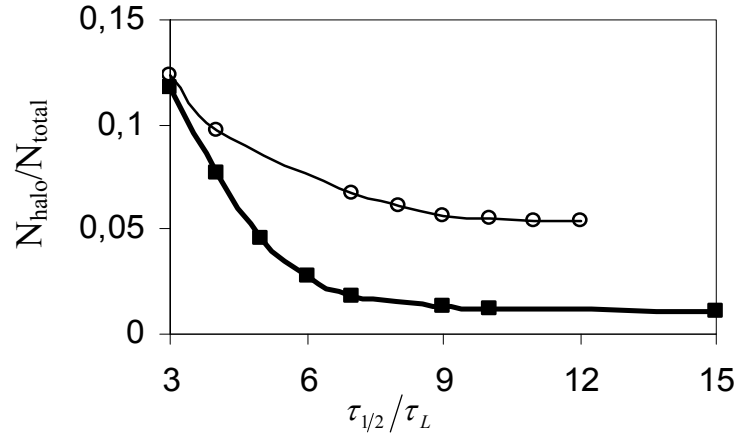

Figure 3.21: Halo fraction of all simulation particles *versus* characteristic transition time, $\tau_{1/2}$. Circles correspond to $(\sigma/\sigma_{vac})_i = 0.43$, and squares to $(\sigma/\sigma_{vac})_i = 0.25$ [Dorf *et al*., 2007].

time, $\tau_{1/2}$, for different values of the beam intensity. Note that the small, non-vanishing fraction of beam halo particles is present in the final state even for the case of an adiabatic compression. This is due to the fact that the quantitative halo definition selects a fraction of high-energy beam edge particles as halo particles. This fraction is exponentially small for a space-charge-dominated beam, but it increases with decreasing beam intensity since the mismatch frequency approaches the frequency distribution of the betatron oscillators (see. Sec. 3.5.1).

3.5.3 Spectral Analysis of Strong Mismatch Relaxation and Intense Beam Transport Limits

The spectral analysis of a mismatched beam distribution (Sec. 3.5.1) has been demonstrated to be a powerful tool for studies of nonlinear transverse dynamics of an intense beam propagating through a periods-focusing lattice. In particular, it can provide the opportunity to carry out a quantitative analysis of halo production by a beam mismatch (Secs. 3.5.1 and 3.5.2). In this section, we make use of this new formalism to study other critical problems in intense beam transport.

The spectral evolution of a beam core during the relaxation of a beam mismatch:

In the previous sections the analysis was focused on beam halo production by a beam mismatch. However, it is of particular interest to study the evolution of the beam core

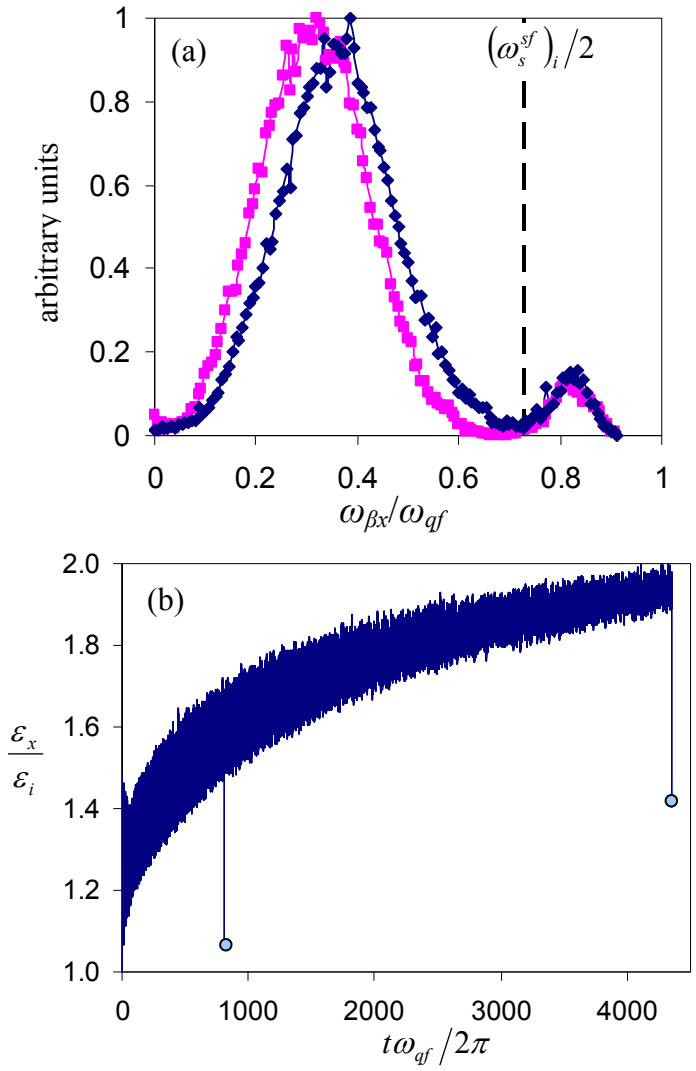

Figure 3.22 (Color): Strong mismatch relaxation for the case of a space-charge-dominated beam with $\sigma/\sigma_{vac} = 0.25$ ($s_b = 0.9999$). Shown are plots of (a) the beam betatron density distribution function calculated at $t_1 = 810.35 \times 2\pi/\omega_{qf}$ (red), and $t_2 = 4350.35 \times 2\pi/\omega_{qf}$ (blue); and (b) evolution of the beam transverse emittance. The dots illustrate the values of the beam transverse emittance at the time instants t_1 and t_2 when the halo particles are removed from the corresponding beam distributions. The beam mismatch is introduce by an instantaneous increase in the lattice strength to $\omega_{qf} = 1.4\omega_{qi}$. Results are obtained using the WARP code for a smooth-focusing force.

during the relaxation of a beam mismatch. Figure 3.22(a) shows the evolution of the beam betatron frequency distribution obtained within the smooth-focusing approximation for the case of a space-charge-dominated beam with $\left(\sigma/\sigma_{vac}\right)_i = 0.25$. For this simulation, the mismatch was introduced by an instantaneous compression of the lattice amplitude to the value $\omega_{qf}/\omega_{qi} = 1.4$. Shown in Fig. 3.22(a) are the frequency distributions calculated at the time instants corresponding to $t_1 = 810.35 \times 2\pi/\omega_{qf}$ and $t_2 = 4350.35 \times 2\pi/\omega_{qf}$. It is interesting to note that the "bump-on-tail" structure in Fig. 3.22(a) attributed to the beam halo remains nearly the same, whereas the difference is clear in the core region. This means that most of the beam halo is generated on a time-scale shorter than the time-scale of the beam core evolution. Finally, we note that the core relaxation process also leads to an increase in the beam emittance. Figure 3.22(b) illustrates the evolution of the beam transverse emittance during the mismatch relaxation process. It is readily seen that the beam emittance continues to grow during the time period between t_1 and t_2, when most of the halo is generated. To further elucidate this, we compare the values of the beam emittance calculated at t_1 and t_2 after removing halo particles from the corresponding beam distributions. The corresponding values of the beam emittance calculated for the beam distributions without halo particles, are shown by the dots in Fig. 3.22(b), and clearly demonstrate an increase in the beam emittance due to the beam core relaxation.

Spectral analysis of intense beam transport limits:

As noted earlier in Sec. 2.2.5, intense beam transport stability limits is one of the critical problems in intense beam transport. Of particular importance here are the higher-order resonance effects that limit stable intense beam propagation in the region of high vacuum phase advance, where $\sigma_{vac}^2 - \sigma^2 > (2\pi/3)^2/2$. In this section, we use the spectral analysis of the beam distribution to provide insights into that problem. The betatron frequency distributions for an intense beam with $\sigma/\sigma_{vac} = 0.3$ propagating through a quadrupole lattice are shown in Fig. 3.23(a) for different values of the lattice vacuum phase advance. For these simulations a semi-Gaussian beam distribution is loaded into a quadrupole lattice as described in Sec. 3.3, and the corresponding evolution of the beam transverse emittance is shown in Fig. 3.23(c). As evident from Figs. 3.23(a) and 3.23(b), as the vacuum phase advance increases and the system parameters approach the instability criteria, the core of the betatron frequency distribution remains the same. However, the distribution tail function increases in extent. This observation can support the analysis developed in [Lund and Chawla, 2006], which proposes that the emittance growth can be attributed to high-energy beam edge particles that diffuse outside of the beam core sufficiently to participate in the higher-order resonances, thereby increasing the statistical beam area in the transverse phase space, i.e., the beam transverse emittance.

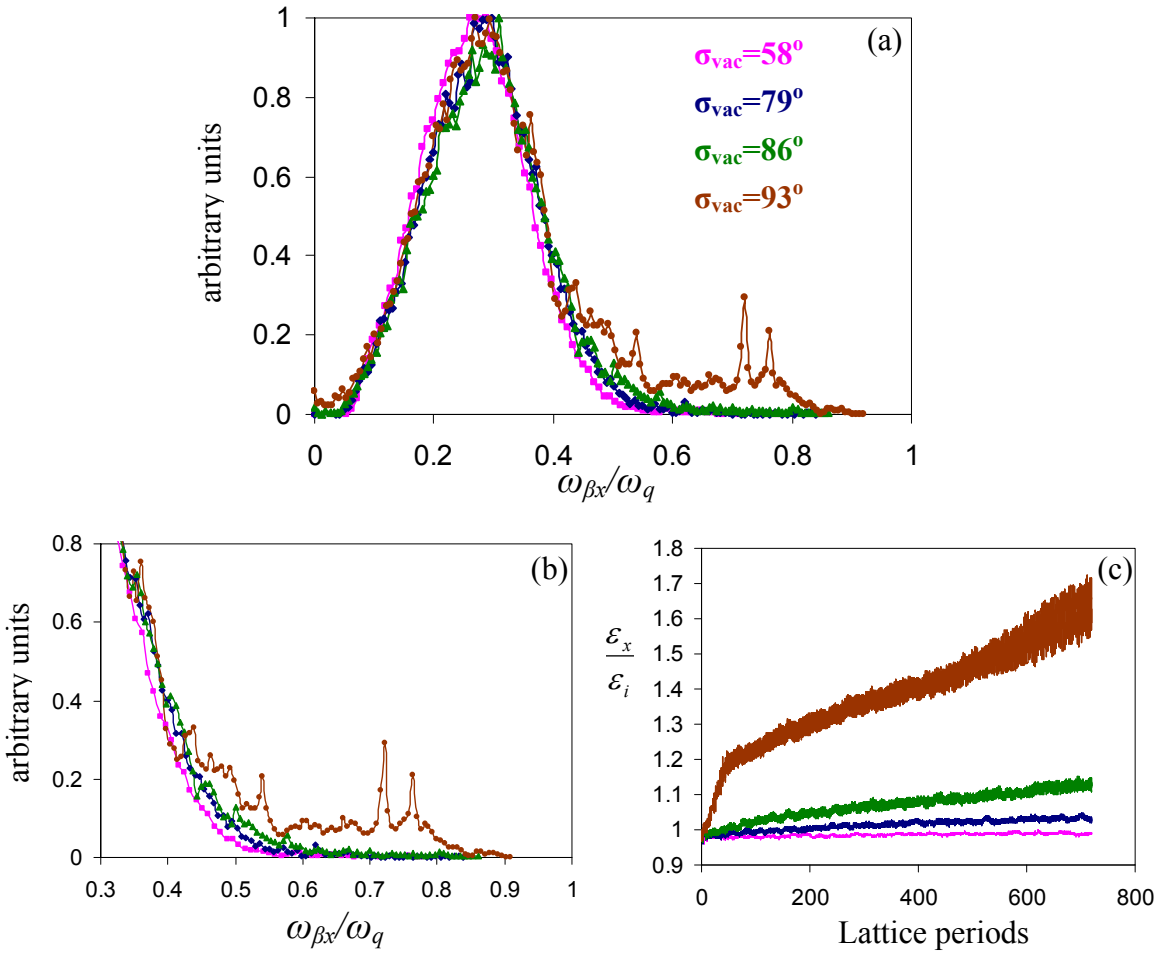

Figure 3.23 (Color): Dynamics of a space-charge-dominated beam with $\sigma/\sigma_{vac}=0.3$ in a quadrupole lattice for the case where the system parameters are near the transport stability limit $\sigma_{vac}^2-\sigma^2\cong(2\pi/3)^2/2$. Shown are plots of (a) the beam betatron distribution function for increasing values of the vacuum phase advance corresponding to $\sigma_{vac}=58^0$ (pink), $\sigma_{vac}=79^0$ (blue), $\sigma_{vac}=86^0$ (green), and $\sigma_{vac}=93^0$ (brown); (b) zoom-in on the tails of the distributions shown in Frame (a); and (c) evolution of the beam transverse emittance. Results are obtained using the WARP code for an alternating-gradient quadrupole field.

3.6 Summary and Discussion

In this chapter, envelope equations and full particle-in-cell numerical simulations using the WARP code have been used to investigate the evolution of the rms beam radius, the emittance growth, and halo formation during the transverse compression of an intense ion beam propagating through an alternating-gradient quadrupole lattice. It was shown that when the lattice transition is smooth (adiabatic) the emittance variation is negligibly small and therefore a constant-emittance approximation can be used as a closure condition for the envelope equations to model the compression process. For the case of a non-adiabatic transition, it was found that the characteristic time scale for the emittance growth is much larger than the transition time required for adiabatic compression. Therefore, even for non-adiabatic compression, the constant-emittance approximation can be used to estimate the beam mismatch produced in the transition region.

The details of halo formation were investigated self-consistently using the WARP code, both in the smooth-focusing approximation and for a quadrupole lattice. In the smooth-focusing approximation, a 2:1 resonance structure was observed for space-charge-dominated beams with almost uniform density profile. For a quadrupole lattice, the beam particle motion in the 4D transverse phase space provides some smearing of the 2:1 resonance structure in the 2D phase-space projection. Nonetheless the width and location of the resonance islands coincide well with the results, obtained in the particle-core model for a quadrupole focusing field [Ikegami, 1999]. It was also found that during halo formation the energy transfers from the collective mismatch oscillations to the

transverse motion of the resonant particles (halo particles). The energy transfer time is of order the phase-mixing (Landau-like damping) time. Therefore, only a few particles populate the halo region during beam propagation through the lattice transition region. Generation of most of the halo particles, and consequently growth of the transverse emittance, occurs during the subsequent beam transport.

In addition, a new spectral technique for the analysis of a mismatched intense beam propagating through an alternating-gradient lattice has been developed. It has been shown that the beataron frequency distribution of a mismatched intense beam has a "bump-on-tail" structure attributed to the beam halo particles. Based on this phenomenon, a quantitative definition of halo particles produced by a beam mismatch has been proposed, which provided an opportunity to carry out quantitative studies of the halo production during the transverse beam compression. It has also been found that the analysis, based upon the spectral method, can provide important physical insights into other critical problems in intense beam transport, such as strong mismatch relaxation and space-charge transport limits. In particular, it has been demonstrated that during strong mismatch relaxation, most of the beam halo is generated on a time-scale shorter than the time-scale for the beam core relaxation. Furthermore, it has been observed that the core relaxation process also leads to an increase in the beam emittance. Finally, the spectral analysis of a beam distribution loaded into a quadrupole lattice for the case where the system parameters lie near the transport stability limit, $\sigma_{vac}^2 - \sigma^2 \approx (2\pi/3)^2/2$, has been performed. It has been shown that as the system parameters approach the stability limit,

the core of the beam betatron distribution does not change significantly, whereas the tail of the distribution increases. This observation supports the analysis developed in [Lund and Chawla, 2006], which proposed that the emittance growth can be attributed to high-energy beam edge particles that diffuse outside the beam core sufficiently to participate in the higher-order resonances, thereby increasing the statistical beam area in transverse phase space.

Chapter 4

Intense Ion Beam Transport through a Background Plasma Along a Solenoidal Magnetic Field

4.1 Introduction

Neutralization and focusing of a charged particle beam by a background plasma form the basis for a variety of applications to high energy accelerators and colliders [Chen, 1985; Joshi, 2007], ion-beam-driven high energy density physics and fusion [Roy *et al*., 2005, Yu *et al*., 2005, Kaganovich *et al*., 2010], and astrophysics [Gruzinov, 2001; Medvedev *et al*., 2005]. As noted earlier, one of the modern approaches to ion beam compression for heavy ion fusion applications is to use a dense background plasma which charge neutralizes the ion charge bunch, and hence facilitates compression of the bunch against strong space-charge forces. In a typical design of a heavy ion driver, a radially convergent ion beam with an imposed head-to-tail longitudinal velocity tilt propagates through the drift section filled with a neutralizing background plasma, where nearly ballistic compression occurs provided the beam charge and current are well-neutralized.

Additional control and focusing of the beam pulse can be provided by the application of a solenoidal magnetic field in the neutralizing region [Lee and Sudan, 1971; Chu and Rostoker, 1973; Rosinskii and Rukhlin, 1973; Berk and Pearlstein, 1976; Johnson, *et al*., 1988]. It has recently been demonstrated that even a weak magnetic field of order 100 G can significantly affect the transverse dynamics of an ion beam propagating through a background plasma [Kaganovich *et al*., 2007; Dorf *et al*., 2009c]. Although, in many regimes of practical interest, the direct $V \times B$ magnetic force exerted by a 100 G field has a negligible influence on the massive beam and plasma ions, the dynamics of the background plasma electrons can be significantly affected by the presence of the magnetic field. As a result, strong collective electromagnetic self-fields can be produced inside the dense plasma and can have a pronounced influence on the ion beam dynamics. It should be noted that such weak values of magnetic field can be present inside the neutralizing drift section of a heavy ion driver over distances of a few meters from the strong final focus solenoid, which is placed downstream of the drift section in order to provide additional transverse focusing of an ion beam (Chapter 1). It is therefore of particular practical importance to asses the influence of a weak solenodial magnetic field on the dynamics of an ion beam pulse propagating through a background plasma.

It has been found that the properties of the background plasma response are significantly different depending on whether the value of the solenoidal magnetic field is below or above the threshold value specified by $\omega_{ce}^{cr} = 2\beta_b \omega_{pe}$. Here, ω_{ce} and ω_{pe} are the electron cyclotron and plasma frequencies, respectively, and $\beta_b = v_b / c$ is the directed ion

beam velocity normalized to the speed of light *c*. Note that the threshold value of the magnetic field can be expressed as $B_c = 2\beta_b \left(n_p \left[cm^{-3} \right] / 10^{11} \right)^{1/2} kG$, where n_p is the background plasma density. For instance, for an ion beam with $\beta_b \sim 0.05$ propagating through a background plasma with density n_p~10^{11} cm^{-3}, this corresponds to a relatively weak magnetic field of order 100 G. The paramagnetic plasma response and the defocusing effect of a radial self-electric field, generated due to a local polarization of the magnetized plasma background, have been demonstrated for the case where $\omega_{ce} < 2\beta_b \omega_{pe}$ [Kaganovich *et al*., 2007; Kaganovich *et al*., 2008]. In contrast, for the case of $\omega_{ce} > 2\beta_b \omega_{pe}$, the plasma response is diamagnetic, and the radial self-electric field is focusing [Dorf *et al*., 2009c; Dorf *et al*., 2010]. It is interesting to note that the qualitatively different local plasma responses are separated by the critical value of magnetic field $\omega_{ce} = \omega_{ce}^{cr}$, which corresponds to the resonant excitation of large-amplitude wave-field perturbations [Volokitin *et al*., 1995; Dorf *et al*., 2010].

This introductory section is organized as follows. Section 4.1.1 briefly reviews neutralization of the ion beam space-charge and current for the case where the ion beam propagates through an unmagnetized plasma. The effects of a weak solenoidal magnetic field, $\omega_{ce} < 2\beta_b \omega_{pe}$, applied along the beam propagation direction are summarized in Sec. 4.1.2. It is demonstrated for the case of a long ion beam pulse that the so-called *slice approximation*, which does not account for the effects of coupling between the longitudinal and transverse dynamics, can adequately describe the background plasma

response in the regime where $\omega_{ce} < 2\beta_b \omega_{pe}$. Finally, Sec. 4.1.3 discusses a qualitative difference between the regimes where $\omega_{ce} < 2\beta_b \omega_{pe}$ and $\omega_{ce} > 2\beta_b \omega_{pe}$, which requires an improved theoretical model to describe the background plasma response in the regime of a moderately strong magnetic field, i.e. $\omega_{ce} > 2\beta_b \omega_{pe}$.

Detailed analytical and numerical studies of ion beam transport through a neutralized background plasma in the regime where $\omega_{ce} \geq 2\beta_b \omega_{pe}$ are presented in the following sections of this chapter. In particular, the theoretical model and assumptions in the present analysis are described Sec. 4.2. In Sec. 4.3 we consider the regime of resonant wave excitation corresponding to $\omega_{ce}^{cr} = 2\beta_b \omega_{pe}$, present the asymptotic time-dependent solution in the linear approximation, and estimate the saturation amplitude due to the nonlinear response of the plasma electrons. The analytical solutions for the electromagnetic field are compared to the results of numerical particle-in-cell simulations in Sec. 4.4. Finally, in Sec. 4.5 a detailed analysis of the local plasma response including the effects of enhanced beam self-focusing is presented.

4.1.1 Ion Beam Transport through an Unmagnetized Plasma

In this section we discuss the conditions for ion beam charge and current neutralization for the case where the ion beam pulse propagates through an unmagnetized neutralizing cold plasma background [Kaganovich *et al*., 2001]. It has been demonstrated that the beam space-charge is well-neutralized provided the beam is nonrelativistic and the beam

pulse duration τ_b is much longer than the electron plasma period, i.e., $\omega_{pe}\tau_b >> 2\pi$. In the opposite limit, $\omega_{pe}\tau_b << 2\pi$, electrostatic plasma waves are excited by the moving ion beam that considerably reduces the degree of charge neutralization.

The key parameter for good current neutralization is the *collisionless electron skin depth* $\delta_p = c/\omega_{pe}$. The beam current is well-neutralized by the *electron return current* provided the beam radius is large compared to the electron skin depth, i.e., $r_b > c/\omega_{pe}$. In the opposite limit, i.e., $r_b < c/\omega_{pe}$, the total electron return current is still equal to the beam current, however it is distributed over distances of order c/ω_{pe}, which is now much broader than the ion beam current profile. Therefore, the electron return current density is less than the ion beam current density by a factor of order $\omega_{pe} r_b / c$. The condition for current neutralization, i.e., $r_b > c/\omega_{pe}$, can be conveniently expressed in terms of the beam current as $I_b > 4.25(\beta_b n_b / n_e) kA$, where n_b and n_e are the beam density and electron density, respectively.

It is important to note that the ion beam charge is neutralized mostly by the action of the electrostatic electric field, whereas the electron return current is driven by the inductive electric field generated by the inhomogeneous magnetic flux of the ion beam pulse in the reference frame of the background plasma. Electrons are accelerated in the direction of beam propagation, and thus the electrons tend to neutralize the current as well as the space charge [Kaganovich *et al*., 2001; Kaganovich *et al*., 2010]. In order to elucidate the dynamics of the plasma electrons, a reduced nonlinear analytical model has

been developed [Kaganovich *et al*., 2001]. The model uses the fact that Maxwell's equations for the electromagnetic fields and the fluid equations for the electrons possess a conservation law for the generalized vorticity [Buneman, 1952; Kaganovich *et al*., 2001], defined by

$$\Omega = \nabla \times \mathbf{p}_e - \frac{e}{c}\mathbf{B}, \tag{4.1}$$

where $\mathbf{p}_e$ is the electron fluid momentum, $\mathbf{B}$ is the self-magnetic field, and $-e$ is the electron charge. For a long ion beam pulse with $l_b >> r_b$, where l_b is the characteristic length of the beam pulse, it follows that

$$B_\varphi = -\frac{c}{e}\frac{\partial p_{ez}}{\partial r}, \tag{4.2}$$

where we have used the fact that the generalized vorticity is zero in front of the beam pulse. The neutralizing return electron current can now be obtained from the Ampere's law, provided the displacement current can be neglected [Kaganovich *et al*., 2001]. Substituting Eq. (4.2) into Ampere's law, and assuming azimuthally symmetric ion beam we obtain

$$-\frac{1}{r}\frac{\partial}{\partial r} r \frac{\partial}{\partial r} V_{ez} = \frac{\omega_{pe}^2}{c^2 n_e}\left(Z_b n_b V_b - n_e V_{ez}\right). \tag{4.3}$$

Here, V_{ez} is the longitudinal component of the electron velocity, and $\omega_{pe} = \sqrt{4\pi e^2 n_e / m_e}$, where m_e is the electron mass. A high degree of the beam current neutralization is now evident for the case where the beam radius is greater than the electron skin depth,

$r_b > c/\omega_{pe}$, since the left-hand-side of Eq. (4.3) is small compared to the electron current term on the right-hand-side of the equation.

It is of particular importance to calculate the radial component of the Lorentz force, F_r, acting on the beam ions. Neglecting by the inertia terms in the electron radial momentum balance equation, the self-electric field can be estimated as [Kaganovich *et al*., 2001]

$$E_r = \frac{1}{c} V_{ez} B_\varphi = -\frac{m_e}{2e} \frac{\partial}{\partial r} V_{ez}^2 , \tag{4.4}$$

where Eq. (4.2) for a long beam pulse has been used. In the nonrelativistic limit, for the radial component of the Lorentz force we obtain [Kaganovich *et al*., 2001]

$$F_r = Z_b e \left(E_r - \frac{V_b}{c} B_\varphi \right) = Z_b m_e (V_b - V_{ez}) \frac{\partial V_{ez}}{\partial r} . \tag{4.5}$$

It follows from Eqs. (4.3) and (4.5) that the total force acting on beam ions is focusing ($F_r < 0$). This phenomenon is known as *self-magnetic pinching effect*, and can be used in many practical applications involving neutrazlied ion beam transport. For instance, this self-focusing can compensate for the transverse spreading of the ion bunch, thus providing self-pinched ion beam transport over long distances [Hahn and Lee, 1996; Ottinger *et al*., 2000]. Note that for the case where the plasma is sufficiently dense $n_b << n_e$ (linear regime), the electron velocity is small compared to the beam velocity, $V_{ez} << V_b$, and the magnetic component of the Lorentz force has dominant influence on the beam ions compared to weak nonlinear effects of the electric field component .

4.1.2 Effects of a Weak Magnetic Field ($\omega_{ce}<2\beta_b\omega_{pe}$)

In this section we summarize the effects of a weak solenoidal magnetic field on the degrees of beam charge neutralization and current neutralization [Kaganovich *et al*., 2007; Kaganovich *et al*., 2008]. The significant difference from the "unmagnetized case" with no applied magnetic field (Sec. 4.1.1) is that a small radial displacement, δr, of a background plasma electron is now accompanied by a strong azimuthal rotation of the electrons around the beam axis. Indeed, due to the conservation of canonical angular momentum for the case of an azimuthally symmetric ion beam, variations of magnetic flux through the electron orbit set up a large kinetic component of the canonical angular momentum, i.e., the electrons start to rotate about the beam axis (axis of symmetry of the beam-plasma system) with a high angular velocity $V_{e\varphi}$ (Fig. 4.1). Because the $V_{e\varphi}\times B_z$ force should be mostly balanced by a radial self-electric field, the electron rotation results in a plasma polarization and produces a much larger self-electric field than in the limit with no applied field [Kaganovich *et al*., 2007; Kaganovich *et al*., 2008]. Another important consequence of the strong electron rotation is the generation of an azimuthal self-magnetic field, which is much larger than in the limit with no applied solenoidal field [Kaganovich *et al*., 2007; Kaganovich *et al*., 2008].

In order to calculate the electromagnetic self-field generated by an ion beam pulse propagating through a neutralizing plasma along a uniform magnetic field $\mathbf{B}_{ext}=B_{ext}\hat{\mathbf{z}}$, the following reduced linear ($n_b<<n_e$) analytical model has been developed [Kaganovich *et al*., 2007]. We express the induced magnetic field as $\mathbf{B}=\nabla\times\mathbf{A}$ and make

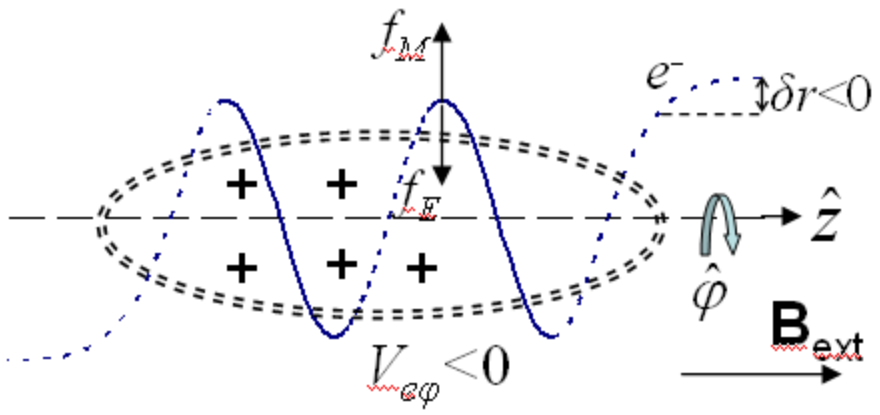

Figure 4.1: (Color) Schematic illustration of large self-electric field production. The radial displacement, δr, of the electron position is accompanied by a fast azimuthal rotation around the beam axis (blue curve). A strong radial electric force $f_E = -eE_r$ is produced in order to balance the radial component of the magnetic force $f_M = -(e/c)V_{e\varphi}B_{ext}$. The double-dashed line illustrates the ion beam pulse outline.

use of the transverse Coulomb gauge, $\nabla_\perp \cdot \mathbf{A} = 0$. Assuming a long beam pulse with $l_b >> r_b$ and $\omega_{pe}\tau_b >> 1$, the displacement current can be neglected compared to the electron current [Kaganovich *et al*., 2001], and Ampere's equations can be expressed as

$$-\frac{1}{r}\frac{\partial}{\partial r}\left(r\frac{\partial A_z}{\partial r}\right) = \frac{4\pi e}{c}\left(Z_b n_b V_b - n_e V_{ez}\right), \tag{4.6}$$

$$\frac{\partial}{\partial r}\left(\frac{1}{r}\frac{\partial\left(rA_\phi\right)}{\partial r}\right) = \frac{4\pi e}{c}n_e V_{e\phi}. \tag{4.7}$$

Here, $V_{e\varphi}$ and V_{ez} are the azimuthal and longitudinal components of the electron flow velocity, respectively. The electron flow velocity can be calculated making use of the conservation of generalized vorticity [Buneman, 1952; Kaganovich *et al*., 2001]

$$\left(\frac{\partial}{\partial t}+\mathbf{V_e}\cdot\nabla\right)\left(\frac{\mathbf{\Omega}}{n_e}\right)=\left(\frac{\mathbf{\Omega}}{n_e}\cdot\nabla\right)\mathbf{V_e}\,, \tag{4.8}$$

where the generalized vorticity is defined as $\mathbf{\Omega}=\nabla\times\left(m_e\mathbf{V_e}-e\mathbf{A}/c\right)$, and $\mathbf{V_e}$ is the electron flow velocity. Projecting out the longitudinal and azimuthal components of Eq. (4.8), we obtain [Kaganovich *et al*., 2007]

$$V_{ez}=\frac{e}{m_e c}A_z-\frac{B_{ext}}{4\pi m_e V_b n_e}\frac{1}{r}\frac{\partial\left(rA_\varphi\right)}{\partial r}, \tag{4.9}$$

$$V_{e\varphi}\left(1+\frac{\omega_{ce}^2}{\omega_{pe}^2}\right)=\frac{e}{m_e c}A_\varphi+\frac{B_{ext}}{4\pi m_e V_b n_e}\frac{\partial A_z}{\partial r}\,. \tag{4.10}$$

In deriving Eqs. (4.9)-(4.10) we have taken into account, for $n_b<<n_e$, that the radial component of the electron force balance equation gives $E_r=-V_{e\varphi}B_0/c$, where Poisson's equation can be used to determine the radial electric field. Equations (4.6)-(4.7) together with Eqs.(4.9)-(4.10) constitute the self-consistent *slice* model for describing the self-electromagnetic field perturbation excited by a long ion beam pulse propagating through a background plasma along a solenoidal magnetic field.

Figure 4.2 shows a comparison of analytical theory and the LSP [LSP, 1999] particle-in-cell (PIC) simulation results for the self-magnetic field, the perturbation in the solenoidal magnetic field, and the radial electric field in the ion-beam pulse [Kaganovich *et al*., 2007]. The PIC simulations have performed in slab geometry, because the numerical noise tends to be larger in cylindrical geometry due to the singularity on the axis (r=0). Accordingly, the results of the analytical model in Fig. 4.2 have been obtained from Eqs. (4.6)-(4.10) in slab geometry. The parameters of this illustrative example

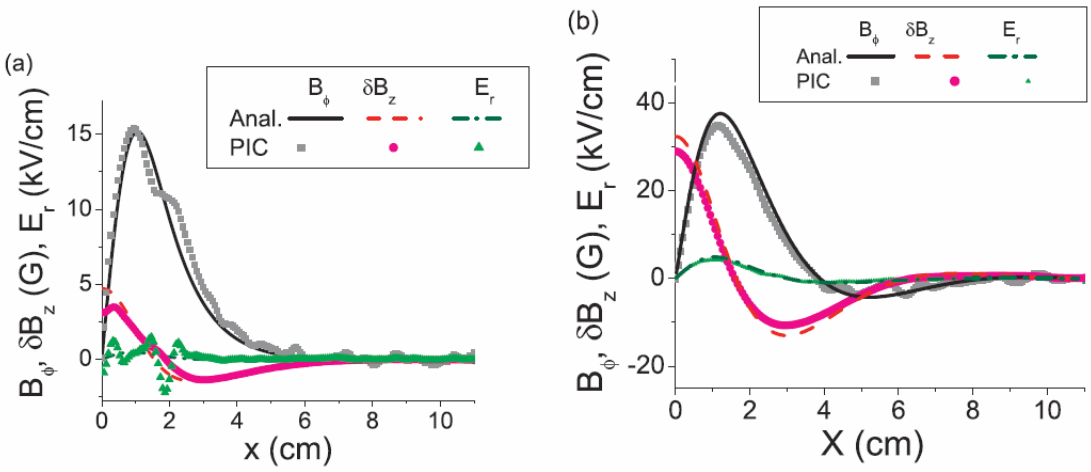

Figure 4.2: (Color) Comparison of analytical theory and LSP simulation results for the azimuthal self-magnetic field, the perturbation in the solenoidal magnetic field, and the radial self-electric field in a perpendicular slice of the beam pulse. The ion beam moves with velocity β_b=0.33c along the z axis. The beam density profile is Gaussian with r_b=1 cm, l_b=17 cm, and $n_{b0}=n_p/8=3\times10^{10}$ cm^3. The values of the applied magnetic field B_{ext} are the following: (a) B_{ext}=300 G; and (b) B_{ext}=900 G [Kaganovich *et al*., 2007].

correspond to a Gaussian ion beam pulse with density profile $n_b=n_{b0}\exp\left[-r^2/r_b^2-(z-vt)^2/l_b^2\right]$ with effective beam radius, r_b=1 cm, and beam pulse half-length, l_b=17 cm, propagating with velocity v_b=0.33c through a background plasma with density $n_p=8n_{b0}=2.4\times10^{11}cm^{-3}$. For this choice of beam parameters, the electron skin depth is approximately equal to the beam radius, $r_b\sim\delta_p=c/\omega_{pe}$. It is readily seen from Fig. 4.2 that as the applied magnetic field increases from B_{ext}=300 G ($\omega_{ce}/2\omega_{pe}\beta_b=0.28$) to B_{ext}=900 G ($\omega_{ce}/2\omega_{pe}\beta_b=0.85$) there is a sizeable increase in

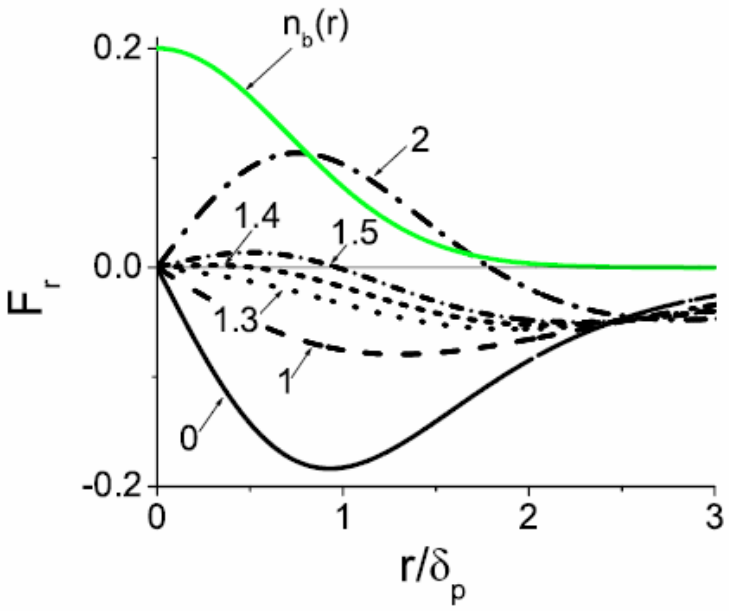

Figure 4.3: (Color) The normalized radial force $F_r/\left(Z_b^2 n_{b0} m_e v_b^2/n_p \delta_p\right)$ acting on the beam particles for different values of the parameter $\omega_{ce}^2/\omega_{pe}^2\beta_b^2$. The gray (green) line shows the Gaussian density profile multiplied by 0.2 in order to fit the profile in the plot. The beam radius is equal to the skin depth, $r_b=\delta_b$. [Kaganovich *et al*., 2007].

the azimuthal component of the self-magnetic field, and radial component of the self-electric field. Furthermore, it is interesting to note that the plasma response is paramagnetic, with $\delta B_z = B_z - B_{ext} > 0$, for the main part of the beam aperture.

Finally, it is of particular practical importance to calculate the radial component of the total Lorentz force, $F_r = Z_b e\left(E_r - \beta_b B_\varphi\right)$, acting on the beam ions. Making use of $E_r = -V_{e\varphi} B_0/c$, the force can be determined from the solutions to Eqs. (4.6)-(4.10). Figure 4.3 shows the radial profile of the normalized radial force calculated from Eqs. (4.6)-(4.10) in cylindrical geometry for various values of the parameter $\omega_{ce}^2/\beta_b^2\omega_{pe}^2$

[Kaganovich *et al*., 2007]. It is interesting to note that the force is changing from focusing to defocusing for the main part of the beam pulse as the applied magnetic field increases. The radial force is nearly zero when $\omega_{ce}^2 / \beta_b^2 \omega_{pe}^2 = 1.5$. This value can be optimal for beam transport over long distances to avoid the pinching effect [Kaganovich *et al*., 2007].

4.1.3 Effects of a Moderately Strong Magnetic Field ($\omega_{ce}>2\beta_b\omega_{pe}$)

An important difference between the two regimes, i.e., $\omega_{ce} < 2\beta_b\omega_{pe}$ and $\omega_{ce} > 2\beta_b\omega_{pe}$, appears to be due to excitation of electromagnetic wave-field perturbations, which propagate oblique to the beam axis for the case where the applied magnetic field exceeds the threshold value corresponding to $\omega_{ce}^{cr} = 2\beta_b\omega_{pe}$ [Kaganovich *et al*., 2008; Dorf *et al*, 2010]. Therefore, the slice approximation used for the analysis of the case where $\omega_{ce} < 2\beta_b\omega_{pe}$ (Sec. 4.1.2), and not taking into account the effects of coupling between the longitudinal and transverse dynamics cannot, in general, be applied to the case where $\omega_{ce} > 2\beta_b\omega_{pe}$, and a different approach has been developed [Dorf *et al*., 2010]. Here, we emphasize again that the threshold value of the magnetic field in many practical applications corresponds to a relatively weak magnetic field. For instance, for an ion beam with $\beta_b \sim 0.05$ propagating through a background plasma with density $n_p \sim 10^{11} cm^{-3}$, the threshold magnetic field is of order 100 G. The magnetic fields above such weak values can be present inside the neutralizing drift section of an ion driver over

distances of a few meters (Chapter 1), and therefore theoretical studies of the case where $\omega_{ce} > 2\beta_b \omega_{pe}$ are of particular practical importance.

In the present analysis, we consider a fast ion beam pulse with velocity much greater than the Alfven velocity, and therefore the beam ions cannot interact effectively with ion Alfven wave excitations. Furthermore, we assume a smooth beam density profile with a characteristic axial length scale for density variation, l_b, much greater than the wavelength of electron plasma wave excitations, $l_b >> v_b / \omega_{pe}$. Therefore, electrostatic electron plasma wave excitations are also significantly suppressed [Kaganovich *et al*., 2001; Kaganovich *et al*., 2004]. However, if a sufficiently strong ambient magnetic field with $\omega_{ce} > 2\beta_b \omega_{pe}$ is present inside the neutralizing region, the ion beam pulse can effectively interact with the electromagnetic electron whistler branch of the plasma dispersion relation [Oliver *et al*., 1994; Krafft and Starodubtsev, 2002]. Therefore, in the present studies we analyze excitation of the whistler branch by an ion beam pulse propagating through a neutralizing plasma along a solenoidal magnetic field, and assess its influence on the degrees of beam charge neutralization and current neutralization, and the transverse beam dynamics.

The fundamental problem of whistler wave-field perturbations excited by a charged particle beam propagating in a magnetized plasma has been extensively studied for several decades, and various methods have been developed [Ahiezer *et al*., 1974]. Recent interest in this problem has been motivated by possible use of charged particle beams for space communications [Lavergnat and Pellat, 1979; Krafft *et al*., 1994; Krafft

and Starodubtsev, 2002]. Propagating in the magnetized ionosphere or the magnetosphere plasma, charged particle beams can excite whistler wave-field perturbations, and therefore can be used as compact on-board emitters in the very-low-frequency range, replacing large-apertures electromagnetic antennas. Analytical and numerical studies of whistler branch excitations by a density-modulated electron beam propagating through a background plasma along a uniform magnetic field, including both linear and nonlinear effects have been reported in [Volokitin *et al*., 1995; Volokitin *et al*., 1997; Krafft and Volokitin, 1998]. However, in those calculations the case of a thin beam with $r_b << k_\perp^{-1}$ has been considered, and the effects of the transverse beam structure have not been taken into account. Here, r_b is the characteristic beam radius, and $k_\perp$ is the perpendicular component of the whistler wave vector. Note that in contrast to space-physics phenomena, where the wavelength of the whistler waves is large compared to the beam radius, for the parameters typical of neutralized intense ion beam transport applications, the beam radius can be comparable to the perpendicular wavelength. Furthermore, an axially-continuous, density-modulated beam with modulation period l_m has been considered in previous works [Volokitin *et al*., 1995; Volokitin *et al*., 1997; Krafft and Volokitin, 1998], and therefore a monochromatic wave excitation with frequency $\omega = v_b / l_m$ was obtained. Note that a finite-length ion beam pulse with a bell-shaped (not modulated) axial density profile used in intense beam transport applications can excite a broad frequency spectrum with a characteristic frequency $\omega \sim v_b / l_b$ and bandwidth $\delta\omega \sim \omega$. Therefore, in the present analysis we consider excitation of the electromagnetic

whistler branch by a finite-length ion beam pulse propagating through a background plasma along a solenidal magnetic field, taking into account the effects of the longitudinal and transverse beam structures.

In the following sections we demonstrate that the total electromagnetic field excited by the ion beam pulse can be conveniently represented as the sum of two components: a *local* field component, corresponding to the local polarization of the background plasma, and rapidly decaying to zero outside the beam pulse; and a *wave* field component that can extend far outside the beam. It is then shown that in the regime where $\omega_{ce} >> 2\beta_b\omega_{pe}$ the local-field component has the dominant influence on the transverse beam dynamics. Moreover, in this limit, a positive charge of the ion beam pulse becomes over-compensated by the plasma electrons, resulting in an enhanced transverse focusing of the beam ions [Dorf *et al*., 2009c; Dorf *et al*., 2010]. Note that for the case where $\omega_{ce} < 2\beta_b\omega_{pe}$ considered in Sec. 4.1.2, the beam charge is under-neutralized, and the radial electric field has a defocusing effect. Furthermore, it is found that the local plasma response is changing from paramagnetic for the $\omega_{ce} < 2\beta_b\omega_{pe}$ case [Kaganovich *et al*., 2007], to diamagnetic for the $\omega_{ce} > 2\beta_b\omega_{pe}$ case [Dorf *et al*., 2010].

A plausible heuristic description of qualitatively different regimes of ion beam interaction with the background plasma can be given based on the analysis of the balance between the electric and magnetic forces acting on a rotating background plasma electron [Fig. 4.4]. Figure 4.4(a) shows the case of under-neutralized beam space-charge corresponding to $\omega_{ce} < 2\beta_b\omega_{pe}$. In this regime the net positive charge of the ion

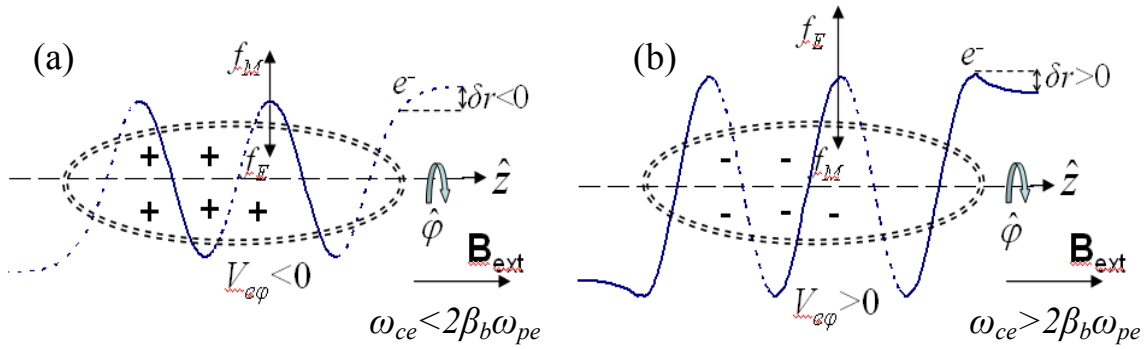

Figure 4.4: (Color) Two different regimes of ion beam interaction with a background plasma. (a) Corresponds to $\omega_{ce}<2\beta_b\omega_{pe}$; the beam charge is under-neutralized, the radial self-electric field is defocusing, $E_r>0$, and the plasma response is paramagnetic, $\delta B_z>0$. (b) Corresponds to $\omega_{ce}>2\beta_b\omega_{pe}$; the beam charge is over-neutralized, the radial self-electric field is dedefocusing, $E_r<0$, and the plasma response is diamagnetic, $\delta B_z<0$. The blue curves illustrate the trajectory of a background plasma electron; the double-dashed lines illustrate the ion beam outline, $f_E=-eE_r$ and $f_M=-(e/c)V_{e\varphi}B_{ext}$.

beam attracts a plasma electron, i.e., $\delta r<0$. Due to conservation of canonical angular momentum, a decrease in the magnetic flux through the electron orbit provides electron angular rotation in the negative azimuthal direction, $V_{e\varphi}<0$. As a result, the radial component of the magnetic force acting on the electron is positive, $f_M=-eB_{ext}V_{e\varphi}/c>0$, and is balanced by the positive (defocusing) radial component of the electric field, $E_r>0$. Note that the positive azimuthal component of the electron current, $j_{e\varphi}=-en_eV_{e\varphi}>0$, produces a positive (paramagnetic) perturbation of the longitudinal magnetic field, $\delta B_z>0$. In contrast, for the case where the beam space charge is over-

neutralized [Fig. 4.4(b)] a plasma electron moves radially outward as the ion beam approaches, i.e., $\delta r > 0$, and an increase in the magnetic flux is associated with the positive azimuthal component of the electron velocity, $V_{e\varphi} > 0$. This leads to a diamagnetic effect, $\delta B_z < 0$, and also a focusing electric field, $E_r < 0$, is generated to provide force balance on the plasma electrons.

It is interesting to note that the threshold value of the magnetic field, $\omega_{ce}^{cr} = 2\beta_b \omega_{pe}$, which separates these qualitatively different regimes of ion beam interaction with the background plasma, corresponds to the resonant excitation of a large-amplitude wave-field component [Volokitin *et al*., 1995, Dorf *et al*., 2010]. This effect of resonant wave excitation can be utilized for diagnostic purposes. Indeed, placing a pick-up loop outside the beam pulse and varying the amplitude of the applied magnetic field, a large-amplitude signal will be detected when the applied magnetic field approaches the threshold value specified by $\omega_{ce}^{cr} = 2\beta_b \omega_{pe}$. Therefore, it is expected that this scheme can be utilized as a passive diagnostic tool to measure the beam velocity or plasma density [Dorf *et al*., 2010].

4.2 Theoretical Model

In this section we calculate the electromagnetic field excitation generated by an ion beam pulse propagating through a cold background plasma with a constant velocity, v_b, along a uniform magnetic field $\mathbf{B}_{ext} = B_{ext}\hat{z}$. The beam carries a current $j_b = Z_b e v_b n_b (z - v_b t, x)$,

where Z_b is the beam ion charge state, -e is the electron charge, n_b is the beam number density, and x and z are the transverse and longitudinal coordinates, respectively. For simplicity in the analytical studies, we consider here 2D slab (x,z) geometry, and the results of numerical simulations in cylindrical (r,z) geometry are presented in Sec. 4.3. Provided the beam density is small compared to the plasma density ($n_b << n_p$) , we assume a linear (small-signal) plasma response and obtain the following equation for the Fourier transforms of the perturbed electromagnetic field components $\mathbf{E} = \int d\mathbf{k} d\omega \mathbf{E}_{\omega,\mathbf{k}} \exp\left(-i\omega t + ik_x x + ik_z z\right)$, and $\mathbf{B} = \int d\mathbf{k} d\omega \mathbf{B}_{\omega,\mathbf{k}} \exp\left(-i\omega t + ik_x x + ik_z z\right)$, where

$$k^2 \mathbf{E}_{\omega,\mathbf{k}} - \mathbf{k}\left(\mathbf{k}\cdot\mathbf{E}_{\omega,\mathbf{k}}\right) - \frac{\omega^2}{c^2}\vec{\varepsilon}\cdot\mathbf{E}_{\omega,\mathbf{k}} = 4\pi i \frac{\omega}{c^2}\mathbf{j}_{\omega,\mathbf{k}}. \tag{4.11}$$

Here, $\vec{\varepsilon}$ is the dielectric tensor describing linear response of the cold plasma electrons [Ahiezer *et al*., 1974] with $\varepsilon_{xx} = \varepsilon_{yy} = 1 - \omega_{pe}^2 / \left(\omega^2 - \omega_{ce}^2\right)$, $\varepsilon_{zz} = 1 - \omega_{pe}^2 / \omega^2$, and $\varepsilon_{xy} = -\varepsilon_{yx} = i\omega_{pe}^2 \omega_{ce} / \left[\omega\left(\omega^2 - \omega_{ce}^2\right)\right]$, where $\omega_{pe} = \left(4\pi e^2 n_p / m_e\right)^{1/2}$ is the plasma frequency, $\omega_{ce} = eB_{ext} / m_e c$ is the electron cyclotron frequency, and the plasma ion response is neglected provided $\omega >> \sqrt{\omega_{ce}\omega_{ci}}$ [Lifshitz and Pitaevskii, 1981]. Here, $\omega_{ci} = eB_{ext} / m_i c$ is the ion cyclotron frequency, and m_e and m_i are the electron mass and ion mass, respectively. Finally, we neglected perturbations in the ion beam motion, assuming that the time duration of beam-plasma interaction is smaller than the characteristic time for the ion beam response [Startsev *et al*., 2008]. The space-time Fourier transform of the

beam current is specified by $\mathbf{j}_{\omega,\mathbf{k}} = Z_b e \mathbf{v}_b n_{\mathbf{k}}(k_x,k_z)\delta(\omega - k_z v_b)$, where $n_{\mathbf{k}} = \int d\xi dx n_b(x,\xi)\exp(-ik_x x - ik_z \xi)$.

It is straightforward to show for this model of the beam current that Eq. (4.11) yields a steady-state solution, in which all quantities depend on z and t solely through the combination $\xi = z - v_b t$. In what follows, we assume that the beam pulse is sufficiently long, with $r_b << l_b$ and $\omega \sim v_b / l_b << \omega_{pe}$. Note that the latter condition implies that electrostatic electron plasma wave excitations are significantly suppressed [Kaganovich *et al*., 2001]. Finally, in this section, for simplicity we assume that $\omega_{ce} << \omega_{pe}$, and a general analysis for the case of an arbitrary ratio of ω_{ce}/ω_{pe} can be found in Appendix A. For present purposes, it is particularly important to analyze the x-component of the electric field perturbations, E_x, and the y-component of the magnetic field perturbations, B_y, which determine the transverse dynamics of the beam particles. After some straightforward algebra we obtain the following Fourier transforms of the transverse electromagnetic field components [Dorf *et al*., 2010],

$$\frac{eE^x_{\omega,\mathbf{k}}}{m_e \omega_{pe} c} = -i \frac{c^3 Z_b k_x k^2 \omega_{ce}^2}{n_p \omega_{pe} \left(\omega_{pe}^2 + c^2 k^2\right)^2} \frac{k_z^2 v_b^2 n_{\mathbf{k}} \delta(\omega - k_z v_b)}{\omega^2 - \omega_{wh}^2(k_x,k_z)}, \tag{4.12}$$

$$\frac{eB^y_{\omega,\mathbf{k}}}{m_e \omega_{pe} c} = -i \frac{\beta_b Z_b \omega_{pe} c k_x}{n_p \left(\omega_{pe}^2 + c^2 k^2\right)} \frac{k_z^2 v_b^2 n_{\mathbf{k}} \delta(\omega - k_z v_b)}{\omega^2 - \omega_{wh}^2(k_x,k_z)}, \tag{4.13}$$

where use has been made of Faraday's equation, $(\omega/c)\mathbf{B}_{\omega,\mathbf{k}} = \mathbf{k} \times \mathbf{E}$, to obtain the perturbed magnetic field component. Here, $\beta_b = v_b/c$, $k^2 = k_x^2 + k_z^2$, and

$$\omega_{wh}^2\left(k_x,k_z\right)=\frac{\omega_{ce}^2k^2k_z^2}{\left(k^2+\omega_{pe}^2/c^2\right)^2}\,, \tag{4.14}$$

is the dispersion relation for the electron whistler branch. The electromagnetic field perturbations E_x and B_y, can now be obtained by applying inverse space-time Fourier transforms to Eqs. (4.12) and (4.13). Integration over the frequency ω readily gives

$$\frac{eE_{\mathbf{k}}^x}{m_e\omega_{pe}c}=-i\frac{c^3Z_bk_xk^2\omega_{ce}^2}{n_p\omega_{pe}\left(\omega_{pe}^2+c^2k^2\right)^2}\frac{k_z^2v_b^2n_{\mathbf{k}}\exp\left(-ik_zvt\right)}{k_z^2v^2-\omega_{wh}^2\left(k_x,k_z\right)}\,, \tag{4.15}$$

$$\frac{eB_{\mathbf{k}}^y}{m_e\omega_{pe}c}=-i\frac{\beta Z_b\omega_{pe}ck_x}{n_p\left(\omega_{pe}^2+c^2k^2\right)}\frac{k_z^2v_b^2n_{\mathbf{k}}\exp\left(-ik_zvt\right)}{k_z^2v^2-\omega_{wh}^2\left(k_x,k_z\right)}\,. \tag{4.16}$$

It is evident that the onset of wave-field generation by the beam pulse corresponds to existence of real solutions to

$$\omega_{wh}^2\left(k_x,k_z\right)=k_z^2v_b^2\,. \tag{4.17}$$

Note that the condition in Eq. (4.17) is equivalent to the resonance condition for Cherenkov radiation, namely $V_z^{ph}=v_b$, where V_z^{ph} is the z-component of the whistler wave phase velocity.

Excitation of the whistler wave field perturbations is associated with the poles (singularities) in Eqs. (4.15)-(4.16), which provides a challenge in calculating the inverse Fourier integration. In what follows, first, based on the dispersion relation [Eq. (4.14)] and the Cherenkov condition [Eq. (4.17)], properties of the excited whistler waves are investigated (Sec. 4.2.1). Then, the singularities are properly treated by carrying out the integration along corresponding Landau contours in the complex **k**-plane, and the steady-

state solution for the excited electromagnetic field perturbations is obtained (Sec. 4.2.2). Finally, the time evolution of the excited electromagnetic perturbations is discussed in Sec. 4.2.3, and the influence of the excited wave field on the degrees of a beam charge neutralization and current neutralization is assessed in Sec. 4.2.4.

4.2.1 Properties of the Excited Whistler Waves

It is straightforward to show that real solutions to Eq. (4.17) exist, provided

$$\alpha = \omega_{ce} / 2\beta_b \omega_{pe} > 1, \tag{4.18}$$

as illustrated in Fig. 4.5(a). For this case, the solutions $k^2 = k_{em,qs}^2$ correspond to the long-wavelength electromagnetic part of the whistler branch, $k = k_{em} < \omega_{pe}/c$, and the short-wavelength quasi-electrostatic part, $k = k_{qs} > \omega_{pe}/c$ [Fig. 4.5(a)]. In the limit where $\alpha >> 1$ the solutions are approximately given by

$$k_{qs} \cong \frac{2\alpha\omega_{pe}}{c},\ k_{em} \cong \frac{\omega_{pe}}{2\alpha c}. \tag{4.19}$$

Note that for a long beam pulse with $k_z^{-1} \sim l_b >> k_{qs,em}^{-1}$ the transverse wave vectors of the excited wave field are approximately given by $k_x \approx \pm k_{qs,em}$ [see Fig. 4.5(b)].

The directions of the *x*-component of the group velocity V_{gx} for the excited wave field are illustrated in Fig. 4.5(b). Note that the quasi-electrostatic and the long-wavelength electromagnetic whistler waves with the same signs of phase velocity have opposite signs of group velocity, V_{gx}. Furthermore, it can be shown that the *z*-component

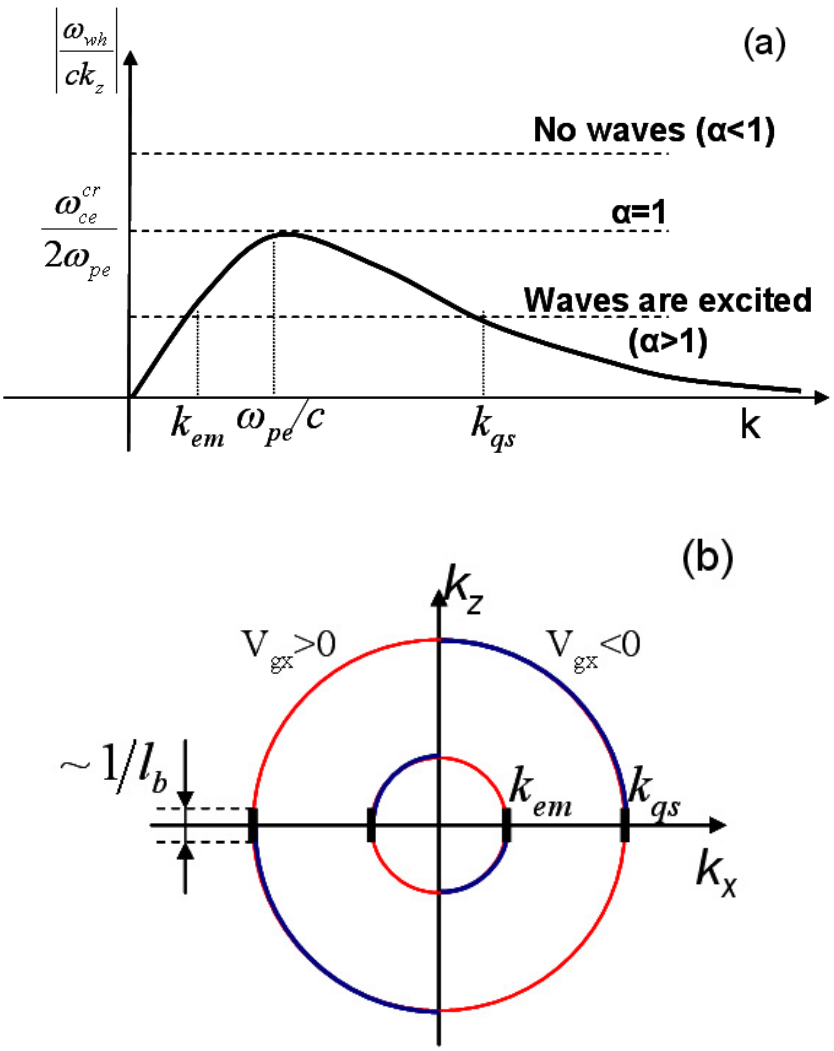

Figure 4.5: (Color) Plots of solutions to Eq. (4.17) corresponding to the wave vectors of the excited whistler wave-field. (a) The absolute value of the normalized z-component of the whistler wave phase velocity (solid curve) is intersected by different values of the normalized beam velocity β_b (dashed lines). (b) The circles on the plane (k_x,k_z) illustrate the solutions to Eq. (4.17). For the case of a long beam pulse with $l_b >> k_{qs,w}^{-1}$, the wave vectors primarily excited are illustrated by the short vertical bold lines. Red and blue colors illustrate positive and negative signs, respectively, of the x-component of the group velocity for the excited waves.

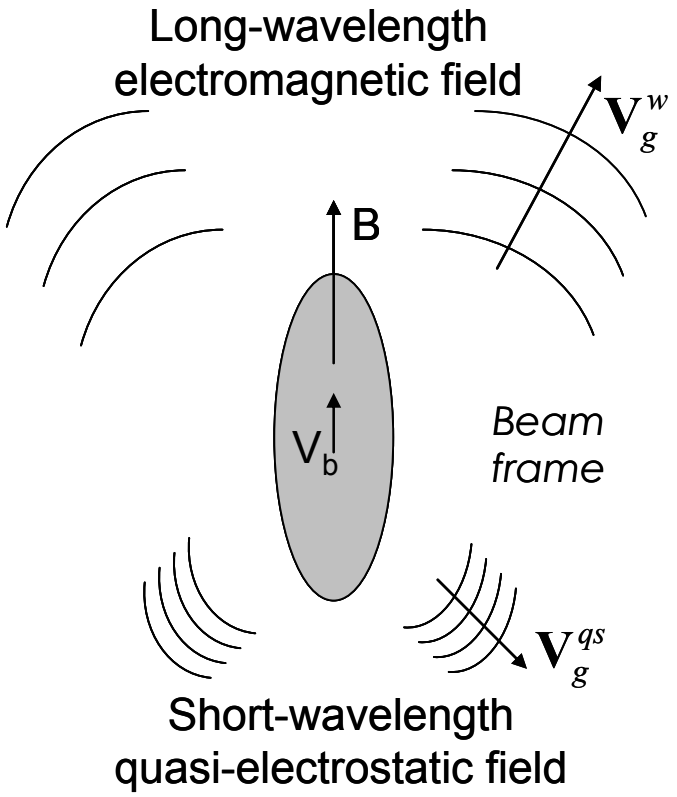

Figure 4.6: Schematic illustration of whistler waves excited by the ion beam pulse. In the beam frame of reference, the long-wavelength electromagnetic wave-field propagates ahead of the beam pulse, and the short-wavelength quasi-electrostatic wave-field propagates toward the beam tail.

of the group velocity for the short-wavelength quasi-electrostatic wave field is smaller than the beam velocity. In contrast, the long-wavelength electromagnetic wave field propagates in the *z*-direction faster than the beam. *Therefore, the long-wavelength electromagnetic perturbations excited by the beam tail can propagate along the beam and influence the dynamics of the beam head.* A schematic illustration of the whistler wave excitations is shown in Fig. 4.6 [Dorf *et al*., 2010].

4.2.2 Wave-Field and Local-Field Components of the Excited Electromagnetic Perturbations

Wave-field excitations for the case where $\alpha > 1$ are associated with the poles in Eqs. (4.15)-(4.16), which appear in the real space of the wave vector components (k_x,k_z). Note, for the case of a long beam pulse, $k_z^{-1} \sim l_b >> k_{qs,em}^{-1}$, that the pole locations on the real k_x-axis depend weakly on the value of k_z, i.e., $k_x \cong \pm k_{em,qs}\left(1 - k_z^2 / 2k_{em,qs}^2\right)$. It is therefore convenient to carry out the inverse Fourier integration, first along the k_x-axis, and then along the k_z-axis. To properly account for the pole contributions, the integration over k_x-space should be carried out along the Landau contour, C_L, as illustrated in Fig 4.7 [Dorf *et al*., 2010]. Note that integration along the contour C_L shows that sufficiently far outside the beam only wave fields with a positive (negative) x-component of group velocity propagate in the region x>0 (x<0).

To demonstrate this fact, as an illustrative example, we consider the simple case where the spectrum of the beam density is an analytical function in the complex k_x-plane, which satisfies $n_{\mathbf{k}} \exp\left(-|k_x x|\right) \to 0$ for large values of $|k_x|$. Considering x>0, and closing the Landau contour through a semi-circle of an infinitely large radius lying in the upper-plane [Figs. 4.7(a) and 4.7(b)], we readily obtain that the wave field excitations correspond to contributions from the poles at k_x=–k_{em} and k_x=k_{qs} for k_z<0, and at k_x=k_{em} and k_x=-k_{qs} for k_z>0. Note that the group velocity of these waves is indeed directed away from the beam, i.e., V_{gx}>0 [see. Fig. 4.5(b)]. Finally, it should be pointed out that the integration contours C_L are different for the cases where k_z>0 and k_z<0. Therefore, even

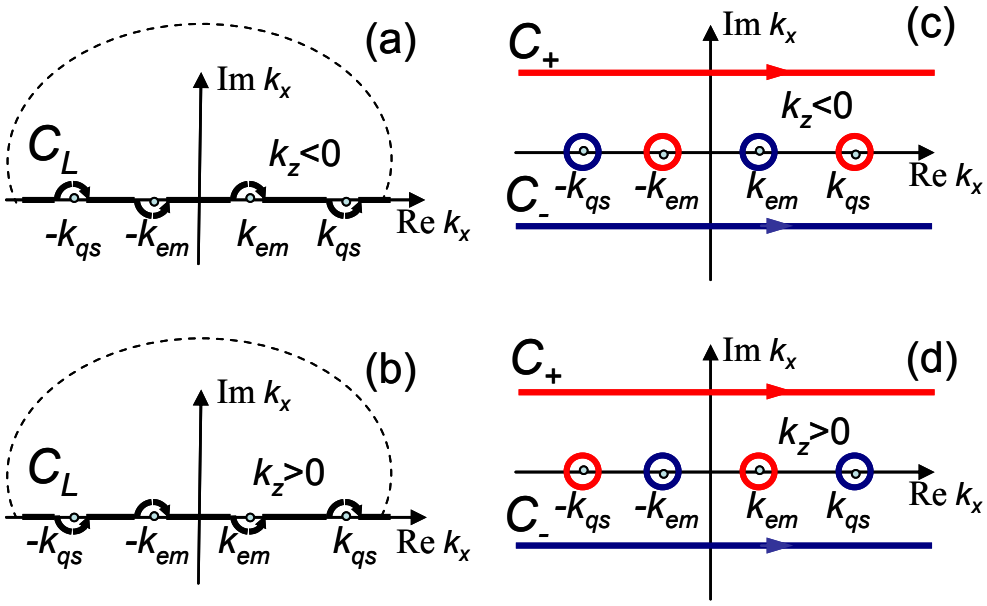

Figure 4.7: (Color) Integration contours used for evaluation of the integrals in Eqs. (4.15)-(4.16). Frames (a) and (b) show Landau contours C_L corresponding to $k_z<0$ and $k_z>0$, respectively. Frames (c) and (d) illustrate contours of integration equivalent to the ones shown in Frames (a) and (b), respectively. Red and blue colors are used to illustrate the integration contours for $x>0$ and $x<0$, respectively.

for a symmetric longitudinal beam density profile, the electromagnetic field perturbations are not, in general, symmetric around the beam center, implying oblique wave propagation.

For present purposes, it is convenient to represent the integration along the contour C_L for $x>0$ ($x<0$) as an integral along a slightly shifted upward (downward) contour C_+ (C_-) lying below (above) the poles of $n_{\mathbf{k}}$, plus (minus) the residues of the relevant on-axis poles [Figs. 4.7(c) and 4.7(d)]. For a beam with a smooth radial profile, it can be shown that the contribution from the on-axis poles corresponds to the wave-field

components of the electromagnetic field perturbation (E_x^W, B_y^W) extending far outside the beam, and the integrals along the paths C_+ and C_- correspond to the local-field components (E_x^{loc}, B_y^{loc}) that rapidly decay to zero outside the beam. Assuming $k_z << k_{em,qs}$ for a sufficiently long beam pulse, we obtain the following approximate expressions for the wave-field components of the electromagnetic field perturbation for *x>0* [Dorf *et al*., 2010],

$$\frac{eB_y^W}{m_e\omega_{pe}c} = \frac{2\pi\omega_{pe}\beta_b Z_b}{cn_p\left(k_{qs}^2 - k_{em}^2\right)}\left(b_{em} + b_{qs}\right), \tag{4.20}$$

$$\frac{eE_x^W}{m_e\omega_{pe}c} = \frac{2\pi Z_b\omega_{ce}^2}{cn_p\omega_{pe}\left(k_{qs}^2 - k_{em}^2\right)}\left(e_{em} + e_{qs}\right). \tag{4.21}$$

Here,

$$b_{qs,em} = \pm\left(k_{qs,em}^2 + \omega_{pe}^2/c^2\right)\int_0^\infty dk_z n_{\mathbf{k}}\left(k_{qs,em}, k_z\right)\cos\left[k_z\xi \mp k_{qs,em}\left(1 - k_z^2/2k_{qs,em}^2\right)x\right], \tag{4.22}$$

$$e_{qs,em} = \pm k_{qs,em}^2\int_0^\infty dk_z n_{\mathbf{k}}\left(k_{qs,em}, k_z\right)\cos\left[k_z\xi \mp k_{qs,em}\left(1 - k_z^2/2k_{qs,em}^2\right)x\right], \tag{4.23}$$

are the electric and magnetic components corresponding to the quasi-electrostatic (with subscript "*qs*") and the long-wavelength electromagnetic (with subscript "*em*") waves, respectively, and $\xi = z - v_b t$. Note that the correction term, $\delta\varphi = \left(k_z^2/2k_{em,qs}\right)x$, which we only retained in the phase of the wave-field component, yields a curvature in the phase fronts, and a corresponding decrease in the wave-field amplitude for $x \geq l_b^2 k_{em,qs}$. The local fields are given for *x*>0 by [Dorf *et al*., 2010]

$$\frac{eB_y^{loc}}{m_e\omega_{pe}c} = -i\int_{-\infty}^{\infty} dk_z e^{ik_z\xi}\int_{C_+} dk_x e^{ik_x x} n_{\mathbf{k}} \frac{\omega_{pe}\beta Z_b k_x\left(k_x^2+\omega_{pe}^2/c^2\right)}{cn_p\left(k_x^2-k_{em}^2\right)\left(k_x^2-k_{qs}^2\right)}, \tag{4.24}$$

$$\frac{eE_x^{loc}}{m_e\omega_{pe}c} = -i\int_{-\infty}^{\infty} dk_z e^{ik_z\xi}\int_{C_+} dk_x e^{ik_x x} n_{\mathbf{k}} \frac{Z_b k_x^3\omega_{ce}^2}{cn_p\omega_{pe}\left(k_x^2-k_{em}^2\right)\left(k_x^2-k_{qs}^2\right)}. \tag{4.25}$$

It should be noted that for the case where the beam density profile is specified by $n_b(x, z-v_bt) = n_x(x)n_z(z-v_bt)$, the integration over the k_z-space can be carried out independently from the k_x-space integration. Therefore, the axial dependence of the local fields is determined solely by the beam density axial profile, that is $\left(E^{loc}, B^{loc}\right) = n_z(z-v_bt)\Phi_{E,B}(x)$. In contrast, it is readily seen from Eqs. (4.20)-(4.23) that the wave field propagates obliquely to the beam. This implies a coupling between the transverse and longitudinal dynamics of the system, and therefore limits the validity of the slice approximation.

Features of the steady-state whistler wave excitation are shown in Fig. 4.8 for the following illustrative parameters: $n_b = n_{b0}\exp\left[-r^2/r_b^2-(z-v_bt)^2/l_b^2\right]$, l_b=10c/ω_{pe} (beam pulse duration τ_b=l_b/v_b=30.3/ω_{pe}), v_b=0.33c, n_{b0}=0.05n_p, n_p=2.4·10^{11} cm^{-3}, and B_{ext}=1600 G [Dorf *et al*., 2010]. It is readily seen for a wide-aperture beam, r_b=2.5c/ω_{pe}, that the long-wavelength electromagnetic part of the whistler branch is primarily excited [Fig. 4.8 (a)], and the amplitude of the quasi-electrostatic wave field is exponentially small [see Eq. (4.22)]. In contrast, for the case of a thinner beam, r_b=0.5c/ω_{pe}, the short-wavelength quasi-electrostatic waves are primarily represented in the excited spectrum [Fig. 4.8(b)] due to the large excitation factor, $\left(k_{qs}^2+\omega_{pe}^2/c^2\right)$, in front of the integral in Eq. (4.22).

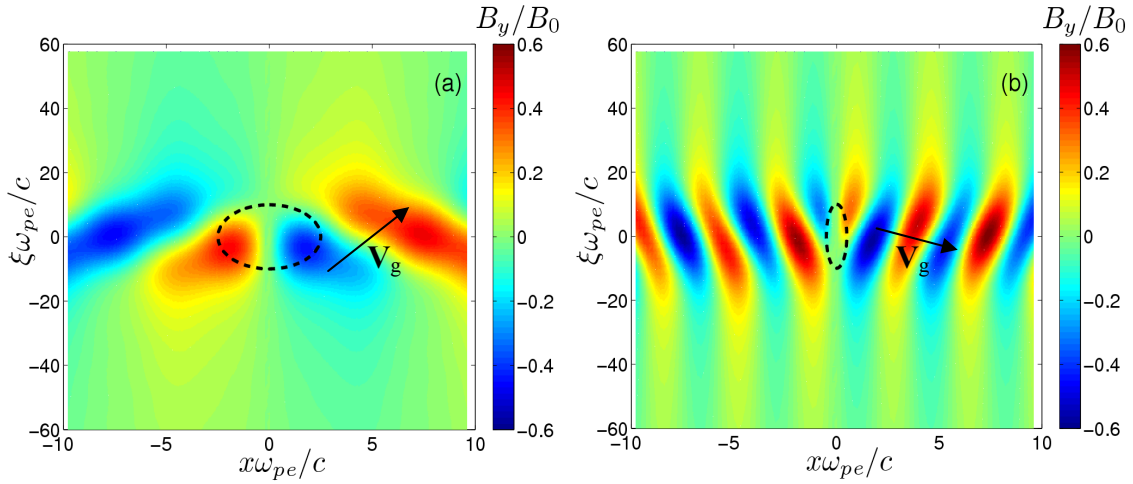

Figure 4.8: (Color) Plots of the steady-state amplitude of the transverse magnetic field perturbations B_y. The beam-plasma parameters correspond to Z_b=1, l_b=10c/ω_{pe}, β_b=0.33, and n_p=2.4·10^{11} cm^{-3}. The applied magnetic field, B_{ext}=1600 G, corresponds to $\alpha=\omega_{ce}/(2\beta_b\omega_{pe})$=1.54. The frames show (a) primarily excitation of long-wavelength electromagnetic waves by a wide-aperture ion beam with r_b=2.5c/ω_{pe}; and (b) primarily excitation of short-wavelength quasi-electrostatic waves by a thin beam with r_b=0.5c/ω_{pe}. The information used in obtaining the plots is obtained from Eqs. (A1)-(A7). The normalization factor in Frames (a) and (b) is given by $B_0=4\pi n_{b0}Z_b e\beta_b r_b$. The arrows schematically illustrate the direction of the wave packet group velocity. The dashed lines correspond to the contour of constant beam density corresponding to the effective beam radius r_b.

Note that for the parameters in this illustrative example, $\omega_{ce} \sim \omega_{pe}$, and therefore to obtain the plots in Fig.4.8, we used Eqs. (A1)-(A7), which include ω_{ce}/ω_{pe} correction terms.

4.2.3 Time Evolution of the Wave-Field Perturbations

It should be noted that the denominators in Eqs. (4.20)-(4.21) can be expressed as

$$k_{qs}^2 - k_{em}^2 = 4\alpha\sqrt{\alpha^2 - 1}\,\omega_{pe}^2 / c^2 \,, \tag{4.26}$$

and it readily follows that there is strong resonant wave excitation for the case where the poles are merging, corresponding to $\alpha = \omega_{ce}/2\beta\omega_{pe} = 1$ and $k_{qs} = k_{em} = \omega_{pe}/c$ [see Fig. 4.5(a)]. Indeed, it can be shown in the limit $\alpha = 1$ that the group velocity of an excited wave packet becomes equal to the beam velocity, i.e., $V_{gx} = 0$, $V_{gz} = v_b$. That is the wave packet is moving together with the beam pulse, and can therefore be amplified to very large amplitude (during a very long time interval), assuming a linear plasma response. The wave-field intensity, however, will be saturated either by nonlinear processes or due to dissipation (collisions). Note that the local fields specified by Eqs. (4.24)-(4.25) do not have singularities at $\alpha = 1$.

For the case where $\alpha > 1$, the wave-field amplitude reaches a finite quasi-steady-state limit with a characteristic time scale of $\tau_s \sim \min\{r_b/V_{gx}, l_b/|V_{gz} - v_b|\}$. This time interval is required for an initial transient wave packet to propagate sufficiently outside the beam pulse. For the excited wave vectors specified by Eq. (4.7), it can be shown that $V_{gx}/(V_{gz} - v_b) = k_x/k_z$. Therefore, for a sufficiently long beam pulse with $l_b >> k_{qs,em}^{-1}$, the wave perturbations propagate primarily in the transverse direction, and leave the beam in the time period $\tau_s \sim r_b/V_{gx}$. For the case where $\alpha \geq 1$ and $r_b \sim c/\omega_{pe}$, making use of Eqs. (4.14) and (4.17), we obtain $\tau_s \sim r_b/V_{gx} \sim l_b/v_b$. That is, the time scale for achieving a

quasi-steady-state is of order the beam pulse duration, and is therefore much longer than the plasma period, i.e.,

$$\tau_s \sim l_b / v_b >> 1/\omega_{pe} \tag{4.27}$$

Note that this result is significantly different from the case B_{ext}=0, where the characteristic time to reach a quasi-steady-state is of order of the plasma period [Dorf *et al*., 2010].

4.2.4 Influence of the Excited Wave Field on Beam Charge Neutralization and Current Neutralization

It is of particular interest for neutralized beam transport applications to estimate the degrees of beam charge neutralization and current neutralization associated with the excited wave field. Here, we consider the case where $\alpha \geq 1$, and the limit where $\alpha >> 1$ and the analysis of the local-field component is addressed in Sec. 4.5. It is convenient to introduce $E_0 = 4\pi n_{b0} Z_b e r_b$ and $B_0 = 4\pi n_{b0} Z_b e \beta_b r_b$ that represent, respectively, the characteristic transverse self-electric field and self-magnetic field generated by an ion beam propagating in vacuum. Here, n_{b0} and r_b are the characteristic values of the beam density and radius. The degrees of beam charge neutralization and current neutralization can now be effectively measured by E_x/E_0 and B_y/B_0. Considering, for simplicity, a Gaussian beam density profile with $n_{\mathbf{k}} = (r_b l_b / 4\pi) n_{b0} \exp\left[-r_b^2 k_x^2/4 - l_b^2 k_z^2/4\right]$, it follows from Eqs. (4.20)-(4.23) that the degrees of beam charge neutralization and current neutralization associated with the wave field excitations is given by [Dorf *et al*., 2010]

$$\frac{B_y^W}{B_0} \sim \sqrt{\pi}\,\frac{\max\left\{c^2k_{qs}^2/\omega_{pe}^2\exp\left(-r_b^2k_{qs}^2/4\right),\exp\left(-r_b^2k_{em}^2/4\right)\right\}}{4\alpha\sqrt{\alpha^2-1}}, \tag{4.28}$$

$$\frac{E_x^W}{E_0} \sim \sqrt{\pi}\,\frac{\omega_{ce}^2}{\omega_{pe}^2}\,\frac{\max\left\{\left(c^2k_{qs}^2/\omega_{pe}^2\right)\exp\left(-r_b^2k_{qs}^2/4\right),\left(c^2k_{em}^2/\omega_{pe}^2\right)\exp\left(-r_b^2k_{em}^2/4\right)\right\}}{4\alpha\sqrt{\alpha^2-1}}. \tag{4.29}$$

It readily follows from Eqs. (4.28)-(4.29), for the case where $r_bk_{em}/2 \le 1$ and $\alpha \ge 1$, that the beam current is not neutralized, i.e., $B_y^W/B_0 \sim 1$. The beam charge is, however, well-neutralized, i.e., $E_x^W/E_0 << 1$, provided $\omega_{ce} << \omega_{pe}$ [this is due to the factor $\omega_{ce}^2/\omega_{pe}^2$ in Eq. (4.29)]. For the case where $\omega_{ce} \sim \omega_{pe}$, the degree of charge neutralization decreases, giving $E_x^W/E_0 \sim 1$, (see Appendix A), which is consistent with the analysis in [Kaganovich *et al*., 2008].

4.3 Resonant Wave Excitation: The Asymptotic Time-Dependent Solution

In the previous section, it was demonstrated for the critical case where $\alpha = 1$, that very-large-amplitude wave-field excitations are predicted by the linear theory for a quasi-steady-state solution. This effect of large-amplitude wave-field excitations in the limit of merging poles corresponding to $\alpha = \omega_{ce}/2\beta\omega_{pe} = 1$ and $k_{qs} = k_{em} = \omega_{pe}/c$ (so-called double pole case) has been previously reported in [Volokitin *et al*., 1995; Volokitin *et al*., 1997] for the case of an axially-continuous and thin ($r_bk_\perp << 1$) electron beam with a

periodically modulated axial density profile. In those calculations, weak dissipation (due to collisions) [Volokitin *et al*., 1995], or nonlinear interaction between the beam electrons and the excited whistler waves [Volokitin *et al*., 1997] were assumed in order to estimate the saturated amplitude of the electromagnetic field perturbations. In the present analysis we obtain the asymptotic time-dependent solution for the wave amplitude in the linear approximation. Furthermore, we discuss a possible mechanism for saturation of the wave field intensity associated with the nonlinear response of the background plasma electrons, which can drive the system off resonance [Dorf *et al*., 2010]. Provided the beam ions are sufficiently massive, the saturation determined by this mechanism can occur before the nonlinear interaction between the beam ions and the excited whistler waves becomes important.

To describe the time evolution of the electromagnetic field perturbation excited by the ion beam pulse, we solve here an initial-value problem, making use of Laplace transforms with respect to time. Note that the temporal Fourier transform used in Sec. II yields only the steady-state solution. In this section, we assume that the initial electromagnetic field is zero everywhere, and the beam current (source) is instantaneously turned on at t=0, i.e., $j_b = Z_b e n_b (z - v_b t, x) H(t)$, where $H(t)$ is the Heaviside step function defined by H(t)=0 for t<0, and H(t)=1 for t≥0. Similar to Eq. (4.3), we obtain that the space (Fourier) - time (Laplace) transform of the perturbed transverse magnetic field is given by [Dorf *et al*., 2010]

$$\frac{eB^{y}_{\omega,\mathbf{k}}}{m_e\omega_{pe}c} = -\frac{1}{2\pi}\frac{\omega_{pe}\beta_b^3 c^3 Z_b k_z^2 k_x}{n_p\left(\omega_{pe}^2 + c^2k^2\right)}\frac{n_{\mathbf{k}}}{\left[\omega^2 - \omega_{wh}^2\left(k_x,k_z\right)\right](\omega - k_z v_b)}. \tag{4.30}$$

The inverse Laplace time transform performed in the complex ω-plane readily gives

$$\frac{eB^{y}_{\mathbf{k}}}{m_e\omega_{pe}c} = -i\frac{\omega_{pe}\beta_b^3 c^3 Z_b k_z^2 k_x n_{\mathbf{k}}}{n_p\left(\omega_{pe}^2 + c^2k^2\right)}\left[\frac{\exp\left(-ik_z v_b t\right)}{k_z^2 v_b^2 - \omega_{wh}^2} + \frac{\exp\left(-i\omega_{wh}t\right)}{2\omega_{wh}\left(\omega_{wh} - k_z v_b\right)} + \frac{\exp\left(i\omega_{wh}t\right)}{2\omega_{wh}\left(\omega_{wh} + k_z v_b\right)}\right]. \tag{4.31}$$

Note that the first term inside the brackets in Eq. (4.31) corresponds to the steady-state solution [compare with Eq. (4.16)], in which all quantities depend on t and z exclusively through the combination $\xi = z - v_b t$. The other two terms describe the time evolution of the transient excitations. Assuming a sufficiently long beam pulse, $k_z^{-1} \sim l_b >> k_{qs,em}^{-1}$, for the double-pole case corresponding to $\alpha = \omega_{ce}/2\beta_b\omega_{pe} = 1$, Eq. (4.31) takes the form

$$\frac{eB^{y}_{\mathbf{k}}}{m_e\omega_{pe}c} = -i\frac{\omega_{pe}\beta_b^3 c Z_b k_z^2 k_x n_{\mathbf{k}}}{2\omega_{wh}k_z v_b n_p}\left[-\frac{\exp\left(-i\omega_{wh}t\right) - \exp\left(-ik_z v_b t\right)}{\left(k_x - \omega_{pe}/c\right)^2} + \frac{\exp\left(i\omega_{wh}t\right) - \exp\left(-ik_z v_b t\right)}{\left(k_x + \omega_{pe}/c\right)^2}\right]. \tag{4.32}$$

The right-hand side of Eq. (4.32) has two critical points on the real k_x-axis corresponding to $k_x = \pm\omega_{pe}/c$. However, for the case where $\alpha = 1$, the dispersion relation yields $\omega_{wh}\left(\pm\omega_{pe}/c, k_z\right) = \pm k_z v_b$. Furthermore, the x-component of the group velocity is equal to zero at the critical points, $V_{gx}\left(k_x = \pm\omega_{pe}/c, k_z\right) = 0$. Therefore, the time-dependent solution in Eq. (4.32) is regular at the critical points, $k_x = \pm\omega_{pe}/c$, and

the inverse Fourier integration in k_x-space can be carried out along the real axis. Note that at large times, $\omega_{wh}t >> 1$, the contribution to the integral comes mainly from the regions near the points of stationary phase, where $\partial\omega_{wh}/\partial k_x \equiv V_{gx} = 0$, which coincide with the critical points $k_x = \pm\omega_{pe}/c$. The asymptotic time-dependant solution is then given by

$$\frac{eB_{k_z}^y}{m_e\omega_{pe}c} = -\frac{\omega_{pe}^2\beta_b Z_b e^{-ik_z v_b t}}{c^2 n_p} n_{\mathbf{k}}\left(\frac{\omega_{pe}}{c}, k_z\right)\sin\left(\frac{\omega_{pe}}{c}x\right)\int_{-\infty}^{\infty} d\Delta k_x \frac{\exp\left[i\,\mathrm{sgn}(k_z)\,\omega''_{wh}\Delta k_x^2\, t/2\right]-1}{\Delta k_x^2}, \tag{4.33}$$

where $B_{k_z}^y = \int_{-\infty}^{\infty} dk_x B_{\mathbf{k}}^y e^{ik_x x}$, $\omega''_{wh} = \left|\left[\partial^2\omega_{wh}/\partial k_x^2\right]_{k_x=\omega_{pe}/c}\right| = c^3|k_z|\beta_b/\omega_{pe}^2$, and it has been assumed that $n_{\mathbf{k}}(\omega_{pe}/c, k_z) = n_{\mathbf{k}}(-\omega_{pe}/c, k_z)$. Noting that $\int_{-\infty}^{\infty} dx\left[\exp(\pm ix^2)-1\right]/x^2 = \sqrt{2\pi}(\pm i - 1)$, we obtain [Dorf *et al*., 2010]

$$\frac{eB_y}{m_e\omega_{pe}c} = \sqrt{t}\,\frac{2\sqrt{\pi}\,\omega_{pe}v_b^{3/2}Z_b}{n_p}\sin\left(\frac{\omega_{pe}}{c}x\right)N_z(z), \tag{4.34}$$

where

$$N_z = \int_0^{\infty} dk_z\sqrt{k_z}\,n_{\mathbf{k}}\left(\frac{\omega_{pe}}{c}, k_z\right)\left[\cos(k_z\xi)+\sin(k_z\xi)\right], \tag{4.35}$$

and a symmetric beam profile with $n_{\mathbf{k}}(\omega_{pe}/c, k_z) = n_{\mathbf{k}}(\omega_{pe}/c, -k_z)$ has been assumed. Equations (4.34)-(4.35) describe the asymptotic evolution of the wave field for the double

pole case corresponding to $\alpha = \omega_{ce}/2\beta\omega_{pe} = 1$. It is readily seen from Eq. (4.34) that at sufficiently large times, $\omega''_{wh} t/r_b^2 >> 1$, the amplitude of the magnetic field is given by

$$B_y \sim \sqrt{v_b t/l_b}\, Z_b e n_b \beta_b r_b , \tag{4.36}$$

provided the beam radius is of the order of or smaller than the electron skin depth.

As the amplitude of the resonantly-excited electromagnetic field perturbation increases, nonlinear processes can provide saturation of the energy transfer from the beam to the wave field. Here, we consider a plausible mechanism to describe saturation of the wave field intensity, in which the enhanced electromagnetic field perturbation generated by the ion beam pulse modifies properties of the whistler waves, and drives the system off resonance. Indeed, as the longitudinal component of the magnetic field perturbation B_z increases, the resonance condition becomes less accurate, $\alpha_{NL} = \omega_{ce}^{NL}/2\beta_b\omega_{pe} > 1$, where $\omega_{ce}^{NL} = e(B_0 + B_z)/m_e c$. Recalling that the form of the resonant denominator is given by $1/\left(\alpha\sqrt{\alpha^2 - 1}\right)$, the normalized magnitude of the perturbed longitudinal magnetic field $\Delta\alpha \equiv (eB_z/m_e c)/\left(2\beta_b\omega_{pe}\right)$ can be estimated by $\Delta\alpha \sim Z_b \left(n_b/n_p\right)\left(r_b\omega_{pe}/c\right)\left[\left(1+\Delta\alpha^2\right)-1\right]^{-1/2}$ provided the beam radius is of the order of or smaller than the electron skin depth [see Eq. (B5)]. It now follows that the wave-field intensity saturates at the approximate level

$$\Delta\alpha \sim Z_b^{2/3} \left(n_b/n_p\right)^{2/3} \left(r_b\omega_{pe}/c\right)^{2/3} . \tag{4.37}$$

For the case of low beam density, $n_b << n_p$, this amplitude of the electromagnetic field perturbation is significantly higher compared to the case of non-resonant excitation, $\alpha > 1$, where the normalized steady-state amplitude is proportional to n_b / n_p. Finally, we emphasize that although the mechanism considered for the wave-field intensity saturation seems plausible, further detailed analytical and numerical studies are required to validate it.

The resonant excitation of whistler waves has been observed in numerical particle-in-cell simulations performed using the two-dimensional slab (x,z) version of the LSP code taking into account electromagnetic effects [Dorf *et al*., 2010]. As an illustrative example, we consider a Gaussian ion beam pulse, $n_b = 0.05 n_p \exp\left[-r^2 / r_b^2 - (z - v_b t)^2 / l_b^2 \right]$, with effective beam radius r_b=0.92c/ω_{pe}, and beam pulse half-length, l_b=9.2c/ω_{pe} (beam pulse duration $\tau_b = l_b / v_b$=27.8/ω_{pe}), propagating with velocity v_b=0.33c through a background plasma with density, $n_p = 2.4 \times 10^{11}$ cm^{-3}. In the numerical simulations, the ion beam is injected through the lower boundary of the simulation domain into an unperturbed magnetized plasma, and it propagates in the z-direction exciting electromagnetic field perturbations. Figure 4.9 shows the results of the numerical simulations for the time-evolution of the maximum value of the perturbed transverse magnetic field B_y. Note that for the parameters in this illustrative example, $\omega_{ce} \sim \omega_{pe}$ and β_b=0.33, and therefore a generalized analysis for arbitrary value of ω_{ce}/ω_{pe}

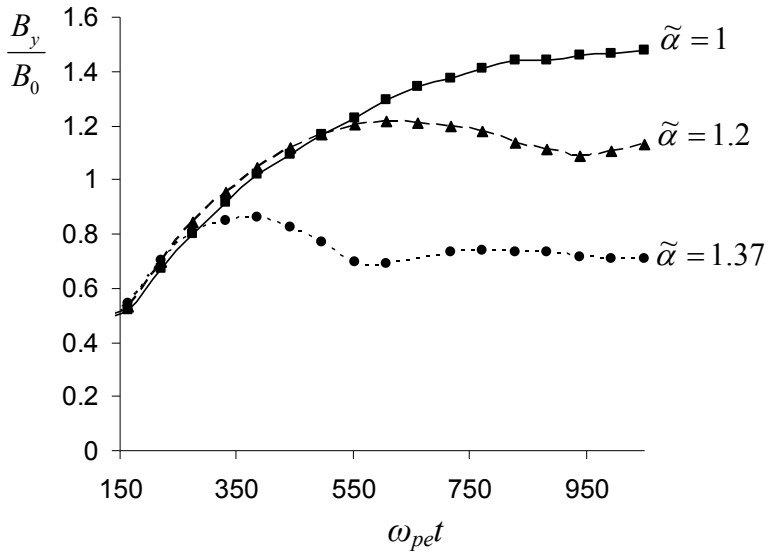

Figure 4.9: Time evolution of the maximum value of the normalized perturbed transverse magnetic field plotted for different vales of the applied magnetic field. The beam-plasma parameters correspond to Z_b=1, r_b=0.92c/ω_{pe}, l_b=9.2c/ω_{pe}, β_b=0.33, and $n_p = 2.4\times10^{11}\,\mathrm{cm}^{-3}$. The applied magnetic field corresponds to $\tilde{\alpha}=1$ (solid curve), $\tilde{\alpha}=1.2$ (dashed curve), and $\tilde{\alpha}=1.37$ (dotted curve). Results are obtained using the (x,z) slab model of the LSP code.

should be carried out in order to estimate corrections to the resonance condition. The analysis shows (see Appendix A) that the resonant excitation of the wave field should occur at $\tilde{\alpha}=\omega_{ce}\left(1-\beta_b^2\right)/\left(2\beta_b\omega_{pe}\right)=1$ [Kaganovich *et al*., 2007]. It is readily seen from Fig. 4.9 that as the magnitude of the applied uniform longitudinal magnetic field, B_{ext}, approaches the critical value corresponding to $\tilde{\alpha}=1$, the saturation amplitude of the perturbed magnetic field increases, as well as the time interval required to achieve a quasi-steady-state. Note that the perturbed transverse magnetic field shown in Fig. 4.9 is

normalized to the magnetic self-field of an unneutralized beam, $B_0 = 4\pi n_{b0} Z_b e \beta_b r_b$. It is evident, for the quasi-steady-state regime, that the beam current is unneutralized, $B_y \sim B_0$, which is consistent with the analysis performed in Sec. 4.2.4.

Finally, it should be noted that the effect of resonant large-amplitude wave field excitations can be utilized for diagnostic purposes in experiments where an ion beam pulse propagates through a background plasma along an applied solenoidal magnetic field [Dorf *et al*., 2010]. Indeed, measuring the perturbed azimuthal magnetic field, for instance, in the vicinity of the chamber wall, it can be expected to obtain the following dependence on the value of the applied magnetic field. First, at low values of the applied magnetic field, $\alpha = \omega_{ce} / 2\beta_b \omega_{pe} < 1$, the wave-field component of the electromagnetic field perturbation is not excited, and the excited signal is exponentially small. As the magnetic field increases, and the threshold value of $\alpha = \omega_{ce} / 2\beta_b \omega_{pe} = 1$ is reached, a large-amplitude signal corresponding to resonant wave excitation will be detected. Finally, further increase in the magnitude of the applied magnetic field, $\alpha = \omega_{ce} / 2\beta_b \omega_{pe} > 1$, will lead to a decrease in the amplitude of the excited signal. Provided the directed beam velocity is known, this diagnostic can be used, for instance, for passive measurements of the background plasma density. Indeed, determining the threshold magnitude of the applied magnetic field, B_c, from the experimental data, the plasma density can be readily obtained from $\omega_{pe} = \omega_{ce}(B_c) / 2\beta_b$.

4.4 Comparison of Analytical Theory with Numerical Simulations

In this section we present the results of the numerical simulations performed with the particle-in-cell (PIC) code LSP and compare it with the analytical solutions described in Sec. 4.2 [Dorf *et al*., 2010]. Figure 4.10(a) shows the results obtained with the 2D slab (x,z) version of the code for the amplitude of the y-component of the perturbed magnetic field, when a quasi-steady-state is reached. The corresponding analytical solution [Eqs. (A1)-(A7)] is shown in Fig. 4.10(b). The following parameters have been used for this illustrative example: $n_b = 0.05 n_p \exp\left[-r^2/r_b^2 - (z - v_b t)^2/l_b^2\right]$, r_b=0.92c/ω_{pe}, l_b=10r_b (beam pulse duration τ_b=l_b/v_b=27.8/ω_{pe}), v_b=0.33c, $n_p = 2.4\times10^{11}$ cm^{-3}, and B_{ext}=1600 G . It is readily seen from Figs. 4.10(a) and 4.10(b) that the results of the numerical simulations and analytical theory are found to be in very good agreement. Indeed, the characteristic amplitude of the electromagnetic field perturbation, wavelength, angle of the propagation, etc., are quite similar.

In addition, to verify the approximate analytical solution specified by Eqs. (A1)-(A7), we first solved Eq. (4.11) for arbitrary values of ω/ω_{ce} , ω/ω_{pe} , and ω_{pe}/ω_{ce} , and then numerically calculated the inverse *fast* Fourier transforms (FFT). Note that in the regime where a wave field is excited, the Fourier transforms of the perturbed electromagnetic fields contain singularities in real (k_x,k_z)-space. Therefore, the numerical integration of the fast Fourier transforms performed along the real k_x- and k_z- axes would

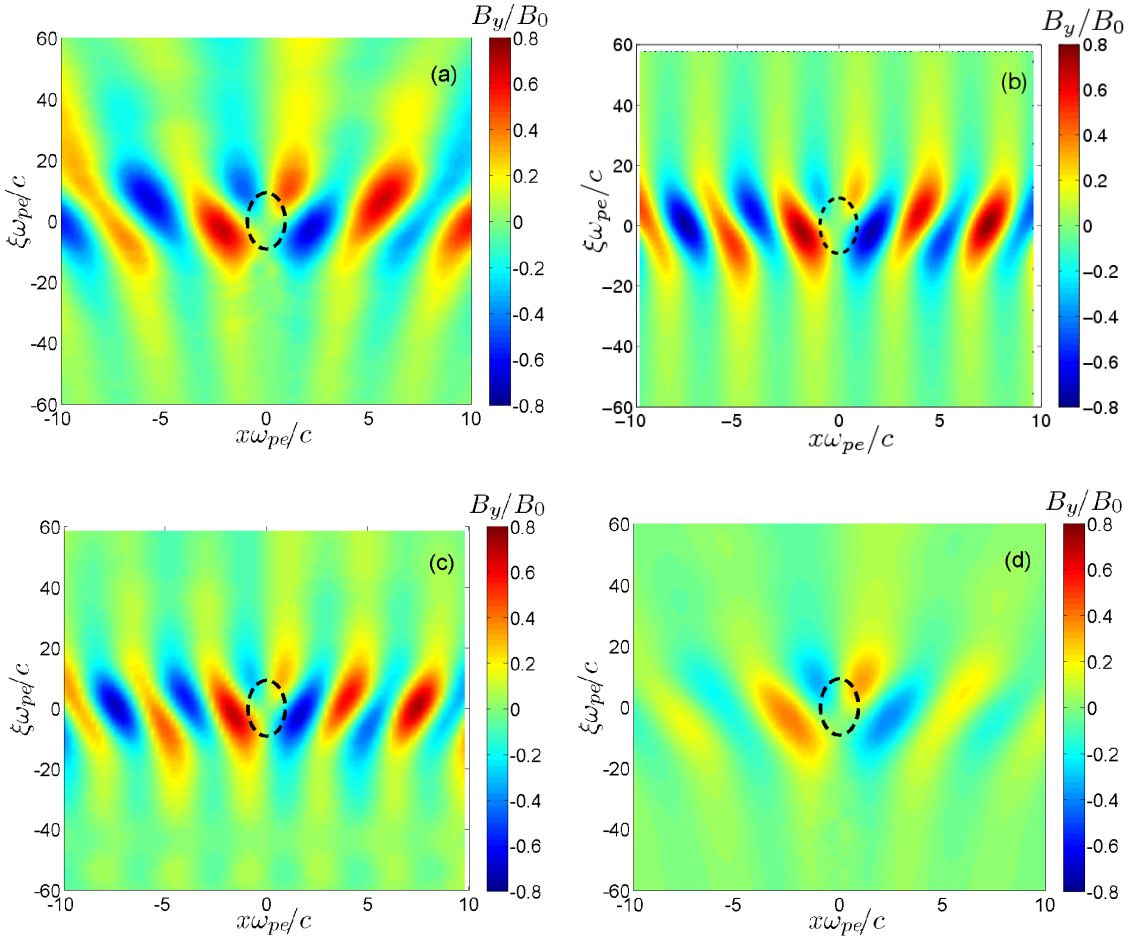

Figure 4.10: (Color) Plots of the steady-state amplitude of the transverse magnetic field perturbation B_y. The beam-plasma parameters correspond to Z_b=1, r_b=0.92c/ω_{pe}, l_b=10r_b, β_b=0.33, and n_p =2.4×10^{11} cm^{-3}. The applied magnetic field, B_{ext}=1600 G, corresponds to $\alpha=\omega_{ce}/(2\beta_b\omega_{pe})$=1.54. The Frames correspond to: (a) results of numerical simulations obtained using the (x,z) slab version of the LSP code; (b) the analytical solution given by Eqs. (A1)-(A7); (c) numerical calculation of fast Fourier transforms, assuming weak collisions $\nu=0.005/\tau_b$; and (d) the results of numerical simulations obtained using the (r,z) cylindrical version of the LSP code. The dashed lines correspond to contours of constant beam density corresponding to the effective beam radius r_b.

diverge. To remove the singularities from the real axis, weak collisions have been assumed for the plasma electron response. Correspondingly, the components of the dielectric tensor, $\vec{\varepsilon}$, should be modified according to $\varepsilon_{xx} = \varepsilon_{yy} = 1 - \omega_{pe}^2 (\omega + i\nu) \Big/ \left[\omega \left((\omega + i\nu)^2 - \omega_{ce}^2 \right) \right]$, $\varepsilon_{zz} = 1 - \omega_{pe}^2 \Big/ \left[\omega (\omega + i\nu) \right]$, and $\varepsilon_{xy} = -\varepsilon_{yx} = i\,\omega_{pe}^2 \omega_{ce} \Big/ \left[\omega \left((\omega + i\nu)^2 - \omega_{ce}^2 \right) \right]$, where ν is the effective collision frequency. In the limit of zero collision frequency, the numerical fast Fourier transforms calculation should yield the analytical solutions given in Eqs. (A1)-(A7). The results obtained in the numerical fast Fourier transforms calculation for the case of weak dissipation, $\nu = 0.005/\tau_b$, demonstrate very good agreement with the analytical solution [compare Fig. 4.10(b) and Fig 4.10(c)].

It is of particular interest to compare the results obtained for the case of (*x*,*z*) slab geometry [Figs. 4.10(a) – 4.10(c)] to the case of cylindrical (*r*,*z*) geometry. The results of the numerical simulation obtained using the 2D (*r*,*z*) cylindrical version of the LSP code for the same system parameters are shown in Fig. 4.10(d). Results of the (*r*,*z*) LSP simulations demonstrate similar wavelength and propagation angle for the excited wave field. However, the amplitude of the perturbed electromagnetic field is smaller. Furthermore, it decays more rapidly outside the beam pulse, compared to the case of the slab beam pulse [compare Fig. 4.10(a) and 4.10(d)]. Note for an infinitely long beam that the amplitude of an excited electromagnetic field decreases as 1/*r* for the case of cylindrical geometry, and does not decrease for the case of 2D slab geometry. This can

provide a plausible explanation of the difference in the wave-field amplitude observed in cylindrical and slab geometries.

4.5 Self-Focusing of an Intense Ion Beam Pulse

In this section, making use of Eqs. (4.20)-(4.25), we calculate the transverse component of the Lorentz force, $F_x = Z_b eE_x - Z_b e\beta_b B_y$, acting on the beam particles. In Sec. 4.2 it has been shown that the excited wave field perturbations propagate oblique to the beam with characteristic longitudinal wave number $k_z \sim l_b^{-1}$. Therefore, the contribution of the wave-field component to the total Lorentz force can have opposite signs for the beam head and the beam tail. That is, it produces a focusing effect in the beam head and a defocusing effect in the beam tail, or *vice versa*. In contrast, the longitudinal profile of the local-field amplitude is the same as the longitudinal beam density profile (see Sec. 4.2.2). Therefore, the local fields provide a focusing (or defocusing) effect over the entire length of the ion beam pulse. It is therefore important, in practical applications involving control over the beam aperture, to identify the parameter regimes where the local component of the electromagnetic field perturbation has the dominant influence on the beam transverse dynamics.

This section is organized as follows. In Sec. 4.5.1 regimes of dominant influence of local fields on the beam transverse dynamics are identified and the transverse component of the self-focusing force is calculated. Properties of the self-focusing force

are investigated in Sec. 4.5.2. In particular for the case where $r_b << c/\omega_{pe}$, it is shown that the collective self-focusing force acting on the beam particles in the presence of a weak solenoidal magnetic field can be significantly stronger than the self-pinching force in the limit B_{ext}=0. Also, the influence of the self-focusing effects on the beam dynamics in NDCX-I and NDCX-II is assessed. Properties of the local plasma response are discussed in Sec. 4.5.3. Finally, the self-focusing force is obtained for the case of cylindrical (*r*,*z*) geometry making use of the slice approximation in Sec. 4.5.4, and the possibility of using an electrostatic model for describing plasma response and transverse beam dynamics is discussed in Sec. 4.5.5.

4.5.1 Dominant Influence of Local Fields

It has been demonstrated in Secs. 4.2.3 and 4.3 for the critical case where $\alpha = 1$, that a large-amplitude wave field is exited. Here, we consider the case where $\alpha >> 1$ ($\omega_{ce} >> 2\beta_b \omega_{pe}$). Furthermore, we assume $r_b >> k_{qs}^{-1}$, or equivalently, $r_b >> c/(2\alpha\omega_{pe})$ in the limit where $\alpha >> 1$. This implies an exponentially small level of the short-wavelength, quasi-electrostatic wave excitations for the case of a smooth radial beam density profile. Making use of Eqs. (4.20)-(4.23), it is straightforward to show for the case where $r_b >> k_{qs}^{-1}$, that the contribution of the wave-field component of the electromagnetic field perturbation to the transverse Lorentz force is given approximately by [Dorf *et al*., 2010]

$$F_x^W = Z_b e\left(E_x^W - \beta_b B_y^W\right) \approx 2\pi Z_b^2 \frac{m_e V_b^2}{R} \frac{1-\left(4\alpha^2-1\right)k_{em}^2 c^2/\omega_{pe}^2}{4\alpha\sqrt{\alpha^2-1}}, \tag{4.38}$$

where

$$\frac{1}{R} = \frac{\omega_{pe}^2}{c^2}\frac{1}{n_p}\int_0^\infty dk_z n_{\mathbf{k}}\left(k_{em}, k_z\right)\cos\left[k_z\xi + k_{em}x\right]. \tag{4.39}$$

Recall, for $\alpha >> 1$, that the characteristic wave vector for the excited long-wavelength electromagnetic wave field is given by $k_{em} = \omega_{pe}/2\alpha c$, and therefore the wave field contribution to the Lorentz force vanishes for $\alpha >> 1$. To obtain the local field contribution, it is convenient to represent the local fields specified by Eqs. (4.24)-(4.25) in the following form

$$e\beta_b B_y^{loc} = -iZ_b m_e v_b^2 \int d\mathbf{k} \frac{k_x\left(k_x^2 + \omega_{pe}^2/c^2\right)n_{\mathbf{k}} e^{ik_x x + ik_z\xi}}{4\alpha\sqrt{\alpha^2-1}n_p}\left[\frac{1}{k_x^2 - k_{qs}^2} - \frac{1}{k_x^2 - k_{em}^2}\right], \tag{4.40}$$

$$eE_x^{loc} = -iZ_b m_e v_b^2 \int d\mathbf{k} \frac{\alpha k_x^3 n_{\mathbf{k}} e^{ik_x x + ik_z\xi}}{\sqrt{\alpha^2-1}n_p}\left[\frac{1}{k_x^2 - k_{qs}^2} - \frac{1}{k_x^2 - k_{em}^2}\right]. \tag{4.41}$$

For the case where

$$\alpha >> 1 \text{ and } r_b >> k_{qs}^{-1} = \frac{c}{2\alpha\omega_{pe}} \tag{4.42}$$

we can neglect by the first terms inside the brackets in Eqs. (4.40) and (4.41), and after some straightforward algebra we obtain that the local field contribution, which constitutes most of the transverse Lorentz force, is given by [Dorf *et al*., 2010]

$$F_x \approx Z_b e E_x^{loc} - Z_b e \beta_b B_y^{loc} = Z_b^2 m_e v_b^2 \frac{1}{n_p} \frac{dn_b}{dx}. \tag{4.43}$$

The analysis in Appendix A, performed for an arbitrary ratio of ω_{ce}/ω_{pe}, shows that for the case of a nonrelativistic ion beam the Lorentz force is still given by Eq. (4.43), provided

$$\alpha >> 1 \quad \text{and} \quad r_b >> \tilde{k}_{qs}^{-1} = \left(1 + \omega_{ce}^2/\omega_{pe}^2\right)^{1/2} \frac{c}{2\alpha\omega_{pe}}. \tag{4.44}$$

Note that the transverse component of the Lorentz force [Eq. (4.43)] is proportional to the gradient of the beam density. Therefore, for the case of a bell-shaped beam density profile, self-focusing of the beam occurs. Furthermore, it is interesting to note that an annular beam will not pinch to the axis provided the beam dynamics is governed by the force in Eq. (4.43). However, the outer beam radius will decrease and the inner beam radius will increase, resulting in a decrease in the thickness of the annulus and an increase in the beam density. Also, note that the self-focusing in Eq. (4.43) can very effectively balance the ion beam thermal pressure, which is also proportional to the gradient of the beam density

Although the total influence of the magnetic and electric field components, B_y^W and E_x^W, of the wave field perturbation results in a destructive interference in estimating the transverse Lorentz force [see Eq. (4.38)], it is of particular interest to estimate the separate contribution of the wave field component to the Lorentz force, and compare it to the contribution of the local field component. For illustrative purposes, we consider here

a Gaussian beam density profile with $n_{\mathbf{k}} = (r_b l_b/4\pi) n_{b0} \exp\left[-r_b^2 k_x^2/4 - l_b^2 k_z^2/4\right]$. Making use of Eqs. (4.20)–(4.23), it is straightforward to show that the contribution of the wave field component can be estimated by [Dorf *et al*., 2010]

$$eE_x^W \sim e\beta_b B_y^W \sim Z_b m_e v_b^2 \frac{\omega_{pe}^2 r_b}{\alpha^2 c^2} \frac{n_{b0}}{n_p} \exp\left(-\frac{r_b^2 k_{em}^2}{4}\right), \tag{4.45}$$

provided the conditions in Eq. (4.42) are satisfied. Similar expressions can be obtained for the local fields using Eqs. (4.40)-(4.41), i.e.,

$$eE_x^{loc} \sim Z_b m_e v_b^2 \frac{n_{b0}}{r_b n_p} \frac{1}{\max\left(1, k_{em}^2 r_b^2\right)}, \tag{4.46}$$

$$e\beta_b B_y^{loc} \sim Z_b m_e v_b^2 \frac{n_{b0}}{\alpha^2 r_b n_p} \frac{\max\left(1, \omega_{pe}^2 r_b^2/c^2\right)}{\max\left(1, k_{em}^2 r_b^2\right)}, \tag{4.47}$$

It readily follows from Eqs. (4.45)-(4.47), for the case where the beam radius is small compared to the wavelength of the long-wavelength electromagnetic waves, $r_b k_{em} << 1$, that the *local electric field* has the dominant contribution to the transverse component of the Lorentz force. As the beam radius increases and becomes of order the electromagnetic wave-field wavelength, $r_b k_{em} \sim 1$, the separate contributions from all components of the perturbed electromagnetic field become of the same order, i.e., $E_x^{loc} \sim E_x^W \sim \beta_b B_x^{loc} \sim \beta_b B_x^W$. With a further increase in the beam radius, $r_b k_{em} >> 1$, the *local magnetic field* contribution becomes dominant, and both the quasi-electrostatic and long-wavelength electromagnetic wave-field components are exited to exponentially small levels for the case of a smooth beam density profile.

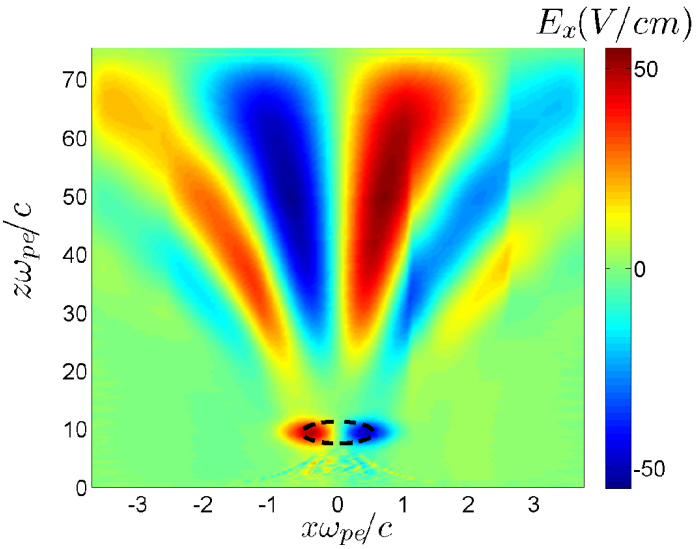

Figure 4.11: (Color) Plot of the perturbed transverse self-electric field corresponding to t_s=8.1 τ_b=54 ns. The system parameters correspond to Z_b=1, r_b=0.55c/ω_{pe}, τ_b=75/ω_{pe}, β_b=0.05, B_{ext}=300 G, and $\alpha=\omega_{ce}/2\beta_b\omega_{pe}$=9.35. The results are obtained using the 2D (x,z) version of the LSP code. The dashed curve corresponds to the contour of constant beam density corresponding to the effective beam radius r_b.

The time evolution of the electromagnetic field perturbation for the case where $\alpha >> 1$ and $k_{qs}^{-1} << r_b << k_{em}^{-1}$, which corresponds to a dominant influence of the local self-electric field, has been studied using the LSP simulation code. Figure 4.11 shows a plot of the perturbed transverse self-electric field at the simulation time t_s=8.1 τ_b =54 ns. The beam-plasma parameters considered for this illustrative example correspond to $n_b = 0.13 n_p \exp\left[-r^2/r_b^2 - (z - v_b t)^2/l_b^2\right]$, n_p=10^{10}cm^{-3}, Z_b=1, r_b=0.55c/ω_{pe}, τ_b=37.5/ω_{pe}, β_b=0.05, B_{ext}=300 G, and $\alpha=\omega_{ce}/2\beta_b\omega_{pe}$=9.35. The wave structure in front of the beam pulse corresponds to a transient wave-field perturbations associated with the initial beam

penetration into the plasma through the boundary at $z = 0$. Note that these transient perturbations do not interact with the ion beam pulse effectively, because they do not satisfy the Cherenkov criteria in Eq. (4.17). Therefore, the energy content in the corresponding wave field is attributed only to the initial beam penetration into the plasma, and is not related to the beam energy later in time. As the transient wave-field perturbations leave the beam on the characteristic time scale $\tau_s \sim \min\{r_b/V_{gx},\ l_b/|V_{gz}-v_b|\}$ (see Sec. 4.2.3), the local component of the self-electric field exhibits the dominant influence on the ion beam transverse dynamics, as evident from Fig. 4.11. The intensity of the excited wave field satisfying the condition in Eq. (4.17) is negligible, which is consistent with the analytical calculations performed in this section.

4.5.2 Enhanced Ion Beam Self-Focusing

In Sec. 4.3.1, it was demonstrated for the case where $\alpha = \omega_{ce}/2\beta_b\omega_{pe} >> 1$ and $r_b >> c/(2\alpha\omega_{pe})$, that the local fields have the dominant influence on the transverse dynamics of the ion beam particles. In this regime, focusing is provided over the entire length of the beam pulse and the corresponding self-focusing force acting on the beam ions is specified by Eq. (4.43). It is of particular interest to compare this self-focusing force to the self-pinching force acting on the ion beam particles for the case where the ion beam pulse propagates through an unmagnetized plasma, i.e., B_{ext}=0 [Dorf *et al*., 2009c]. Indeed, even for this simple case the beam charge is typically better neutralized than the beam current, and the self-pinching force is produced by the net self-magnetic field (see

Sec. 4.1.1). This self-pinching can be utilized for a variety of applications, including self-pinched ion beam transport [Ottinger *et al*., 2000], and heavy ion beam focusing [Hahn and Lee, 1996]. Note that for the case where B_{ext}=0, the beam current is almost unneutralized in the limit where the beam radius is small compared to the electron skin depth, $r_b << c/\omega_{pe}$. Therefore, the self-pinching effect is a maximum in this regime, and the transverse component of the self-pinching force is given by

$$F_0 \cong -Z_b e \beta_b B_y = -\frac{4\pi}{c^2} Z_b^2 e^2 v_b^2 \int_0^x n_b dx \tag{4.48}$$

For the case where $r_b << c/\omega_{pe}$, the ratio of the collective self-focusing force in the presence of an applied magnetic field [Eq. (4.43)] to the self-pinching force, F_0, in the limit B_{ext}=0 case, can be estimated as $F_x / F_0 \sim \left(c/r_b \omega_{pe}\right)^2 >> 1$ [Dorf *et al*., 2009c]. That is, the self-focusing of an ion beam pulse propagating through a neutralizing plasma can be significantly enhanced by the application of a solenoidal magnetic field satisfying $\alpha = \omega_{ce}/2\beta_b \omega_{pe} >> 1$. Here, we emphasize again that the threshold value $\alpha_{cr} = 1$ typically corresponds to a weak magnetic field (see Sec. 4.1). Also recall, that he condition $r_b << c/\omega_{pe}$ can be rewritten in terms of the beam current I_b as $I_b << 4.25\beta_b \left(n_b/n_p\right)$kA . Note that for a typical ion beam injector aperture of the order of 1 cm, the beam radius (~ 1 cm) is small compared to the electron skin depth provided the beam and plasma density are in the range of $n_b < n_p < 2.8\times 10^{11}/(r_b[cm])^2\, cm^{-3}$, which are typical parameters for several beam transport applications [Roy *et al*, 2005; Seidl *et*

al., 2009; Friedman *et al*., 2009]. Therefore, this self-focusing enhancement can be of considerable practical importance.

As a practical example, here we consider parameters characteristic of the present Neutralized Drift Compression Experiment (NDCX-I) [Seidl *et al*., 2009] and its future upgrade NDCX-II [Friedman *et al*., 2009], which are designed to study the energy deposition from the intense ion beam onto a target. The experiments involve neutralized compression of an intense ion beam pulse with radius r_b~1 cm as it propagates through a long drift section with length L_d~200 cm filled with a background plasma with density n_p~10^{11} cm^{-3}. As it exits the drift section, the beam passes through a strong magnetic lens with magnetic field B_s=8 T, and length L_s~10cm, which provides additional transverse focusing. For the currently operating NDCX-I experiment, typical beam parameters correspond to $\beta_b^I = 0.004$, $m_i^I = 39$ a.u., $Z_b^I = 1$. The planned NDCX-II experiment is aimed at operating at higher beam energies: $\beta_b^{II} = 0.032$, $m_i^{II} = 7$ a.u., $Z_b^{II} = 1$. The corresponding values of the critical magnetic field are given by $B_c^I = 65$ G and $B_c^{II} = 8$ G, for NDCX-I and NDCX-II parameters, respectively. The fringe magnetic field of the strong magnetic lens can penetrate deeply into the drift section at a magnitude much larger than $B_c^{I,II}$, thus providing conditions for enhanced self-focusing for both NDCX-I and NDCX-II. Moreover, the integrated effect of the beam self-focusing inside the drift section filled with the background plasma can become comparable to the focusing effect of the strong magnetic lens. Introducing the dimensionless parameters $\delta = F_{sf} L_d / F_s L_s$,

where $F_s \sim m_b \omega_{cb}^2 r_b / 4$ is the magnetic focusing force acting on the beam ions inside the lens, and $F_{sf} \sim m_e v_b^2 / r_b$ is the self-focusing force ($n_b \sim n_e$ is assumed), we readily obtain $\delta^I = 0.04$ and $\delta^{II} = 0.5$ for the parameters characteristic of NDCX-I and NDCX-II respectively. Here, m_b and ω_{cb} are the ion beam mass and cyclotron frequency, respectively. Therefore, the plasma-induced collective focusing effect in a several hundred gauss magnetic field can become comparable to the focusing effect of a strong 8 Tesla final focus solenoid for the design parameters characteristic of NDCX-II.

The enhancement of the self-focusing force in the presence of a weak applied magnetic field has been observed in electromagnetic particle-in-cell simulations performed using the 2D (x,z) slice version of the LSP code [Dorf *et al*., 2010]. As an illustrative example, we consider a Gaussian ion beam pulse, $n_b = 0.13 n_p \exp\left[-r^2 / r_b^2 - (z - v_b t)^2 / l_b^2 \right]$, with effective beam radius, $r_b = 0.55 c/\omega_{pe}$, and beam pulse half-length, $l_b = 1.875 c/\omega_{pe}$ (beam pulse duration $\tau_b = 37.5/\omega_{pe}$), propagating with velocity $v_b = 0.05c$ through a background plasma with density $n_p = 10^{10}$ cm^{-3}. The results of the numerical simulations shown in Fig. 4.12 demonstrate the significant (~10 times) enhancement of the transverse component of the Lorentz force due to an applied magnetic field of $B_{ext} = 300$ G. Figure 4.12 shows the *total* transverse focusing force (i.e., the sum of the magnetic and electric component of the Lorentz force) acting on the beam ions in the presence of an applied magnetic field (green, blue, and pink curves), and for the case where an external magnetic field is not applied (purple curve). The units of the electric field, *V/cm*, are chosen for practical representation of its numerical value. Note

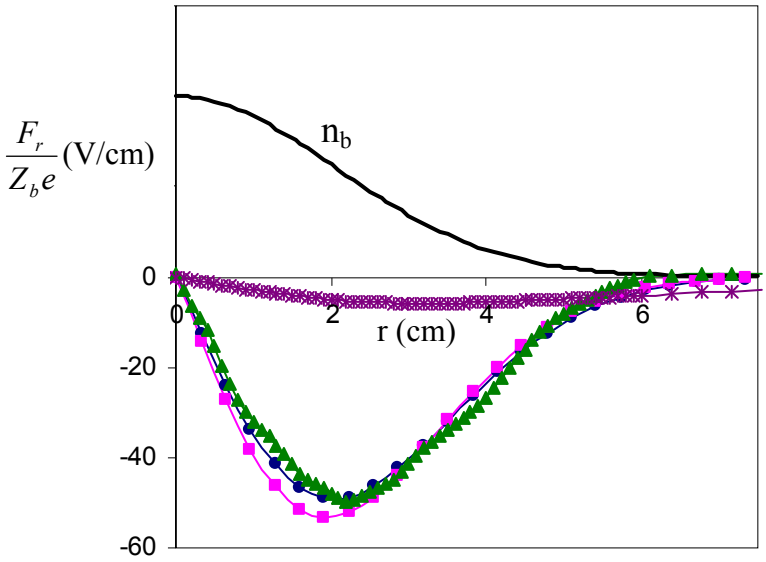

Figure 4.12: (Color) Radial dependence of the normalized focusing force at the beam center. The results of the numerical simulations correspond to B_{ext}=300 G and $\alpha=\omega_{ce}/2\beta_b\omega_{pe}$=9.35 (green curve), and ω_{ce}=0 (purple curve). The analytical results in Eq. (4.43), are shown by the blue curve, the pink curve demonstrates the analytical predictions obtained by performing integration in Eqs. (A1)-(A7). The beam-plasma parameters correspond to Z_b=1, $r_b=0.55c/\omega_{pe}$, $\tau_b=75/\omega_{pe}$, β_b=0.05, and $n_p=10^{10}$ cm^{-3}. The black curve corresponds to the radial beam density profile.

that the results of the numerical simulations are found to be in very good agreement with the approximate analytical solution given by Eq. (4.43) (blue curve), and with the more accurate analytical solutions given by Eqs. (A1)-(A7) (pink curve).

4.5.3 Properties of the Local Plasma Response

As demonstrated above, the local component of the self-electric field provides the dominant contribution to the transverse Lorentz force for the case where $\alpha = \omega_{ce}/2\beta_b\omega_{pe} >> 1$ and $k_{qs}^{-1} << r_b << k_{em}^{-1}$ (or equivalently, $c/2\alpha\omega_{pe} << r_b << 2\alpha c/\omega_{pe}$). Form Eq. (4.43) it now readily follows that

$$Z_b e E_x \approx Z_b^2 m_e v_b^2 \frac{1}{n_p}\frac{dn_b}{dx}, \tag{4.49}$$

and therefore, for the case of a bell-shaped beam density profile, the transverse electric self-field produces a focusing effect on the ion beam pulse. This implies that a positive charge of the ion beam pulse becomes *over-compensated* by the background plasma electrons [Dorf *et al*., 2009c]. In the same parameter regime, the *z*-component of the magnetic field perturbation is specified by (see Appendix B)

$$\frac{eB_z^{loc}}{m_e\omega_{pe}c} \approx -\frac{Z_b\beta_b^2\omega_{pe}}{\omega_{ce}n_p} n_b(x,z), \tag{4.50}$$

indicating a diamagnetic plasma response.

As noted earlier a defocusing self-electric field and a paramagnetic plasma response were found for the case where $\alpha < 1$ (Sec. 4.1.2). This means that the qualitatively different local plasma responses for the cases where $\alpha < 1$ and $\alpha > 1$ are separated by the critical case where $\alpha = 1$, corresponding to resonant excitation of large-amplitude wave-field perturbations.

The analytical calculation demonstrating the dramatic change of the local plasma response with an increase of an applied magnetic field has also been verified by the results of 2D (x,z) LSP simulations (Fig. 4.13) [Dorf *et al*., 2010]. The parameters chosen for the illustrative example in Fig. 4.13 correspond to $n_b = 0.13 n_p \exp\left[-r^2/r_b^2 - (z - v_b t)^2/l_b^2\right]$, r_b=0.55c/ω_{pe}, l_b=1.875c/ω_{pe}, v_b=0.05c, and n_p=10^{10} cm^{-3}. One can readily see that the paramagnetic plasma response [Fig. 4.13(b)], and the defocusing effect of the transverse self-electric field [Fig. 4.13(a)] for the case where $\alpha = 0.78$, change to a diamagnetic plasma response [Fig. 4.13(d)] and a focusing effect of the self-electric field [Fig. 4.13(c)] for $\alpha = 9.35$. Note that the longitudinal oscillations in Fig. 4.13(a) are an artifact of the numerical code, and a smooth longitudinal dependence can be obtained by increasing the space-time resolution along with the number of macro-particles. Figures 4.13(e) and 4.13(f) show the approximate analytical solutions for the transverse component of the electric field [Eq. (4.49)], and the longitudinal component of the magnetic field [Eq. (4.50)], respectively. Finally, note that the magnitude of the transverse electric field perturbation is significantly increased by an increase in the applied magnetic field [compare Figs. 4.13(a) and 4.13(c)]. This strong transverse electric field provides the enhanced ion beam focusing, as discussed above.

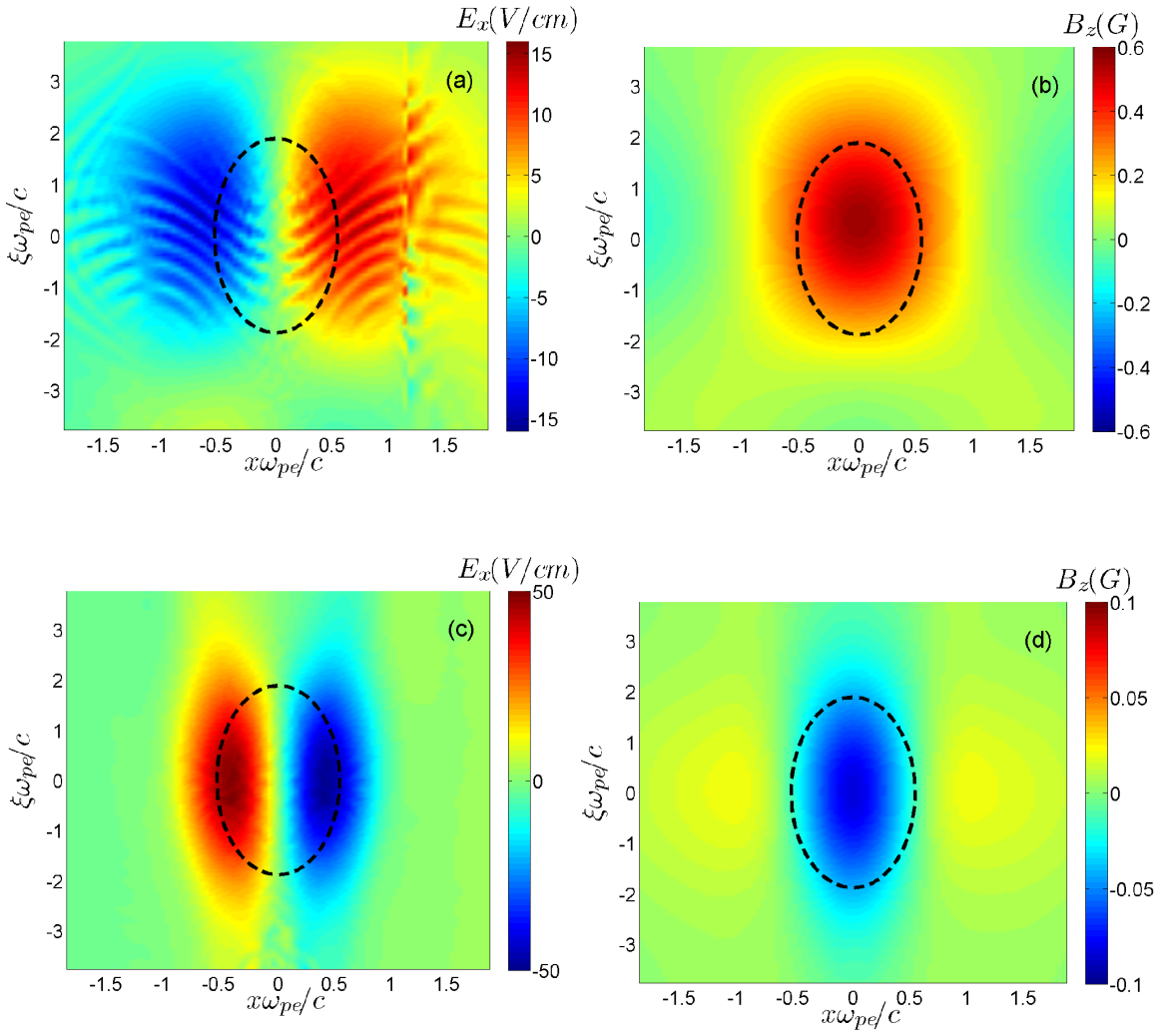
$E_x(V/cm)$
(a)
$B_z(G)$
(b)
(c)
(d)
$\xi\omega_{pe}/c$
$x\omega_{pe}/c$

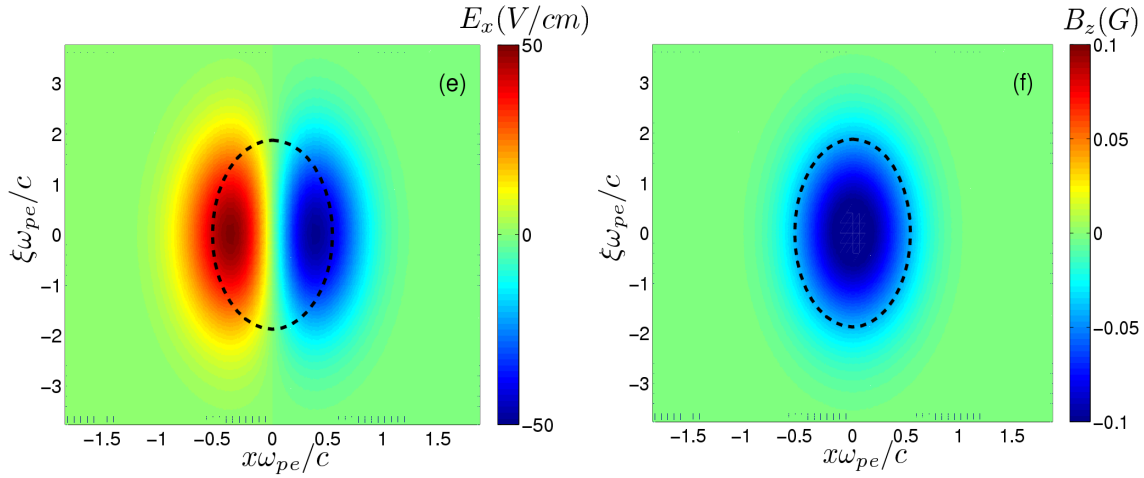

Figure 4.13: (Color) Plots of the transverse self-electric field (left) and longitudinal self-magnetic field (right) of an ion beam pulse with Z_b=1, r_b=0.55c/ω_{pe}, l_b=1.875c/ω_{pe}, and v_b=0.05c propagating through a background plasma with n_p=10^{10} cm^{-3} along a solenoidal magnetic field. Frames (a) and (b) correspond to the results of 2D (x,z) LSP simulations for B_{ext}=25 G. Frames (c) and (d) correspond to the results of 2D (x,z) LSP simulations for B_{ext}=300 G. Frames (e) and (f) correspond to the approximate analytical solutions given by Eq. (4.49) and Eq. (4.50), respectively. Note the significantly different local plasma responses between the cases where α=0.78 [Frames (a) and (b)] and α=9.35 [Frames (c) and (d)]. Dashed lines correspond to contours of constant beam density corresponding to the effective beam radius r_b.

4.5.4 Slice Model for Enhanced Self-Focusing

In the previous section (Sec. 4.5.1) we have demonstrated the dominant influence of the local fields for the case where $\alpha >> 1$ and $r_b k_{qs}^{-1} >> 1$. Also, as noted earlier (Sec. 4.2.2) the axial dependence of the local fields is determined solely by the beam density axial profile, that is $\left(E^{loc}, B^{loc}\right) = n_z(z - v_b t)\Phi_{E,B}(x)$, and it is therefore appealing to make use of the reduced slice model (Sec. 4.1.2) for description of local fields. A simplified calculation of the collective focusing force based on the slice model has been performed in [Dorf *et al*., 2009c] for the case of cylindrical (*r,z*) geometry. It is instructive to reproduce that analysis here, since it is more intuitive and allows one to obtain the expression for the self-focusing force [Eq. (4.43)] and the conditions for its validity [Eq. (4.44)] avoiding the tedious calculations required for the general analysis of the excited electromagnetic field perturbations (Sec. 4.2).

For the case of cylindrical geometry the radial component of the Lorentz force is specified by

$$F_r = Z_b e\left(E_r - \beta_b B_\varphi\right) \tag{4.51}$$

Here, B_φ and E_r are the azimuthal component of the self-magnetic field, and the radial component of the self-electric field, respectively. As before (Sec. 4.2), here we assume immobile plasma ions, cold plasma electrons, and investigate the axisymmetric steady-state solution, where all quantities depend on t and z solely through the combination $\xi = z - v_b t$. Assuming that the beam density is small compared to the electron density ($n_b << n_e$),

we solve for the collisionless linear plasma response, in which the nonrelativistic plasma electron dynamics is governed to leading order by

$$m_e v_b \frac{\partial \mathbf{V_e}}{\partial \xi} = \frac{e}{c}[\mathbf{V_e} \times \mathbf{B_{ext}}] + e\mathbf{E} \,. \tag{4.52}$$

Here, $\mathbf{V_e}$ is the electron flow velocity and we have made use of $\partial/\partial t = -v_b \, \partial/\partial \xi$ for the steady-state electron response. Applying the curl operator to the both sides of Eq. (4.52) and making use of Faraday law, we readily obtain

$$m_e v_b \frac{\partial}{\partial \xi}\left(\nabla \times \mathbf{V_e} - \frac{e}{m_e c}\mathbf{B} \right) = \frac{e}{c} \nabla \times [\mathbf{V_e} \times \mathbf{B_{ext}}]. \tag{4.53}$$

In cylindrical coordinates the φ-component of Eq. (4.53) yields

$$m_e v_b \frac{\partial V_{ez}}{\partial r} = -\frac{e}{c} B_{ext} V_{e\varphi} - \frac{e}{c} B_\varphi v_b + m_e v_b \frac{\partial V_{er}}{\partial \xi} \,, \tag{4.54}$$

and the radial component of Eq. (4.52) is

$$m_e v_b \frac{\partial V_{er}}{\partial \xi} = \frac{e}{c} B_{ext} V_{e\varphi} + eE_r \,. \tag{4.55}$$

Using Eqs. (4.54) and (4.55) to determine $E_r - \beta_b B_\varphi$, we find that the radial component of the Lorentz force in Eq. (2) is given by

$$F_r = Z_b e E_r - \frac{Z_b e}{c} v_b B_\varphi = Z_b m_e v_b \frac{\partial V_{ez}}{\partial r} \,. \tag{4.56}$$

For the case where the beam current is fully neutralized, i.e., $n_e V_{ez} = Z_b n_b v_b$, Eq. (4.56) takes on the simple form

$$F_r = Z_b^2 m_e v_b^2 \frac{1}{n_e}\frac{dn_b}{dr}\,. \tag{4.57}$$

Note that Eq. (4.57) is equivalent to Eq. (4.43) obtained in Sec. 4.5.1, where the the radial coordinate, r, is replaced with transverse coordinate, x.

In order to find the conditions for the beam current neutralization, here we make use of the slice model (Sec. 4.1.2) specified by Eqs. (4.6)-(4.10). Taking the radial derivative of Eq. (4.6) and making use of equations (4.7), (4.9) and (4.10) we obtain [Dorf *et al*., 2009c]

$$-\frac{\partial}{\partial r}\left(\frac{1}{r}\frac{\partial}{\partial r}\left(r\frac{\partial A_z}{\partial r}\right)\right)=\frac{4\pi}{c}\frac{\partial j_z}{\partial r}=\frac{4\pi e}{c}Z_b v_b \frac{dn_b}{dr}+\frac{1}{r_{ge}^2}\frac{\partial A_z}{\partial r}+\frac{v_b\omega_{pe}^2}{c^2\omega_{ce}r_{ge}^2}A_\varphi-\frac{\partial}{\partial r}\left(\frac{\omega_{pe}^2}{c^2}A_z\right), \tag{4.58}$$

where the effective electron gyroradius r_{ge} is defined by

$$r_{ge} \equiv \frac{v_b}{\omega_{ce}}\left(1+\omega_{ce}^2/\omega_{pe}^2\right)^{1/2} \tag{4.59}$$

It now follows for the case where the beam radius is large compared to the effective electron gyroradius

$$r_b >> r_{ge}\,, \tag{4.60}$$

that the left-hand side of Eq. (4.58) is small compared to the term $r_{ge}^{-2}\left(\partial A_z/\partial r\right)$ on the right-hand side, and therefore the beam current is neutralized. Note that the condition in Eq. (4.60) is consistent with the second condition in Eq. (4.44), i.e., $r_b >> \widetilde{k}_{qs}^{-1}$, obtained in the generalized analysis (Sec. 4.5.1). The first condition in Eq. (4.44), i.e., $\alpha >> 1$, is required however to validate the use of the slice approximation.

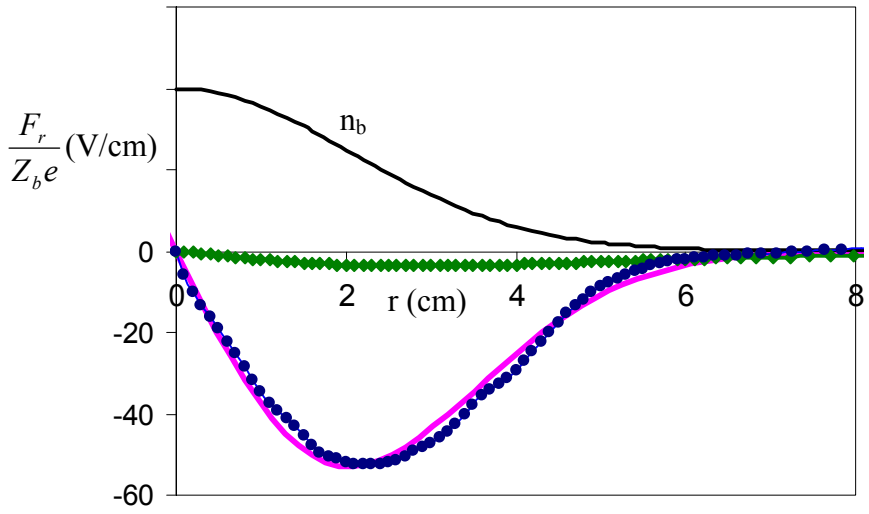

Figure 4.14: (Color) Radial dependence of the normalized focusing force at the beam center. The results of the numerical 2D (r,z) LSP simulations correspond to B_0=300 G and $\omega_{ce}/\beta_b\omega_{pe}$=18.7 (blue curve), and ω_{ce}=0 (green curve). The analytical results in Eq. (4.57), are shown by the pink curve. The beam-plasma parameters correspond to Z_b=1, r_b=0.55c/ω_{pe}, τ_b=37.5/ω_{pe}, β_b=0.05, and n_p=10^{10} cm^{-3}. The black curve corresponds to the radial beam density profile.

The analytical analysis for the case of a cylindrical ion beam has been compared with the results of the numerical simulations performed using the 2D (r,z) cylindrical version of the LSP code [Dorf *et al*., 2009c]. As an illustrative example, we consider a Gaussian ion beam pulse with density profile $n_b = 0.14 n_p \exp\left[-r^2/r_b^2 - (z-vt)^2/l_b^2\right]$ with effective beam radius, r_b=0.55c/ω_{pe}, and beam pulse half-length, l_b=1.875c/ω_{pe} (beam pulse duration τ_b=37.5/ω_{pe}), propagating with velocity v_b=0.05c through a background plasma with density n_p=10^{10} cm^{-3}. Figure 4.14 shows the *total* normalized radial self-focusing force (i.e., the sum of the electric and magnetic components of the Lorentz

force), $F_r/Z_b e$, and the units of electric field, *V/cm*, are chosen for practical representation of its numerical value. It is readily seen from Fig. 4.14 that the results of the numerical simulations (blue dots) are found to be in good agreement with the analytical predictions given in Eq. (4.57) (pink curve) for the case where B_{ext}=300 G, corresponding to $\alpha = 9.35$. The green curve in Fig. 4.14 corresponds to the results of the numerical simulations in the limit B_{ext}=0 G. A significant increase in the self-focusing force in the presence of a weak magnetic field (B_{ext}=300 G) is evident. Similarly to the case of Cartesian (x,z) geometry considered in Sec. 4.5.3, the ratio of the collective self-focusing force in the presence of an applied magnetic field [Eq. (4.57)] to the self-pinching force, F_0, in the limit B_{ext}=0 case, can be estimated as $F_r/F_0 \sim \left(c/r_b\omega_{pe}\right)^2 >> 1$ for the case of a cylindrical beam with $r_b << c/\omega_{pe}$ [Dorf *et al*., 2009c].

We emphasize again that the nature of the self-focusing effect is different for the cases where the external magnetic field is zero or not. In the absence of an applied magnetic field, the self-focusing force is due to the self-magnetic field of the beam pulse. In contrast, if an external solenoidal magnetic field is applied, the beam current becomes well-neutralized and the self-magnetic field is significantly suppressed, provided the conditions in Eq. (4.44) are satisfied. Nevertheless, the total self-focusing force is increased for the case where $r_b<c/\omega_{pe}$. Since the magnetic component of the Lorentz force is suppressed, the main focusing contribution comes from the strong radial electric field. Figure 4.15(a) illustrates the radial component of the self-electric field generated by an

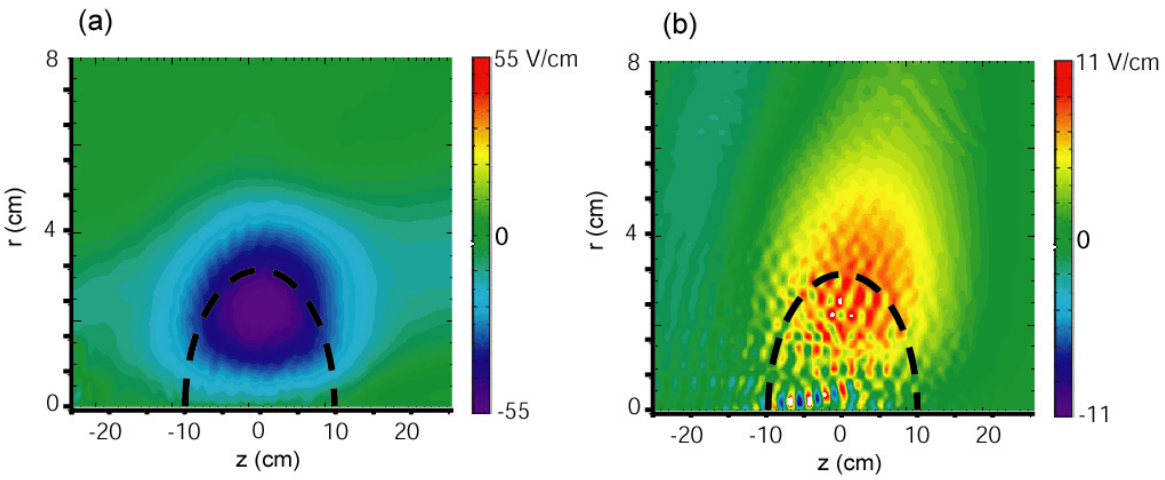

Figure 4.15: (Color) Plots of the radial self-electric field corresponding to (a) B_0=300 G ($\omega_{ce}/\beta_b\omega_{pe}$=18.7) and (b) B_0=25 G ($\omega_{ce}/\beta_b\omega_{pe}$=1.56). Other parameters are the same as in Fig. 4.14. Zero value of the axial coordinate corresponds to the beam center. Dashed lines correspond to the contour of constant beam density corresponding to the effective beam radius. Results are obtained with the 2D (*r*,*z*) cylindrical version of the LSP code.

ion beam pulse propagating through a magnetized background plasma [Dorf *et al.*, 2009c]. The system parameters assumed in this simulation are the same as for Fig. 4.14, and the 2D cylindrical version of the LSP code is used. The results of the numerical simulations show that the contribution of the electric component to the total Lorentz force (Fig. 4.14) constitutes more than 99%.

Finally, figure 4.15(b) illustrates the radial component of the self-electric field obtained in the numerical (*r*,*z*) simulations for the case where $\alpha = 0.78$ corresponding to B_{ext}=25 G [Dorf *et al.*, 2009c]. Consistent with the analysis in Sec. 4.5.3, the self-electric field is changing from defocusing to focusing with an increase of the applied magnetic field above the threshold value [compare Figs. 4.15(a) and 4.15(b)].

4.5.5 Electrostatic Model for Enhanced Self-Focusing

In the previous sections the electromagnetic effects have been taking into account for describing the dynamics of background plasma electrons, and the self-focusing force calculations. It is however interesting to note that the self-focusing force specified by Eq. (4.57) can be obtained within an electrostatic model provided the condition in Eq. (4.60) is satisfied. The electrostatic approximation is often used in numerical codes for simulations of a heavy ion driver (e.g., the electrostatic version of the WARP code), and therefore this result can be of particular practical importance.

As in previous sections, here we consider immobile plasma ions, cold background plasma electrons, and assume linear electron response, provided $n_b << n_e$. The axisymmetric steady-state solution where all quantities depends solely on the combination $\xi = z - v_b t$ is described in the electrostatic approximation by the cold-fluid equations for electrons

$$-v_b \frac{\partial}{\partial \xi} \delta n_e + n_p \frac{1}{r} \frac{\partial}{\partial r} V_{er} + n_p \frac{\partial}{\partial \xi} V_{ez} = 0 \tag{4.61}$$

$$-m_e v_b \frac{\partial V_{e\varphi}}{\partial \xi} = \frac{e}{c} V_{er} B_{ext} \tag{4.62}$$

$$-m_e v_b \frac{\partial V_{er}}{\partial \xi} = e \frac{\partial \varphi}{\partial \xi} - \frac{e}{c} V_{e\varphi} B_{ext} \tag{4.63}$$

$$-m_e v_b \frac{\partial V_{ez}}{\partial \xi} = e \frac{\partial \varphi}{\partial z} \tag{4.64}$$

and Poisson's equation for the electrostatic field, $\mathbf{E} = -\nabla \varphi$

$$\frac{\partial^2}{\partial \xi^2}\varphi + \frac{1}{r}\frac{\partial}{\partial r}\left(r\frac{\partial}{\partial r}\varphi\right) = -4\pi e\left(Z_b n_b - \delta n_e\right) \tag{4.65}$$

Here, $\delta n_e = n_e - n_p$, where n_p is the unperturbed plasma density away form the beam, and we have made use of $\partial/\partial t = -v_b\,\partial/\partial\xi$ and $\partial/\partial z = \partial/\partial\xi$ for the steady-state electron response. Finally, note that in the linear approximation, the magnetic $V_e \times B$ force corresponding to the magnetic field perturbations is of the second order, and therefore does not appear in Eqs. (4.62)-(4.63).

From Eqs. (4.62)-(4.63) it follows that

$$\frac{1}{\omega_{ce}} m_e v_b^2 \frac{\partial^2}{\partial \xi^2} V_{e\varphi} = e\frac{\partial}{\partial r}\varphi - \frac{e}{c} V_{e\varphi} B_{ext}\,. \tag{4.66}$$

Assuming that the ion beam pulse is sufficiently long with $l_b >> v_b/\omega_{ce}$, we readily obtain

$$V_{e\varphi} = -\frac{1}{cB_{ext}}\frac{\partial}{\partial r}\varphi\,, \tag{4.67}$$

and

$$V_{er} = -\frac{cv_b}{\omega_{ce}B_{ext}}\frac{\partial}{\partial z}\frac{\partial}{\partial r}\varphi\,. \tag{4.68}$$

Combining Eqs. (4.68), (4.64) and (4.61) yields

$$-v_b\frac{\partial}{\partial \xi}\delta n_e - \frac{n_p}{r}\frac{\partial}{\partial r}\left(r\frac{cv_b}{\omega_{ce}B_{ext}}\frac{\partial}{\partial \xi}\frac{\partial}{\partial r}\varphi\right) - \frac{n_p e}{m_e v_b}\frac{\partial}{\partial \xi}\varphi = 0\,. \tag{4.69}$$

Making use of Poisson's equation (4.65) and assuming $\partial^2/\partial\xi^2 \sim 1/l_b^2 << \omega_{pe}^2/v_b^2$ we obtain

$$\left(1+\frac{\omega_{pe}^2}{\omega_{ce}^2}\right)\frac{1}{r}\frac{\partial}{\partial r}\left(r\frac{\partial}{\partial r}\varphi\right)+\frac{\omega_{pe}^2}{v_b^2}\varphi=-4\pi Z_b e n_b\,. \tag{4.70}$$

It now follows from Eq. (4.70) for the case where $r >> r_{ge} \equiv \left(v_b/\omega_{ce}\right)\left(1+\omega_{ce}^2/\omega_{pe}^2\right)^{1/2}$ that

$$e\varphi=-Z_b m_e v_b^2\frac{n_b}{n_p}\,, \tag{4.71}$$

which is consistent with the results obtained in the previous sections [e.g. Eq. (4.49)].

It should be noted, however, that the analysis presented in this section only demonstrates that in the limit $r >> r_{ge}$ the electrostatic model predicts the same electric field as that obtained in the generalized analysis for the case where $\alpha >> 1$ and $r >> r_{ge}$ (Sec. 4.5.3). Additional analysis has to be performed in order to determine the regime of validity of the electrostatic approximation. Recall that for the case where $\alpha < 1$ the return electron current is driven primarily by the inductive electric field (Sec. 4.1.1); and for the case where $\alpha \approx 1$ large-amplitude electromagnetic wave fields can be excited (Sec. 4.3). These effects are not described by the electrostatic model. We emphasize here that electrostatic numerical codes are often used for simulations of an ion driver, and it is therefore of particular practical importance to identify the conditions where the electrostatic modeling can adequately describe the ion beam dynamics inside the neutralized drift section. This should be a subject of future studies.

4.6 Summary and Discussion

In the present chapter, the electromagnetic field perturbation excited by a long ion beam pulse propagating through a neutralizing background plasma along a moderately strong solenoidal magnetic field satisfying $\omega_{ce} \geq 2\beta_b \omega_{pe}$ was studied analytically, and by means of numerical simulations using the electromagnetic particle-in-cell code LSP. It was demonstrated that the total electromagnetic field perturbation excited by an ion beam pulse with a smooth radial density profile can be conveniently represented as the sum of a local-field component, rapidly decaying to zero outside the beam pulse, and a wave-field component that can extend far outside the beam. The wave field is represented by a long-wavelength electromagnetic component with $|k_x|=k_{em}<\omega_{pe}/c$, and a short-wavelength quasi-electrostatic component with $|k_x|=k_{qs}>\omega_{pe}/c$. Note that the longitudinal component of the electromagnetic wave group velocity is greater than the beam velocity. Therefore, the long-wavelength electromagnetic perturbations excited by the tail of the beam pulse can propagate along the beam and influence the dynamics of the beam head. The system reaches a quasi-steady-state when the wave packet of the initial transient excitation propagates sufficiently far outside the beam. It was found, for a sufficiently long ion beam pulse, that the time-scale for achieving a quasi-steady-state can be of order the beam pulse duration, and is therefore much longer than the inverse plasma frequency. This result is significantly different from the case $B_{ext}=0$, where the characteristic time to reach a steady-state is of the order of the plasma period.

It was also shown that the wave-field excitations propagate obliquely to the beam with a characteristic wavelength of $k_z \sim 1/l_b$. Therefore, their contributions to the transverse component of the Lorentz force can have opposite signs for the beam head and the beam tail. In contrast, the longitudinal profile of the local-field amplitude is the same as the longitudinal beam density profile. Therefore, the transverse local fields have the same sign over the entire length of the ion beam pulse. It is therefore important, in practical applications involving control over the beam aperture, to identify the parameter regimes where the local component of the electromagnetic field perturbation has the dominant influence on the beam transverse dynamics.

It was demonstrated, in the regime where $\omega_{ce} >> 2\beta_b\omega_{pe}$ and $r_b k_{qs} >> 1$, that the local-field component primarily determines the transverse dynamics of the beam particles; and the wave fields produce a negligible transverse force. Moreover, a positive charge of the ion beam pulse becomes over-compensated by the plasma electrons, and the associated strong transverse-focusing self-electric field has the dominant influence on the beam ions, compared with the magnetic field, provided $k_{qs}^{-1} << r_b << k_{em}^{-1}$. It was also shown, for the case where the beam radius is small compared to the electron skin depth, that the self-focusing force is significantly enhanced compared to the self-focusing force acting on the beam particles in the absence of an applied magnetic field. In addition, the local diamagnetic plasma response is observed in the numerical simulations, and is also predicted analytically for $\omega_{ce} >> 2\beta_b\omega_{pe}$. Note that these results differ significantly from the case $\omega_{ce} < 2\beta_b\omega_{pe}$, where the transverse electric field is defocusing, and the plasma

response is paramagnetic. The qualitatively different local plasma responses are separated by the critical field case where $\omega_{ce}^{cr} = 2\beta_b \omega_{pe}$, corresponding to the resonant excitation of large-amplitude wave-field perturbations. In the present analysis, the asymptotic time-dependent solution was obtained for this critical case, and the saturation intensity of the wave-field perturbations, determined from the nonlinear response of the background plasma electrons, was estimated. In addition, a plausible application of the resonant wave excitation effect for diagnostic purposes was discussed.

The effects of an applied solenoidal magnetic field on neutralized ion beam transport described in this chapter has been assessed for the presently operating Neutralized Drift Compression Experiment NDCX-I and its future upgrade NDCX-II (Chapter 1). The design of the NDCX facilities first involves the neutralized drift compression of the ion beam pulse, and then additional transverse focusing on the target plane by a strong (several Tesla) final-focus solenoid. The critical magnetic field $\omega_{ce}^{cr} = 2\beta_b \omega_{pe}$ corresponds to a relatively weak magnetic field of the order of 10 G (for NDCX-I) and 100 G (for NDCX-II). The magnetic fringe fields of the final-focus solenoid larger than this value can penetrate deep into the drift section thus providing conditions for enhanced beam self-focusing. It has been demonstrated for the parameters characteristic of NDCX-II experiment that the integrated effect of the beam self-focusing inside the drift section filled with the background plasma can be comparable to the focusing effect of the strong magnetic lens. For the parameters characteristic of the

NDCX-I experiment, the effects of the self-focusing are much smaller than the focusing effect of the strong magnetic lens.

Chapter 5

Collective Focusing of Intense Ion Beam Pulses

In the previous Chapter it was shown that even a weak solenoidal magnetic field of order 100 G can have a significant influence on the dynamics of an intense ion beam pulse propagating through a neutralizing background plasma. In particular, recent analytical calculations and numerical simulations demonstrated enhanced ion beam self-focusing induced by the collective dynamics of the plasma electrons [Dorf *et al*., 2009c]. However, it should also be pointed out that the collective effects of a neutralizing electron background in a weak solenoidal magnetic field were also utilized in a magnetic focusing scheme proposed by S. Robertson a few decades ago [Robertson, 1982]. In this Chapter we discuss this focusing scheme, significant extension of the theoretical model, and the possibility of its implementation for final focusing of intense ion beams in the Neutralizing Drift Compression Experiment-I (NDCX-I)

5.1 Introduction

In the collective focusing scheme proposed by S. Robertson (hereafter referred to as a collective focusing lens), a weak magnetic lens provides strong focusing of an intense ion beam pulse carrying an equal amount of neutralizing electron background [Robertson, 1982]. For instance, a solenoidal magnetic field of several hundred gauss can focus an intense neutralized ion beam within a short distance of several centimeters. Note that for a single-species nonneutral ion beam, a several Tesla magnetic field would be required to achieve the same focal length. The enhanced focusing in a collective focusing lens is provided by a strong self-electric field, which is produced by the collective dynamics of the neutralizing electrons.

A detailed analysis of the collective focusing lens is performed in the following sections. However, the main features of the collective focusing lens can be outlined as follows. First, let us review principles of operation of a conventional magnetic lens for the case of a single-species charged particle beam. Moving from a region of a zero magnetic field into the magnetic lens, a beam particle acquires the azimuthal angular momentum as the magnetic flux through its orbit increases. As a result, a radial focusing $V \times B$ force is acting on the beam particles inside the lens. For the case where the ion beam drags a neutralizing co-moving electron background into the magnetic lens, the neutralizing electrons entering the lens experience much stronger magnetic focusing than the beam ions and tend to build up a negative charge around the lens axis. As a result, an electrostatic ambipolar electric field develops that significantly increases the total

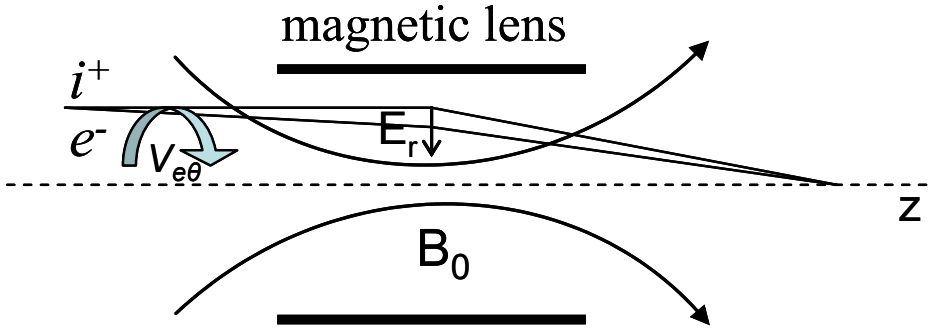

Figure 5.1: (Color) Schematic illustration of collective focusing lens operation. Traversing the fall-off region of the solenoidal magnetic field, the co-moving electrons acquire a fast rotation around the lens axis due to conservation of the canonical angular momentum. As a results, a strong radial electric force is produced in order to balance the $V \times B$ magnetic force. This electric force has a dominant influence on the radial dynamics of the beam ions.

focusing force acting on the beam ions [Fig. 5.1]. Note that the neutralizing electrons should enter the lens from a region of a zero magnetic field in order to acquire the azimuthal angular momentum necessary for the radial $V \times B$ magnetic focusing to occur inside the lens. Therefore, the collective focusing will only occur if there is no background plasma or secondary electrons inside the lens. Otherwise, the rotating electrons co-moving with the ion beam will be rapidly replaced by the "non-rotating" background plasma electrons inside the lens and the enhanced collective focusing will be suppressed [Kraft *et al*., 1987]. However, it should be noted that in this case the collective self-focusing associated with ion beam propagation through a background plasma discussed in Chapter 4 can occur instead. Detailed comparison of the collective

focusing of a neutralized beam inside a magnetic lens and the enhanced self-focusing of an ion beam propagating through a background plasma along a solenoidal magnetic field is described below in this chapter.

Many applications of ion-beam-driven high energy density physics including heavy ion fusion and high-energy ion beam production from intense laser-matter interaction require ion beam focusing and involve the presence of a neutralizing electron background. It is therefore of particular practical importance to investigate the feasibility of using a collective focusing lens for these applications. This would allow for the use of weak (several hundred Gauss) magnetic fields instead of several Tesla conventional magnetic lens, thus significantly facilitating the technical realization of ion beam focusing.

For instance, in a current design of a typical heavy ion driver a strong (several Tesla) magnetic solenoid is used to provide final transverse focusing of an ion beam as it leaves the drift section filled with a neutralizing background plasma [Yu *et al*., 2005]. Due to the strong space-charge self-fields of an intense ion beam pulse, a neutralizing plasma is also required inside the magnetic solenoid. Note that apart from the challenge of using a several Tesla magnetic solenoid, filling it with a background plasma provides additional technical challenges [Roy *et al*., 2009]. However, the use of the collective focusing concept can significantly simplify the technical realization of the beam final focus. Indeed, a neutralizing electron background can be dragged by the ion beam from the plasma that fills the magnetic-field-free drift section. The required magnetic field of the final focus solenoid can be lowered to the range of several hundred Gauss. Finally, a

neutralizing plasma background is not required (should not be present) inside the final focus solenoid. As a practical example, here we present results of advanced numerical simulations demonstrating the feasibility of tight collective focusing of intense ion beams for the Neutralizing Drift Compression Experiment-I (NDCX-I) [Seidl *et al*., 2009].

A collective focusing lens can also be utilized in laser generation of a high-energy ion beam, where the energetic ions are produced and accelerated by the interaction of an intense laser beam pulse with a thin foil [Snavely *et al*., 2000]. In order to decrease the divergence of the produced ion beam, a strong (several Tesla) focusing solenoidal magnetic field is used in some experiments [Harres *et al*., 2010]. However, along with the ions, a free-moving electron background is also produced, and therefore it is appealing to utilize the collective focusing concept for these applications as well.

The original concept of a collective focusing lens involved two conditions for the enhanced focusing to occur. First, a neutralized ion beam should be sufficiently dense, $\omega_{pe} >> \omega_{ce}$, to maintain quasi-neutrality inside the magnetic solenoid [Robertson, 1982]. Here, ω_{pe} and ω_{ce} are the electron plasma frequency and the electron cyclotron frequency, respectively. Second, perturbations in the applied solenoidal magnetic field due to the neutralized beam self-fields should be small. This condition can be expressed as $r_b << c/\omega_{pe}$, or equivalently, $I_b[\mathrm{kA}] << 4.25\beta_b$ [Robertson, 1982; Robertson, 1983], where r_b is the beam radius, I_b is the beam current, and β_b is the directed beam velocity normalized to the speed of light c. However, in many practical applications to high energy density physics involving ion beam transport, the beam parameters may not be

consistent with the above conditions. In particular, laser-produced high energy short ion beam pulses are very dense, with the beam radius typically larger than the collisionless electron skin-depth, i.e., $r_b > c/\omega_{pe}$ [Snavely *et al*., 2000; Harres *et al*., 2010]. Also, propagation of a neutralized (by co-moving electrons) ion beam along a strong solenoidal magnetic field with $\omega_{ce} > \omega_{pe}$ can occur both in a heavy ion driver [Seidl *et al*., 2009] and in the laser production of collimated ion beams [Harres *et al*., 2010] when a conventional several Tesla magnetic lens is used for ion beam focusing. Therefore, the extension of previous theoretical models [Robertson, 1982] to the cases where $\omega_{ce} > \omega_{pe}$ or $r_b > c/\omega_{pe}$ is of particular practical importance. In the present work, we investigate the operation of a collective focusing lens in these regimes, making use of advanced numerical simulations and reduced analytical models.

The present chapter is organized as follows. The original analysis of a collective focusing lens is summarized in Sec. 5.2. Section 5.3 presents results of advanced numerical simulations demonstrating the feasibility of tight collective focusing of intense ion beams for the Neutralizing Drift Compression Experiment-I (NDCX-I). The effects of the *nonneutral* collective focusing in a strong magnetic field, i.e., $\omega_{ce} > \omega_{pe}$, and its influence on the ion beam dynamics in the NCDX-I are investigated in Sec. 5.4. Finally, an analysis of collective focusing lens operation in the regime where the beam radius is comparable to or larger than the collisionless electron skin depth, i.e., $r_b > c/\omega_{pe}$, is performed in Sec. 5.5.

5.2 A Collective Focusing Lens

In this section we summarize the concept of a collective focusing lens proposed and experimentally verified by S. Robertson [Robertson, 1982; Krafft *et al*., 1985; Krafft, 1986; Kraft *et al*., 1987]. Consider a magnetic lens (magnetic solenoid) where a solenoidal magnetic field is nearly uniform inside the lens, $\mathbf{B} \cong B_0 \hat{\mathbf{z}}$, and decreases rapidly to zero outside the lens. Note that the applied solenoidal magnetic field has a non-zero radial component, B_r, in the field fall-off region. When an ion beam carrying an equal amount of neutralizing electrons enters the lens along the axis of the solenodial field, both the electron and ion species acquire an angular momentum (Fig. 5.1). This occurs due to the $V_z \times B_r$ force, but can be conveniently calculated from the conservation of the canonical angular momentum, $P_{\theta\alpha} = m_\alpha r^2 \, d\theta_\alpha / dt - q_\alpha r A_\theta$. Here, (r, θ) corresponds to the cylindrical polar coordinates, A_θ is the azimuthal component of the magnetic field vector potential, $\nabla \times \mathbf{A} = \mathbf{B}$, m_α and q_α are the species mass and charge, respectively, and the subscript $\alpha = e, i$ denotes electrons or ions, respectively. Provided a neutralized beam enters the lens from a region of a zero magnetic field and does not significantly perturb the applied magnetic field of the lens, it follows that inside the lens $\omega_\alpha \equiv d\theta_\alpha / dt = \Omega_\alpha / 2$, where $\Omega_\alpha = q_\alpha B_0 / m_\alpha c$, and initially non-rotating electrons and ions are assumed. The evolution of the particles radial coordinate inside the lens is then governed by

$$\frac{d^2}{dt^2} r_\alpha + \frac{1}{4} r_\alpha \Omega_\alpha^2 - \frac{q_\alpha}{m_\alpha} E_r = 0 . \tag{5.1}$$

Note that the second term on the left-hand-side of Eq. (5.1) corresponds to the difference between the centrifugal force, $m_e \Omega_e^2 r/4$, and the $V_\theta \times B$ magnetic force, $-m_e \Omega_e^2 r/2$.

In the original derivation for the case of a quasi-neutral ion beam, the identical radial motion of the electrons and ions was assumed, i.e., $r_e(z,t) = r_i(z,t)$ [S. Robertson, 1982]. From Eq. (5.1) it therefore follows for the case of a singly-charged ion beam that

$$\frac{d^2}{dt^2} r_\alpha + \frac{1}{4} r_\alpha \Omega_e \Omega_i = 0 , \tag{5.2}$$

and for the electric field we obtain $eE_r = -(m_i - m_e)\Omega_i \Omega_e r/4$. Neglecting the electron mass, we readily obtain that the strong ambipolar electric field that provides the enhanced collective focusing is given by

$$E_r = -m_e \Omega_e^2 \frac{r}{4e} . \tag{5.3}$$

Note that the electric field in Eq. (5.3) provides the balance between the magnetic $V_\theta \times B$ force, the centrifugal force, and the ambipolar electrostatic force acting on neutralizing electrons inside the lens. Furthermore, as pointed out in [D. Boercker *et al*., 1991], the same results for the electric field [Eq. (5.3)] was obtained by R. Davidson in [Davidson, 1976] where the possible equilibrium states for a plasma in a constant axial magnetic field were considered. Finally, a comprehensive analysis of a collective focusing lens including the thermal effects of the co-moving electrons can be found in [Robertson, 1986; Krafft, 1986].

In the *thin* lens limit, where the radial displacement of beam particles within a lens is small, and the neutralized beam drifts to a focus outside the lens, the focal length of the collective focusing lens is given by [Robertson, 1982]

$$L_f^{coll} = -v_b r_b / \Delta v_r \cong 4v_b^2 / (\Omega_e \Omega_i L_s). \tag{5.4}$$

Here, v_b is the axial beam velocity, L_s is the length of the magnetic solenoid, r_b is the beam radius, and Δv_r is the radial velocity acquired within the lens. Note that the focal length of a "conventional" magnetic lens is given in the thin-lens approximation for a single-species ion beam by

$$L_f^m \cong 4v_b^2 / (\Omega_i^2 L_s). \tag{5.5}$$

Equation (5.5) follows from Eq. (5.1), assuming that $E_r \cong 0$, provided the beam space-charge is weak or well-neutralized by a background plasma. Comparing Eqs. (5.4) and (5.5) it follows that for a given focal length, the magnetic field required for a neutralized beam is smaller by a factor of $\sqrt{m_i / m_e}$. Note that the collective focusing effect was originally observed by S Robertson in [Robertson, 1982] in the thin-lens limit, and the following work by R. Kraft [Kraft *et al*., 1987] investigated collective focusing for the case where the focal point lies within a focusing solenoid.

The quasi-neutrality condition, i.e., $n_e - n_i << n_i$, that has been assumed in the above analysis can be expressed in terms of practical system parameters by making use of Poisson's equation and Eq. (5.3). Here, n_e and n_i are the electron and ion number

densities, respectively. After some straightforward algebra it follows that the quasi-neutrality is maintained provided [Robertson, 1982]

$$\omega_{pe}^2 >> \frac{1}{2}\Omega_e^2 . \tag{5.6}$$

It has been also assumed that the axial magnetic field perturbations due to the beam are small. The azimuthal current density is primarily attributed to the electron rotation and is given inside the lens by $j_e = n_e e r \Omega_e / 2$. Making use of Ampere's law, it is straightforward to show that the perturbations are small provided

$$\frac{1}{2} r_b << \frac{c}{\omega_{pe}}, \tag{5.7}$$

i.e., is the beam radius is smaller than the collisionless electron skin depth [Robertson, 1982].

In conclusion, it is of particular interest to compare the focusing effect of a collective focusing lens to the enhanced self-focusing of an ion beam propagating through a background neutralizing plasma along a solenoidal magnetic field (Secs. 4.5.2 and 4.5.4). For both cases, the enhanced focusing is provided by a strong radial electric field, which is produced to balance the magnetic $V \times B$ force acting on the rotating neutralizing electrons. Note, however, that for the case of a collective focusing lens, the rotation of the co-moving electron beam is acquired due to variations of the applied solenoidal magnetic field from zero outside the lens to the maximum value inside the lens. In contrast, for the case of plasma-induced self-focusing, the background plasma electrons are initially immersed in an applied magnetic field, and variations of the

magnetic flux that determines the electron rotation are associated with a small radial displacement of the electron orbits in the presence of the ion beam self-fields. For this reason the plasma-induced enhanced self-focusing can be observed even for the case of a uniform applied magnetic field. In contrast, in order for the enhanced focusing to occur inside a collective focusing lens, the neutralized beam has to traverse the fall-off region of a solenoidal field. Moreover, here we emphasize again that the value of the plasma-induced self-focusing force [Eq. (4.43)] does not depend on the local value of the applied magnetic field. The value of the applied magnetic field however determines the conditions for the enhanced self-focusing to occur [see Eq. (4.44)].

The ratio of the focusing force acting on beam ions inside a collective focusing lens, F_{coll}, to the plasma-induced self-focusing force in the presence of an applied magnetic field, F_{sf}, can be estimated as

$$\frac{F_{coll}}{F_{sf}} \sim \frac{1}{4} \frac{r_b^2 \Omega_e^2}{v_b^2} . \tag{5.8}$$

In obtaining the estimate in Eq. (5.8), it has been assumed that $\partial/\partial r \sim 1/r_b$ and $Z_b n_b \sim n_p$ in the expression for the plasma-induced self-focusing force [Eq. (4.43)]. Furthermore, the force in Eq. (5.2) governing the neutralized beam dynamics inside the collective focusing lens has been generalized to the case of an arbitrary charge-state of the beam ions. It is interesting to note that in the limit where the beam radius is of order the effective gyroradius given by $r_{ge} = v_b/\Omega_e$ for $\Omega_e << \omega_{pe}$, the effects become of the same

order, i.e., $F_{coll} \sim F_{sf}$. Note, however, that the effective gyroradius corresponds to the minimum threshold value of the beam radius in the condition in Eq. (4.44).

Finally, we comment on the significant suppression of the total focusing effect that has been observed in the experiments in [Kraft *et al*., 1987] when a neutralizing plasma was produced inside a collective focusing lens. Although the enhanced plasma-induced self-focusing could still occur inside the magnetic lens with the presence of the background plasma, its influence on the ion beam dynamics would be much less than the original effects of the collective focusing lens. Indeed, a simple calculation shows that for the parameters of the experiments in [Kraft *et al*., 1987] the ratio in Eq. (5.8) is much less than unity.

5.3 Collective Focusing Lens for the NDCX-I Final Focus

As noted earlier, it is appealing to make use of a collective focusing lens in a design of a heavy ion driver final focus section. As a practical illustrative example, in this section we consider the Neutralized Drift Compression Experiment-I (NDCX-I), which is a scaled heavy-ion driver built in order to determine the physical and technological limits of neutralized ion beam compression (Chapter 1). Figure 5.2 shows a schematic of the NDCX-I final focus section. Leaving the long neutralized drift section, the radially and longitudinally convergent ion beam pulse passes through a strong (8 Tesla) final focusing

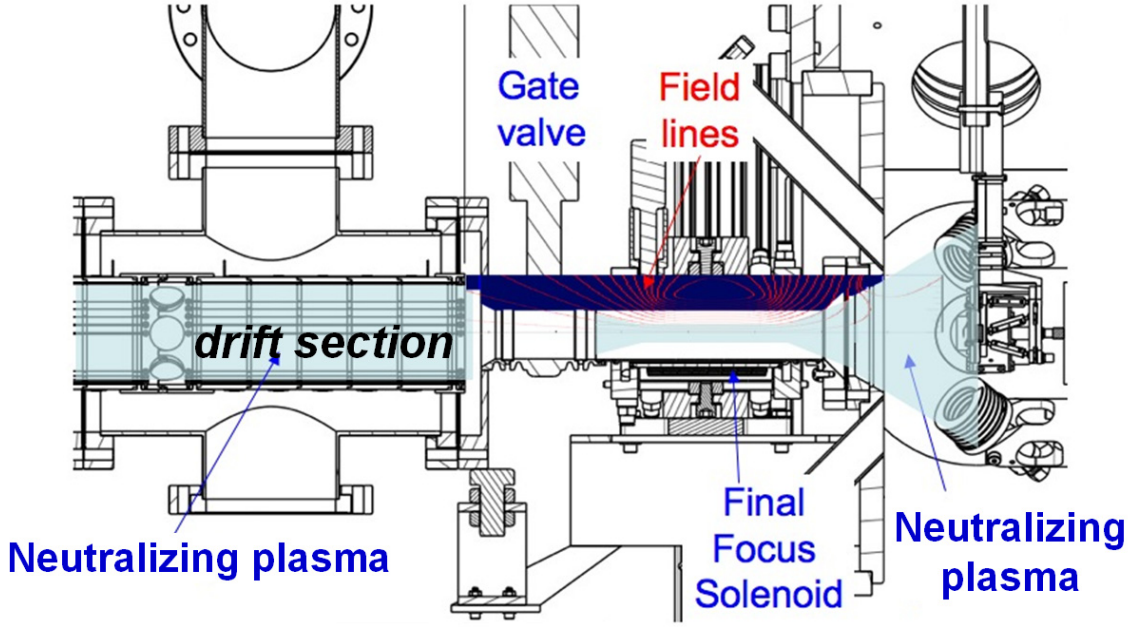

Figure 5.2: (Color) Schematic of the NDCX-I final focus section showing regions filled with neutralizing plasma. The neutralizing plasma inside the drift section is created by a ferroelectric plasma source (FEPS). The final focus solenoid is filled with a background plasma injected by four cathodic-arc plasma sources (only two are shown in the figure).

solenoid (FFS), which provides additional transverse focusing. The target plane is located downstream the final focus solenoid, and is not shown in the figure. In order to compensate for the strong space-charge forces of the compressed ion beam pulse, the final focus solenoid has to be filled with a neutralizing plasma. In the current design, four cathodic-arc plasma sources (CAPS) are used to inject plasma into the final focus solenoid. The sources are placed out of the line-of-sight of the beamline in order to avoid interaction with the ion beam and angled toward the axis of the final focus solenoid (Fig. 5.2). Here, we emphasize again that filling the strong magnetic solenoid with a

neutralizing plasma is itself a challenging problem [Roy *et al*., 2009], and providing improved neutralizing plasma background inside the final focus solenoid is still one of the critical problems in NDCX-I optimization.

The final beam focusing can be significantly facilitated by using the concept of a collective focusing lens, which requires minimum modifications to the current NDCX-I configuration. Indeed, in order to test the collective focusing, one needs to lower the final focus solenoid magnetic field from 8 Tesla to several hundred Gauss and turn off the cathodic-arc plasma sources. It is then expected that the beam will drag the required neutralizing co-moving electrons from the background plasma that fills the drift section [Humphries, 1978; Humphries *et al*., 1981; Kraft and Kusse, 1987; Callahan, 1996; Welch *et al*., 2002; Sharp *et al*., 2004] and will experience strong collective focusing inside the magnetic solenoid. In this section we present results of advanced numerical simulations demonstrating the feasibility of tight collective focusing of an intense ion beam for NDCX-I. In Sec. 5.3.1 an idealized model not taking into account the effects of the beam simultaneous convergence is considered, and the physical limits of the collective focusing are discussed. In Sec. 5.3.2 a practical design for NDCX-I collective final focus is proposed.

5.3.1 Idealized Model: Numerical Studies

In this section we present results of the particle-in-cell numerical simulations of an idealized model for the NDCX-I final beam focus (Fig. 5.3). The simulations are

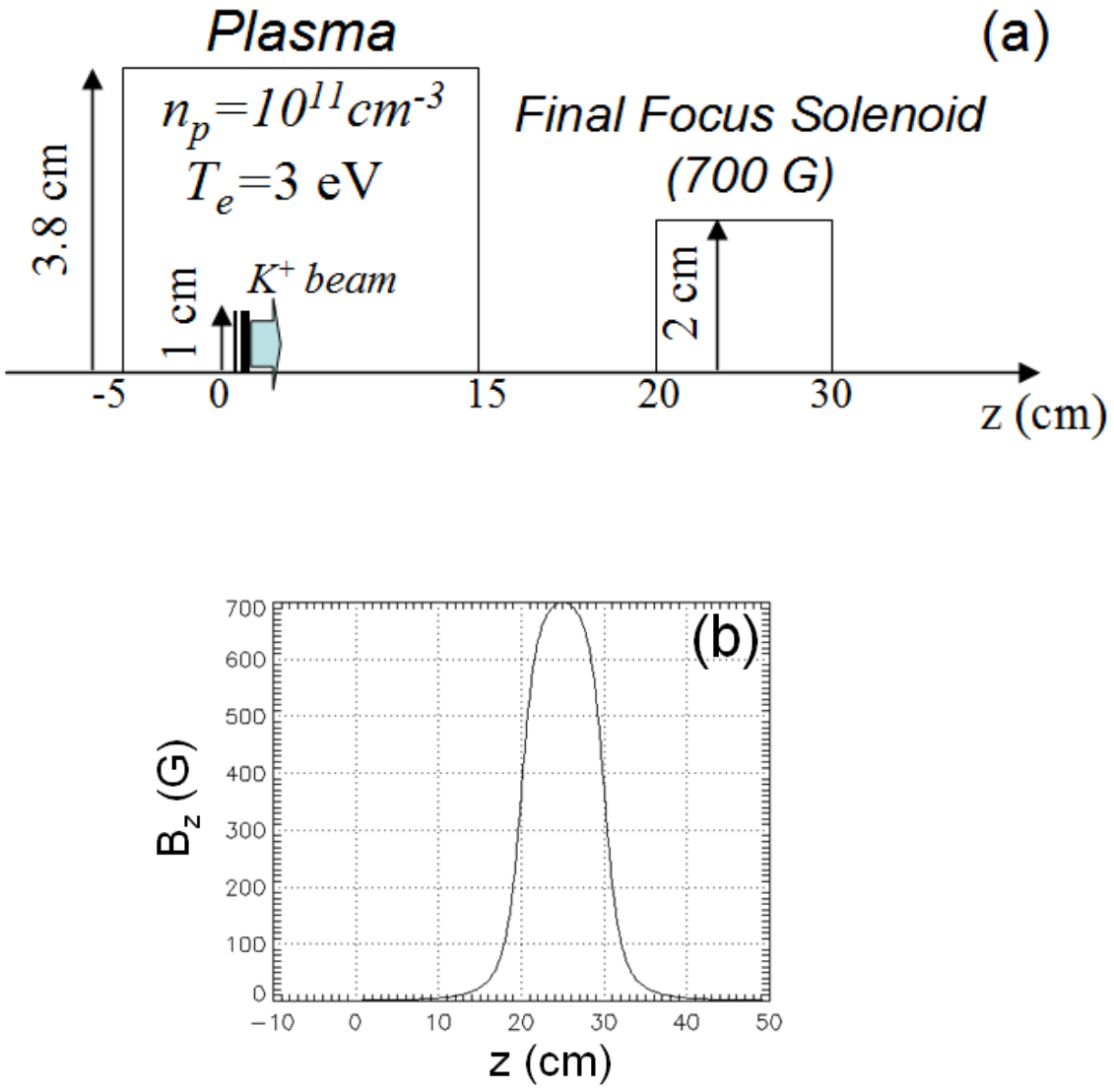

Figure 5.3: An idealized model of the NDCX-I final beam focus. (a) Schematic of the numerical LSP simulation. (b) The longitudinal profile of the applied axial magnetic field of the 700 G final focus solenoid.

performed in cylindrical (r,z) geometry with the exact implicit electromagnetic version of the LSP code [LSP, 1999]. In the idealized model, the Potassium (K^+) ion beam is injected through the plane z=0 located inside the drift section near its downstream end. To model the short downstream part of the neutralizing drift section, a plasma layer is placed between z=-5 cm and z=15 cm. The plasma density is assumed to be uniform with n_p=10^{11} cm^{-3}, and the electron and ion temperatures are taken to be T_{e0}=T_{i0}=3 eV. The final focus solenoid (FFS) with radius R_s=2 cm and length L_s=10 cm is centered at z_c=25 cm, and the following initial beam parameters are considered for this idealized model: the injected beam density is n_{b0}=10^{10} cm^{-3}; the directed energy of beam ions is E_b=320 keV, which corresponds to $\beta_b = v_b / c \approx 0.0042$; the radial beam density profile is flat-top with the outer beam radius r_{b0}=1 cm; the duration of ion beam injection is $\tau_b = 40$ ns, which corresponds to the beam length l_b≈5 cm; and the transverse and longitudinal beam temperatures are assumed to be T_b=0.2 eV. In the simulations, the injected ion beam pulse is allowed to drag the electrons when leaving the plasma layer. Therefore, in order to maintain charge-neutrality of the system, electron emission is established at the radial plasma boundary, R_p=3.8 cm, which coincides with the conducting radial boundary of the simulation domain. The fine radial grid spacing with $\Delta r_f = 0.01\,\text{cm}$ is used in the range of $r \in [0,1]\,\text{cm}$, and a coarse grid with $\Delta r_c = 0.2\,\text{cm}$ is used for the remainder of the radial domain extension. The grid spacing in z-direction is $\Delta z = 0.2\,\text{cm}$, and the time step is $\Delta t = 0.016\,\text{ns}$.

Note that the present simulations do not resolve the plasma oscillation wavelength, $\lambda_p = v_b/\omega_p$, which is an important parameter in the physics of beam neutralization by a background plasma [Humphries, 1978; Kaganovich *et al*., 2001]. However, consistent with the more detailed numerical simulations in [Humphries *et al*., 1981] and experimental observations in [Kraft and Kusse, 1987], in our simulations the space-charge and current of the ion beam is well-neutralized as it leaves the plasma layer, which is sufficient for present purposes. Furthermore, due to some uncertainty in the background plasma parameters in the NDCX-I, e.g., the electron temperature, and the plasma fall-off density profile, a computationally intensive improvement of the neutralization analysis would not necessarily provide much better insight into the design of the NDCX-I collective final focus section.

Figure 5.4 presents the results of the numerical simulations for the case where the magnetic field inside the final focus solenoid is B_0=700 G. The ion beam comes to a tight focus at $z_f \approx 30\,\text{cm}$, with ~700 times increase in the number density, $n_f \approx 7\times10^{12}\,\text{cm}^{-3}$ [Fig. 5.4(a)]. The radial electric field inside the lens is shown in Fig. 5.4(b), and agrees well with the analytical predictions in Eq. (5.3) for $r \le 0.4\,\text{cm}$. Note that for the parameters of this illustrative example, most of the beam compression occurs within the lens; the focal plane is located slightly downstream the end of the solenoid. Accordingly, the beam radius corresponding to the plot in Fig. 5.4(b) is about a half of its initial value.

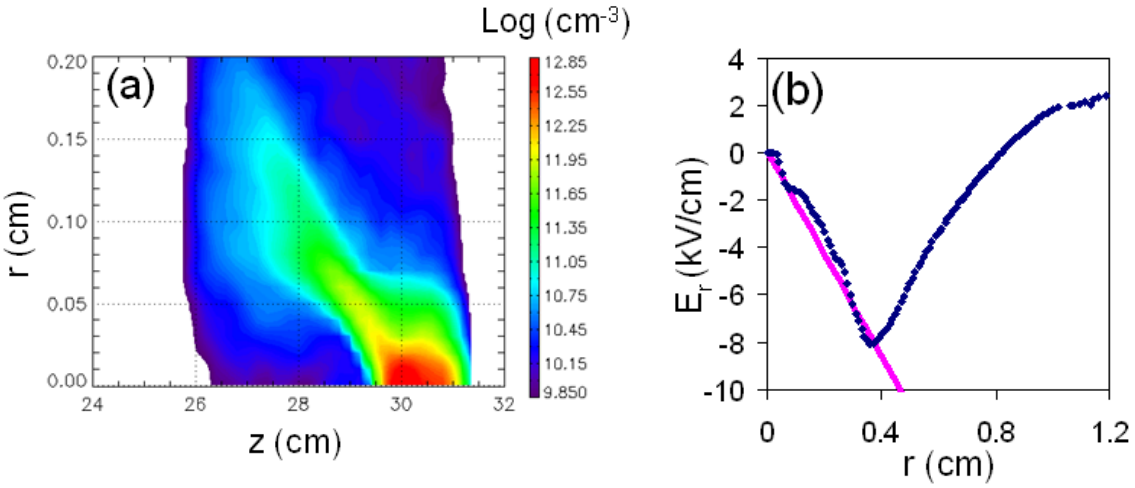

Figure 5.4: (Color) Results of the numerical simulations performed with the LSP code for the idealized model of the NDCX-I final beam focus. (a) Plot of the ion beam density at the focal plane corresponding to t=250 ns. (b) Radial dependence of the radial electric field inside the lens corresponding to z=25 cm and t=220 ns (blue dots). The analytical results in Eq. (5.3) are shown by the pink solid line in Frame (b).

It is of particular practical importance to discuss the physical limits of the collective focusing. Figure 5.5 shows the system parameters slightly upstream of the focal plane, including the ion beam density [Fig. 5.5(a)], the electron density [Fig. 5.5(b)], and the radial component of the electric field [Fig. 5.5(c)]. It is readily seen that near the focal plane, the total space-charge density is positive, and the radial electric field is defocusing. This means that the compression of the co-moving electron beam comes to stagnation, whereas the ion beam still undergoes compression. This "final" ion beam compression is inertial, i.e., it occurs against the ion beam space-charge forces due to the ion beam radial convergence generated by the collective focusing. The plausible explanation of the electron transverse stagnation can be given by means of thermal

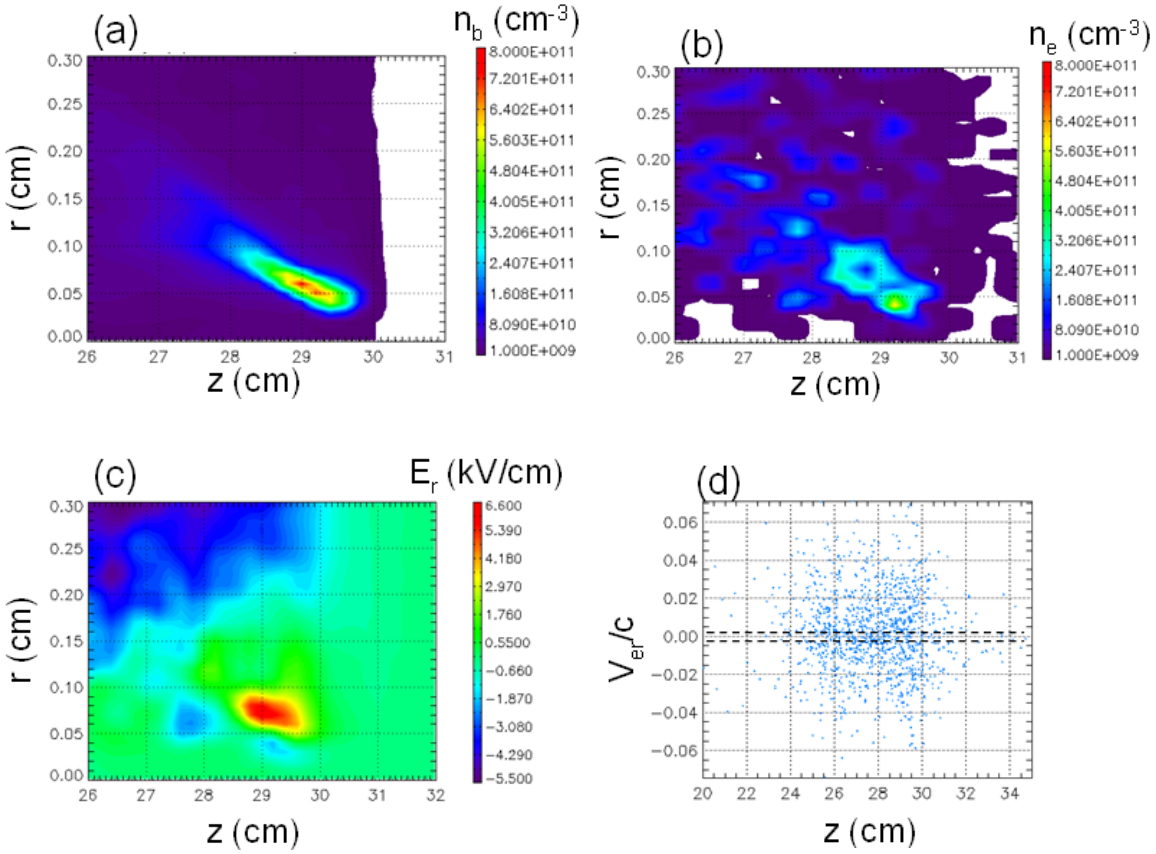

Figure 5.5: (Color) Effects of electron heating on collective beam focusing. Shown are plots of (a) ion beam density, (b) electron density, (c) radial electric field, and (d) electron phase-space (V_{er}/c,z). The results are obtained at time t=240 ns. The horizontal dashed lines in Frame (d) correspond to a characteristic initial electron thermal velocity specified by $\sqrt{T_{e0}/m_e}$. Results are obtained using the LSP code for the idealized model of the NDCX-I final beam focus.

effects [Robertson, 1986]. Indeed, neglecting small electron inertia, the radial force balance equation for the electron fluid includes the focusing magnetic force, $-m_e\Omega_e^2 r/2$, the defocusing centrifugal force $m_e\Omega_e^2 r/4$, the defocusing electric force, eE_r, and the thermal pressure term, $\nabla p_e/n_e$. As the effective transverse electron temperature increases during compression, the electric field required to balance the magnetic electron focusing decreases. Finally, when the magnetic force is completely balanced by the thermal pressure, the electron compression comes to stagnation. A small additional compression of the co-moving electron beam, however, is still possible due to the positive radial electric field generated during the "inertial" ion beam compression. The parameters of the electron beam at the stagnation point can be estimated from

$$T_{es} \sim m_e\Omega_e^2 \frac{r_{es}^2}{4}. \tag{5.9}$$

Here, r_e and T_e are the electron beam radius and the effective transverse temperature. At the time corresponding to the plots in Fig. 5.5, the electron beam radius is r_e~0.1 cm, and it follows from Eq. (5.9) that T_e~215 eV. The corresponding normalized value of the effective radial thermal velocity, $\beta_{er} \sim c^{-1}\sqrt{T_e/m_e} = 0.02$, is consistent with the results of the numerical simulations shown in Fig. 5.5(d). It is interesting to note that the value of the effective transverse temperature observed in the simulations is approximately consistent with the adiabatic compression of the electron beam, where $r_e^2 T_e \approx const$.

In the simulations presented here, the initial effective transverse temperature of the co-moving neutralizing electrons can be attributed to the isotropic thermal

distribution of the electrons inside the plasma layer. However, even for the case where the background plasma electron are cold, it has been demonstrated both computationally [Humphries *et al*., 1981] and in experiments [Kraft and Kusse, 1987] that the longitudinal velocity distribution of the co-moving neutralizing electrons dragged from the background plasma is bell-shaped with an approximate width of v_b, and a mean velocity of v_b. This longitudinal velocity can in turn provide the spreading in the transverse electron velocity due to the coupling between the longitudinal and transverse electron motion caused by finite transverse geometry effects and various collective effects. Therefore, the electron-temperature-induced limit of the collective focusing scheme can still occur even if a cold background plasma is used as a source of neutralizing electrons.

Note that the radial ion beam density profile shown in Fig. 5.5(a) is hollow. This can be due to nonlinearities in radial profile of the focusing electric field near the axis [Fig. 5.4(b)]. However, it is important to point out that the ion beam profile is bell-shaped at the focus, as seen in Fig. 5.4(a). Furthermore, it has been observed in the numerical simulations that the radial profile of the electric field becomes nearly linear, when the magnetic solenoid is moved further downstream from the drift section in order to decrease the value of the fringe magnetic fields inside the plasma layer (Sec. 5.4). It also should be noted that nonlinear aberrations can be produced due to the thermal spreading in the transverse velocity distribution of a co-moving electron beam [Krafft, 1986].

For the parameters of the illustrative example shown in Fig. 5.4, the focal plane lies near the downstream end of the final focus solenoid (FFS). For practical purposes,

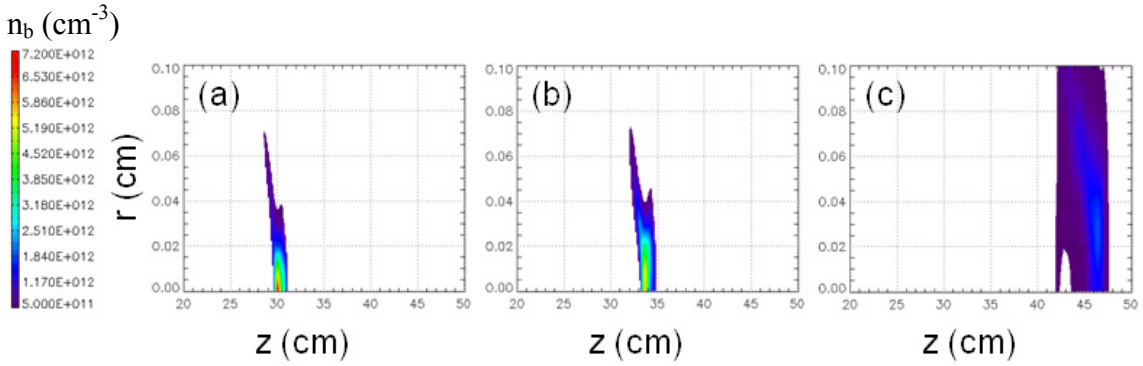

Figure 5.6: (Color) Ion beam density at the focal plane for different values of the magnetic solenoid strength, B_0. The plots correspond to (a) B_0=700 G, (b) B_0=700 G, and (c) B_0=300 G. Results are obtained using the LSP code for the idealized model of the NDCX-I final beam focus

however, it can be important to have a gap between the final focus solenoid and the target plane (beam focal plane). Figure 5.6 illustrates the beam density at focus for different values of the final focus solenoid magnetic strength. It is readily seen that the focal plane can be moved downstream by lowering the magnetic strength of the solenoid. However, the compressed beam density decreases with a decrease in the applied magnetic field. A plausible explanation for this includes the following. First, electron stagnation can occur earlier, in accordance with Eq. (5.9). Second, the "inertial" phase of the ion beam compression is more pronounced for a stronger magnetic field, because a steeper convergent angle is acquired during the collective compression inside the final focus solenoid.

5.3.2 Practical Design of the NDCX-I Final Focus

In the previous section an idealized model of the NDCX-I collective final focus section was considered. The model did not take into account the effects of the beam's simultaneous, longitudinal and transverse, convergence. However, in the actual NDCX-I configuration, the ion beam acquires a radial convergence angle and a head-to-tail longitudinal velocity tilt before entering the neutralizing drift section (Chapter 1). The beam distribution evolves inside the drift section, and it is of particular practical importance to assess the feasibility of a tight collective final focus for the case of a more realistic beam distribution at the exit of the drift section.

Figure 5.7 illustrate a schematic of the simulation configuration presented in this section. The beam ions are injected through the upstream boundary of the simulation domain at z_{inj}=0. The injected beam current is I_b=27 mA, the directed energy of K^+ beam ions is E_b=300 keV, the radial beam density profile is flat-top, with outer beam radius r_{b0}=1.6 cm; the duration of the ion beam injection is $\tau_p \sim 500$ ns, and both the transverse and longitudinal beam temperatures are T_b=0.094 eV. The initial radial convergence corresponds to a ballistic focus at L_{conv}=80 cm, i.e., $\Delta v_{r0}/v_b \equiv r_{b0}/L_{conv} = 0.02$. After injection, the beam propagates through the induction bunching module, where a time-dependent voltage shown in Fig. 5.8 is applied in the tilt gap between z_{g1}=8 cm and z_{g2}=11 cm. The beam then enters a long, L_d=231 cm, drift section filled with a background neutralizing plasma. Most of the simultaneous compression occurs inside the drift section. However, to provide the additional transverse collective focusing a short,

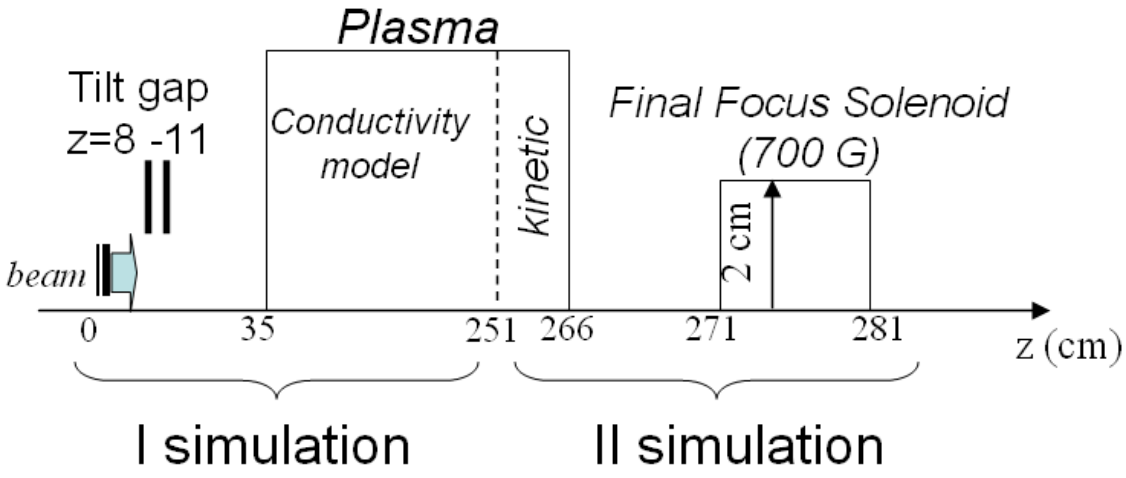

Figure 5.7: Schematic of the numerical LSP simulation configuration for the NDCX-I including the longitudinal velocity tilt and initial radial convergence of the ion beam.

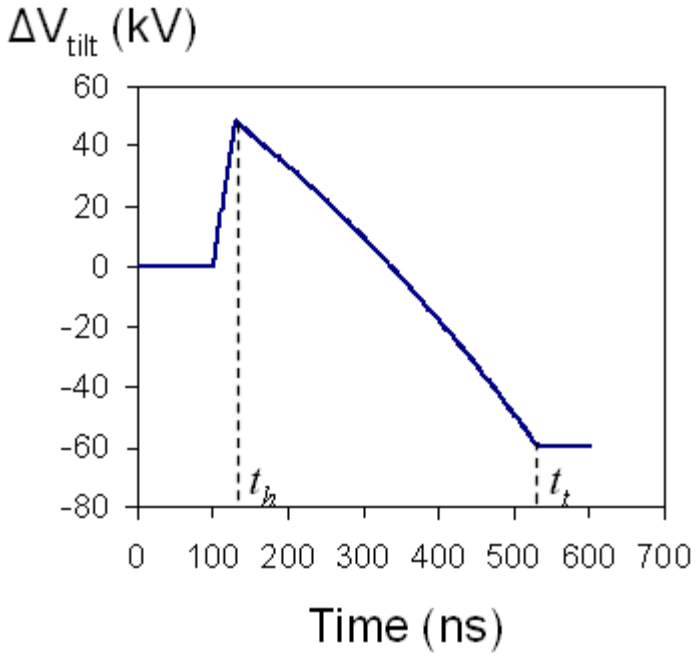

Figure 5.8: The tilt-gap voltage waveform used in the numerical simulations.

L_s=10 cm, final focus solenoid with radius R_s=2 cm is placed downstream of the beamline after the drift section. It is centered at z_s=276 cm, and the on-axis magnetic field inside the solenoid is B_0=700 G. Leaving the drift section, the beam is allowed to drag the co-moving electron background from the background plasma, and a tight collective final focus is expected to be observed in the simulations.

The voltage ramp between the time instants t_h=130 ns and t_t=530 ns in Fig. 5.8 provides the longitudinal compression of only the $\tau_c = 400$ ns portion of the entire ion beam pulse; and the front part of the beam that propagates through the tilt gap during $t<t_h$ corresponds to the longitudinally uncompressed beam *prepulse*. Here, the subscripts "*h*" and "*t*" denote the head and tail of the beam pulse, respectively. The head of the compressing beam portion experiences a net decelerating electric force, and the tail experiences a net accelerating force. Thus, this part of the ion beam acquires a head-to-tail velocity tilt that causes the tail of the compressing beam portion to meet its head at the longitudinal focal plane. Note that the voltage ramp between t_h and t_t assumed in the simulations (Fig. 5.8) corresponds to the so-called idealized voltage waveform given by [Welch *et al*., 2005; Sefkow, 2007]

$$\Delta V_{tilt} = \frac{m_b c^2}{2e}\left[\beta_b^2 - \left(\frac{\beta_h}{1 - c\beta_h (t - t_h)/L_f}\right)^2\right]. \tag{5.10}$$

Here, $\beta_b = v_b/c = 0.004$ is the normalized directed beam velocity upstream of the tilt gap, $\beta_h = 0.0037$ is the normalized head-velocity of the compressing beam part, and L_f=273 cm corresponds to the drift length to the ideal longitudinal focal plane. It is

straightforward to show for ballistic compression of a cold beam that different longitudinal beam slices will come to the same focal plane at $z_{foc}^{id} = z_{g2} + L_f = 284\,\text{cm}$, provided their velocity is determined according to $m_b v_{slice}^2(t) = 2\left[m_b v_b^2 - e\Delta V_{tilt}(t)\right]$ at the tilt gap exit, i.e. $z=z_{g2}$.

The ideal longitudinal compression is degraded by thermal effects, and the time-dependent effects of the longitudinal beam dynamics associated with a finite length of the tilt gap [Sefkow, 2007; Sefkow and Davidson, 2007]. Furthermore, traversing the finite-length tilt gap, the beam particles receive a time-dependent divergence angle [Sefkow, 2007; Sefkow *et al*., 2009]. Note that the steep initial convergence angle corresponding to L_{conv}=80 cm (instead of $z_{foc}^{id} = 284\,\text{cm}$), is taken to partially compensate for this divergence. However, due to the time-dependent nature of the effect, simultaneous longitudinal and transverse beam compression is still degraded due to variations in the z-location of the transverse focal plane for different beam slices [Sefkow *et al*., 2009, Kaganovich *et al*., 2009]. The tilt gap is included in the simulations as a gap between two long conducting cylinders with radii R_g=3.8 cm aligned along the z-axis, which corresponds to the induction bunching module configuration used in NDCX-I; and the voltage difference $\Delta V_{tilt}(t)$ is applied to the cylinder surfaces. Therefore, the finite-size tilt gap effects are adequately described by the present simulations. Note that among the deleterious technological effects limiting simultaneous beam compression is a discrepancy between the ideal voltage waveform in Eq. (5.10) and the waveform generated by the induction bunching module in NDCX-I. This effect is considered in

detail in [Sefkow 2007; Kaganovich *et al*., 2009], and is outside the scope of the present work.

It has been demonstrated that a background plasma with $n_p > n_b$ can provide a high degree of the beam charge and current neutralization [Kaganovich *et al*., 2010]. Furthermore, it can be shown that collective streaming processes do not have a significant influence on ion beam dynamics due to the thermal effects of the background plasma electrons. Therefore, it is appealing to use a fluid model for the background plasma, instead of a full kinetic description to simulate the ion beam pulse shaping during its simultaneous compression inside the long drift section. However, the kinetic effects of the co-moving electrons are of particular importance for the collective focusing of the beam pulse. Accordingly, the entire simulation domain is divided into two parts. The simulation of the long upstream part, from z=0 to z_L=251 cm, utilizes the conductivity model for a background plasma, where a sufficiently high value of the conductivity is chosen to provide complete beam neutralization. The downstream part, from z_L=251 cm to z_{end}=301 cm, that includes a short downstream part of the drift section and the final focus section, is simulated by making use of a fully kinetic model for the background plasma electrons and ions. For this downstream simulation we take the plasma density to be $n_p=10^{11}$ cm^{-3}, the electron temperature T_e=3 eV, and the massive plasma ions are assumed to be cold. As in the previous section, to maintain charge-neutrality of the system, electron emission is established at the radial plasma boundary, R_p=3.8 cm, which coincides with the conducting radial boundary of the downstream simulation domain. The beam ions are treated as a kinetic species throughout the entire simulation domain. We

emphasize again that the use of the fluid model for most of the neutralizing plasma inside the drift section allows for a great reduction of the total computational time.

Finally, the following space-time resolutions for the upstream and downstream simulations are used. For most of the upstream simulation domain, except for a narrow region near $z=z_L$, we take $\Delta z^I = 1\,\text{cm}$, and the grid resolution in the radial direction includes 10 grid points for the region $r \in [0;0.2]$ cm, 10 grid points for $r \in [0.2;1]$ cm, and 35 grid points for $r \in [1;5]$ cm. For the short downstream simulation region, we take $\Delta z^{II} = 0.2\,\text{cm}$, and the grid resolution in the radial direction includes 40 grid points for the region $r \in [0;0.2]$ cm, 100 grid points for $r \in [0.2;2]$ cm, and 19 grid points for $r \in [2;3.8]$ cm. Here, Δz^I and Δz^{II} denote the grid spacing in the z-direction for the upstream and downstream simulations, respectively. To simulate the beam propagation through the long drift section the time step $\Delta t^I = 0.0066\,\text{ns}$ is used, and when the beam propagates through the final focus section, we take $\Delta t^{II} = 0.005\,\text{ns}$.

The results of the numerical simulations performed with the LSP code [LSP, 1999] are shown in Figs. 5.9 and 5.10. Figure 5.9(a) illustrates the pre-compressed ion beam pulse density at the exit of the drift section. The beam density is zero downstream of the plane z=274 cm, because the downstream simulation ignores most of the prepulse part of the beam. Recall, that one of the conditions for the collective focusing to occur requires the electron plasma density to be higher than the electron cyclotron frequency inside a magnetic solenoid [Eq. (5.6)]. Due to the simultaneous neutralized pre-compression providing $n_b \sim 10^{10}$ cm^{-3} near the exit of the drift section this condition is

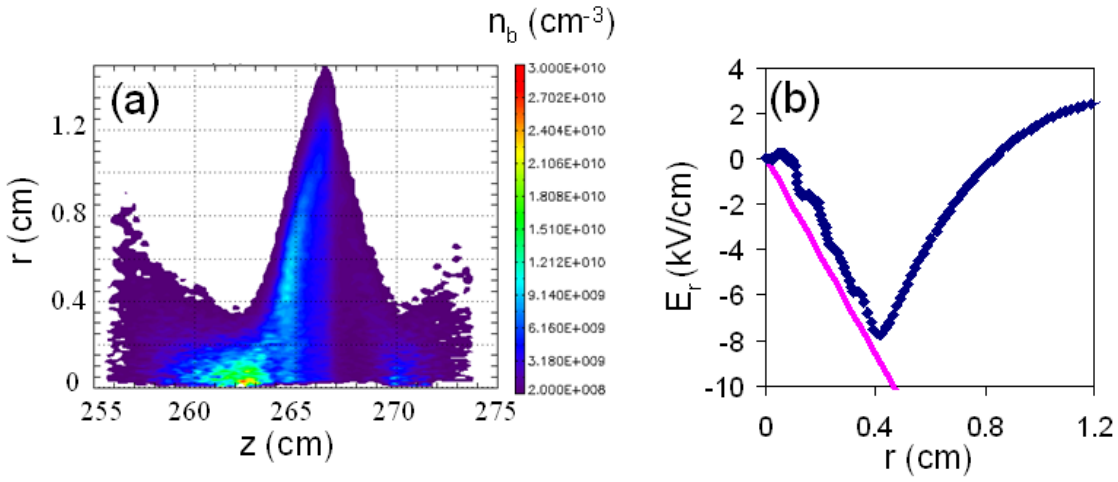

Figure 5.9: (Color) Results of the numerical LSP simulations of the ion beam dynamics in the NDCX-I including the initial head-to-tail velocity tilt and the radial convergence angle. Shown are plots of (a) the ion beam density at the exit of the neutralized drift section corresponding to t=2450 ns, and (b) radial dependence of the radial electric field inside the magnetic lens at the center of the final focus solenoid, z=276 cm, corresponding to t=2535 ns (blue dots). The analytical results in Eq. (5.3) are shown by the solid pink line in Frame (b).

nearly satisfied. Note that the idealized simulation in Sec. 5.3.2 assumes a similar initial density of the ion beam pulse, and the tight collective focus is demonstrated. Figure 5.9(b) illustrates the radial electric field inside the solenoid, which agrees well with the analytical predictions in Eq. (5.3). A plot of the beam density at the transverse focal plane is shown in Fig. 5.10(a). It is readily seen that a tight transverse collective focus with the on-axis (peak) value of the compressed beam pulse $n_{comp}\approx 5.5*10^{12}$ cm^{-3} occurs in the simulations. The time evolution of the ion beam current at z_{tf}=281.6 cm corresponding to the transverse focal plane is shown in Fig. 5.10(b). Figure 5.10(b) demonstrates strong ~80X longitudinal compression, with the peak current I_p=2.2 A, and a compressed ion

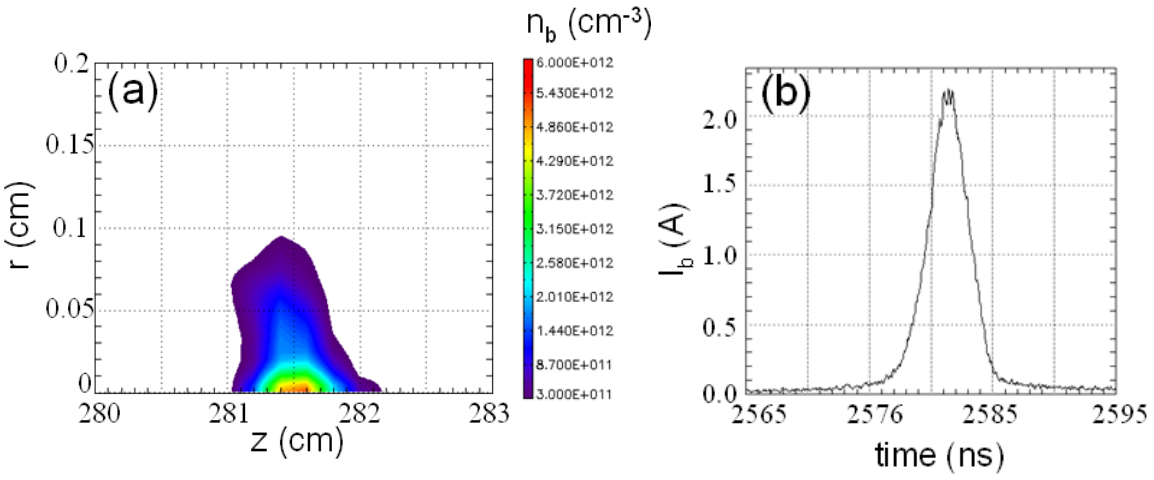

Figure 5.10: (Color) The ion beam parameters at the transverse focal plane. Shown are plots of (a) the ion beam density corresponding to t=2580 ns, and (b) the time evolution of the ion beam current at the transverse focal plane corresponding to z=281.6 cm. The results are obtained in numerical LSP simulations of the ion beam dynamics in NDCX-I including the initial head-to-tail velocity tilt and the radial convergence angle.

beam pulse duration of a few nanoseconds. Note that for the parameters of the present simulations the longitudinal focal plane does not exactly coincide with the transverse focal plane. It is slightly shifted downstream to z_{lf}=283.2 cm, with a peak current increase of a few percent. Therefore, further optimization studies can provide insights into the NDCX-I design with slightly improved simultaneous compression. However, even the present illustrative simulations demonstrate the feasibility of a very tight collective focusing of the ion beam pulse in NDCX-I, and the compressed beam parameters are similar to the results of the simulations performed for the case where 8 T final focus solenoid is used, and complete beam neutralization is assumed from the drift section entrance to the target plane [Siedl *et al*., 2009].

In conclusion, it is important to point out that the long prepulse part of the ion beam in the NDCX-I can produce a significant amount of the background electrons by preheating the target. Therefore, it may be important to remove those electrons from the beam-line. Otherwise they can possibly leak into the final focus solenoid, thus reducing the collective focusing of the compressing part of the beam pulse (Sec. 2.1). Note that the entire ion beam pulse undergoes simultaneous compression in the new NDCX-II facility [Friedman *et al*., 2009]. Therefore, the absence of the prepusle part of the ion beam makes the concept of final collective focusing even more attractive for the planned NDCX-II facility.

5.4 Nonneutral Collective Focusing

The original analysis of a collective focusing lens [Robertson, 1982] assumed quasi-neutral compression, which is provided by the condition that the electron cyclotron frequency corresponding to the magnetic field inside a solenoid, Ω_e, is greater than the electron plasma frequency of an incident neutralized beam, ω_{pe}^0 (Sec. 5.2). However, it is of particular importance for several practical applications including the Neutralized Drift Compression Experiment-I to investigate the collective focusing in a strong magnetic field with $\Omega_e > \omega_{pe}^0$. In this case, the quasi-neutrality condition inside the beam can break down, and it is important to determine the distribution of the radial electric field inside the beam, which is now supported by a pronounced charge separation. In this section we

investigate general features of this nonneutral collective focusing (Sec. 5.4.1), and discuss its influence on the beam dynamics in the Neutralized Drift Compression Experiment-I (Sec. 5.4.2).

5.4.1 Collective Electron Dynamics during Nonneutral Compression

We start the analysis by determining the conditions for a pronounced charge separation to occur inside an ion beam that carries an equal amount of the electron background into a strong solenoidal magnetic field. Figure 5.11(a) illustrates a neutralized ion beam that propagates through an increasing solenoidal magnetic field, B(z). For simplicity, we assume a uniform radial beam density distribution for the initial beam state, with the flat-top density n_{b0} and the outer beam radius r_{b0}. The ion beam is moving from a region of zero magnetic field, where its charge and current are completely neutralized by a co-moving monoenergetic electron beam. We denote the electron cyclotron frequency corresponding to the maximum value of the magnetic field B_0 inside a magnetic solenoid by $\Omega_e \equiv eB_0/m_e c$, and assume that $\Omega_e > \omega_{pe}^0 = \sqrt{4\pi e^2 n_{b0}/m_e}$. Note that the condition $\Omega_e > \omega_{pe}^0$ itself does not necessarily imply that the quasi-neutrality is not maintained during the transverse compression. Indeed, for the case of light and low-energy beam ions, and weak longitudinal gradients of the solenoidal magnetic field, the quasi-neutrality will be maintained inside the beam, provided the increase in the electron plasma frequency due to the ion beam compression occurs more rapidly than the increase in the magnetic field, i.e.,

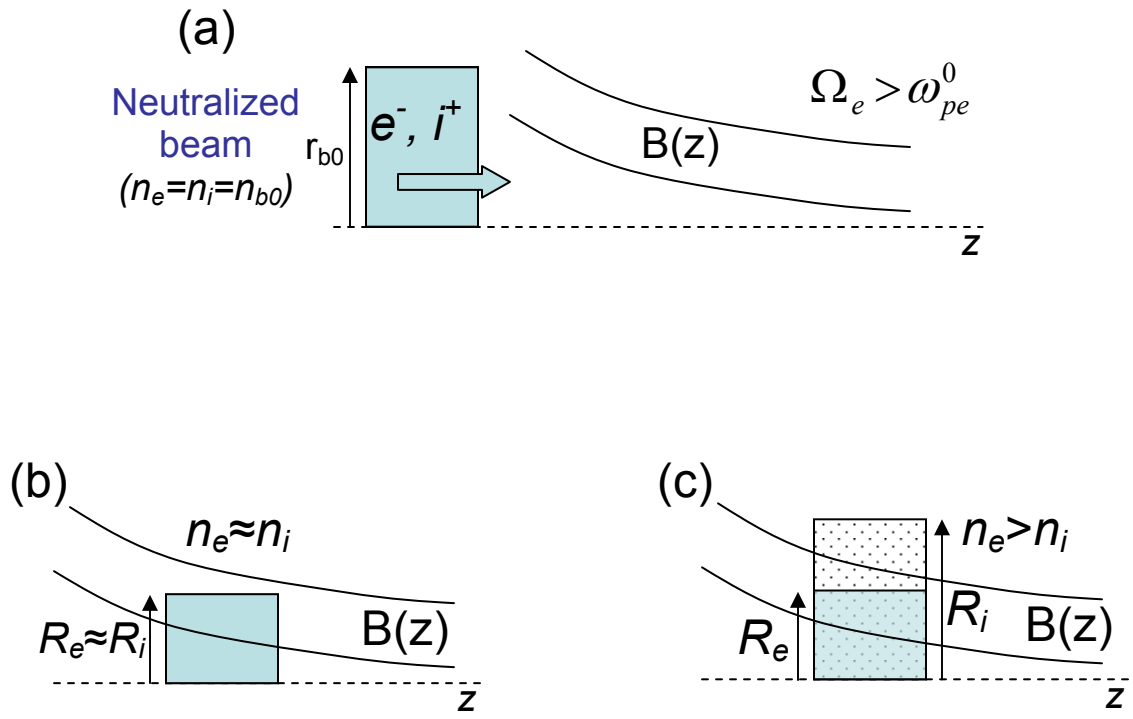

Figure 5.11: (Color) (a) Schematic illustration of a neutralized ion beam propagating along a strong solenoidal magnetic field with $\Omega_e > \omega_{pe}^0$. Two possible regimes of collective beam focusing correspond to: (a) quasi-neutral collective focusing where quasi-neutrality is maintained inside the beam during compression, and (b) nonneutral collective focusing associated with a pronounced build-up of negative charge around the beam axis.

$$\omega_{pe}^{b}(z) >> \omega_{ce}(z). \tag{5.11}$$

Here, $\omega_{pe}^{b} = \sqrt{4\pi e^2 n_i(z)/m_e}$, $\omega_{ce} = eB(z)/m_e c$, and $n_i(z)$ is the local value of the ion beam density. For simplicity, we assume a short ion beam pulse with characteristic length that is much smaller than the longitudinal length-scale for variations of the magnetic field. The condition in Eq. (5.11) can be expressed as

$$\frac{R_i(z)}{r_{b0}} << \frac{\omega_{pe}^{0}}{\omega_{ce}(z)}, \tag{5.12}$$

and the evolution of the ion beam outer radius, $R_i(z)$, for the case of a quasi-neutral compression is given by

$$\frac{d^2 R_i}{dz^2} = -\frac{m_e}{m_b}\frac{R_i}{4}\frac{\omega_{ce}^2}{v_b^2}. \tag{5.13}$$

In the limit of a high-energy heavy-ion beam and steep magnetic field gradients, Eqs. (5.12)-(5.13) may not have a self-consistent solution. In this case the quasi-neutrality inside the beam is no longer maintained, and the nonneutral collective focusing occurs.

In order to determine the transverse beam dynamics for the case of nonneutral collective focusing, one needs to investigate the distribution of the strong radial electric field inside the beam. For this purpose we have performed advanced numerical simulations with the particle-in-cell code LSP [LSP, 1999]. Note that the schematic of the present simulations shown in Fig. 5.12 is similar to the one used in Sec. 5.3.1 (Fig. 5.3) for the simulation of the idealized final beam focus in the NDCX-I. However, here the distance between the plasma layer and the focusing solenoid is increased in order to

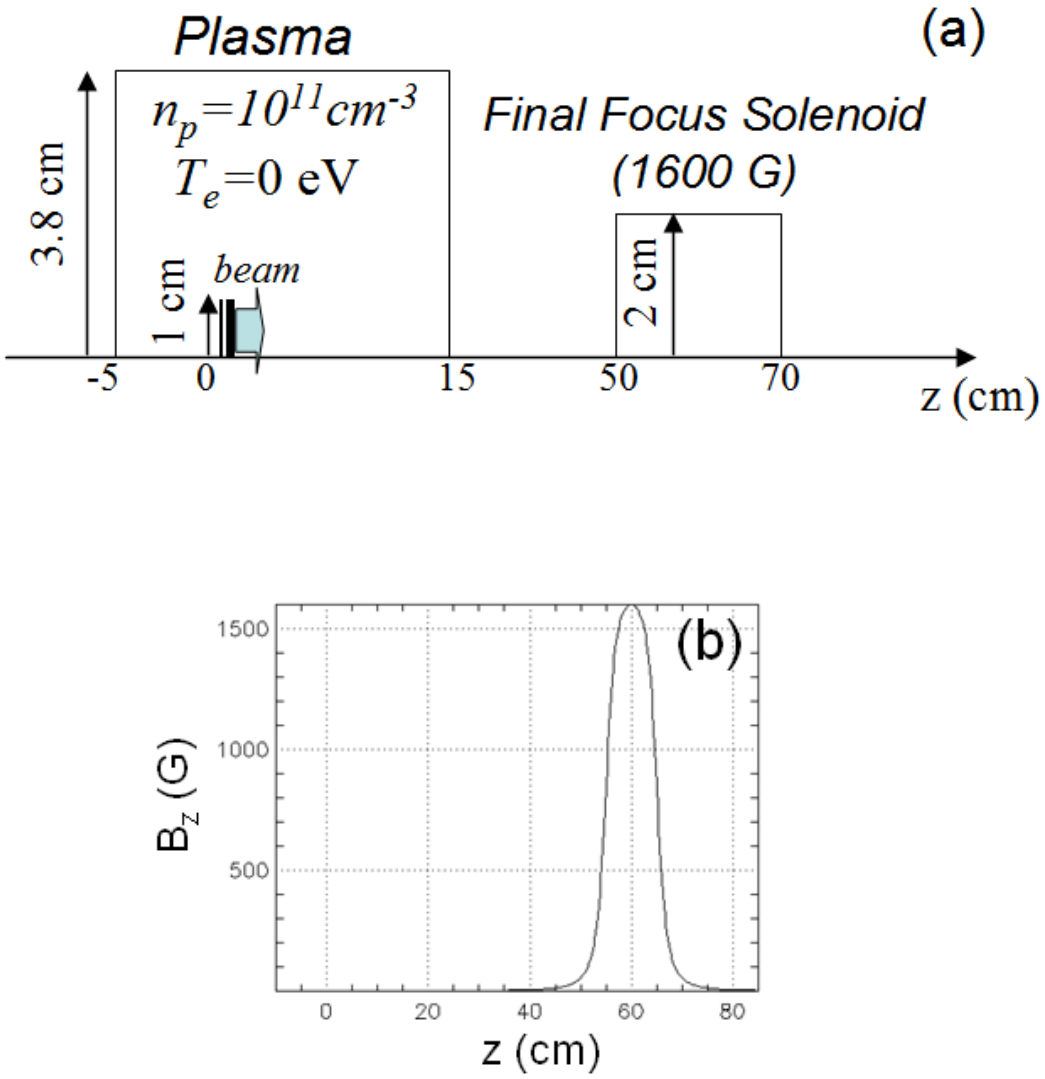

Figure 5.12: Collective focusing in a strong solenoidal magnetic field with $\Omega_e = 5\omega_{pe}^0$. (a) Schematic of the LSP simulations. (b) Longitudinal profile of the applied axial magnetic field.

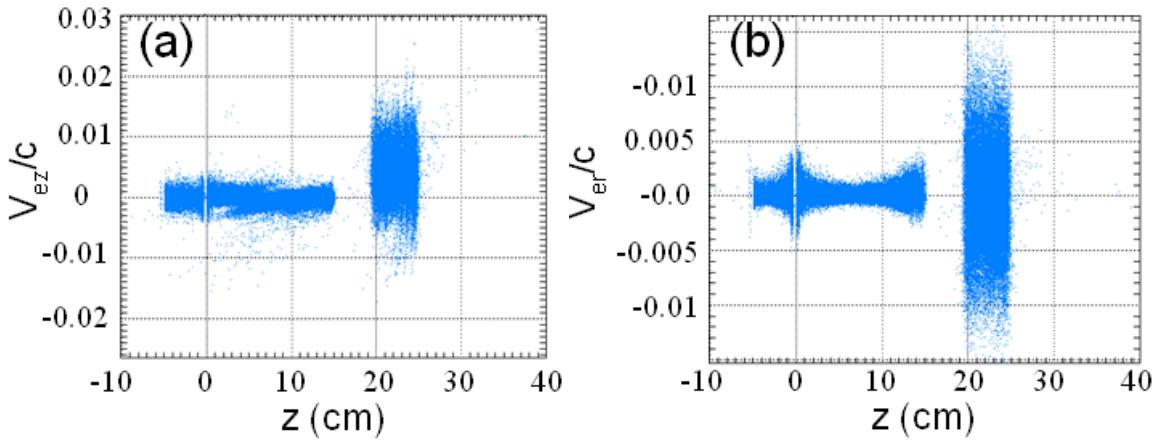

Figure 5.13: (Color) Thermal spreading of the co-moving neutralizing electron beam. Plots correspond to (a) longitudinal phase-space (V_{ez}/c, z), and (b) the transverse velocity spreading (V_{er}/c, z). The velocity spreading of the initial cold background plasma electrons located from z=-5 cm to z=15 cm is attributed to numerical heating. The time instant corresponds to t=200 ns, and the results are obtained with numerical LSP simulations.

decrease the value of the magnetic fringe fields inside the plasma. Furthermore, in an attempt to provide quiescent neutralization of the ion beam as it leaves the background plasma layer, cold plasma electrons are assumed, and a gradual decrease in the plasma density is introduced near the downstream end of the layer, that is n_p=10^{11} cm^{-3} for z<12 cm and then theplasma density is linearly decreased to zero over a distance of l_{edge}=8 cm. Note that the numerical simulations with axial grid spacing $\Delta z = 0.2$ cm and time step $\Delta t = 0.005$ ns demonstrate that the velocity spread in the electron distribution is of order the ion beam velocity (Fig. 5.13). To model the beam, we take r_{b0}=1 cm, n_{b0}=10^{10} cm^{-3}, Z_b=1, β_b=0.0042, l_b≈5 cm, and infinitely massive beam ions are assumed for simplicity.

The maximum value of the magnetic field inside the focusing solenoid is B_0=1600 G, which corresponds to $\Omega_e = 5\omega_{pe}^0$, and the longitudinal profile of the on-axis magnetic field is shown in Fig. 5.12(b).

The results of the numerical simulations for an illustrative time t=500 ns, when the beam is at the center of the magnetic solenoid, are shown in Fig. 5.14. As the co-moving electrons enter the magnetic solenoid the electrons acquire a strong azimuthal rotation due to conservation of canonical angular momentum [Fig. 5.14(a)]. The resulting $V \times B$ magnetic focusing force, along with the centrifugal force, are compensated by the strong radial self-electric field [Fig. 5.14(b)]. However, for considered parameters $\omega_{pe}^b = \omega_{pe}^0 = \Omega_e / 5$, the condition in Eq. (5.11) is violated, and a strong charge separation occurs in order to support the radial self-electric field [Fig. 5.14(c)]. Simulations show [Fig. 5.14(b)] that inside the electron beam, i.e., $r<R_e(z)$, the electric field is nearly linear, and is given by

$$E_r = -V_{e\theta} B_0 / c + m_e V_{e\theta}^2 / (er) = -m_e \omega_{ce}^2(z) r / 4e . \tag{5.14}$$

Here, $R_e(z)$ is the characteristic outer radius of the electron beam, and $R_e<R_i$ [Fig. 5.14(c)]. The nonlinear electric field in the region $R_e < r < R_i$ can be determined from Poisson's equation

$$\frac{1}{r}\frac{\partial}{\partial r}\left(r \frac{\partial \varphi}{\partial r} \right) = -4\pi Z_b e n_i(z), \tag{5.15}$$

which is to be solved subject to the boundary condition,

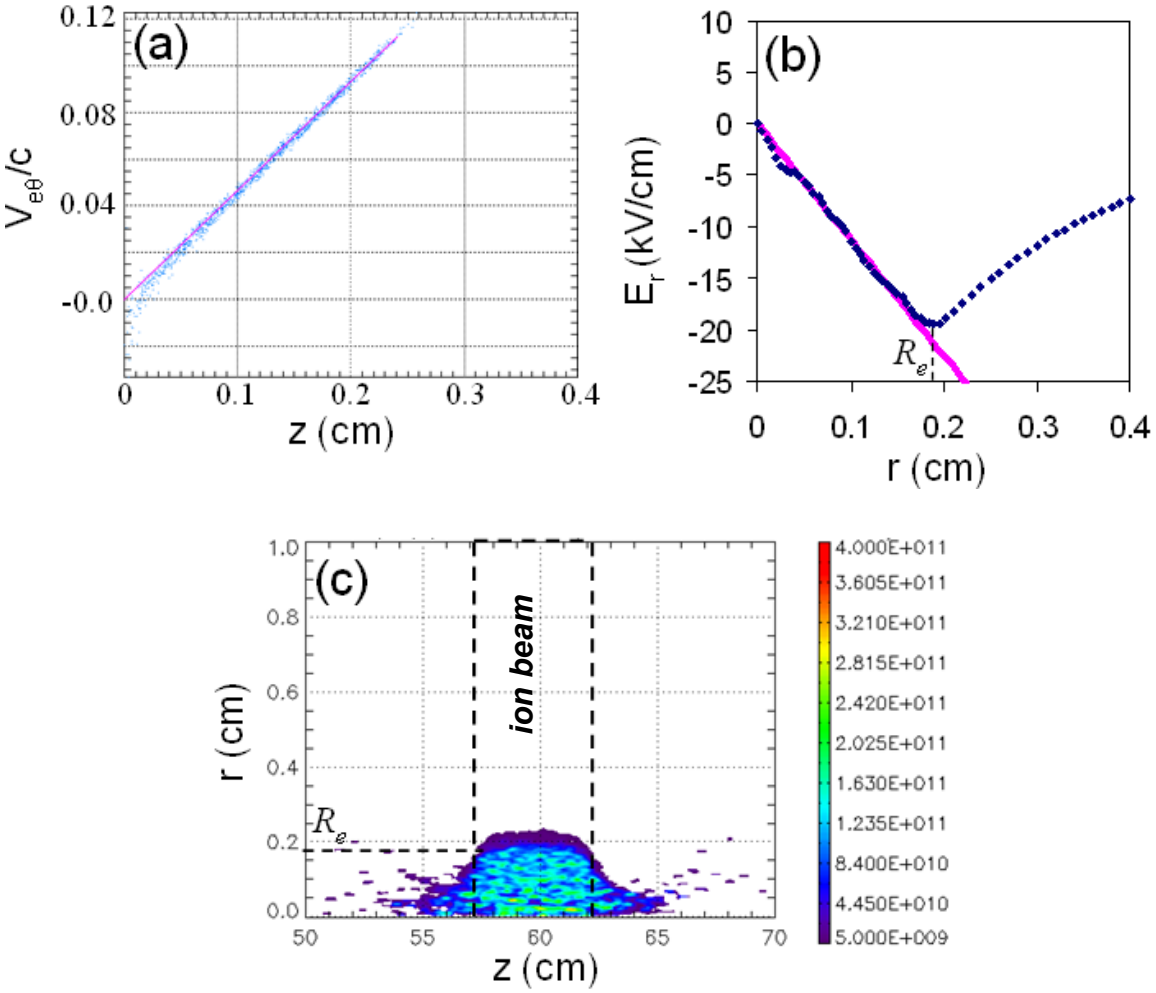

Figure 5.14: (Color) Nonneutral collective focusing. Shown are plots of (a) the electron phase-space ($V_{e\theta}/c$,r), where the blue dots correspond to the results of the LSP simulations, and the estimate $V_{e\theta}=\omega_{ce}r/2$ is shown by the solid pink line; (b) radial dependence of the radial electric field at the center of the magnetic solenoid, z=60 cm, where the blue dots correspond to the results of the LSP simulations, and the analytical estimate in Eq. (5.14) is shown by the solid pink line; and (c) electron density obtained in the LSP simulations. The dashed black lines in Frame (c) outline the ion beam, and R_e corresponds to the characteristic electron beam radius. The time for the illustrated results corresponds to t=500 ns.

$$\left.\frac{\partial \varphi}{\partial r}\right|_{r=R_e(z)} = m_e \frac{\omega_{ce}^2(z) R_e(z)}{4e} . \tag{5.16}$$

In Eq. (5.15), the longitudinal derivatives have been neglected provided the beam is sufficiently long with $l_b >> r_{b0}$. Note that the solution to Eqs. (5.15)-(5.16) is, in general, nonlinear even for a uniform ion beam density profile. As a result, the aberration effects caused by nonlinearities in the focusing electric field can significantly degrade the transverse focal spot.

In order to complete the description of the generated radial electric field, one needs to determine the evolution of the electron beam radius. The electron beam is being dragged into a strong solenoidal magnetic field by an intense heavy ion beam. The rotational energy of the electrons and the electrostatic field energy arise from the directed energy of the ion beam; and the magnetic pressure force is globally balanced by the longitudinal variations of the electrostatic potential. However, the density profile of the co-moving electron beam can still diffuse in the longitudinal direction as the beam propagates in the increasing magnetic field [Fig. 5.14(c)]. Consistent with that fact, a fraction of the electron beam particles with negative values of longitudinal velocity has been observed in the simulations. In the present approximate analysis, we neglect the longitudinal broadening of the electron beam density profile, and assume that $n_e R_e^2 \sim n_{b0} r_{b0}^2$. For the case of a sufficiently long beam with $l_b >> r_{b0}$, it follows from Eq. (5.14) that the electron beam density is uniform, and is specified by

$$\frac{1}{2}\frac{\omega_{ce}^2}{\omega_{pe}^2} = 1 - \frac{Z_b n_i}{n_e}, \tag{5.17}$$

where $\omega_{pe}^2 = 4\pi e^2 n_e(z)/m_e$. For the case of strong nonneutral compression with $n_e >> Z_b n_b$, it readily follows from Eq. (5.17) that the condition $\omega_{pe}(z) \approx \omega_{ce}(z)/\sqrt{2}$ is maintained during the compression of the co-moving electron beam. Making use of charge conservation of the co-moving electron beam, we obtain for the case of strong nonneutral compression that

$$R_e(z) \sim \sqrt{2} r_{b0} \frac{\omega_{pe}^0}{\omega_{ce}(z)}. \tag{5.18}$$

Equations (5.14)-(5.16) together with Eq. (5.18) provide an approximate self-consistent estimate of the radial focusing electric field inside the ion beam. We now discuss the validity of Eq. (5.14) that demonstrates the balance between the $V \times B$ magnetic focusing force, the centrifugal force, and the self-electric radial force acting on the background electrons. Equation (5.14) follows from the more general Eq. (5.1), provided the electron inertial term, i.e., the first term on the left-hand-side of Eq. (5.1), can be neglected. Making use of Eq. (5.18), it follows that the force-balance equation (5.14) is valid provided

$$l_m^2 >> v_b^2/\omega_{ce}, \tag{5.19}$$

where l_m is the characteristic length-scale for variations of the applied magnetic field.

In conclusion, it is interesting to point out that the co-moving electron beam compression does not follow the magnetic field lines. Indeed, the radius of a constant

magnetic flux tube is given by $R_{flux} \propto 1/\sqrt{\omega_{ce}}$, whereas the electron beam executes steeper compression with $R_e \propto 1/\omega_{ce}$. Note, however, that for this system the electron gyro-radius is large, and comparable to the beam radius, and furthermore, the electric field is strong. Therefore, the "drift approximation", which implies conservation of a particle's magnetic moment (magnetic flux through a particle's orbit), and is often used for description of magnetic fusion plasma flows, is not valid for the present system.

5.4.2 Influence of Nonneutral Collective Focusing on the Beam Dynamics in the NDCX-I

The design of the NDCX-I final focus section has included a relatively long, $l_g \approx 12$ cm, gap between the downstream end of the neutralizing drift section and the upstream end of the 8 T final focus solenoid (FFS). The presence of the gap has been primarily stipulated by the gate valve included in the NDCX-I configuration, as shown in Fig. 5.2. Recent experimental and numerical studies have demonstrated a lack of neutralizing plasma in the gap region. Although moderate beam space charge ($n_b \sim 10^9$-10^{10} cm^{-3}) can be compensated by the plasma electrons dragged by the ion beam from the drift region, collective phenomena occurring in the neutralized beam as it traverses the fringe magnetic field at the upstream end of the final focus solenoid can significantly influence transverse focusing of the ion beam. This field is of the order of several kG, and therefore strong enough that the electron cyclotron frequency is small compared to the plasma

frequency, i.e., $\omega_{pe} < \omega_{ce}$, where $\omega_{pe} = \sqrt{4\pi n_b e^2 / m_e}$ and $\omega_{ce} = eB/m_e c$ are the electron plasma and cyclotron frequencies, respectively. For parameters characteristic of NDCX-I the condition in Eq. (5.11) is not satisfied, and collective nonneutral focusing occurs inside the gap [Sec. 5.4.1]. An excess of beam ion charge develops at intermediate radii, while an excess of negative charge develops in the gap region near the axis of the system, providing a strong radial focusing field, which can affect the beam's final focus.

To investigate the influence of collective effects inside the gap on transverse focusing of the beam, we have performed idealized numerical simulations with the LSP particle-in-cell code (Fig. 5.15). In the simulations, we take the densities of the neutralizing plasma inside the drift section created by a ferroelectric plasma source, and the neutralizing plasma inside the final focus solenoid created by cathodic-arc plasma sources to be 10^{10} cm^{-3} and 10^{12} cm^{-3}, respectively. The electron temperature for both plasmas is assumed to be 3 eV. The plasmas are treated fully kinetically, allowing for the background electrons to flow into the gap should the forces on them induce such motion. Singly ionized Potassium (K^+) beam ions with an energy of 320 keV are injected into the simulation through an aperture of r_{b0}=1 cm located inside the drift section. To model the effects of the beam prepulse, for the first 40 ns, of the total beam pulse the beam current was set to be 0.028 A (prepulse), and for the second 40 ns, the beam current was set to be 0.12 A (compressed portion of the beam). Neither the initial convergence angle nor the longitudinal velocity tilt were included in the simulations.

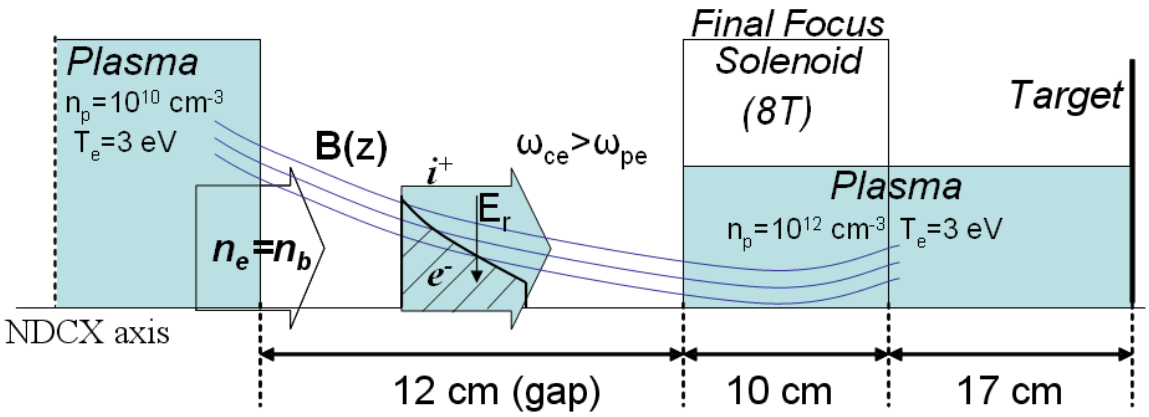

Figure 5.15: (Color) Influence of collective focusing inside the gap between the neutralizing drift region and the final focus solenoid on the ion beam dynamics in NDCX-I. Schematic of the LSP numerical simulation configuration showing regions filled with a neutralizing plasma.

The results of the numerical simulations are shown in Figs. 5.16-5.18. Figures 5.16(a) and 5.16(b) show the ion beam density and the density of the electron background dragged from the drift section. The radial self-electric field at the same time instant is shown in Fig. 5.16(c). To demonstrate the influence of the radial electric focusing inside the gap we plot the beam density near the downstream end of the final focus solenoid [Fig. 5.17(a)], and compare it to the beam density in the "ideal neutralization" case where a dense background plasma initially fills the entire gap [Fig. 5.17(b)]. One can see that collective effects in the gap between the neutralizing plasmas induce premature beam focusing. As the beam propagates from the downstream end of the final focus solenoid to the target, a slight decrease in the on-axis beam density is observed. Figure 5.18 (a) shows the beam density at the target plane, and Figure 5.18(b) corresponds to the "ideal neutralization" case. Note that due to the anharmonic field of the collective focusing

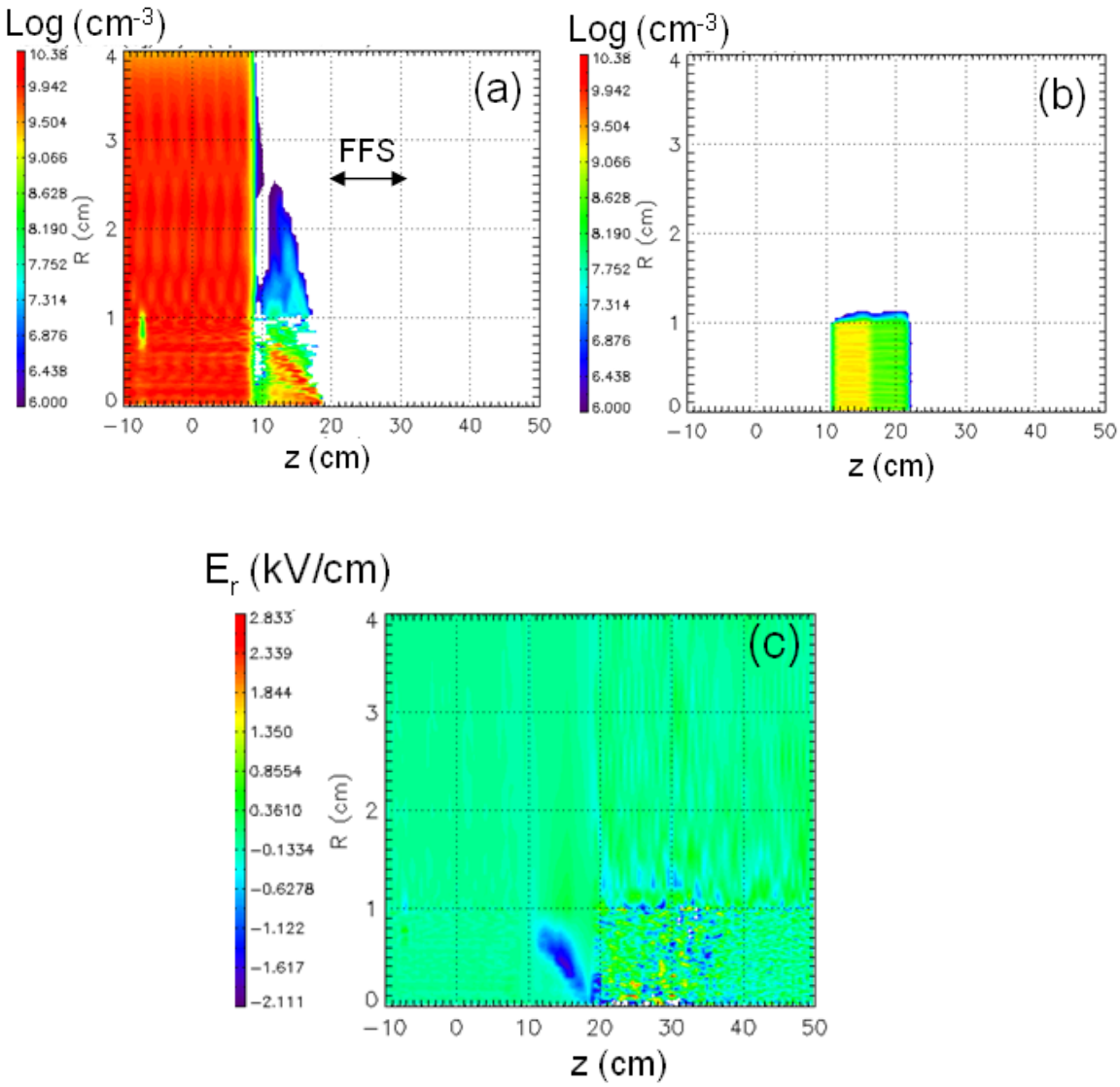

Figure 5.16: (Color) LSP simulations of collective nonneutral focusing inside the gap between the neutralizing plasmas at t=230 ns. Shown are plots of (a) number density of the electrons dragged from the drift section, (b) ion beam density, and (c) radial self-electric field. The double-arrowed line in Frame (a) illustrates the position of the final

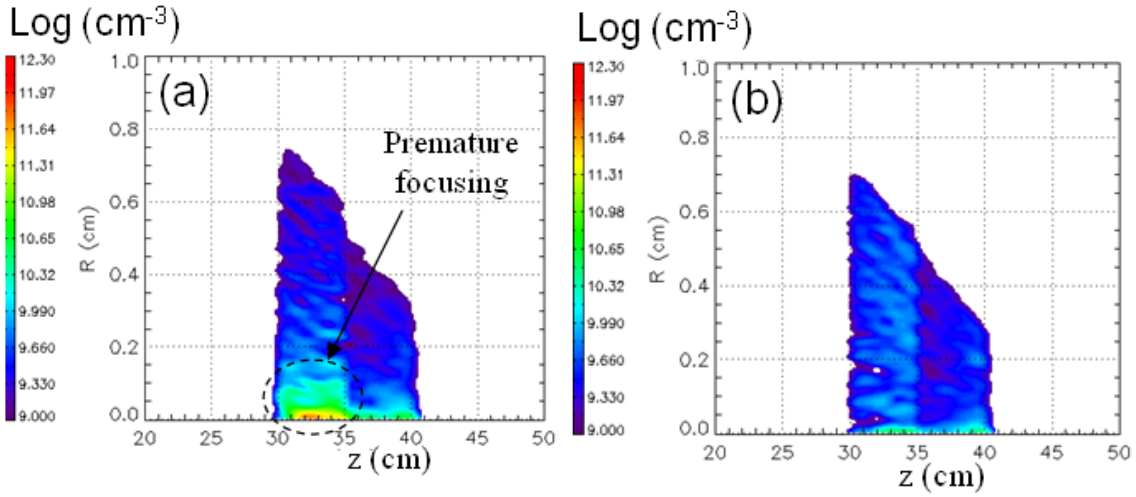

Figure 5.17: (Color) Ion beam density at the downstream end of the final focus solenoid at t=380 ns. (a) The background plasma is initially absent inside the gap between the drift section and the final focus solenoid. (b) Ideal neutralization case corresponding to the initial presence of a neutralizing plasma with density n_p=10^{10} cm^{-3} across the entire gap. Results are obtained with the LSP numerical simulations.

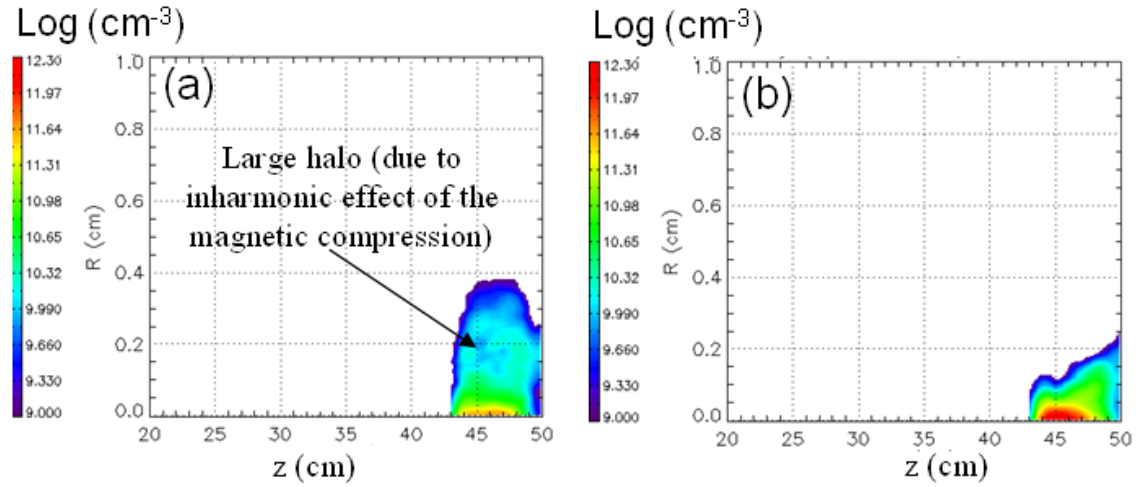

Figure 5.18: (Color) Ion beam density at the target region at t=490 ns. (a) The background plasma is initially absent inside the gap between the drift section and the final focus solenoid. (b) Ideal neutralization case corresponding to the initial presence of a neutralizing plasma with density n_p=10^{10} cm^{-3} across the entire gap. Results are obtained with the LSP numerical simulations.

force, a large tail of halo ions develops around the focused beam core, and the peak beam density is reduced by a factor of about four relative to the "ideal neutralization" case [compare Figs. 5.18(a) and 5.18(b)].

The influence of collective focusing inside the gap on the transverse beam focusing properties was studied for different values of the ion beam density. It was found that the radial electric field is greater for higher beam densities. Therefore, the degrading influence of collective effects is less pronounced for the beam prepulse than for the compressed portion of the beam. This is consistent with the experimental observations demonstrating better transverse focusing of the beam prepulse. In other studies, we found that the collective focusing effect persists even for longer beam pulses, e.g., long enough (410 ns) that the beam itself provides a conducting path across the gap. Finally, we note that the effects of the collective focusing inside the gap were also investigated making use of the numerical simulations performed with the WARP code. Both codes yielded similar results.

In order to mitigate the deleterious effects induced by collective nonneutral focusing inside the gap, the configuration of the NDCX-I has been optimized. The gate valve has been relocated upstream of the beamline, allowing for a shorter gap of only 5 cm. The experiments on the ion beam simultaneous compression including final focusing by the 8 T final focus solenoid and the shorter gap are currently being carried out on the NDCX-I facility. Finally, note that the gap length of 5 cm have been used in the simulations presented in previous sections.

5.5 Collective Focusing of a High-Intensity Ion Beam with $r_b \geq c/\omega_{pe}$

As noted earlier, to assure small perturbations in the applied solenoidal magnetic field produced by the azimuthal component of the electron current, the beam radius has to be smaller than the collisionless electron skin-depth, i.e., $r_b << c/\omega_{pe}$. In this section, we present an analytical self-consistent calculation of the magnetic field perturbation, and discuss the collective focusing lens operation for arbitrary values of $r_b \omega_{pe}/c$.

Conservation of the canonical angular momentum for co-moving electrons gives (sec. 5.1)

$$m_e V_{e\theta} = \frac{e}{c} A_\theta , \tag{5.20}$$

where $V_{e\theta}$ is the azimuthal component of the electron velocity, and initially non-rotating electrons are considered. Assuming that the beam radius is smaller than the beam pulse length, and smaller than the characteristic length-scale for variations of the applied solenoidal magnetic field, i.e., $r_b << l_b, l_m$, we obtain from Ampere's equation

$$\frac{\partial}{\partial r}\left(\frac{1}{r}\frac{\partial}{\partial r}\left(rA_\theta\right)\right) = \frac{4\pi}{c} e n_e V_{e\theta} . \tag{5.21}$$

Assuming, for simplicity, a uniform radial beam density profile with $n_e = n_i = n_b$ for $r \leq r_b$, and $n_e = n_i = 0$ for $r > r_b$, Eq. (5.21) is to be solved subject to the boundary condition

$$\left[\frac{1}{r}\frac{\partial}{\partial r}\left(rA_\theta\right)\right]_{r=r_b} = B_s\,, \tag{5.22}$$

where B_s is the applied solenoidal magnetic field. Combining Eqs. (5.20) and (5.21) gives

$$\frac{\partial}{\partial \bar{r}}\left(\frac{1}{\bar{r}}\frac{\partial}{\partial \bar{r}}\left(\bar{r}A_\theta\right)\right) = A_\theta\,, \tag{5.23}$$

where $\bar{r} = r_b\omega_{pe}/c$. Solving Eqs. (5.22)-(5.23), it follows that the longitudinal component of the total magnetic field, i.e., $B_z = r^{-1}\,\partial\left(rA_\theta\right)/\partial r$, is given by

$$B_z = B_s\,\frac{I_0\left(r\omega_{pe}/c\right)}{I_0\left(r_b\omega_{pe}/c\right)}, \tag{5.24}$$

where $I_0(x)$ is the modified Bessel function. Plots of the total magnetic field $B_z(r)$, i.e., the sum of the beam-generated and the applied magnetic fields, for different values of $r_b\omega_{pe}/c$ are shown in Fig. 5.19. Note that attenuation of the applied magnetic field results in a decrease in the focusing electric field since $E_r = -V_{e\theta}B_z/2c$. Furthermore, nonlinearities in the magnetic field profile provide aberrations that can degrade the transverse focus. However, it is interesting to note that even for large values of $r_b\omega_{pe}/c$, the outer edge of the beam still experiences collective focusing (Fig. 5.19). It is therefore of great interest to carry out detailed self-consistent studies including the effects of the beam radial profile evolution, in order to estimate the applied magnetic field required to collimate or focus the intense ion beam.

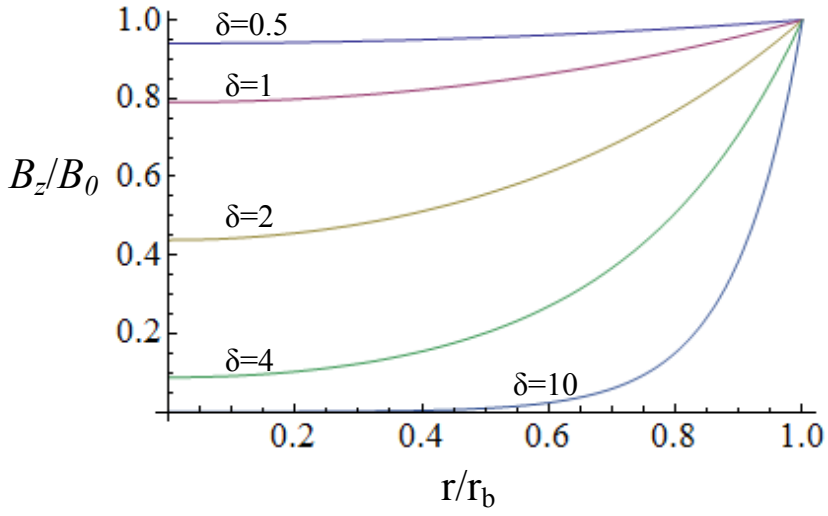

Figure 5.19: (Color) Radial dependance of the of the total magnetic field, i.e., the sum of the beam-induced and applied magnetic fields, for different values of $\delta = r_b \omega_{pe} / c$.

5.6 Summary and Discussion

In the present chapter the collective focusing scheme in which a weak magnetic lens provides strong focusing of an intense ion beam pulse carrying an equal amount of neutralizing electron background has been reviewed. This collective focusing can allow for the use of weak (several hundred Gauss) magnetic fields instead of the several Tesla fields used for conventional magnetic lens, thus significantly facilitating the technical realization of ion beam focusing for several applications of high energy density physics. As a practical example, the feasibility of tight collective focusing of intense ion beams for the Neutralizing Drift Compression Experiment-I (NDCX-I) has been demonstrated in this Chapter with the advanced numerical simulations.

The physical limits of collective ion beam focusing in NDCX-I have been discussed. In particular, the influence of the electron heating during the compression on the collective beam focusing has been investigated. It has been demonstrated that an increase in the thermal electron pressure, results in a decrease in the collective-focusing self-electric force. The analytical estimate of the effective electron temperature corresponding to the loss of collective focusing has been found to be consistent with the results of numerical simulations.

The original analysis of collective focusing, assuming quasi-neutral transverse beam compression with $\omega_{ce} << \omega_{pe}$, has been extended to the case of nonneutral collective focusing, that can occur when the beam propagates in a strong solenoidal magnetic field with $\omega_{pe}^{b} = \sqrt{4\pi e^2 n_i / m_e} < \omega_{ce}$. This case can be of particular importance for several practical applications, including laser-production of high-energy ions, where a strong solenoidal magnetic field is used to collimate the divergent ion beam [Harres *et al*., 2010]; and a heavy-ion fusion driver, where a strong magnetic solenoid is often used for final beam focusing [Yu *et al*., 2005]. For the case of nonneutral collective focusing, the electron background executes a steeper compression compared to that of the beam ions, and as a result an excess of negative charge develops near the solenoidal axis. It has been shown for the case of strong nonneutral compression, with $n_e >> n_i$ near the beam axis, that $\omega_{pe} \approx \omega_{ce} / \sqrt{2}$ is maintained inside the electron beam, and that the electron beam radius decreases as $R_e \propto 1/\omega_{ce}$. The focusing radial electric field inside the electron

beam, $r < R_e$, is found to be linear with $E_r = -m_e \omega_{ce}^2 (z) r / 4e$. However nonlinearities in the region $R_e < r < R_i$ cause aberrations, and can degrade the quality of the transverse ion beam focus. The influence of nonneutral collective focusing on the ion beam dynamics in NDCX-I has been investigated. It has been demonstrated that premature focusing and large halo development can occur due to intense collective nonneutral focusing in the gap between the drift section and the final focus solenoid.

Finally, the original analysis of the collective focusing, which assumes small perturbations of the applied solenoidal magnetic field implied by $r_b << c/\omega_{pe}$, has been extended to the case of an arbitrary ratio of $\omega_{pe} r_b / c$. The perturbation in the solenoidal magnetic field produced by the azimuthal component of the electron beam current has been calculated self-consistently, and strong nonlinearities in the total magnetic field have been demonstrated for $r_b \geq c/\omega_{pe}$. However, it has been found that even for large values of $r_b \omega_{pe} / c$, the outer edge of the ion beam pulse still experiences efficient collective focusing.

Chapter 6

Conclusions and Future Research

Present design concepts for heavy ion drivers for ion-beam-driven high energy density physics and warm dense matter applications, and for heavy ion fusion involve the acceleration and compression of intense heavy ion beams to a small spot size on the target. Ion beam acceleration and transport in vacuum is provided by a periodic focusing lattice. Then, a dense background plasma is used to neutralize the beam space-charge during the compression process. Finally, additional transverse focusing is typically provided by a strong (several Tesla) final focus solenoid. In this thesis, several critical problems of intense ion beam transport in an ion driver have been investigated by means of advanced numerical particle-in-cell simulations and reduced analytical models. In particular, a numerical method for the formation of a quasi-equilibrium beam distribution matched to a periodic focusing lattice by means of the adiabatic turn-on of the oscillating focusing field has been developed. The production of halo particles due to beam mismatch has been discussed, and a novel spectral method for the quantitative definition of beam halo has been proposed. Also, the propagation of an intense ion beam through a neutralizing plasma has been investigated with emphasis on the effects of a weak solenoidal magnetic field applied along the beam propagation direction. It has been found that ion beam self-focusing can be significantly enhanced by the application of a weak magnetic field of order 100 G. Finally, the concept of collective focusing of intense ion

beam pulses has been reviewed, and the feasibility of a tight collective focus of an ion beam pulse in the Neutralized Drift Compression Experiment has been demonstrated in numerical simulations.

The results presented in each chapter of this thesis are summarized in Sec. 6.1, and Sec. 6.2 suggests several future research tasks.

6.1 Conclusions

In this section a summary of the main results of this thesis research is presented.

In **Chapter 2** of this thesis, the formation of a quasi-equilibrium beam distribution matched to an alternating-gradient quadrupole focusing lattice by means of the adiabatic turn-on of the oscillating focusing field was studied using particle-in-cell simulations. Quiescent beam propagation over several hundred lattice periods was demonstrated for a broad range of beam intensities and vacuum phase advances describing the strength of the oscillating focusing field. Properties of the matched beam quasi-equlibrium obtained in numerical simulations were investigated and compared with the predictions of the analytical theory developed by Davidson *et al*. in [Davidson *et al*., 1999]. In accordance with the theory, the numerical simulations demonstrated self-similar evolution of the beam density profile for $\sigma_v \le 66^0$. However, for higher values of vacuum phase advance (for instance, $\sigma_v = 87.5^0$) the self-similarity feature became less accurate over a wide range of beam intensities, which demonstrates the validity limits of the

theory. The numerical scheme for describing formation of a quasi-equilibrium beam distribution, matched to an alternating-gradient quadrupole focusing lattice, was generalized to the case of a periodic-focusing solenoidal lattice. Furthermore, various distributions were considered for the initial beam equilibrium. The self-similar evolution of the matched-beam density profile was observed for general choice of initial distribution function and lattice type.

In **Chapter 3** of this thesis, the transverse compression of an intense ion beam propagating through an alternating-gradient quadrupole lattice was investigated. In particular, the conditions on how smooth (adiabatic) the lattice transition should be to assure that beam matching is maintained during the compression were determined. For the case of nonadiabatic compression, halo particle production by a beam mismatch acquired during the compression stage was studied. In order to perform a quantitative analysis of this effect, a novel spectral method for halo particle definition was developed. The method is based on the observation that the betataron frequency distribution of a mismatched intense beam has a "bump-on-tail" structure attributed to the beam halo particles. It was found that most of the bump is located to the right of the half-value of the mismatch oscillation frequency, which allowed us to formulate the following simple quantitative definition of a halo particle. *If the particle betatron frequency is greater than one-half of the mismatch oscillation frequency then it designated as a halo particle*. The method based upon the spectral analysis of a mismatched beam distribution was also applied to other critical problems of intense beam transport. In particular, it was demonstrated that during strong mismatch relaxation most of the beam halo is generated

on a time-scale shorter than the time-scale for the beam core relaxation. Furthermore, it was shown that the core relaxation process also leads to an increase in the beam emittance. Finally, the spectral analysis of a beam distribution loaded into a quadrupole lattice for the case where the system parameters lie near the transport stability limit, $\sigma_{vac}^2 - \sigma^2 \approx (2\pi/3)^2/2$, was performed. It was found that as the system parameters approach the stability limit, the core of the beam betatron distribution does not change significantly, whereas the tail of the distribution increases.

In **Chapter 4** of this thesis, the influence of weak solenoidal magnetic fields of order 100 G on intense ion beam pulse transport through a dense background neutralizing plasma was investigated. The weak fringe magnetic field (~100 G) of a strong (several Tesla) final focus solenoid can penetrate deep into the long drift section filled with a neutralizing plasma, making this problem to be of particular importance for the design of an ion driver. The analysis presented in this thesis extended studies of ion beam transport through a background plasma along a solenoidal magnetic field by Kaganovich *et al*. [Kaganovich *et al*., 2008] to the important regime of moderate magnetic field strength satisfying $\omega_{ce} \geq 2\beta_b\omega_{pe}$. Here, ω_{ce} and ω_{pe} are the electron cyclotron frequency and electron plasma frequency, respectively, and $\beta_b = V_b/c$ is the directed ion beam velocity normalized to the speed of light. The electromagnetic field perturbations excited by the ion beam pulse in this regime were calculated analytically and verified by comparison with the numerical simulations. It was demonstrated that the total electromagnetic field perturbation excited by an ion beam pulse with a smooth radial density profile can be

conveniently represented as the sum of a local-field component, rapidly decaying to zero outside the beam pulse, and a wave-field component that can extend far outside the beam. It was found in the regime where $\omega_{ce} \cong 2\beta_b \omega_{pe}$ that there is strong excitation of the wave-field component corresponding to whistler waves, and the possible use of this effect for diagnostic purposes has been discussed. However, the contribution of wave-field excitations to the transverse component of the Lorentz force can have opposite signs for the beam head and the beam tail. Therefore, for practical application involving control of the beam aperture, it is important to identify a parameter regime where the local component of the electromagnetic field perturbation, which provides focusing over the entire length of the ion beam pulse, has the dominant influence on the beam transverse dynamics. It was demonstrated, in the regime where $\omega_{ce} >> 2\beta_b \omega_{pe}$ and $r_b >> V_b \left(1 + \omega_{ce}^2 / \omega_{pe}^2\right)^{1/2} / \omega_{ce}$, that the local-field component primarily determines the transverse dynamics of the beam particles, and the wave fields produce a negligible transverse force. Moreover, a positive charge of the ion beam pulse becomes over-compensated by the plasma electrons, and the associated strong transverse-focusing self-electric field has the dominant influence on the beam ions, compared to the self-magnetic field, provided $V_b \left(1 + \omega_{ce}^2 / \omega_{pe}^2\right)^{1/2} / \omega_{ce} << r_b << \left(c / \omega_{pe}\right)\left(\omega_{ce} / \beta_b \omega_{pe}\right)$. It was also shown, for the case where the beam radius is small compared to the electron skin depth, that the self-focusing force is significantly enhanced compared to the self-focusing force acting on the beam particles in the absence of an applied magnetic field. In addition, the local

diamagnetic plasma response was observed in the numerical simulations, and was also predicted analytically for $\omega_{ce} >> 2\beta_b\omega_{pe}$. These results were found to differ significantly from the case $\omega_{ce} < 2\beta_b\omega_{pe}$, where the transverse electric field is defocusing, and the plasma response is paramagnetic. Finally, the effect of the plasma-induced enhanced self-focusing of an intense ion beam pulse in the presence of weak fringe solenoidal magnetic fields was shown to be important for the planned Neutralized Drift Compression Experiment-II (NDCX-II).

In the **Chapter 5** of this thesis, the collective focusing scheme proposed by S. Robertson [Robertson, 1982] in which a weak magnetic lens provides strong focusing of an intense ion beam pulse carrying an equal amount of neutralizing electron background was discussed. For instance, such a collective focusing lens with a magnetic field strength of several hundred gauss can focus an intense neutralized ion beam within a short distance of several centimeters. The enhanced focusing inside the lens is provided by a strong self-electric field, which is produced by the collective electron dynamics. The chapter then presented results of advanced numerical simulations demonstrating the feasibility of tight final beam focus that can be achieved in the Neutralizing Drift Compression Experiment (NDCX-I) by using a several hundred gauss collective focusing lens instead of a several Tesla conventional magnetic solenoid. The numerical simulations were performed with the LSP particle-in-cell (PIC) code, and the results of the simulations were found to be in very good agreement with analytical predictions. The collective focusing limitations due to possible heating of the co-moving electrons during

transverse compression were discussed. In addition, the original analysis of the collective lens operation, which assumes quasineutrality (provided by $\omega_{ce}<<\omega_{pe}$), and small perturbations of the applied solenoidal magnetic field (provided by $r_b<<c/\omega_{pe}$), was extended to the cases of $\omega_{ce}\geq\omega_{pe}$ and $r_b\geq c/\omega_{pe}$. Here, r_b is the beam radius, ω_{pe} is the electron plasma frequency inside the incident neutralized beam, and ω_{ce} is the electron cyclotron frequency inside the lens. In particular, it was demonstrated for the case where $\omega_{pe}<\omega_{ce}$ that *nonneutral* compression corresponding to an excess of negative charge near the solenoidal axis can occur. The distribution of the radial self-electric focusing field for the case of strong nonneutral compression was calculated. Strong nonlinearities in the radial dependence of the electric field were found, and its influence on the ion beam dynamics in NDCX-I was analyzed. Finally, for the case where $r_b \geq c/\omega_{pe}$, the perturbation in the solenoidal magnetic field produced by the azimuthal component of the electron beam current was calculated self-consistently, and strong nonlinearities in the total magnetic field were demonstrated. However, it was found that even for large values of $r_b\omega_{pe}/c$, the outer edge of the ion beam pulse still experiences efficient collective focusing.

6.2 Future Research

An improved theoretical understating of transport properties of an intense ion beam pulse propagating in an ion driver is critical for applications to ion-beam-driven warm dense matter, high energy physics, and heavy ion fusion. Based on the studies presented in this thesis, several future research tasks can be suggested as follows.

The numerical simulations discussed in **Chapter 2** of this thesis demonstrate self-similar evolution of the beam density profile for a quasiequilibrium beam distribution matched to a periodic focusing lattice. For this case, i.e., self-similar evolution of the beam density with the density profile being approximately constant on elliptical contours [Eqs. (2.43)-(2.44)], analytical expressions for the beam self-fields can be derived for an arbitrary beam density shape function [Sacherer, 1971; Davidson and Qin, 2001a]. Making use of this calculations for the beam self-fields, properties of a matched-beam quasi-equilibrium can now be accurately described using a particle-core model (see Sec. 2.2.5), which requires much less computational effort compared to full particle-in-cell simulations. In particular, the particle-core model with the beam self-field calculated according to [Sacherer, 1971; Davidson and Qin, 2001a] can be used to investigated the higher-order resonance structure, and provide insights into the problem of space-charge transport limits. We would like to emphasize here that although the particle-core model has been previously typically used for analysis of a Kapchinskij-Vladimirskij (KV) matched beam distribution, the present numerical studies demonstrating the self-similar beam density evolution for a wide range of initial (smooth-focusing) beam equilibria

validate the use of the particle-core model for a wide range of beam quasiequlibria matched to a periodic focusing lattice.

In **Chapter 3** of this thesis a novel spectral method for quantitative definition of a beam halo particle is proposed. The method is based on the observation of a bump-on-tail structure, which appears in the betratron frequency distribution of an intense mismatched beam. The bump is located near the half-value of the mismatch oscillations frequency, and in the studies presented here, the linear approximation for the mismatch-oscillation frequency has been used for the "cut-off" frequency when selecting beam halo particles. However, it was pointed out that a few more halo particles can be selected if an improved model including nonlinear effects and accounting for the width and shape of the mismatch oscillations frequency spectrum is employed for determination of the "cut-off" frequency. Improving the criteria for defining a beam halo particle is of particular importance for a more quantitative analysis of beam halo production, and should be the subject of future studies.

In **Chapter 4** ion beam transport through a dense background neutralizing plasma along a solenoidal magnetic field has been investigated. In particular, enhanced ion beam self-focusing in the presence of a weak magnetic field has been found, and the self-focusing force has been calculated for a steady-state regime, assuming infinitely massive beam ions [Eq. 4.57]. It is of particular practical interest to extend the present studies to the case of finite mass of the beam ions, and describe the ion beam pulse shaping self-consistently, including the effects of enhanced ion beam self-focusing. The results of these studies should then be analyzed for the parameters characteristic of the Neutralizing

Drift Compression Experiment-II (NDCX-II), where the effects of enhanced plasma-induced self-focusing can be important. Furthermore, the present studies assume cold plasma electrons and a linear (small-signal) plasma response. It is of great interest to consider nonlinear effects and the thermal effects of the background plasma electrons, and asses their influence on ion beam self-focusing and whistler wave excitation.

In **Chapter 5** the collective focusing of an intense neutralized ion beam pulse was considered. The original analysis of the collective focusing, which assumes quasineutrality provided by $\omega_{ce}<<\omega_{pe}$, was extended to the case of nonneutral compression that can occur for the case where $\omega_{ce}\geq\omega_{pe}$, and a reduced analytical model was developed to describe the distribution of the radial self-electric field. It is of particular interest to apply this analytical model to the self-consistent analysis of the transverse dynamics of an ion beam pulse. Furthermore, the original analysis of the collective focusing, which also assumes small perturbations of the applied solenoidal magnetic field provided by $r_b<<c/\omega_{pe}$, was extended to the case where $r_b\geq c/\omega_{pe}$, and an analytical model was developed to describe the decrease in the total solenoidal magnetic field due to the presence of the neutralized beam self-fields. It is of particular interest to apply the analytical model developed in this thesis to the self-consistent analysis of the collective lens operation in the regime where $r_b\geq c/\omega_{pe}$. Here, we emphasize again that the regimes of collective focusing corresponding to the cases where $r_b\geq c/\omega_{pe}$ and $\omega_{ce}\geq\omega_{pe}$, are of particular importance for laser-production of high-energy ions and ion drivers for high energy physics applications and heavy ion fusion.

Appendix A

Electromagnetic Field Perturbations for the Case of Arbitrary Ratio of ω_{ce}/ω_{pe}

Equations (4.24)-(4.25) can be generalized to the case of an arbitrary ratio of ω_{ce}/ω_{pe}. Assuming $\omega \sim v_b/l_b << \omega_{pe}, \omega_{ce}$ and $l_b >> r_b, \tilde{k}_{em,qs}^{-1}$, after some straightforward algebra one can show that the electromagnetic field perturbations for $0 < x << l_b^2 \tilde{k}_{em,qs}$ are given by

$$\frac{eB_y^W}{m_e \omega_{pe} c} = \frac{2\pi \omega_{pe} \beta_b Z_b}{c n_p \left(\tilde{k}_{qs}^2 - \tilde{k}_{em}^2 \right)} \left(b_{em} + b_{qs} \right), \tag{A1}$$

$$\frac{eE_x^W}{m_e \omega_{pe} c} = \frac{2\pi Z_b \omega_{ce}^2}{c n_p \omega_{pe} \left(\tilde{k}_{qs}^2 - \tilde{k}_{em}^2 \right)} \left(e_{em} + e_{qs} \right), \tag{A2}$$

$$b_{qs,em} = \pm \left(\tilde{k}_{qs,em}^2 + \frac{\omega_{pe}^2}{c^2 \left(1 + \omega_{ce}^2 / \omega_{pe}^2 \right)} \right) \int_0^\infty dk_z n_{\mathbf{k}} \left(\tilde{k}_{qs,em}, k_z \right) \cos\left(k_z \xi \mp \tilde{k}_{qs,em} x \right), \tag{A3}$$

$$e_{qs,em} = \pm \left[\tilde{k}_{qs,em}^2 \Big/ \left(1 + \omega_{ce}^2 / \omega_{pe}^2 \right) \right] \int_0^\infty dk_z n_{\mathbf{k}} \left(\tilde{k}_{qs,em}, k_z \right) \cos\left(k_z \xi \mp \tilde{k}_{qs,em} x \right), \tag{A4}$$

$$\frac{eB_y^{loc}}{m_e \omega_{pe} c} = -i \int_{-\infty}^{\infty} dk_z e^{ik_z \xi} \int_{C_+} dk_x e^{ik_x x} n_{\mathbf{k}} \frac{\omega_{pe} \beta_b Z_b k_x}{c n_p \left(k_x^2 - \tilde{k}_{em}^2 \right) \left(k_x^2 - \tilde{k}_{qs}^2 \right)} \left(k_x^2 + \frac{\omega_{pe}^2 / c^2}{1 + \omega_{ce}^2 / \omega_{pe}^2} \right), \tag{A5}$$

$$\frac{eE_x^{loc}}{m_e\omega_{pe}c} = -i\int_{-\infty}^{\infty} dk_z e^{ik_z\xi} \int_{C_+} dk_x e^{ik_x x} n_{\mathbf{k}} \frac{Z_b k_x^3 \omega_{ce}^2 / \left(1+\omega_{ce}^2/\omega_{pe}^2\right)}{cn_p\omega_{pe}\left(k_x^2-\tilde{k}_{em}^2\right)\left(k_x^2-\tilde{k}_{qs}^2\right)}. \tag{A6}$$

Here, $\tilde{k}_{em,qs}$ are the solutions to the generalized dispersion relation

$$c^4k_x^4\left(1+\frac{\omega_{pe}^2}{\omega_{ce}^2}\right)+\left[\frac{2\omega_{pe}^4}{\omega_{ce}^2}-\frac{\left(1-\beta_b^2\right)\omega_{pe}^2}{\beta_b^2}\right]c^2k_x^2+\frac{\omega_{pe}^6}{\omega_{ce}^2}=0. \tag{A7}$$

Equations (A1)-(A7) describe the electromagnetic field perturbation excited by an ion beam pulse for an arbitrary ratio of ω_{ce}/ω_{pe}, and furthermore for an arbitrary beam velocity, including the case of a relativistic ion beam. The dynamics of the background plasma electrons, however, are assumed to be nonrelativistic, which requires that the beam density be much smaller the plasma density ($n_b<<n_p$).

The onset of wave generation, corresponding to the existence of real solutions to Eq. (A7), is now determined by the condition $\tilde{\alpha}=\omega_{ce}\left(1-\beta_b^2\right)/2\beta_b\omega_{pe}>1$. In the limit where $\tilde{\alpha}>>1$ and $\beta_b<<1$, the solutions to Eq. (A7) can be approximated by $\tilde{k}_{qs}=2\alpha\omega_{pe}\Big/\left[c\left(1+\omega_{ce}^2/\omega_{pe}^2\right)^{1/2}\right]$ and $\tilde{k}_{em}=\omega_{pe}/(2\alpha c)$, where $\alpha=\omega_{ce}/2\beta_b\omega_{pe}$. Making use of Eqs. (A1)-(A6), we can then reproduce the main results obtained earlier in the present paper. Repeating the analysis performed in Sec. 4.3, after some straightforward algebra, we find that the asymptotic time-dependent solution for the critical case corresponding to $\tilde{\alpha}=1$ is given by

$$\frac{eB^y}{m_e\omega_{pe}c}=4\sqrt{\pi}\sqrt{t}\,\frac{\beta_b^2\tilde{k}_c\omega_{pe}Z_b\sin\left(\tilde{k}_c x\right)N_z(z)}{n_p\left(\tilde{k}_c^2+\omega_{pe}^2/c^2\right)\sqrt{\left|\partial^2\tilde{V}_z^{ph}/\partial k_x^2\right|_{k_x=\tilde{k}_c}}}, \tag{A8}$$

$$N_z = \int_0^\infty dk_z \sqrt{k_z}\, n_{\mathbf{k}}\left(\tilde{k}_c, k_z\right)\left[\cos\left(k_z\xi\right) + \sin\left(k_z\xi\right)\right], \tag{A9}$$

where the critical value of the wave vector, $\tilde{k}_c$, corresponding to the solution of Eq. (A7) for $\tilde{\alpha} = 1$, is given by

$$\tilde{k}_c = \left(\frac{1+\beta_b^2}{1-\beta_b^2}\frac{\omega_{pe}^2}{c^2}\frac{1}{\left[1+\omega_{ce}^2/\omega_{pe}^2\right]}\right)^{1/2}, \tag{A10}$$

and the longitudinal component of the wave phase velocity is defined by

$$\tilde{V}_{ph}^z = \frac{\tilde{\omega}_{wh}}{k_z} = \frac{k_x\omega_c}{\sqrt{\left[k_x^2 + \omega_{pe}^2/c^2\right]\left[k_x^2\left(1+\omega_{ce}^2/\omega_{pe}^2\right) + \omega_{pe}^2/c^2\right]}}. \tag{A11}$$

Similarly, repeating the analysis performed in Sec. 4.5.1, after some straightforward algebra one can demonstrate that for a non-relativistic beam, $\beta_b << 1$, with $r_b\tilde{k}_{qs} >> 1$, the total wave-field contribution to the transverse component of the Lorentz force vanishes, and the transverse force produced by the local field perturbation is still determined by Eq. (4.43), i.e.,

$$F_x = Z_b^2 m_e v_b^2 \frac{1}{n_p}\frac{dn_b}{dx}. \tag{A12}$$

Appendix B

Axial Magnetic Field Perturbation and Local Diamagnetic Plasma Response for $\alpha=\omega_{ce}/2\beta_b\omega_{pe}>>1$

Making use of Eq. (4.11), after some straightforward algebra we find for an arbitrary ratio of ω_{ce}/ω_{pe} that the longitudinal component of the magnetic field perturbation is given by $B_z = B_z^W + B_z^{loc}$, where the local component, B_z^{loc}, and the wave component, B_z^W, are specified for $0 < x << l_b^2 \tilde{k}_{em,qs}$ by

$$\frac{eB_z^W}{m_e\omega_{pe}c} = \frac{2\pi Z_b\omega_{ce}\omega_{pe}}{n_p\left(\tilde{k}_{qs}^2 - \tilde{k}_{em}^2\right)}\left(b_z^w + b_z^{qs}\right), \tag{B1}$$

$$b_z^{em,qs} = \left[\tilde{k}_{em,qs}\Big/\left(1+\omega_c^2/\omega_p^2\right)\right]\int_0^\infty dk_z n_{\mathbf{k}}\left(\tilde{k}_{em,qs},k_z\right)\sin\left(k_z z \pm \tilde{k}_{em,qs}x\right), \tag{B2}$$

$$\frac{eB_z^{loc}}{m_e\omega_{pe}c} = \int_{-\infty}^{\infty} dk_z e^{ik_z\xi}\int_{C_+} dk_x e^{ik_x x} n_{\mathbf{k}}\frac{Z_b k_x^2\omega_{ce}\omega_{pe}\Big/\left(1+\omega_{ce}^2/\omega_{pe}^2\right)}{c^2 n_p\left(k_x^2-\tilde{k}_{em}^2\right)\left(k_x^2-\tilde{k}_{qs}^2\right)}. \tag{B3}$$

It follows for the case of a nonrelativistic beam, β_b<<1, propagating through a background plasma with $\alpha = \omega_{ce}/2\beta_b\omega_{pe} >> 1$, that the local z-component of the magnetic field perturbation is much greater than the wave-field z-component, and is given approximately by

$$\frac{eB_z^{loc}}{m_e\omega_{pe}c} \approx -\frac{Z_b\beta_b^2\omega_{pe}}{\omega_{ce}n_p} n_b(x,z), \tag{B4}$$

provided the beam radius r_b satisfies $\tilde{k}_{qs}^{-1} << r_b << \tilde{k}_{em}^{-1}$, or equivalently, $c\left(1+\omega_c^2/\omega_p^2\right)/\left(2\alpha\omega_{pe}\right) << r_b << 2\alpha\, c/\omega_{pe}$ in the limit $\alpha >> 1$. Equation (B4) demonstrates the diamagnetic plasma response, in accordance with the results obtained in the numerical simulations.

For the critical case where $\alpha = \omega_{ce}/2\beta_b\omega_{pe} \approx 1$, assuming a nonrelativistic ion beam, $\beta_b << 1$, after some straightforward algebra it follows from Eqs. (B1)-(B2) that $\Delta\alpha \equiv \left(eB_z/m_ec\right)/\left(2\beta_b\omega_{pe}\right)$ can be estimated by

$$\Delta\alpha \sim Z_b\left(n_b/n_p\right)\left(r_b\omega_{pe}/c\right)\left[\left(1+\Delta\alpha^2\right)-1\right]^{-1/2}, \tag{B5}$$

provided the beam radius is of the order of or smaller than the electron skin depth. Note that in obtaining Eq. (B5), we have used the fact that $\omega_{ce} << \omega_{pe}$, which is required by the resonance condition, $\alpha = \omega_{ce}/2\beta_b\omega_{pe} = 1$, for the case of a nonrelativistic ion beam pulse.

Bibliography

Ahiezer, A. I., Ahiezer, I. A., Polovin, R. V., Sitenko, A. G., and Stepanov, K. N. (1974). *Plasma Electrodynamics*. Nauka, Moscow.

Allen, C. K., Chan, K. C. D., Colestock, P. L., Crandall, K. R., Garnett, R. W., Gilpatrick, J. D., Lysenko, W., Qiang, J., Schneider, J. D., Schulze, M. E., Sheffield, R. L., Smith, H. V., and Wangler, T. P. (2002). Beam-Halo Measurements in High-Current Proton Beams. *Phys. Rev. Lett.* **89**, 214802.

Allen, C. K., and Wangler, T. P. (2002). Beam Halo Definitions Based upon Moments of the Particle Distribution. *Phys. Rev. ST Accel. Beams* **5**, 124202.

Arnold, R. C. (1978). Heavy-Ion Beam Inertial-Confinement Fusion. *Nature* **276**, 19.

Batygin, Y. K. (1996). Adiabatic Matching of a Nonuniform Intense Charged-Particle Beam into the Focusing Channel. *Phys. Rev. E* **54**, 5673.

Berk, H. L., and Pearlstein, L. D. Plasma Return Currents in a Magnetic field.(1976). *Phys. Fluids* **19**, 1831.

Boercker, D. B., Sanders, D. M., Storer, J., and Falabella, S. (1991). Modeling Plasma Flow in Straight and Curved Solenoids. *J. Appl. Phys.* **69**, 115.

Buneman, O. (1952). Circulation in the Flow of Electricity: Dirac's New Variables. *Proc. R. Soc. A* **215**, 346.

Callahan, D. (1996). Chamber Propagation Physics for Heavy Ion Fusion. *Fusion Eng. Design* **32–33**, 441.

Chanell, P. J. (1999). Systematic Solution of the Vlasov–Poisson Equations for Charged Particle Beams. *Phys. Plasmas* **6**, 982.

Chao, A.W. (1993). *Physics of Collective Beam Instabilities in High Energy Accelerators.* John Willey & Sons, Inc., New York.

Chen, P., Dawson, J. M., Huff, R. W., and Katsouleas, T (1985). Acceleration of Electrons by the Interaction of a Bunched Electron Beam with a Plasma. *Phys. Rev. Lett.* **54**, 693.

Chu, K. R., and Rostoker, N. Relativistic Electron Beam Neutralization in a Dense Magnetized Plasma. (1973). *Phys. Fluids* **16**, 1472.

Chung, M., Gilson, E. P., Dorf, M., Davidson, R. C., Efthimion, P. C., and Majeski, R. (2007). Experiments on Transverse Compression of a Long Charge Bunch in a Linear Paul Trap. *Phys. Rev. ST Accel. Beams* **10**, 064202.

Clauser, T., Stagno, V., Variale, V. (1999). Damping Effect in the Beam Envelope Amplitude Oscillations in Mismatched High Intensity Ion Beams. *Proceedings of the 1999 Particle Accelerator Conference*, 1779.

Brown, N. and Reiser, M. (1995). Thermal Equilibrium of Bunched Charged Particle Beams. Phys. Plasmas **2**, 965.

Davidson, R. C. (1976). Vlasov Equilibrium and Nonlocal Stability Properties of an Inhomogeneous Plasma Column. *Phys. Fluids* **19**, 1189.

Davidson, R. C. (1990). *The Physics of Nonneutral Plasmas.* Addison-Wesley, Reading, Massachusetts.

Davidson, R. C., Lee, W. W., and Stoltz, P. (1998). Statistically-Averaged Rate Equations for Intense Nonneutral Beam Propagation though a Periodic Solenoidal Focusing Field Based on the Nonlinear Vlasov-Maxwell Equations. *Phys. Plasmas* **5**, 279.

Davidson, R. C. and Chen, C. (1998). Kinetic Description of Intense Nonneutral Beam Propagation through a Periodic Solenoidal Focusing Field Based on the Nonlinear Vlasov-Maxwell Equations. *Particle Accelerators* **59**, 175.

Davidson, R. C. and Qin, H. (1999). Single-Parameter Characterization of the Thermal Equilibrium Density Profile for Intense Non-Neutral Charged Particle Beams. *Phys. Rev. ST Accel. Beams* **2**, 114401.

Davidson, R. C., Qin, H., and Channell, P. J. (1999). Periodically-Focused Solutions to the Nonlinear Vlasov-Maxwell Equations for Intense Beam Propagation through an Alternating-Gradient Field. *Phys. Rev. ST Accel. Beams* **2**, 074401.

Davidson, R. C. and Qin, H. (2001a). *Physics of Intense Charged Particle Beams in High Energy Accelerators*. World Scientific, Singapore.

Davidson, R. C. and Qin. H. (2001b). Guiding-Center Vlasov-Maxwell Description of Intense Beam Propagation through a Periodic Focusing Field. *Phys. Rev. ST Accel. Beams* **4**, 104401.

Davidson, R. C. (2002). Frontiers in High Energy Density Physics - The X-Games of Contemporary Science. *Board on Physics and Astronomy News, 1, December, 2002, National Academies Press*.

Davidson, R. C. and Qin, H. (2005). Kinetic Description of Neutralized Drift Compression and Transverse Focusing of Intense Ion Charge Bunches. *Phys. Rev. ST Accel. Beams* **8**, 064201.

Davidson, R. C., Dorf, M. A., Kaganovich, I. D., Qin, H., Sefkow, A. B., Startsev, E. A., Welch, D. R., Rose, D. V., and Lund, S. M. (2009). Survey of Collective

Instabilities and Beam-Plasma Interactions in Intense Heavy Ion Beams. *Nucl. Instrum. Methods Phys. Res. A* **606,** 11.

Dorf, M., Davidson, R. C., Startsev, E. (2006). Transverse Compression of an Intense Ion Beam Propagating through an Alternating-Gradient Quadrupole Lattice. *Phys. Rev. ST Accel. Beams* **9**, 034202.

Dorf, M., Davidson, R. C., Startsev, E. (2007). Particle-in-Cell Simulations of Halo Particle Production in Intense Charged Particle Beams Propagating Through a Quadrupole Focusing Field with Varying Lattice Amplitude. *Proceedings of the 2007 Particle Accelerator Conference*, 3669.

Dorf, M., Davidson, R. C., Startsev, E., and Qin, H. (2009a). Adiabatic Formation of a Matched-Beam Distribution for an Alternating-Gradient Quadrupole Lattice. *Phys. Plasmas*, **16**, 123107.

Dorf, M., Davidson, R. C., Startsev, E., and Qin, H. (2009b). Adiabatic Formation and Properties of a Quasi-Equilibrium Beam Distribution Matched to a Periodic Focusing Lattice. *Proceedings of the 2009 Patricle Accelerator Conference,* in press.

Dorf, M., Kaganovich, I. D., Startsev, E., and Davidson, R. C. (2009c). Enhanced Self-Focusing of an Ion Beam Propagating through a Background Plasma along a Solenoidal Magnetic Field. *Phys. Rev. Lett.* **103**, 075003.

Dorf, M., Kaganovich, I. D., Startsev, E., and Davidson, R. C. (2010). Whistler Wave Excitation and Effects of Self-Focusing on Ion Beam Propagation through a Background Plasma along a Solenoidal Magnetic Field. *Phys. Plasmas*, **17**, 023103.

Efthimion, P. C., Gilson, E. P., Davidson, R.C., Grisham, L., Logan, B. G., Seidl, P. A., Waldron, W., and Yu, S. S. (2007). Ferroelectric Plasma Source for Heavy Ion Beam Charge Neutralization. *Nucl. Instrum. Methods Phys. Res. A* **577,** 203.

Fraiman, G. M. (2001). private communications.

Friedman, A., Grote, D. P., and Haber, I. (1992). Three-Dimensional Particle Simulation of Heavy-Ion Fusion Beams. *Phys. Fluids B* **4**, 2203.

Friedman, A. (2007). Figure adopted from the contributed talk presented at 49th Annual Meeting of the American Physical Society, Division of Plasma Physics, abstract ID: BAPS.2007.DPP.BO3.4.

Friedman, A., Barnard, J. J., Briggs, R. J., Davidson, R. C., Dorf, M., Grote, D. P., Henestroza, E., Lee, E. P., Leitner, M. A., Logan, B. G., Sefkow, A. B., Sharp, W. M., Waldron, W. L., Welch, D. R., and Yu, S. S. (2009). Toward a Physics Design for NDCX-II, an Ion Accelerator for Warm Dense Matter and HIF Target Physics Studies. *Nucl. Instrum. Methods Phys. Res. A* **606,** 6.

Friedman, A., Barnard, J. J., Cohen, R. H., Grote, D. P., Lund, S. M., Sharp, W. M., Faltens, A., Henestroza, E., Jung, J. –Y., Kwan, J. W., Lee, E. P., Leitner, M. A., Logan, B. G., Vay, J.-L., Waldron, W. L., Davidson, R. C., Dorf, M., Gilson, E. P., and Kaganovich, I. D. (2010). Beam Dynamics of the Neutralized Drift Compression Experiment-II – a Novel Pulse-Compressing Ion Accelerator. *Phys. Plasmas* **17**, 056704.

Gilson, E. P., Davidson, R. C., Efthimion, P. C., and Majeski, R. (2004). Paul Trap Simulator Experiment to Simulate Intense Beam Propagation in Alternating Gradient Transport Systems. *Phys. Rev. Lett.* **92**, 155002.

Gilson, E. P., Chung, M., Davidson, R. C., Efthimion, P. C., Majeski, R., and Startsev, E. A. (2005). Simulation of Long-Distance Beam Propagation in the Paul Trap Simulator Experiment. *Nucl. Instrum. Methods Phys. Res. A* **544**, 171.

Gilson, E. P., Chung, M., Davidson, R. C., Dorf, M., Efthimion, P. C., and Majeski, R. (2006). Experimental Simulations of Beam Propagation over Large Distances in a Compact Linear Paul Trap. *Phys. Plasmas* **13**, 056705.

Gilson, E. P., Chung, M., Davidson, R. C., Efthimion, P. C., and Majeski, R. (2007). Transverse Beam Compression on the Paul Trap Simulator Experiment. *Phys. Rev. ST Accel. Beams* **10**, 124201.

Gluckstern, R. L. (1994). Analytical Model for Halo Formation in High Current Ion Linacs. *Phys. Rev. Lett*. **73**, 1247.

Groening, L., Barth, W., Bayer, W., Clemente, G., Dahl, L., Forck, P., Gerhard, P., Hofmann, I., Kaiser, M. S., Maier, M., Mickat, S., Milosic, T., Jeon, D., and Uriot, D. (2009). Experimental Evidence of the 90° Stop Band in the GSI UNILAC. *Phys. Rev. Lett.* **102**, 234801.

Grote, D. P., Friedman, A., Haber, I., Fawley, W., and Vay, J. L. (1998). New Developments in WARP: Progress Toward End-to-End Simulation. *Nucl. Instrum. Methods Phys. Res. A* **415**, 428.

Gruzinov, A. (2001). Gamma-Ray Burst Phenomenology, Shock Dynamo, and the First Magnetic Fields. *Astrophys. J. Lett.* **563**, L15.

Hahn, K., and Lee, E. (1996). A Study of Stripped Pinched-Beam Transport for Heavy Ion Fusion. *Fusion Eng. Des.* **32–33**, 417.

Harres, K., Alber, I., Tauschwitz, A., Bagnoud, V., Daido, H., Günther, M., Nürnberg, F., Otten, A., Schollmeier, M., Schütrumpf, J., Tampo, M., and Roth, M. (2010).

Beam Collimation and Transport of Quasineutral Laser-Accelerated Protons by a Solenoid Field. *Phys. Plasmas* **17**, 023107.

Henestroza, E., Eylon, S., Roy, P. K., Yu, S. S., Anders, A., Bieniosek, F. M., Greenway, W. G., Logan, B. G., MacGill, R. A., Shuman, D. B., Vanecek, D. L., Waldron, W. L., Sharp, W. M., Houck, T. L., Davidson, R. C., Efthimion, P. C., Gilson, E. P., Sefkow, A. B., Welch, D. R., Rose, D. V., and Olson, C. L. (2004). Design and Characterization of a Neutralized-Transport Experiment for Heavy-Ion Fusion. *Phys. Rev. ST Accel. Beams* **7**, 083501.

HIFS-VNL (2008). White Paper on Heavy-Ion-Beam-Driven High Energy Density Physics and Inertial Fusion. Digital Edition available at http://hifweb.lbl.gov/public/papers/HIFSwhitepaper.pdf.

Horioka, K., Kawamura, T., Nakajima, M., Kondo, K., Ogawa, M., Oguri, Y., Hasegawa, J., Kawata, S., Kikuchi, T., Sasaki, T., Murakami, M., Takayama, K. (2009). Activities on Heavy Ion Inertial Fusion and Beam-Driven High Energy Density Science in Japan. *Nucl. Instrum. Methods Phys. Res. A* **606**, 1.

Hoffmann, D. H. H., Fortov, V. E., Kuster, M., Mintsev, V., Sharkov, B. Y., Tahir, N. A., Udrea, S., Varentsov, D., Weyrich, K. (2009). High Energy Density Physics Generated by Intense Heavy Ion Beams. *Astrophys. Space. Sci.* **322**, 167.

Hofmann, I., Laslett, L. J., Smith, L., and Haber, I. (1983). Stability of the Kapchinskij-Vladimirskij (K-V) Distribution in Long Periodic Transport Systems. *Part. Accel.* **13**, 145.

Humphries, S. Jr. (1978). Intense Ion-Beam Neutralization in Free Space. *Appl. Phys. Lett.* **32**, 792.

Humphries, S. Jr., Lockner, T. R., Poukey, J. W., and Quintenz, J. P. (1981). One-Dimensional Ion-Beam Neutralization by Cold Electrons. *Phys. Rev. Lett.* **46**, 995.

Ikegami, M. (1999). Particle-Core Analysis of Mismatched Beams in a Periodic Focusing Channel. *Phys. Rev. E* **59**, 2330.

Jeon, D., Groening, L., and Franchetti, L. Fourth Order Resonance of a High Intensity Linear Accelerator. *Phys. Rev. ST Accel. Beams* **12**, 054204.

Johnson, J. C., Angelo, N. D'., and Merlino, R. L. (1988). Ion-Beam Focusing in a Double-Plasma Device. *IEEE Trans. Plasma Sci.* **16,** 590.

Joshi, C. (2007). The Development of Laser- and Beam-Driven Plasma Accelerators as an Experimental Field. *Phys. Plasmas* **14**, 055501.

Kapchinskij, I. M. and Vladimirskij, V. V. (1959). Limitations of Proton Beam Current in a Strong-Focusing Linear Accelerator Associated with the Beam Space Charge. In *Proceedings of the International Conference on High Energy Accelerators and Instrumentation*, page 274. CERN Scientific Information Service, Geneva.

Kaganovich, I. D., Shvets, G., Startsev, E., and Davidson, R. C. (2001). Nonlinear Charge and Current Neutralization of an Ion Beam Pulse in a Pre-Formed Plasma. *Phys. Plasmas* **8**, 4180.

Kaganovich, I. D., Startsev, E. A., Sefkow, A. B., and Davidson, R. C. (2007). Charge and Current Neutralization of an Ion Beam Pulse Propagating in a Background Plasma along a Solenoidal Magnetic Field. *Phys. Rev. Lett.* **99**, 235002.

Kaganovich, I. D., Startsev, E. A., Sefkow, A. B., and Davidson, R. C. (2008). Controlling Charge and Current Neutralization of an Ion Beam Pulse in a

Background Plasma by Application of a Solenoidal Magnetic Field: Weak Magnetic Field Limit. *Phys. Plasmas.* **15**, 103108

Kaganovich, I. D., Davidson, R. C., Dorf, M., Startsev, E. A., Sefkow, A. B., Barnard, J. J., Friedman, A., Lee, E. P., Lidia, S. M., Logan, B. G., Roy, P. K., Seidl, P. A., and Welch, D. R. (2009). Designing Neutralized Drift Compression for Focusing of Intense Beam Pulses in Background Plasma. *Proceedings of the 2009 Patricle Accelerator Conference,* in press.

Kaganovich, I. D., Davidson, R. C., Dorf, M. A., Startsev, E. A., Sefkow, A. B., Lee, E. P., and Friedman A. (2010). Physics of Neutralization of Intense High-Energy Ion Beam Pulses by Electrons. *Phys. Plasmas* **17**, 056703.

Krafft, C., Thévenet, P., Matthieussent, G., Lundin, B., Belmont, G., Lembège, B., Solomon, J., Lavergnat, J., and Lehner, T. (1994). Whistler Wave Emission by a Modulated Electron Beam. *Phys. Rev. Lett.* **72**, 649.

Krafft, C. and Volokitin, A. (1998). Nonlinear Interaction of Whistler Waves with a Modulated Thin Electron Beam. *Phys. Plasmas* **5**, 4243.

Krafft, C. and Starodubtsev, M. (2002). Whistler Excitation by Electron Beams in Laboratory Plasmas. *Planet. Space Sci.* **50**, 129, and references therein.

Krafft, G. A., Kim, C. H., and Smith, L. (1985). The LBL Neutralized Beam Focusing Experiment. *Nuclear Science, IEEE Transactions on* **32**, 2486.

Krafft, G. A. (1986). *Collective Focusing of Intense Nonrelativistic Ion Beams by Co-Moving Electrons.* U.C. Berkeley PhD thesis.

Kraft, R., Kusse, B., and Moschella, J. (1987). Collective Focusing of an Intense Pulsed Ion Beam. *Phys. Fluids* **30**, 245.

Kraft, R. and Kusse, B. (1987). Observations of the Thermalization of the Neutralizing Electrons in Intense Ion Beams. *J. Appl. Phys.* **61**, 2425.

Kwan, J. (2004). Ion Sources for Heavy Ion Fusion. In *The Physics and Technology of Ion Sources*, edited by I. G. Brown, page 311. WILEY-VCH Verlag GmbH & Co. KGaA, Weinheim.

Lavergnat, J. and Pellat, R. (1979). High-Frequency Spontaneous Emission of an Electron Beam Injected Into the Ionospheric Plasma. *J. Geophys. Res.* **84**, 12.

Lawson, J. D. (1958). Perveance and the Bennett Pinch Relation in Partially Neutralized Electron Beams. *J. Electron. Control* **5**, 146.

Lee, R., and Sudan, R. N. (1971). Return Current Induced by a Relativistic Beam Propagating in a Magnetized Plasma. *Phys. Fluids* **14**, 1213.

Lifshitz, E. M., and Pitaevskii, L. P. (1981). *Physical Kinetics.* Pergamon Press, Oxford.

Logan, B. G., Bieniosek, F. M., Celata, C. M., Coleman, J., Greenway, W., Henestroza, E., Kwan, J. W., Lee, E. P., Leitner, M., Roy, P. K., Seidl, P. A., Vay, J.-L., Waldron, W. L., Yu, S. S., Barnard, J. J., Cohen, R. H., Friedman, A., Grote, D. P., Kireeff Covo, M., Molvik, A. W., Lund, S. M., Meier, W. R., Sharp, W., Davidson, R. C., Efthimion, P. C., Gilson, E. P., Grisham, L., Kaganovich, I. D., Qin, H., Sefkow, A. B., Startsev, E.A., Welch, D., Olson, C. (2007). Recent US Advances in Ion-Beam-Driven High Energy Density Physics and Heavy Ion Fusion. *Nucl. Instrum. Methods Phys. Res. A* **577**, 1.

LSP (1999). LSP is a software product of ATK Mission Research, Albuquerque, NM 87110.

Lund, S. M. and Bukh, B. (2004). Stability Properties of the Transverse Envelope Equations Describing Intense Ion Beam Transport. *Phys. Rev. ST Accel. Beams* **7**, 024801.

Lund, S. M. and Chawla, S. R. (2006). Space-Charge Transport Limits of Ion Beams in Periodic Quadrupole Focusing Channels. *Nucl. Instrum. Methods Phys. Res. A* **561**, 203.

Lund, S. M., Kikuchi, T., and Davidson, R. C. (2009). Generation of Initial Vlasov Distributions for Simulation of Charged Particle Beams With High Space-Charge Intensity. *Phys. Rev. ST Accel. Beams,* in press.

Medvedev, M. V., Fiore, M., Fonseca, R. A., Silva, L. O., and Mori, W. B. (2005). Long-Time Evolution of Magnetic Fields in Relativistic Gamma-Ray Burst Shocks. *Astrophys. J. Lett.* **618**, L75.

Okamoto, H., and Ikegami, M. (1997). Simulation Study of Halo Formation in Breathing Round Beams. *Phys. Rev. E* **55**, 4694.

Oliver, B. V., Ryutov, D. D., and Sudan, R. N. (1994). Current Neutralization and Focusing of Intense Ion Beams with a Plasma-Filled Solenoidal Lens. I. *Phys. Plasmas* **1**, 3383.

Ottinger, P. F., Young, F. C., Stephanakis, S. J., Rose, D. V., Neri, J. M., Weber, B. V., Myers, M. C., Hinshelwood, D. D., Mosher, D., Olson, C. L., Welch, D. R. (2000). Self-Pinched Transport of an Intense Proton Peam. Phys. Plasmas **7**, 346.

Prost, L. R., Seidl, P. A., Bieniosek, F. M., Celata, C. M., Faltens, A., Baca, D., Henestroza, E., Kwan, J.W., Leitner, M., Waldron, W. L., Cohen, R., Friedman,

A., Grote, D., Lund, S. M., Molvik, A.W., and Morse, E. (2005). High Current Transport Experiment for Heavy Ion Inertial Fusion. *Phys. Rev. ST Accel. Beams* **8**, 020101.

Qiang, J., Colestock, P. L., Gilpatrick, D., Smith, H.V., Wangler, T. P., Schulze, M. E. (2002). Macroparticle Simulation Studies of a Proton Beam Halo Experiment. *Phys. Rev. ST Accel. Beams* **5**, 124201.

Qin, H., Davidson, R. C., Barnard, J. J., and Lee, E. P. (2004). Drift Compression and Final Focus for Intense Heavy Ion Beams with Nonperiodic, Time-Dependent Lattice. *Phys. Rev. ST Accel. Beams* **7**, 104201.

Qin, H., Davidson, R. C., and Startsev E. (2007). Nonlinear δf Particle Simulations of Collective Excitations and Energy-Anisotropy Instabilities in High-Intensity Bunched Beams**.** *Phys. Rev. ST Accel. Beams* **10**, 064201.

Qin, H., Davidson, R. C., and Startsev E. (2008). Weight Growth due to Resonant Simulation Particles and a Modified δf Algorithm with Smooth Switching Between δf and Total-f Methods. *Phys. Plasmas* **15**, 063101.

Reiser, M. (1994). *Theory and Design of Charged Particle Beams.* Wiley, New York.

Robertson, S. (1982). Collective Focusing of an Intense Ion Beam. *Phys. Rev. Lett.* **48**, 149.

Roberston, S. (1983). Magnetic Guiding, Focusing and Compression of an Intense Charge-Neutral Ion Beam. *Phys. Fluids* **26**, 1129.

Robertson, S. (1986). Collective Focusing of a Charge-Neutral Ion Beam with Warm Electrons. *J. Appl. Phys.* **59**, 1765.

Rosinskii, S. E., and Rukhlin, V. G. (1973). Magnetic and Charge Neutralization of an Electron Beam Injected into a Magnetoactive Plasma. *Sov. Phys. JETP* **37**, 436.

Roy, P. K., Yu, S. S., Henestroza, E., Anders, A., Bieniosek, F. M., Coleman, J., Eylon, S., Greenway, W. G., Leitner, M., Logan, B. G., Waldron, W. L., Welch, D. R., Thoma, C., Sefkow, A. B., Gilson, E. P., Efthimion, P. C., and Davidson, R. C. (2005). Drift Compression of an Intense Neutralized Ion Beam. *Phys. Rev. Lett*. **95**, 234801.

Roy, P. K., Seidl, P. A., Anders, A., Bieniosek, F. M., Coleman, J. E., Gilson, E. P., Greenway, W., Grote, D. P., Jung, J. Y., Leitner, M., Lidia, S. M., Logan, B. G., Sefkow, A. B., Waldron, W. L., Welch, D. R. (2009). A Space-Charge-Neutralizing Plasma for Beam Drift Compression. *Nucl. Instrum. Methods Phys. Res. A* **606,** 22.

Sefkow, A. B. (2007). *Current Density Compression of Intense Ion Beams.* Princeton University PhD thesis.

Sefkow, A. B., and Davidson R. C. (2007). Advanced Numerical Studies of the Neutralized Drift Compression of Intense Ion Beam Pulses. *Phys. Rev. ST Accel. Beams* **10**, 100101.

Sefkow, A. B., Davidson, R. C., and Gilson, E. P. (2008). Advanced Plasma Flow Simulations of Cathodic-Arc and Ferroelectric Plasma Sources for Neutralized Drift Compression Experiments. *Phys. Rev. ST Accel. Beams* **11**, 070101.

Sefkow, A. B., Davidson, R. C., Gilson, E. P., Kaganovich, I. D., Anders, A., Coleman, J., Letner, M., Lidia, S. M., Roy, P. K., Seidl, P. A., Waldron, P. L., Yu,

S. S., and Welch, D. R. (2009). Simulations and Experiments of Intense Ion Beam Current density in Space and Time. *Phys. Plasmas* **16,** 056701.

Seidl, P. A., Anders, A., Bieniosek, F. M., Barnard, J. J., Calanog, J., Chen, A. X., Cohen, R. H., Coleman, J. E., Dorf, M., Gilson, E. P., Grote, D. P., Jung, J. Y., Leitner, M., Lidia, S. M., Logan, B. G., Ni, P., Roy, P. K., Van den Bogert, K., Waldron, W. L., and Welch, D. R. (2009). Progress in Beam Focusing and Compression for Warm-Dense Matter Experiments. *Nucl. Instrum. Methods Phys. Res. A* **606,** 75.

Sharkov, B. Yu. (2007). Overview of Russian Heavy-Ion Inertial Fusion Energy Program. *Nucl. Instrum. Methods Phys. Res. A* **577,** 14.

Sharp, W. M., Callahan, D. A., Tabak, M., Yu, S. S., Peterson, P. F., Rose, D. V., and Welch, D.R. (2004). Chamber-Transport Simulation Results for Heavy-Ion Fusion Drivers. *Nucl. Fusion* **44**, 221.

Snavely, R. A., Key, M. H., Hatchett, S. P., Cowan, T. E., Roth, M., Phillips, T. W., Stoyer, M. A., Henry, E. A., Sangster, T. C., Singh, M. S., Wilks, S. C., MacKinnon, A., Offenberger, A., Pennington, D. M., Yasuike, K., Langdon, A. B., Lasinski, B. F., Johnson, J., Perry, M. D., and Campbell, E. M. (2000). Intense High-Energy Proton Beams from Petawatt-Laser Irradiation of Solids. *Phys. Rev. Lett.* **85**, 2945.

Startsev E., Davidson, R. C., and Qin, H. (2007). Collective Temperature Anisotropy Instabilities in Intense Charged Particle Beams. *Phys. Plasmas* **14**, 056705.

Startsev, E. A., Davidson, R. C., and Dorf, M. (2008). Streaming Instabilities of Intense Charged Particle Beams Propagating along a Solenoidal Magnetic Field in a Background Plasma. *Phys. Plasmas* **15**, 062107.

Startsev, E. A. and Davidson, R. C. (2009). Dynamics of Electromagnetic Two-Stream Interaction Processes During Longitudinal and Transverse Compression of an Intense Ion Beam Pulse Propagating Through Background Plasma. *Nucl. Instrum. Methods Phys. Res. A* **606**, 42.

Startsev, E., Davidson, R. C., and Dorf, M. (2009). Approximate Matched Kinetic Quasi-Equilibrium Solution for an Intense Charged Particle Beam Propagating through a Periodic Focusing Quadrupole Focusing Lattice. *Submitted for publication*.

Strasburg, S. and Davidson, R. C. (2000). Production of Halo Particles by Excitation of Collective Modes in High-Intensity Charge Particle Beams. *Phys. Rev. E* **61**, 5753.

Strasburg, S. and Davidson, R. C. (2001). Warm-Fluid Collective Mode Excitations in Intense Charged Particle Beams with Nonlinear Equilibrium Self-Fields: Test Particle Simulations. *Nucl. Instrum. Methods Phys. Res. A* **464**, 524.

Stoltz, P. H., Davidson, R. C., and Lee, W. W. (1999) Nonlinear δF Simulation Studies of High-Intensity Ion Beam Propagation in a Periodic Focusing Field. *Phys. Plasmas* **6**, 298.

Struckmeier, J. and M. Reiser, M. (1984). Theoretical Studies of Envelope Oscillations and Instabilities of Mismatched Intense Charged-Particle Beams in Periodic Focusing Channels. *Part. Accel*. **14**, 227.

Tiefenback, M. G. and Keffe, D. (1985). Measurements of Stability Limits for a Space-Charge-Dominated Ion Beam in a Long A. G. Transport Channel. *IEEE Trans. Nucl. Sci.* **NS-32**, 2483.

Tiefenback, M. G. (1986). *Space-Charge Limits on the Transport of Ion Beams.* U.C. Berkeley PhD thesis and Lawrence Berkeley Lab Report LBL- 22465.

Variale, V. (2001). Fast Damping in Mismatched High Intensity Beam Transportation. *Phys. Rev. ST Accel. Beams* **4**, 084201.

Volokitin, A., Krafft, C., and Matthieussent, G. (1995). Whistler Waves Produced by a Modulated Electron Beam: Electromagnetic Fields in the Linear Approach. *Phys. Plasmas.* **2**, 4297.

Volokitin, A., Krafft, C., and Matthieussent, G. (1997). Whistler Waves Emission by a Modulated Electron Beam: Nonlinear theory. *Phys. Plasmas.* **4**, 4126.

Wangler, T. P., Crandall, K. R., Ryne, R., and Wang, T. S. (1998). Particle- Core Model for Transverse Dynamics of Beam Halo. *Phys. Rev. ST Accel. Beams* **1**, 084201.

Wangler, T. P., and Crandall, K. R. (2000). Beam Halo in Proton Linac Beams. *Proceedings of the XX International Linac Conference*, 341.

Welch, D. R., Rose, D. V., Sharp, W. M., Olson, C. L., and Yu S. S. (2002). Effects of Preneutralization on Heavy Ion Fusion Chamber Transport. *Laser Particle Beams* **20**, 621.

Welch, D. R., Rose, D. V., Genoni, T. C., Yu, S. S., and Barnard J. J. (2005). Simulations of Neutralized Final Focus. *Nucl. Instrum. Methods Phys. Res. A* **544**, 236.

Yu, S. S., Abbott, R. P., Bangerter, R. O., Barnard, J. J., Briggs, R. J., Callahan, D., Celata, C. M., Davidson, R., Debonnel, C. S., Eylon, S., Faltens, A., Friedman, A., Grote, D. P., Heitzenroeder, P., Henestroza, E., Kaganovich, I., Kwan, J. W., Latkowski, J. F., Lee, E. P., Logan, B. G., Peterson, P. F., Rose, D., Roy, P. K., Sabbi, G.-L., Seidl, P. A., Sharp W. M., and Welch, D. R. (2005). Heavy Ion Fusion (HIF) Driver Point Designs. *Nucl. Instrum. Methods Phys. Res. A* **544**, 294.